

Interfacial Phenomena of Liquids in Contact with Dense CO₂

Vom Promotionsausschuss der
Technischen Universität Hamburg-Harburg
zur Erlangung des akademischen Grades

Doktor-Ingenieurin

genehmigte Dissertation

Von
Yuliana Sutjiadi-Sia
aus Makassar
2008

1. Gutachter : Prof.Dr.-Ing. R. Eggers
2. Gutachter : Prof.Dr.-Ing. S. Kabelac
Prüfungsausschussvorsitzender : Prof.Dr.Dr.h.c. F. Keil
Tag der mündlichen Prüfung : 12.12.2007

Berichte aus der Verfahrenstechnik

Yuliana Sutjadi-Sia

**Interfacial Phenomena
of Liquids in Contact with Dense CO₂**

Shaker Verlag
Aachen 2008

Bibliographic information published by the Deutsche Nationalbibliothek

The Deutsche Nationalbibliothek lists this publication in the Deutsche Nationalbibliografie; detailed bibliographic data are available in the Internet at <http://dnb.d-nb.de>.

Zugl.: Hamburg-Harburg, Techn. Univ., Diss., 2007

Copyright Shaker Verlag 2008

All rights reserved. No part of this publication may be reproduced, stored in a retrieval system, or transmitted, in any form or by any means, electronic, mechanical, photocopying, recording or otherwise, without the prior permission of the publishers.

Printed in Germany.

ISBN 978-3-8322-7072-8

ISSN 0945-1021

Shaker Verlag GmbH • P.O. BOX 101818 • D-52018 Aachen

Phone: 0049/2407/9596-0 • Telefax: 0049/2407/9596-9

Internet: www.shaker.de • e-mail: info@shaker.de

Acknowledgement

If I have seen further, it is by standing upon the shoulders of giants.

Isaac Newton

This thesis is the result of my work as Ph.D. student at the Institute for Thermal Process Engineering, Heat and Mass Transfer at the Hamburg University of Technology in Germany. The research work was a project of DFG (German Research Community) which was conducted in cooperation with the Institute for Thermodynamics at the Helmut Schmidt University, University of the Federal Armed Forces Hamburg.

First of all, I would like to express my deep gratitude to my supervisor, Prof. Dr.-Ing. R. Eggers for giving me the opportunity to work in his group, for the valuable discussions despite his full schedule, for the unfailing motivation and for his openness in listening to some new and not so new research ideas. To Prof. Dr.-Ing. S. Kabelac from the Helmut Schmidt University, many thanks for being the co-evaluator of this thesis, and for proofreading and giving me suggestions on my manuscript for the publication of one part of this work. My sincere gratitude to Prof. Dr. Dr. h.c. F. Keil who chaired the examination committee.

The pleasant working atmosphere in Harburg has helped me a lot to endure life when the research did not deliver the desired results, and enriched my horizon about how a research community works. I am indebted to all my colleagues for their outstanding cooperation, the help they provided for me whenever it was needed and the coffee-break times which brought both fruitful as well as non-scientific significant discussions.

I wish to mention Dr.-Ing. Philip Jaeger who helped me a lot in revising various of my manuscripts which I prepared for the final report of the project, and also on the research proposal submitted to DFG, and papers prepared for conferences. My sincere thanks to Dr.-Ing. Dagmar Dittmar and Dr.-Ing. Henning Marckmann who taught me at the beginning about the field of work, Bärbel Mietzner-Boldt for technical support and Pablo Zacchi for the pleasant atmosphere in the office. For various fruitful academic discussions I would like to thank Dr.-Ing. Philip Jaeger, Dr.-Ing. Dagmar Dittmar and Dr.-Ing. Bastian Arendt.

This work would have not reached its final state without the support of my Master's thesis students and those who helped me as student assistants. They were Karin Dietl, Christian Schacht, Niels Moser, Korhan Cinar, Tania Sainz Martin and Zulema Sanz Raliegos.

Finally, my grateful thanks to my parents, aunts and family in Indonesia who enabled me the study in Germany and without whose support I would have never completed this thesis. To all my friends in Hamburg, thank you.

謹以本書獻給我的父母與姑姑

To my parents and aunts

Contents

1	INTRODUCTION AND AIM OF WORK	1
2	INTERFACIAL TENSION	5
2.1	Thermodynamical Background	8
2.2	Pendant Drop Fundamental Equation	13
2.3	Experimental Setup	17
2.3.1	Interfacial Tension at High Pressure Condition	17
2.3.2	Density at High Pressure Condition	18
2.4	Drop Phenomena	20
2.5	Interfacial Tension Results	23
2.5.1	Static Interfacial Tension	24
2.5.2	Interfacial Tension as Mass Transfer Proceeds	25
3	WETTING CHARACTERISTICS OF A SESSILE DROP	31
3.1	Theoretical Background	32
3.2	Experimental Setup	35
3.3	Some Remarks	37
3.4	Static Wetting Angles	40
3.5	Dynamic Wetting Angles	43
4	ON THE SOLID-VAPOUR INTERFACIAL TENSION	47
4.1	Theoretical Background according to Good and Girifalco	48
4.1.1	Free Energy of Adhesion and Cohesion	48
4.1.2	Quasi-continuum Model	50
4.1.3	Intermolecular Potential Functions	52
4.2	Solid-Vapour Interfacial Tension of Teflon, Glass and Steel Against Carbon Dioxide	57
4.2.1	First Attempt	57
4.2.2	Subsequent Improvements	64
4.3	Some Remarks	66

5	LIQUID RIVULET GEOMETRY	69
5.1	Introduction	69
5.2	Experimental Setup	71
5.3	Qualitative Results	74
5.4	Thickness and Width of Water Rivulet	76
5.5	Theory on Rivulet-wetting Angle	78
5.6	Water Rivulet-wetting Angle	80
5.7	Rivulet Instability	83
6	FLUID DYNAMICS OF FALLING FILM	85
6.1	Nusselt Film Condensation Theory	85
6.2	Wall Model	88
6.3	A Comparison of Measured and Calculated Mean Velocity	88
6.4	Parabolic Velocity Profile	89
6.5	Tau Model	94
6.5.1	Wetting Angle up to 90°	94
6.5.2	Linearization of the Velocity Profiles	100
6.5.3	Wetting Angle above 90°	103
6.6	List of Equations	108
7	VELOCITY PROFILE AND MEAN FILM VELOCITY	113
7.1	Velocity Profile in the Film Phase	114
7.1.1	Wetting Angle up to 90°	115
7.1.2	Wetting Angle above 90°	117
7.2	Mean Film Velocity: Theoretical Background	120
7.2.1	Wetting Angle up to 90°	120
7.2.2	Wetting Angle Above 90°	123
7.3	Experimental and Calculated Mean Velocity	125
7.4	Interdependency of Mass Transfer and Falling Film Thickness	129
7.5	List of Equations	132

8	VELOCITY BOUNDARY LAYER	135
8.1	The Thickness	135
8.2	Fluid Dynamics	136
8.2.1	Wetting Angle up to 90°	136
8.2.2	Wetting Angle above 90°	138
8.3	Velocity Profile	143
8.3.1	Wetting Angle up to 90°	143
8.3.2	Wetting Angle above 90°	144
8.4	The Influence of Fluid Dynamics and Material Properties	146
8.4.1	Constant Film Thickness	148
8.4.2	Constant Mean Velocity	150
8.5	List of Equations	153
9	SHEAR STRESS EXERTED AT RIVULET AND FILM SURFACE	155
9.1	Theoretical Background	155
9.1.1	Wetting Angle up to 90°	155
9.1.2	Wetting Angle above 90°	157
9.2	Mean Surface Shear Stress	159
9.3	List of Equations	161
10	BIBLIOGRAPHY	163
11	APPENDIX	177
11.1	Single Drop	177
11.2	Rivulet	186

Nomenclature

Latin Symbols

a	-	van der Waals attractive constant
A	m^2	Area, cross-section area
A	-	Attractive constant in Lennard Jones potential
b	mm	Half of rivulet width
C	-	Repulsive constant in Lennard Jones potential
C_0	$\frac{cm}{s}$	Integration constant
C_1	$\frac{1}{s}$	Integration constant
f	$\frac{J}{m^2}$	Helmholtz free energy per unit area
f	-	Activity coefficient
F	J	Helmholtz free energy
F	N	Force
g	$\frac{J}{m^2}$	Gibbs free energy per unit area
g	$\frac{m}{s^2}$	Acceleration due to gravity
G	J	Gibbs free energy
h	Js	Planck constant ($6.62 \cdot 10^{-34} Js$)
h	mm	Film / rivulet height
I	eV, J	Ionization energy
k	$\frac{J}{K}, \frac{eV}{K}$	Boltzmann constant ($1.38 \cdot 10^{-23} \frac{J}{K}, 8.617 \cdot 10^{-5} \frac{eV}{K}$)
K	$\frac{1}{mm}$	Curvature
\dot{m}	$\frac{g}{min}$	Mass flow
n	mole	Amount of moles, molecules per unit volume
n	-	Refractive index

Nomenclature

N_A	$\frac{1}{mole}$	Avogadro number $\left(6.02 \cdot 10^{23} \frac{1}{mole}\right)$
p	MPa	Pressure
r	Å	Intermolecular distance
R	mm	Radius
R	$\frac{kJ}{kmol \cdot K}$	Gas constant
R_a	µm	Roughness
s	mm	Arc length
S	$\frac{J}{K}$	Entropy
t	s	Time
T	K	Temperature
U	J	Internal energy
V	m^3	Volume
V	$\frac{m^3}{mole}$	Molar volume
w	$\frac{cm}{s}$	Velocity
\bar{w}	$\frac{g}{min}$	Mean velocity
W	J	Work
x	mm	Coordinate direction
x	-	Mole fraction
X	-	Dimensionless coordinate direction
y	mm	Coordinate direction
z	mm	Coordinate direction
z	mm	Coordinate direction
Z	-	Dimensionless coordinate direction

Greek Symbols

μ	$\frac{kJ}{kmol}$	Chemical potential
σ	$\frac{mN}{m}$	Interfacial tension
Γ	$\frac{kg}{m^2}$	Excess concentration
ρ	$\frac{g}{ml}, \frac{kg}{m^3}$	Density
φ	$^{\circ}, rad$	Angle
β	-	Dimensionless drop parameter
θ	$^{\circ}, rad$	Sessile drop contact angle
Φ	-	Molecular interaction parameter
μ	D, Cm	Dipole moment
α	$cm^3, \frac{Cm^2}{V}$	Polarizability
ν	Hz	Frequency
δ	mm	Thickness
τ	Pa	Shear stress
η	Pa.s	Dynamic viscosity
ε	$^{\circ}, rad$	Angle
α	$^{\circ}, rad$	Angle
Ξ	$\frac{1}{mm \cdot s}$	Parameter which comprises material properties of both, film as well as continuous phase (according to Eq.8-6)
β	$\frac{1}{mm \cdot s}$	Collected material properties according to Eq. 6-8
Φ	$\frac{1}{mm \cdot s} \frac{kg}{m \cdot s}$	Parameter, which comprises material properties of both, film as well as continuous phases (according to Eq. 6-36)
θ_0	$^{\circ}, rad$	Film wetting angle

Indices

μ	Dipolar interaction
0	Equilibrium state
a	Advancing
a,b	Phase
ad	Adhesion
B	Buoyancy
c	Critical
c	Continuous phase
calc	Calculated
coh	Cohesion
disp	Dispersion
exp	Experimental
f	Film
G	Gravitational
i, j	Phase
ind	Induction
line	Linearized
lv	Liquid - vapour
max	Maximum
min	Minimum
par	Parabolic
r	Receding
sat	Saturated
sl	Solid - liquid
sv	Solid - vapour

Summary

Es ist nicht das Wissen, sondern das Lernen, nicht das Besitzen, sondern das Erwerben, nicht das Dasein, sondern das Hinkommen, was den größten Genuß gewährt. Wenn ich eine Sache ganz ins Klare gebracht und erschöpft habe, so wende ich mich davon weg, um wieder ins Dunkle zu gehen; so sonderbar ist der nimmersatte Mensch, hat er ein Gebäude vollendet, so ist es nicht, um ruhig darin zu wohnen, sondern um ein anderes anzufangen.

Carl Friedrich Gauß (1777-1855)

The application of pressurized carbon dioxide in optimizing several processes in chemical engineering characterizes a new era in this field. However, some new questions appear at the same time. In this thesis, an attempt is made to provide a basis for answering those questions and to shed some light in the field of interfacial phenomena and wetting under high pressure conditions as well as fluid dynamics of the falling film coming in touch with dense fluid.

The interfacial tension of water and ethanol pendant drops embedded in high pressure carbon dioxide is measured. The quantitative and qualitative results are reported. Due to the mass transfer between the coexisting phases, some drop phenomena such as drop kicking, eddy and instable emulsification in both phases are observed.

The wetting ability of water and ethanol on horizontal Teflon, steel and glass surfaces in pressurized carbon dioxide is measured. It can be stated that ethanol wets all of the mentioned surfaces better than water, whereas steel can be wetted better than Teflon but, under the same conditions, glass can be wetted best. Generally, the contact angle rises with the pressure until gaseous carbon dioxide turns into supercritical. In supercritical carbon dioxide, the pressure has hardly any effect on the wettability of a system. Beyond the critical pressure of carbon dioxide, regardless of the increasing pressure, the contact angle remains nearly constant.

Both experimentally measureable properties, the liquid-vapour interfacial tension and the contact angle, are correlated in the Young equation. In this equation, two other properties, i.e. the solid-vapour and the solid-liquid interfacial tensions are included but experimentally not measureable. To solve the Young equation, another equation is required. Following the suggestion from Good and Girifalco, an attempt is made to calculate the molecular interaction parameter Φ_{sl} theoretically. This parameter describes the long-range van der Waals molecular interaction between the solid and the liquid. For this purpose, the dipole moment μ , the ionization potential I and the polarizability α are required. For pure liquid materials, it is not hard to find the required data in the literature. But for the solid materials, this is rather complex due to the fact that most of the time, they are mixtures or even polymers. Some assumptions regarding the components which play an important role in the molecular interaction between the solid and the liquid phases are made in order to provide all of the molecular properties required for the computation of the interaction parameter Φ_{sl} . The values of this parameter for the systems water and ethanol in combination with the solid materials Teflon, steel and glass are calculated.

Using the interaction parameter Φ_{sl} , the solid-vapour interfacial tension σ_{sv} for the systems Teflon-carbon dioxide, steel-carbon dioxide and glass-carbon dioxide can be estimated. The validity verification of the solid-vapour interfacial tensions σ_{sv} cannot be conducted experimentally. For this purpose, two conditions have to be fulfilled, an absolute and a sufficient condition. Because the interfacial tension σ_{sv} is a system property, it has to remain the same regardless of the kind of liquid phase that rests on it. This is the absolute condition. That means, the calculated solid-vapour interfacial tension σ_{sv} of the three solid materials against carbon dioxide has to be in the same order of magnitude regardless of whether water or ethanol is included in the system. The second condition, the sufficient condition, also called the applicability condition, is the requirement that the calculated solid-vapour interfacial tension is useable to predict the wettability of other liquids on the given solid material.

Both conditions are very well fulfilled in the system investigated here. In the operating conditions investigated here, the two results of the solid-vapour interfacial tension σ_{sv} of the three solid materials, Teflon, glass and steel, obtained using water and ethanol are in the same order of magnitude. The measured and the calculated contact angle θ by means of the estimated solid-vapour interfacial tension coincide relatively well. It can be concluded that the combination of both the Young equation and the theory of Good and Girifalco, delivers a good chance to estimate the solid-vapour interfacial tension, and thus, also the solid-liquid interfacial tension under high pressure conditions where the miscibility between the phases is not negligible. The difficulties lie however, in the knowledge of the molecular interaction and the right choice of the components which come to interact with each other.

In the second part, the study of the water falling film along vertical glass and stainless steel surfaces embedded in pressurized carbon dioxide is started by measuring the geometry of the film itself. Commonly, the falling film concept known in the process engineering is a thin, wide covering film where the width and the thickness of the film are from different orders of magnitude. Falling film in this sense is not available in this work due to apparatus unavailability. In the experiments, only narrow film can be made accessible. Specifically, this kind of geometry is called a rivulet. For the wetting study of the falling film itself, it is even advantageous to first investigate rivulets and then brings this knowledge, from a rivulet forward to a continuous film. Because, as experience teaches, the wetting behaviour of a falling film is always better than that of a rivulet. In the worst of cases, the wettability of both is the same so that regarding the plant design in the process engineering, one is on the safe side when taking the wettability of rivulets for the falling film apparatus as an orientation.

The measured rivulet thickness and width are combined in one single quantity called the wetting angle. This is performed assuming that the cross-section of the falling film perpendicular to its flow direction is a circular segment. The wetting angle is used as a measure of the wetting degree and to compare the wettability of different systems. In the case of a wide covering thin film, it is believed that either the lateral wetting angle is smaller than or equal to the rivulet wetting angle.

In the literature, the Nusselt film condensation theory is widely used to describe the fluid dynamics of a falling film assuming that the shear stress at the film surface is negligible. However, this condition does not always meet the reality. That is why two other models are suggested to describe the fluid dynamics. The first one is the wall model where the shear stress is maximum and as a result, the liquid molecules at the film surface are stopped completely. They do not flow at all. The second one is the tau model which is more universally valid. Both models, the wall and the tau models, are developed and verified in this thesis.

In the tau model, a velocity boundary layer is assumed where the continuous phase is carried along by the film flow. By means of the Newtonian-liquid shear stress equation, the tau model can be developed. Here, the film phase velocity profile is visualized by means of a computer program written in matlab and the mean film velocity is calculated. The calculated mean film velocity is in a good agreement with the experimental value.

An attempt is made to estimate the interdependency of the change of the film geometry with the mass transfer in cases where the miscibility between the film and the continuous phase is not negligible. This means, through the saturation or the miscibility between the phases, the material properties are changed radically or less radically. And the impact of this change on the film thickness is evaluated.

The transfer of carbon dioxide into the water film phase affects the material properties of the film phase such that the film becomes thinner and takes up carbon dioxide at a faster rate till saturation is reached. The same mechanism is seen in the system containing corn oil and carbon dioxide.

The thickness of the velocity boundary layer can be estimated and the velocity profile in the velocity boundary layer can be visualized by means of a matlab-program. The mean velocity in the boundary layer is calculated as well. The shear stress exerted by the continuous phase at the film surface according to the tau and the wall models is estimated.

Comparing the calculated mean film velocity with the experimental values, it can be said that the tau model is universally valid for high pressure application. This model describes the fluid dynamics very well. At high pressure, the wall model comes very close to the tau model and that is why it is not astonishing that at high pressure conditions, the calculated value according to the wall model shows a good agreement with the experimental one. In the lower pressure range, the wall model assumes a too high shear stress at the surface and thus, is less applicable for such operating conditions.

Although the fluid dynamics developed here consider the rivulet shape, the tau model takes a wide covering thin film into consideration as well and hence, it can be applied also for this geometry at high pressure conditions.

1 Introduction and Aim of Work

A journey of a thousand miles begins with a single step.

Lao Tzu

In daily life as well as in technical and industrial applications, interfaces play an important role in many processes. It is worth noting that dealing with the interface between two phases is unavoidable and in general, the properties of an interface will be affected by physical or chemical changes in either or both of the phases involved. An adequate knowledge and understanding of the interfacial phenomenon provide an advantageous basis in improving and optimizing a process.

In this thesis, several core disciplines such as thermodynamics, interfacial phenomena, surface physical chemistry, wetting, intermolecular long-range interaction and fluid dynamics are combined and observed from an engineering point of view in order to serve as useful tools in creating a link between the natural and the engineering sciences. The main interest of this thesis is to provide the raw, basic principles derived from the natural sciences to be used in the high pressure engineering field.

High pressure engineering, mainly those processes which use carbon dioxide as a solvent, has become more popular [26,67,104,111,116,131,153,155,177]. However, due to the non-inert property of carbon dioxide and the combination of both the interfacial phenomena and high pressure engineering such as supercritical extraction using carbon dioxide, some unanswered questions occur. These questions are closely related to the optimisation of the processes for which precise answers are necessary in order to have an optimally designed column. Some typical columns used in process engineering are tray columns, spray columns, random and structured packing columns. In spray columns, the liquid drop size in the continuous phase (either in a gaseous or a liquid phase) decides the ratio of volume to exchange area [114] and thus, the effectiveness of the heat and mass transfer between the coexisting phases. The liquid drop size is in turn, controlled by its interfacial tension [35,46,51,64,82,131,165,194,197]. Therefore liquid interfacial tensions against carbon dioxide, both gaseous and supercritical, are measured and reported in this work.

Packing columns are developed with the objective to provide a large exchange area between the coexisting phases coming into touch with each other. This is achieved by forming a film phase which flows down the solid material. However, the existence of the solid material to be wetted does not guarantee the formation of a wide covering film. The latter is controlled solely by the wetting characteristics of the systems at the given operating conditions [5,95,132,150,160,178]. In order to provide an adequate answer to this issue, the wetting characteristics of fluid-solid-liquid systems are investigated intensively for both static (single sessile drop) as well as dynamic systems (falling film).

In this thesis, the wetting behaviour of various systems which are relevant for industrial applications is studied. The investigation of the wetting ability comprises the study of a single,

sessile drop which rests on a horizontal surface and, macroscopically seen, is stationary with respect to the continuous phase, and the falling film which, compared to a single liquid drop, contains a larger amount of liquid and conducts a relative motion towards the embedding continuous phase.

The interfacial phenomena study consisting of one single drop is started in Chapter 2 where the interfacial tension of liquid-vapour is explained thermodynamically. The measurement method and the results of the measurements containing pressurized carbon dioxide are also given there. The wetting behaviour of various systems containing a horizontal solid surface, a drop phase and an embedding fluid is reported in Chapter 3. Here, the wettability of a system is given in terms of contact angle. Data from the interfacial tension of liquid-vapour and the contact angle are correlated in a single equation known as Young equation. In Chapter 4 the physical chemistry of the surface and the long-range intermolecular interaction come into play. A second, required correlation consisting of the solid-vapour, the liquid-vapour and the solid-liquid interfacial tension is developed and combined with the initial Young equation in order to estimate the magnitude of the solid-vapour interfacial tension. This second correlation is initially not for high pressure use. Some cautious adaptations, especially in the choice of the molecular properties required, are conducted here with the hope of obtaining the right value of the solid-vapour interfacial tension and so that this quantity can provide the right prediction of the wetting behaviour of a given system.

From Chapter 5 to 9, attention is given to the falling film where the relative motion between the film and the continuous phase is not negligible. To begin with, in Chapter 5 the dimension of the film is measured and both, the thickness and the width of the falling film, are consolidated in one single measure, called the wetting angle [106].

Due to the relative motion of the falling film and the continuous phase, it is necessary to discuss the fluid dynamics. In Chapter 6 two extreme models, the Nusselt and the wall models are introduced. The Nusselt model is known in the literature and applied for the design of falling film apparatus. Here, the shear stress-free state at the film surface is assumed [13,22,108,135,138]. However, working with supercritical carbon dioxide, it is interesting to find out whether the assumption is still justifiable. In case the assumption does not meet the reality, it should be found out how this supercritical phase affects the fluid dynamics of the liquid phase which moves relatively to it.

The wall model describes a state where the shear stress at the film surface is maximum and thus, is the other extreme case. Hence, a third, more universally applicable model is required since the given operating conditions are not always under extreme conditions. The tau model which can be employed on both a wide covering film and a narrow rivulet, is explained and derived in Chapter 6. The mean velocity of the falling film according to these three different calculation models is given and compared with the experimental measured value in Chapter 7.

The tau model postulates the existence of a velocity boundary layer between the film and the continuous phase, and a finite shear stress exerted by the continuous phase on the film phase

due to the relative motion and the large density of the fluid used as the continuous phase (larger friction at the film surface). The thickness and the fluid dynamics in the velocity boundary layer are explained in Chapter 8. In both Chapter 6 and 8, the colour-coded simulation results show the velocity profile in the film and the boundary layer respectively. In the last chapter, the magnitude of the over-the-surface averaged shear stress is shown.

For further investigation of the wetting behaviour and the fluid dynamics under high pressure conditions, experiments with systems containing Teflon, glass, steel (solid material), water, ethanol (liquid phase) and carbon dioxide (continuous phase) are conducted at temperatures up to 373 K and pressures up to 27 MPa.

2 Interfacial Tension

Look for an occupation that you like, and you will not need to labor for a single day in your life.

Confucius

One of the most important properties in the process engineering which decides the effectiveness of a process is the interfacial tension. This thermodynamical property is, for instance, responsible for the wettability of a system consisting of a solid, a liquid and a fluid phase which coexist and are in equilibrium with each other. Interfacial tension is also a main property which controls the size and the shape of a liquid drop in a spray process and therefore, it is of a great importance to know and understand this property in the engineering processes.

Interfacial tension has been the objective of much scientific research carried out for years. The research on the interfacial tension of liquids embedded in pressurized carbon dioxide are listed in Table 2-1.

Even though it has been quite well investigated, it is always important to develop a theoretical solid background for this property. And it is important to fill in gaps that are found in the literature.

Interfacial tension will first be seen from the thermodynamical point of view by means of the Gibbs-Duhem equation, based on which the differential equation of a drop according to Bashforth and Adams [15] can be derived. Upon solving this equation, the interfacial tension of a liquid embedded in a fluid can be estimated if the density difference between the phases and the shape of the drop are known. The influence of adsorption on the interfacial tension is discussed with help of the Gibbs adsorption equation.

There are several interfacial tension measurement methods known:

- capillary rise method
- maximum bubble pressure method
- detachment method: drop weight, du Nuoy ring [118], Wilhelmy slide [198]
- methods based on the shape of static drops or bubbles: pendant drop and sessile or bubble method [15]
- dynamic methods: flow methods, capillary waves, maximum bubble pressure.

Here, only the principles of the pendant drop will be discussed in detail in 2.2, whereas all other measurement methods are explained in detail in many sources, for instance [2,10,197]. A brief explanation of the static drop method used to measure the interfacial tension is given in [4,6,7,43,71,79,163,176].

2.1 Thermodynamical Background

Table 2-1: Overview on already performed interfacial tension research. The investigated systems are liquids against dense carbon dioxide.

Source	Year	System	T [K]	p[MPa]
[81]	1957	mercury	311 - 378	68.9
[81]	1957	water	311 - 411	68.9
[21]	1965	butane	311 - 353	8.2
[97]	1978	water	285 - 318	6.2
[88]	1985	butane	319 - 378	8
[142]	1986	n-Decane	344 - 377	16.5
[65]	1989	n-Tetradecane	344.3	16.38
[82]	1990	linolic + oleic acid	313 - 353	24.6
[82]	1990	n-hexan	313	7.15
[82]	1990	oleic acid	313 - 333	26.2
[82]	1990	pelargonic acid	313 - 353	12.8
[82]	1990	squalan	313 - 353	21.3
[66]	1993	synthetic oil	328 - 339	12.9
[83]	1993	linoleic acid	313 - 353	24.55
[165]	1993	monoglyceride mixtures	313 - 393	25.9
[165]	1993	oleic acid	353 - 373	25.2
[165]	1993	olive oil	313 - 353	24.7
[165]	1993	pertagonic acid	313 - 393	24.8
[165]	1993	stearic acid	353 - 393	26.2
[52]	1994	coffee solution	314 - 344	24
[52]	1994	coffein solution	315	26
[52]	1994	water	314 - 344	28
[127]	1994	oleic acid	313 - 333	17.5
[127]	1994	methyl myristate	313 - 333	12
[127]	1994	methyl palmitate	313 - 333	10
[127]	1994	oleic acid	313 - 333	17.5
[32]	1995	ethanol + water	278 - 338	17.23
[32]	1995	isopropyl alcohol + water	288 - 338	17.23
[32]	1995	methanol + water	278 - 338	15.51
[32]	1995	water	278 - 344	18.61
[61]	1996	water	297 - 348	25
[93]	1996	olive oil	353	42

Table 2-1 (cont.)

Source	Year	System	T [K]	p[MPa]
[93]	1996	coffee oil	323 - 353	48
[93]	1996	corn oil	313 - 393	47.5
[93]	1996	lemon oil	323 - 353	12
[93]	1996	walnut oil	323 - 353	48
[93]	1996	wheat oil	323 - 353	42
137	1996	a - tocopherol	313 - 402	37.1
[194]	1997	water - tert.Butanol	333	7.1
[194]	1997	water	298 - 333	25
[194]	1997	water + 1 M natrium salicylat	298 - 333	25
[194]	1997	water + 1-butanol	333	9
[92]	1998	citrus oil	323 - 353	13.7
[92]	1998	coffee oil	323 - 353	48.1
[92]	1998	coffee solution (40-wt%)	314	24
[92]	1998	coffeine solution (1-wt%)	314	26.1
[92]	1998	corn germ oil	313 - 393	40.9
[92]	1998	corn germ oil	313 - 393	40.9
[92]	1998	olive oil	313 - 353	42.3
[92]	1998	silicone oil	313	30.7
[92]	1998	walnut oil	323 - 353	48.1
[92]	1998	water	314 - 343	27.9
[92]	1998	wheat germ oil	313 - 353	42
[44]	1999	poly (ethylen glycol) nonylphenyl ether	323 - 343	25.5
[148]	1999	ethanol	293 - 355	10.5
[148]	1999	water	303 - 354	31
[173]	2000	crude corn oil	323	30
[173]	2000	coffee oil	323 - 353	40
[173]	2000	lemon oil	323 - 353	12.5
[173]	2000	olive oil	313 - 353	42
[173]	2000	refined corn oil	313 - 393	50
[173]	2000	walnut oil	323 - 353	50
[173]	2000	wheat oil	323 - 353	45
[147]	2001	ethanol	292 - 354	10.5
[170]	2001	decane	344.3	12.71
[35]	2002	vegetable oil	313 - 393	35
[45]	2002	corn germ oil	313 - 393	45

2.1 Thermodynamical Background

Table 2-1 (cont.)

Source	Year	System	T [K]	p[MPa]
[45]	2002	olive oil	353	45
[45]	2002	palm oil	353	46
[45]	2002	wheat germ oil	353	45
[123]	2004	polystyrene	483 - 503	14.2
[130]	2004	synthetic oil PAO	313 - 393	5
[130]	2004	synthetic oil POE	313 - 393	5
[131]	2005	coffee solution	313 - 353	30
[202]	2005	crude oil	300 - 331	31.4
[202]	2005	reservoir brine	300 - 331	31.4
[202]	2005	crude oil + reservoir brine	300 - 331	31.4
[85]	2005	Diesel oil (+ additive)	314-344	20

The liquid interfacial tension against dense fluid is required in the study and estimation of the solid interfacial tension made in Chapter 4. Therefore, the needed data of interfacial tension are measured and reported here. The interfacial tension of water and ethanol and their mixtures are measured against dense carbon dioxide at temperatures up to 313 K and pressures up to 27 MPa. The optical observation made during the mass transfer between the phases is reported in Chapter 2.4, whereas the magnitude of the interfacial tension when equilibrium is reached in Chapter 2.5.1 and finally as the mass transfer between the phases is proceeding in Chapter 2.5.2. The density measurement at high pressure conditions is explained briefly in Chapter 2.3.2 due to the fact that density data is required for the estimation of the interfacial tension by means of pendant drop method.

2.1 Thermodynamical Background

The internal energy of a system or of a homogenous phase α is the energy associated with the random, disordered motion of the molecules at microscopic state and denoted by U , which is a function of the extensive variables entropy S , volume V and the composition of the phase n_i

$$U = f(S, V, n_i). \quad (2-1)$$

If a second homogenous phase β coexists and is in equilibrium with the first phase α and they are separated by a phase boundary, then this is not to be regarded as a simple geometrical plane [37], upon either side of which extend the homogenous phases and that the intensive variables in each bulk phases remain uniform up to this boundary before their values are changed suddenly. This plane is rather a lamina or film of a characteristic thickness within which the intensive quantities such as the density (represents the composition), the temperature and the

pressure change gradually, from the value in the first phase α towards the value in the second phase β [140].

The actual values of the extensive properties for the system as a whole are then different from the sum of the values of the two bulk phases α and β by an excess or deficiency assigned to the surface region [2]. The interfacial phase can be considered as a third phase and handled as self dependent. The internal energy is then not only a function of the extensive variables entropy, volume and composition but also depends on the area A [10]

$$U = f(S, V, A, n_i). \quad (2-2)$$

For an arbitrary set of variations from equilibrium, the variation of the internal energy in the boundary phase is

$$dU = \left(\frac{\partial U}{\partial S} \right)_{V, A, n_i} dS + \left(\frac{\partial U}{\partial V} \right)_{S, A, n_i} dV + \left(\frac{\partial U}{\partial A} \right)_{S, V, n_i} dA + \sum_{i=1}^j \left(\frac{\partial U}{\partial n_i} \right)_{S, V, A, n_{j \neq i}} dn_i \quad (2-3)$$

Each of the internal energy partial derivatives found in Eq. 2-3 is assigned to an intensive variable such as the temperature

$$T = \left(\frac{\partial U}{\partial S} \right)_{V, A, n_i} \quad (2-4)$$

the pressure

$$p = - \left(\frac{\partial U}{\partial V} \right)_{S, A, n_i} \quad (2-5)$$

and the chemical potential

$$\mu_i = \left(\frac{\partial U}{\partial n_i} \right)_{S, V, A, n_{j \neq i}} \quad (2-6)$$

The partial derivative of the internal energy U with respect to the area such as given in the third term in Eq. 2-3 is defined as the interfacial tension

$$\sigma \equiv \left(\frac{\partial U}{\partial A} \right)_{S, V, n_i} \quad (2-7)$$

In analogy to the internal energy U , the same derivation using Helmholtz free energy F

$$F = U - TS = f(T, V, A, n_i) \quad (2-8)$$

and Gibbs free energy G

$$G = U - TS - (-pV) = f(T, p, A, n_i) \quad (2-9)$$

can be performed and thus, the interfacial tension can be written in terms of the partial derivative of the Helmholtz free energy F [99,101]

2.1 Thermodynamical Background

$$\left(\frac{\partial F}{\partial A}\right)_{T,V,n_i} = \sigma \quad (2-10)$$

or in terms of the partial derivative of the Gibbs free energy G with respect to the area A [10,159]

$$\left(\frac{\partial G}{\partial A}\right)_{T,p,n_i} = \sigma. \quad (2-11)$$

In order to find out the influence of adsorption on the interfacial tension, Eq. 2-3 is rewritten

$$dU = TdS - pdV + \sigma dA + \sum_{i=1}^j \mu_i dn_i \quad (2-12)$$

upon integration

$$U = TS - pV + \sigma A + \sum_{i=1}^j \mu_i n_i. \quad (2-13)$$

A complete differentiation of Eq. 2-13

$$dU = TdS + SdT - pdV - Vdp + \sigma dA + Ad\sigma + \sum_{i=1}^j \mu_i dn_i + \sum_{i=1}^j n_i d\mu_i \quad (2-14)$$

has the consequence that the left-hand expression of the Gibbs-Duhem equation [69] (Eq. 2-15) has to be zero

$$SdT - Vdp + Ad\sigma + \sum_{i=1}^j n_i d\mu_i = 0 \quad (2-15)$$

if the expression in Eq. 2-12 is to be maintained.

At a constant temperature and pressure, Eq. 2-15 becomes

$$Ad\sigma + \sum_{i=1}^j n_i d\mu_i = 0 \quad (2-16)$$

and upon introducing the excess concentration Γ

$$\Gamma_i = \frac{n_i}{A} \quad (2-17)$$

the Gibbs adsorption equation is introduced

$$d\sigma = -\sum_{i=1}^j \Gamma_i d\mu_i. \quad (2-18)$$

The chemical potential of a component i is made up of the standard state chemical potential $\mu_{i,0}$ and its partial molar free mixing enthalpy

$$\mu_i = \mu_{i,0} + RT \ln(x_i f_i). \quad (2-19)$$

The partial molar free mixing enthalpy is the product of the gas constant R , the temperature T and the natural logarithm of the molar fraction x_i multiplied by the activity coefficient f_i . Putting the expression of the chemical potential in Eq. 2-19 into Eq. 2-18 and assuming a binary mixture, the following equation is found [168]

$$d\sigma = -\Gamma_2^{(1)} RT d \ln(x_2 f_2). \quad (2-20)$$

In a diluted, binary mixture, the activity coefficient approaches unity

$$\lim_{x_2 \rightarrow 0} f_2 = 1 \quad (2-21)$$

and thus Eq. 2-20 becomes

$$d\sigma = -\Gamma_2^{(1)} RT d \ln(x_2). \quad (2-22)$$

In Eq. 2-22 it can be seen that due to the minus algebraic sign in front of the right-hand term, at constant temperature and pressure, an adsorption, which means a positive concentration gradient, causes a decrease in the interfacial tension. On the contrary, a desorption means a minus gradient of the molar fraction and thus an increase in the interfacial tension (more on this topic can be seen later in Chapter 2.5).

In the following, it will be shown, that the interfacial tension σ can be written in terms of energy, but this is not always equal to the area related (Helmholtz or Gibbs) free energy. For this purpose, the Gibbs free energy G given in Eq. 2-9 is differentiated

$$dG = \left(\frac{\partial G}{\partial T} \right)_{p,A,n_i} dT + \left(\frac{\partial G}{\partial p} \right)_{T,A,n_i} dp + \left(\frac{\partial G}{\partial A} \right)_{T,p,n_i} dA + \sum_{i=1}^j \left(\frac{\partial G}{\partial n_i} \right)_{T,p,A,n_{j \neq i}} dn_i \quad (2-23)$$

and written in terms of the extensive variables entropy S , volume V and the intensive properties interfacial tension σ and the chemical potentials μ

$$dG = -SdT + Vdp + \sigma dA + \sum_{i=1}^j \mu_i dn_i \quad (2-24)$$

if the temperature and the pressure are kept constant

$$dG_{T,p} = \sigma dA + \sum \mu_i dn_i. \quad (2-25)$$

An integration of Eq. 2-25 delivers

$$G = \sigma A + \sum \mu_i n_i \quad (2-26)$$

using the same idea as above, Eq. 2-26 is differentiated completely. Upon maintaining the derivative of the Gibbs free energy such as given in Eq. 2-25, following expression has to be equal to zero

$$Ad\sigma + \sum_{i=1}^j n_i d\mu_i = 0. \quad (2-27)$$

Upon introducing the Gibbs free energy per unit area

$$g = \frac{G}{A} \quad (2-28)$$

Eq. 2-26 becomes

$$g = \sigma + \sum \mu_i \Gamma_i \quad (2-29)$$

and in analogy to this, the Helmholtz free energy per unit area is

$$f = \sigma + \sum \mu_i \Gamma_i . \quad (2-30)$$

In Eq. 2-29 and 2-30 is shown, that when no adsorption takes place, which means the surface excess concentration Γ_i is equal to zero, interfacial tension is equal to the free energy. In cases where the adsorption phenomena are important both properties are definitely not equal [99].

Thermodynamically seen, it is clear and verifiable that surface or interfacial tension is conceptualized in terms of energy, as a measure for the energy or work required to increase the surface area [140]. However, in dealing with this property it is not always obvious whether it should be referred to as an energy or a force.

A common explanation of the phenomenon of interfacial tension is that a liquid drop is observed to behave as if it were surrounded by an elastic skin with a tendency to contract and adopt therefore a nearly spherical shape (depending on the conditions and the solid surface on which it rests). Based on this, it is obvious that this property has a direction (up to now, the discussion about the direction has not yet begun). An energy can never have a direction, but a force does. Therefore interfacial tension is not only referred to as a free energy per unit area, but can also be thought of as a force per unit length [2].

Starting from this point of view, the discussion on the nature of interfacial tension as a force and its direction can be opened. According to Laplace, the explanation about the existence and the occurrence of this property is often found in the competition of the attractive and the repulsive forces between molecules constituting the liquid [37,162]. The molecules in the bulk phase experience solely the attraction force between the neighbouring, like-molecules, also called cohesion. Due to the fact that in the bulk phase a molecule is pulling equally in all directions, the forces cancel each other out and the net of the force is equal to zero. However, at the liquid surface or at the phase interface the molecules experience not only the attraction force inwards towards their own bulk phase but also the adhesion. The net of these forces is believed to result towards the bulk phase and hereby, the interfacial tension is discovered. As a consequence, the interfacial tension is taken to be at right angles with the interface and directed inwards towards the bulk phase.

This seems, however, contradictory to the assumed direction made in the Young equation [204] (this equation will be introduced later in Chapter 3). According to Young, interfacial tension is a tangentially directed force-vector along the unit length along which the force acts. The concept of the tangentially acting force can better be used to explain some phenomena, for instance the contraction of liquid which forms a drop. Here, the interfacial tension can be thought of as the force acting around the circumference of the drop and pulling it in such manner that it remains contracted and in this way maintains its near spherical shape.

Moreover all of the kinds of interfacial tension measurements which belong to the detachment method listed at the beginning of this chapter (drop weight, du Nuüy ring, Wilhelmy slide) implicitly assume a tangentially directed force when talking about the interfacial tension. This knowledge is used in the estimation of the magnitude of the interfacial tension. As an example, the drop weight method which is based on Tate's law [184] will briefly be explained here. In its

simplest form, drops are formed at the tip of a capillary, detached, and collected in a container below the capillary. The weight of liquid is accurately determined later and brought into correlation with the interfacial tension itself

$$F_G = 2\pi R \sigma \quad (2-31)$$

Here, the interfacial tension is understood in terms of the argument that the maximum force available to support the weight of the drop F_G is given by the interfacial tension per unit length σ times the circumference of the tip $2\pi R$. Thus, the interfacial tension is believed to be a tangentially acting force, in this case, opposite to the direction of the acceleration due to the gravitation, and therefore holds the whole weight of the drop. Although in the practical use of the drop weight method, some corrections regarding Tate's law have to be carried out due to the deviation from the idealization made in the estimation, the principle understanding of the direction of the interfacial tension is maintained. The same concept but adapted to the circumstances and conditions (geometry involved, etc.) is also used in other detachment methods such as the du Nuöy ring and the Wilhelmy slide.

Although it is clearly explained that the interfacial tension originates from a force vector which acts tangentially to the surface or interface, this tension is, according to Young and Laplace (see Eq. 2-32), also closely related to the pressure difference between both sides of the curved surface. Obviously, this pressure difference has not only a tangential impact but also, such as expected, a pressure always directed normally towards a surface. This also explains the popular concept of interfacial tension as the unit of work needed to form a unit new surface.

2.2 Pendant Drop Fundamental Equation

The pendant drop fundamental equation according to Bashforth and Adams [15] which correlates the interfacial tension σ and the density difference between the phases with the shape of the drop can best be understood by means of the basic equation of capillarity which was first introduced in 1805 by Young [204, 205] and Laplace [40]

$$\Delta p = \sigma \left(\frac{1}{R_1} + \frac{1}{R_2} \right) \quad (2-32)$$

Equation 2-32 describes the pressure difference Δp over a meniscus between two fluids. The surface or interfacial tension is denoted by σ and the principal radii of the curved surface are R_1 and R_2 . This equation is valid for any arbitrary point P on the surface (see Fig. 2-1 a.)

$$\Delta p_p = \sigma \left(\frac{1}{R_1} + \frac{1}{R_2} \right) \quad (2-33)$$

and at the vertex of the drop both radii have the same quantity and thus

$$\Delta p_{Apex} = \sigma \frac{2}{R} \quad (2-34)$$

2.2 Pendant Drop Fundamental Equation

The apex is taken as the lowest point and used as a reference. In the hydrodynamics the hydrostatic pressure between two points depends on the liquid density ρ or on the density difference $\Delta\rho$ between the phases and the height difference between both points

$$\Delta p_{Apex} - \Delta p_P = \Delta\rho g z. \quad (2-35)$$

Combining the Young-Laplace equation and the hydrostatic pressure between point P and the apex, one obtains

$$\frac{1}{R_1} + \frac{1}{R_2} = \frac{2}{R} - \frac{\Delta\rho g z}{\sigma}. \quad (2-36)$$

The magnitude of the principal radii of the curved surface R_1 and R_2 in Eq. 2-36 are still unknown. In the following, the radius of curvature of a meniscus at a point will be explained and their magnitude will be introduced mathematically.

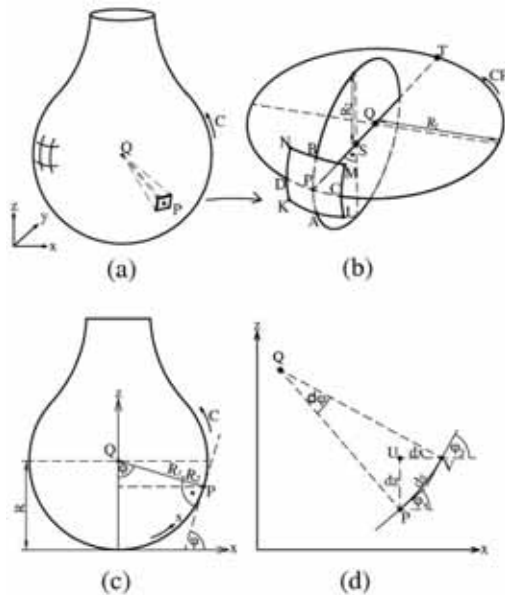


Figure 2-1: a. Pendant drop. b. Curved Surface KLMN cut from the pendant drop. The radii of curvature of the surface KLMN are R_1 and R_2 . c. The geometry of two dimensionally projected pendant drop. d. Infinitesimal length of the curve C, the arc PV.

If, from the surface of a pendant drop (Fig. 2-1 a.), an infinitesimal surface area KLMN is magnified, the curvature of this surface is given by the radius of curvature. Radii of curvature of a meniscus at a point P are the radii of osculating circles R_1 and R_2 at that point (see Fig. 2-1 b.). The two radii of an arbitrarily curved surface describe the surface mathematically and can be obtained as follows. A normal to the surface at the point in question is defined and a plane,

which contains this normal, is passed through the surface. Generally, the line of intersection between these two planes is curved, and the radius of curvature is that for a circle tangent to the line at the point involved [20,25]. A second radius of curvature can be obtained if a second plane perpendicular to the first one is passed through the surface at the point in question. This results in a second line of intersection and a second radius of curvature being obtained. They are the two radii R_1 and R_2 of a curved surface [157]. There is an infinite number of possible pairs of radii which can be used to define a curved surface depending on how the first plane is oriented (the second plane has always to be perpendicular to the first one and still contain the normal defined before). However, the extreme values, i.e. the minimum and the maximum of the radii are called the principal radii of curvature and given in Eq. 2-36 as R_1 and R_2 [201]. Looking at Fig. 2-1c, the position of point P in the polar coordinate system can be described by the angle φ

$$\sin\varphi = \frac{x}{R_1} \quad (2-37)$$

or by means of the arc PV (see Fig. 2-1d)

$$\sin\varphi = \frac{dz}{ds} \quad (2-38)$$

with the Pythagorean theorem

$$ds^2 = dx^2 + dz^2. \quad (2-39)$$

Putting Eq. 2-39 into Eq. 2-38, the following equation is obtained

$$\sin\varphi = \frac{\frac{dz}{dx}}{\left(1 + \left(\frac{dz}{dx}\right)^2\right)^{\frac{1}{2}}}. \quad (2-40)$$

The reciprocal quantity of the radius R_1 can be obtained by putting Eq. 2-40 into Eq. 2-37

$$\frac{1}{R_1} = \frac{\frac{dz}{dx}}{x \left(1 + \left(\frac{dz}{dx}\right)^2\right)^{\frac{1}{2}}}. \quad (2-41)$$

Given that a unit of length along the curve path is ds and that the tangent line changes its direction over ds by an angle $d\varphi$, where φ is the angle of the tangent with the x -axis, then the curvature is given by [191]

$$\lim_{V \rightarrow P} \frac{\Delta\varphi}{\Delta s} = \frac{d\varphi}{ds} = K. \quad (2-42)$$

Written in Leibniz notation, the chain rule for Eq. 2-42

$$\frac{d\varphi}{ds} = \frac{d\varphi}{dx} \cdot \frac{dx}{ds} \quad (2-43)$$

2.2 Pendant Drop Fundamental Equation

with (see Fig. 2-1 d.)

$$\varphi = \arctan\left(\frac{dz}{dx}\right). \quad (2-44)$$

Differentiating the angle φ with respect to x results in

$$\frac{d\varphi}{dx} = \frac{\frac{d^2z}{dx^2}}{1 + \left(\frac{dz}{dx}\right)^2}. \quad (2-45)$$

Upon employing Eq. 2-39, Eq. 2-42 (the radius of a curvature is the reciprocal of the curvature itself [23]) and Eq. 2-45, the curvature K_2 as the reciprocal value of R_2 can be written

$$\frac{1}{R_2} = \frac{d\varphi}{ds} = \frac{\frac{d^2z}{dx^2}}{\left[1 + \left(\frac{dz}{dx}\right)^2\right]^{\frac{3}{2}}}. \quad (2-46)$$

The quantity of the curvatures in Eq. 2-41 and Eq. 2-46 allow the correlation of the drop shape with the material properties like interfacial tension σ and density difference $\Delta\rho$ such as suggested in Eq. 2-36

$$\frac{d^2z}{dx^2} + \frac{1}{x} \cdot \frac{dz}{dx} \left(1 + \left(\frac{dz}{dx}\right)^2\right) = \left(\frac{2}{R} - \frac{\Delta\rho g z}{\sigma}\right) \left[1 + \left(\frac{dz}{dx}\right)^2\right]^{\frac{3}{2}}. \quad (2-47)$$

Equation 2-47 is also known as the pendant drop fundamental equation according to Bashforth and Adams [15] which allows the contactless interfacial tension measurement by means of the optical drop shape measurement and thus, it is possible to measure the interfacial tension at extreme conditions (high pressure and high temperature).

Relating the axes x and z to the radius R

$$X = \frac{x}{R} \quad (2-48)$$

$$Z = \frac{z}{R} \quad (2-49)$$

and collecting the material properties, the acceleration due to gravity and the drop radius R in one single parameter β

$$\beta = \frac{\Delta\rho g R^2}{\sigma}, \quad (2-50)$$

the dimensionless pendant drop fundamental equation can be written in its dimensionless term

$$\frac{d^2Z}{dX^2} + \frac{1}{X} \cdot \frac{dZ}{dX} \left(1 + \left(\frac{dZ}{dX}\right)^2\right) = (2 - \beta Z) \left(1 + \left(\frac{dZ}{dX}\right)^2\right)^{\frac{3}{2}}. \quad (2-51)$$

Upon solving the pendant drop fundamental equation, the interfacial tension can be obtained.

2.3 Experimental Setup

In the following experimental setup of interfacial tension measurement at high pressure conditions will be introduced and explained briefly. For the solution of the pendant drop fundamental equation, the density difference between the coexisting phases is required. The measurement method of this property by means of magnetic suspension balance is given in Chapter 2.3.2.

2.3.1 Interfacial Tension at High Pressure Condition

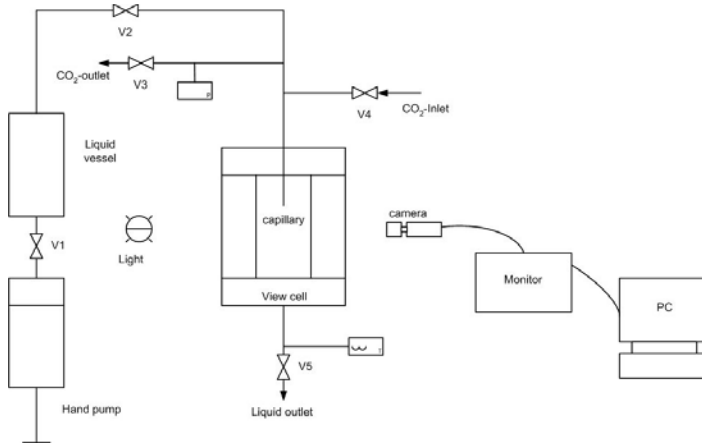


Figure 2-2: Experimental setup for interfacial tension measurement.

The experiment is performed in a small, pressure-resistant view cell made of stainless steel which is designed for the maximal temperature of 393 K and for pressures up to 50 MPa. The view cell is cylindrical and has a volume of approximately 30 ml. Through the circular windows made of sapphire glass a view in the cell during the experiments is possible.

The liquid, whose interfacial tension is to be measured, is stored initially in a pressure-resistant vessel made of stainless steel 1.4571 with a volume of about 36.5 ml. This liquid is pressed into the view cell by means of a hand-pump manufactured by Sitec which can be employed for pressures up to 100 MPa.

The capillary used to hang the liquid drop is also made of stainless steel with an outer diameter of $1/32''$. Unfortunately the cross-section of this capillary is not perfectly round and it is placed in such a direction that the two-dimensional projection of the capillary width is 0.75 mm. The accurate width of the projected capillary is crucial because this quantity is used as a reference to

2.3 Experimental Setup

convert the pixel amount (seen by the software used to process the images) into the standard length unit.

The images of the drops are recorded by means of a camera. Later they are converted and processed by an image processing software called Drop Shape Analysis (DSA) provided by Krüss GmbH. This software makes use of the drop shape which is mathematically fitted and upon solving the fundamental equation, the interfacial tension can be obtained.

2.3.2 Density at High Pressure Condition

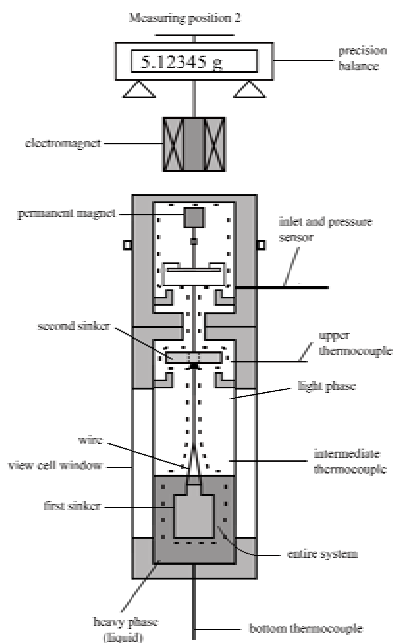


Figure 2-3: Magnetic suspension balance.

The main difficulty in measuring fluid density, i.e. its weight at extreme conditions, for instance at high pressure and high temperature conditions, especially if the miscibility between the coexisting phases is not negligible, is that in conventional gravimetric measurement method, there is always a direct contact between the sample being measured and the weighing device. At extreme conditions a direct contact is neither desirable (high temperature) nor possible (high pressure). This problem is solved by using a magnetic suspension balance where contact-less measurement is possible. Instead of hanging directly at the balance the sample to be investigated is linked to a so-called suspension magnet which consists of a permanent magnet, a

sensor core and a device for decoupling the measuring load. This kind of measurement method is well known and explained in detail in [47,113,129]. Only a brief introduction will be given here.

A three-mode magnetic suspension balance is to be seen in Fig. 2-3. By means of this three-mode magnetic suspension balance, the simultaneous measurement of the densities of two coexisting phases is possible. The heavy phase, for example a liquid, is put in the view cell surrounded by a second, lighter phase. Three measuring positions are possible here:

- Zero point: the permanent magnet is in a freely suspended state, allowing the balance to be tared and calibrated (see Fig. 2-4 a.)
- Measuring point 1: the first sinker is lifted up and its mass is weighed by the balance (see Fig. 2-4 b.)
- Measuring point 2: the second sinker is raised as well and both sinkers are weighed at the same time (see Fig. 2-3).

The density of the coexisting phases can be obtained by means of force balance between the gravitational and the buoyant forces. Subtracting the weight gained in the zero point from the one in first measuring point, the density of the light phase can be calculated. The density of the heavy phase can be estimated by subtracting the weight in the zero from the one in the second measuring point. Furthermore, for the calculation of the density, the mass of the sinkers, the measuring load decoupling and the volume of the sinkers are required (the force balance equations are reported in [8,185]).

This method is suitable not only to be used to measure the density of a fluid but also for any measurement which needs the contact-less gravimetric method such as sorption (kinetic of mass transfer).

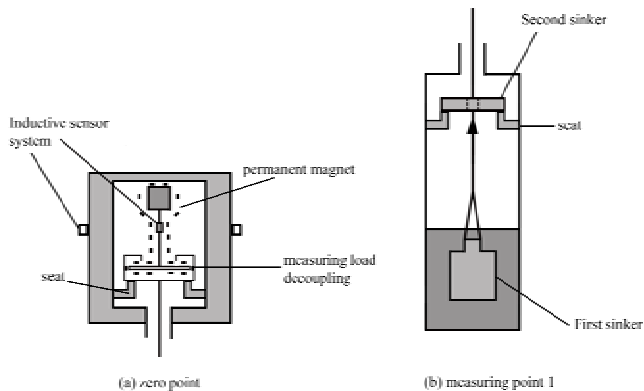


Figure 2-4: Magnetic suspension balance. a. Zero point, b. Measuring point 1.

2.4 Drop Phenomena

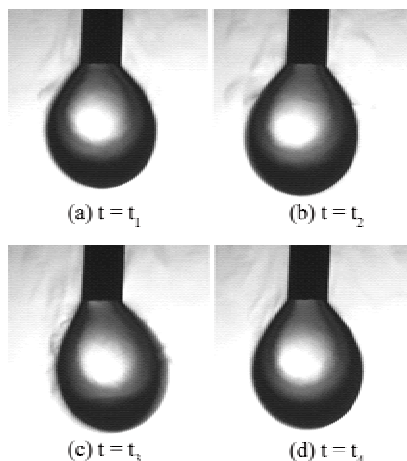


Figure 2-5: Kicking of a drop caused by interfacial turbulence. System: water pendant drop in CO_2 -ethanol (9.1 wt %) mixture at 313 K and 10 MPa. Drop age: $t = 4$ s to 8 s.

During the measurement of the interfacial tension some unique drop phenomena are observed when a system consisting of three components is being involved. Two of the three components form the two coexisting phases, and are nearly immiscible but the third component is well transportable between both phases. An example is water drop in carbon dioxide environment where carbon dioxide is mixed with a certain amount of ethanol. In cases where the system consists of only two components, for example only a water drop in carbon dioxide, these drop phenomena are not seen. These phenomena are related to the mass transfer between the phases as an attempt to reach an equilibrium in the system. Two complicating effects might occur when three components coexist in a system, i.e. the interfacial turbulence and the unstable emulsification [37,50]. Both of them will be explained by means of the observation made on the water pendant drop in CO_2 -ethanol mixture. Carbon dioxide is saturated by either 9.1 wt% or 16.7 wt% ethanol at 313 K. At the beginning, the drop phase consists only of water.

Taking the example given in Fig. 2-5, at some point on the interface an eddy of carbon dioxide brings up more ethanol in the water phase than at other points. This can originate in the temperature gradient or during the formation of the drop due to the forced convection while the drop is pressed against the continuous phase. At those points where the eddies bring up more ethanol, the local interfacial tension is lower than the points containing less ethanol and thus, there is an interfacial tension gradient around the drop (the eddies around the drop can be seen in Fig. 2-5 or even more intensified in Fig. 2-7).

To understand the direction in which the drop kicks, the pressure difference over the drop meniscus has to be explained first. The pressure inside the drop is a little bit higher than that outside of it. The magnitude of the pressure difference can be taken from Chapter 2.5.2 . The pressure is shown in Fig. 2-6(a) with arrows which are directed out of the drop. Actually only forces can be presented by arrows, not pressures. Because pressure does not have a certain direction. It pushes in all direction. The arrows in Fig. 2-6(a) are only there to show that the pressure inside is higher than outside.

The momentary change in the local interfacial tension such as explained above causes a local fall in the pressure difference too. That means, at a certain point, the pressure difference is smaller than at other neighbouring points. As a result, liquid is sucked in the direction where the pressure difference falls. As a help to understand the direction of the liquid motion, imagine a pressurized chamber which is filled with water. If there is an opening at the side of this chamber—which means a fall in the pressure—then the liquid will flow in this direction. Exactly this happens in the drop too. The drop swings in the direction of smaller pressure difference (see Fig. 2-5).

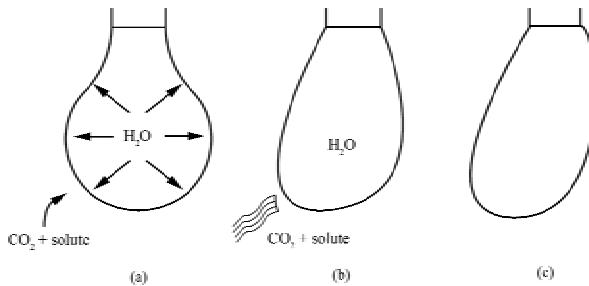


Figure 2-6: Interfacial turbulence around a water drop due to the mass transfer of a solute which changes the local drop interfacial tension. As a result, the drop kicks in the direction of the eddy (c).

In the next step, due to the interfacial tension gradient over the drop surface, ethanol spreads across the surface, followed by rapid diffusion into the drop. However, the spreading itself, enhanced by Marangoni convection, causes liquid movements which, in turn, bring up more CO_2 -ethanol mixture to the same point. Hereby, the originally small effect is intensified.

The phenomenon of drop kicking is seen most violently at the beginning just after the drop is hanging at the tip of the capillary and is damped as time proceeds. The kicking can best be seen at higher pressure.

The second effect, the unstable emulsification is closely related to “diffusion and stranding” and can always be observed during the transfer of the third component from one phase to another. This phenomenon is studied systematically by Shinoda and Friberg [171].

Emulsion is a mixture of two immiscible substances where a dispersed and a continuous phase can be found. Taking the same example, CO_2 eddies move towards the drop phase bringing sufficient amount of ethanol. Larger CO_2 amounts can be transported across the phase interface

when ethanol is dissolved in it. However, at the interface, alcohol diffuses further into the water phase (the solubility of ethanol in water is quite high) whereas the associated CO_2 molecules become thrown out and left behind. They are stranded in the water in the form of fine emulsion drops. This is the so-called unstable emulsification. An emulsification can as well have its origin in the interfacial turbulence. Here, the lowering of the local interfacial tension is stabilized by the formed fine emulsion drops [158].

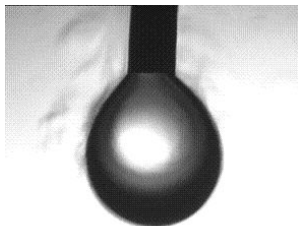


Figure 2-7: Eddy around a water pendant drop in CO_2 -ethanol (9.1 wt%) mixture at 313 K and 10 MPa. Drop age: $t = 3$ s.

The transport of ethanol into the aqueous phase decreases ethanol concentration in the continuous phase. As commonly known, sinking alcohol concentration in carbon dioxide causes a lower density of the continuous phase [16]. Together with the eddies explained before, the free convection due to this density gradient in the continuous phase around the drop can be seen in Fig. 2-7.



Figure 2-8: Stranded CO_2 -bubbles in water pendant drop at 313 K and 27 MPa.

The fine emulsion drops of carbon dioxide are unstable in the water phase. They coagulate and form larger emulsion drops which rise towards the neck of the water drop, such as seen in Fig. 2-8. That is why, this mechanism is called the unstable emulsification. This rising bubbles-effect becomes more intensified at higher pressure and higher concentration of dissolved ethanol in carbon dioxide.

The emulsification can occur in both sides, in the drop as well as in the continuous phase. Actually, the solubility of water in CO_2 is quite limited, but alcohol might permit more water to be dissolved in the continuous phase. However, as ethanol passes into the aqueous phase and

the ethanol concentration in CO_2 becomes less, water becomes stranded in CO_2 and forms stable, fine emulsion drops there. As commonly known, emulsion tends to have a cloudy appearance because the many phase interfaces (fine drops dispersed in continuous phase) scatters light that passes through. This phenomenon is observed and shown in Fig. 2-9. At the beginning, i.e. $t = 8$ s, the picture is very sharp and the drop boundary phase can very well be seen. At $t = 330$ s, the light is scattered in such a way that the picture becomes blurred and less sharp. This effect is seen at 3 MPa and 6 MPa but only when a sufficient amount (16.7 wt%) of ethanol is dissolved in CO_2 .

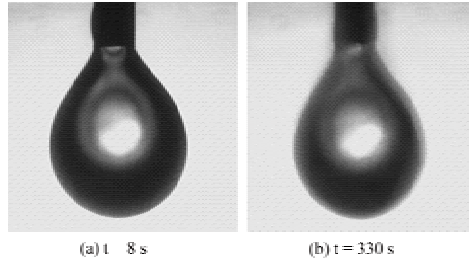


Figure 2-9: Mutual saturation between the water drop and the CO_2 -ethanol (16.7 wt%) continuous phase at 313 K and 3 MPa causes emulsification in each phases. The initial sharp picture at $t = 8$ s becomes cloudy after 330 s because the many phase interfaces scatter light that passes through the emulsion.

These drop phenomena regarding the interfacial turbulence and the unstable emulsification with all their concomitants are reported extensively in the literature:

- Transport of ethanol from carbon dioxide into water [148]
- Acetic acid transported from water into benzene [37]
- Ethanol transported from toluene into water. Toluene is saturated with water and mixed with 14 % ethanol [37]
- Acetone transported from toluene in water [37]
- Methanol transported from toluene into water [50].

2.5 Interfacial Tension Results

In this section, the measurement results of interfacial tension are reported. The interfacial tension depends on the composition of the drop and the embedding phases. That is why, in this section, the interfacial tension results are discussed in two parts, the interfacial tension in the static state and the interfacial tension as mass transfers are proceeding.

At equilibrium—the phases have reached their saturated state—the value of the interfacial tension does not change anymore and depends solely on the operating conditions such as shown in Chapter 2.5.1. The interfacial tension of water and ethanol against carbon dioxide will be

2.5 Interfacial Tension Results

shown in Chapter 2.5.1 as this data is required for further estimation of the interfacial tension σ_{sv} in Chapter 4.

In Chapter 2.5.2 the interfacial tension of aqueous drops against carbon dioxide is shown as a function of time, i.e. as the system is reaching equilibrium condition. The main objective here is to show that the interfacial tension depends on the mass transfer between the phases, i.e. on the adsorption and the desorption. Hereby the interfacial tension can be lowered or increased as the process proceeds until equilibrium is reached. In this section, the effect of the bulk phase on the interfacial tension is discussed in detail.

2.5.1 Static Interfacial Tension

The static interfacial tension of water and ethanol against carbon dioxide at 294 K-313 K is given in Fig. 2-10. Here, the interfacial tension is measured when the mass transfer process has been completed. That means, the concentration equilibrium between the drop and the embedding phases has been reached. The density data required for the calculation of the interfacial tension are taken from the literature: for pure water and pure carbon dioxide [144], water saturated with carbon dioxide [185] and compressed ethanol [33,36].

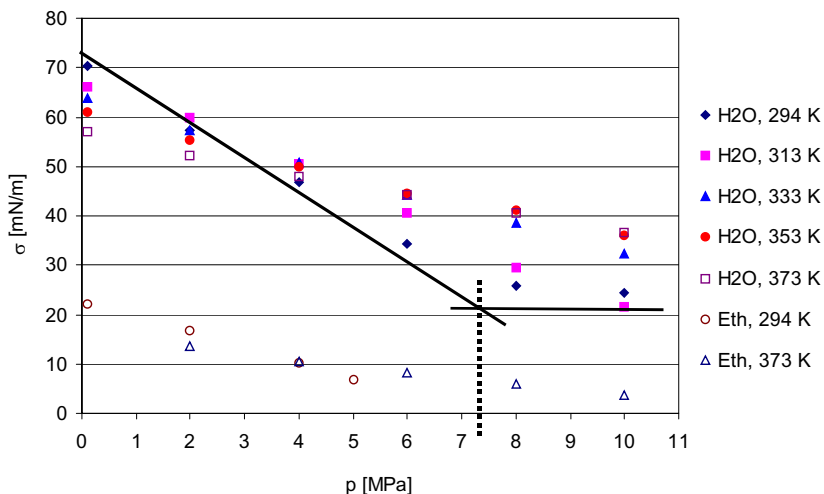


Figure 2-10: Interfacial tension of water and ethanol against dense carbon dioxide.

As can be seen, the interfacial tension of water against carbon dioxide depends on the temperature and the pressure. Along an isobaric where carbon dioxide is still gaseous, the interfacial tension decreases as the temperature increases from 294 K up to 393 K. However, as carbon dioxide turns to supercritical, the interfacial tension decreases with decreasing

temperature. The turning point of this temperature dependence is at around the critical point of carbon dioxide where it changes from the gaseous to a supercritical one.

The value of the interfacial tension decreases first drastically with increasing pressure at every investigated temperature. Increasing pressure means also a higher solubility of carbon dioxide in the drop phase. This is in accordance with the Gibbs adsorption law (see Eq. 2-22) where it is stated, that an adsorption—characterized by an increase in the component concentration x_i —causes a fall in the interfacial tension.

The fall of the interfacial tension in the first part is nearly linear. A further increase in the pressure behind this linear fall does not affect the interfacial tension significantly. From here on, the interfacial tension remains almost constant [81,194]. This is the second linear part of the interfacial tension curve. The linear dependency of the interfacial tension on the pressure at lower pressure conditions can be explained by means of the solubility of carbon dioxide in the drop phase. At lower pressures, the solubility of carbon dioxide in the liquid phase increases linearly with the pressure. However, the gradient of the solubility becomes smaller as the pressure increases until the curve reaches a nearly constant value where the solubility changes hardly with increasing pressure. This is the explanation for the behaviour of the interfacial tension dependency on the pressure. The interfacial tension is lowered with increasing pressure as long as the pressure still has an impact on the CO₂ solubility. Once the drop phase has been saturated, a further increase in the pressure does not bring more carbon dioxide into the drop phase, and thus, it has hardly any influence on the interfacial tension.

The intersection of the first linear and the second horizontal line at 294 K is drawn in Fig. 2-10 and the turning point is approximately at the critical point of carbon dioxide where it turns from the gaseous to the supercritical one at 7.4 MPa.

The interfacial tension of ethanol is far lower than that of water. The same pressure effect can be seen here too. At ambient pressure, it has a value of 22 mN/m but at 5 MPa this value becomes 6.7 mN/m. At 373 K and 10 MPa ethanol has an interfacial tension of only 3.5 mN/m.

2.5.2 Interfacial Tension as Mass Transfer Proceeds

In Fig. 2-11 the interfacial tension of pure water against carbon dioxide at 294 K and 8 MPa, estimated by means of pure drop density as well as mixture density at saturated state, and water-ethanol mixture against presaturated carbon dioxide at 313 K and 10 MPa are shown. The interfacial tension of the two systems change in opposite directions with time.

An increase in the interfacial tension is seen in the water-ethanol mixture. Here, water is mixed with 10 wt% ethanol and the surrounded carbon dioxide phase is also presaturated with a small amount of this mixture. The mixture used for the presaturation of the embedding phase is approximately 5 g. The view cell used here has an inner volume of about 88.5 ml.

Apparently, the embedding phase is not saturated yet. The solubility of ethanol in the carbon dioxide is far higher than the amount provided for the presaturation. That is why ethanol is

2.5 Interfacial Tension Results

transported from the aqueous drop phase to the continuous phase. The desorption of ethanol results in an increase of the drop interfacial tension from the initial value 18.5 mN/m to 21.3 mN/m. Although there are also mutual solubilities of water and carbon dioxide but compared to the amount of dissolved ethanol and its impact on the interfacial tension, they do not affect this property significantly. This desorption phenomenon which causes an increase in the interfacial tension is in good agreement with the Gibb's adsorption law given in Ch. 2.1. The required density data for the calculation of interfacial tension of water-ethanol mixture against carbon dioxide are taken from the literature. The density data of water-ethanol mixture reported in [152] is used. The density change of the continuous phase due to presaturation is assumed to be negligible and the density of pure carbon dioxide in [144] is taken.

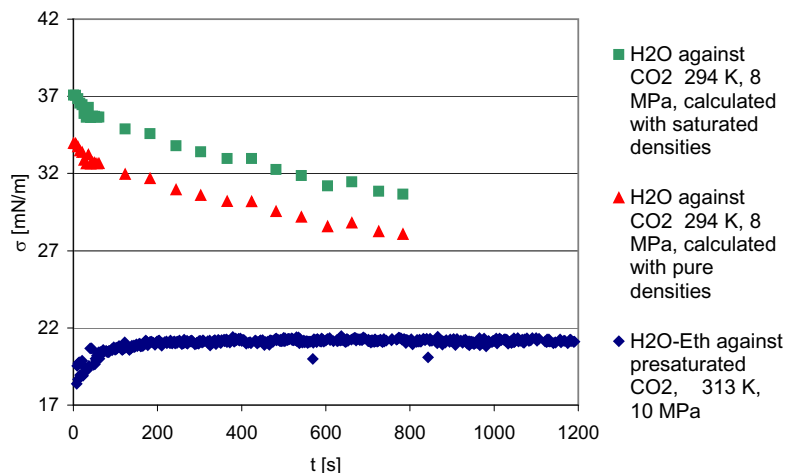


Figure 2-11: Interfacial tension of water and water-ethanol mixture during the mass transfer.

As for the system pure water drop against carbon dioxide, carbon dioxide is brought into the drop phase and lowers the interfacial tension of the water phase according to the Gibbs adsorption law (Eq. 2-18). Here, considering the composition of the drop phase, the calculation of the liquid interfacial tension against carbon dioxide is done twice. First by means of pure water density, and later, by using the saturated density of water and carbon dioxide mixture. In both cases, it is assumed that the continuous phase contains only carbon dioxide. The solubility of water in carbon dioxide is taken as negligible.

Applying the pure densities of water and carbon dioxide, the interfacial tension falls from 34 mN/m to 28 mN/m in 800 s. If the saturated density of the mixture of water and carbon dioxide is taken for the drop phase, the interfacial tension is lowered from 37 mN/m to 30.6 mN/m. It is believed that after 800 s the drop phase is saturated by carbon dioxide so that after 800 s there is no significant change in the interfacial tension.

The consideration about which density is to be used for the drop phase in estimating the interfacial tension—whether the pure density or the mixture density—goes back to the already aged-discussion about what role the bulk phase plays in the interfacial tension. There exist two possibilities. In the first one, the interfacial tension depends solely on the composition of the interface. In the second one, not only the interface but also the bulk phase determines the interfacial tension.

Assuming the first possibility (the interfacial tension is affected solely by the composition of the interface), the static interfacial tension should have been reached instantaneously after the drop is formed. During the formation of the drop, the forced convection around the drop surface governs the mass transfer between the phases. Thus, within a very short period of time, the concentration at the interface has reached saturation. But the fact is, the water drop shape in carbon dioxide still changes during the saturation time of the bulk phase, that is, in 800 s. The alteration in the shape of the drop signals that the static interfacial tension has not yet been obtained. As it can be seen in Fig. 2-11, the interfacial tension still changes with time regardless of whether the pure water density or the mixture density is taken into account in calculating the interfacial tension value. The saturation value is obtained after waiting for 800 s.

Morgner [136] tried to understand this fact by suggesting the idea that the pressure difference over the meniscus is responsible for the drop shape alteration during the measurement. The relaxation of this pressure difference takes some time and causes the change in the drop shape. The alteration of the drop shape has no correlation with the static interfacial tension. To Morgner, the static interfacial tension should have been reached immediately (microseconds) after it hangs at the tip of the capillary.

According to him, the pressure difference Δp perpendicular to an interface changes as much as 100 MPa/Å. That means, an interface of 1 Å thick brings a pressure difference of as high as a maximum of 100 MPa. Assuming a water drop diameter of 5 mm and letting carbon dioxide be transported across the interface, through a computer simulation Morgner stated that due to the transfer of carbon dioxide there is a pressure difference as much as 2 MPa over the interface [136].

To reexamine the validity of Morgner's statement about the magnitude of the pressure difference across the interface, the Young-Laplace Equation (Eq. 2-32) is applied. In this equation, the pressure difference over the meniscus is correlated with the interfacial tension and the principal radii R_1 and R_2 . Here, the radius R_1 in the Young-Laplace Equation is set equal to R_2 (Eq. 2-34). Both radii are the same:

- If the drop geometry is assumed as spherical. In this case, the pressure difference Δp over the meniscus is the same over the whole drop surface.
- At apex, such as given in Eq. 2-34. This means, the pressure difference is calculated only at the point Δp_{Apex} . The drop shape remains as it is (no geometrical simplification is made here).

2.5 Interfacial Tension Results

In the following, the radius of a drop is calculated in cases where the pressure differences over its meniscus are 100 MPa (maximal pressure difference possible) and 2 MPa. The system used here is water in a carbon dioxide environment at 293 K and pressures up to 25 MPa. The interfacial tension data are taken from the literature [61,182]. At 293 K and 0.1 MPa, the interfacial tension of water in a carbon dioxide environment is 70.32 mN/m. Following the suggestion of Morgner, the radius of the drop should be 14 Å (if the pressure difference is 100 MPa) or 7 Å if a pressure difference of 2 MPa is assumed. The theoretical radii obtained from the calculation can be seen in Table 2-2.

Table 2-2: Calculated drop radii assuming a pressure difference of 2 MPa and 100 MPa.

Temp. [K]	p [MPa]	Δp [MPa]	R [Å]	σ [mN/m]	σ Source
293	0.1	2	7	70.32	[182]
293	2	2	6	57.27	[182]
293	4	2	5	46.69	[182]
293	6	2	3	34.38	[182]
293	8	2	3	25.92	[182]
293	10	2	2	24.53	[182]
293	15	2	2	23.1	[61]
293	20	2	2	20.3	[61]
293	25	2	1	13.6	[61]
293	0.1	100	14	70.32	[182]
293	2	100	11	57.27	[182]
293	4	100	9	46.69	[182]
293	6	100	7	34.38	[182]
293	8	100	5	25.92	[182]
293	10	100	5	24.53	[182]
293	15	100	5	23.1	[61]
293	20	100	4	20.3	[61]
293	25	100	3	13.6	[61]

According to the radii values obtained in Tab. 2-2, the radii lie in nanometer range. Macroscopically seen, it is impossible to obtain such drops. Probably, the calculated pressure difference over the meniscus is overestimated. In the following, an attempt is made to calculate the pressure difference over the meniscus of a drop with a diameter of 5 mm. The same system as used in Tab. 2-2 is applied here, water drop in a carbon dioxide environment at 293 K and pressures up to 25 MPa.

It can be seen in Tab. 2-3 that the pressure difference over the meniscus is far lower. The pressure differences calculated here are 10^5 - to 10^7 -times lower than that forecast by Morgner.

Schwuger [168] estimated the pressure difference over the meniscus of a water drop with a diameter of 2 mm. He took an interfacial tension of 73 MPa and found out that the pressure difference is 1.5 mbar (or $1.5 \cdot 10^{-4}$ MPa) which is in the same order of magnitude as the value calculated in Tab. 2-3.

Table 2-3: Calculated pressure difference over the meniscus of a drop whose diameter is 5 mm.

Temp. [K]	p [MPa]	Δp [MPa]	R [mm]	σ [mN/m]	σ Source
293	0.1	5.63E-05	2.5	70.32	[182]
293	2	4.58E-05	2.5	57.27	[182]
293	4	3.74E-05	2.5	46.69	[182]
293	6	2.75E-05	2.5	34.38	[182]
293	8	2.07E-05	2.5	25.92	[182]
293	10	1.96E-05	2.5	24.53	[182]
293	15	1.85E-05	2.5	23.1	[61]
293	20	1.62E-05	2.5	20.3	[61]
293	25	1.09E-05	2.5	13.6	[61]

The pressure difference as shown in Tab. 2-3 seems more reasonable than the one calculated by Morgner. This is due to the fact that a pressure difference—like a concentration and a temperature difference—will cause fluid flow in order to reach an (mechanical) equilibrium. There is no reasonable argument which can explain why even though the pressure difference over the drop meniscus is as high as 2 MPa (or even 100 MPa), macroscopically seen, the drop remains in its static state.

Hence, the idea that it is the pressure difference which causes an alteration in the drop shape during the interfacial measurement is disproved. Later, in his report [136], Morgner also admitted that the pressure difference is not the property which is responsible for the geometry change of the drop. However, he still could not clearly explain what causes the changes in the drop shape during the measurement if the static interfacial tension has really been reached microseconds after the drop is formed.

Although the first possibility cannot be applied to explain the change in interfacial tension with time, Morgner's argument about the instantaneous saturation of the interface is reasonable. It is believed that within a very short period of time the interface is saturated. This does not mean that the concentration equilibrium between the phases has been reached. Even though the interface is saturated, the bulk phase has not yet reached the equilibrium. A certain saturation time is still required to reach equilibrium between those bulk phases.

It is apparent that the composition of the bulk phase does play an important role in the interfacial tension. Even though the saturation of the interface is reached instantaneously as the drop hangs at the tip of the capillary, the static interfacial tension or the saturated interfacial

tension has not yet been reached. The proof that the bulk composition affects the interfacial tension is that the drop shape changes as the mass transfer proceeds. And an alteration in the drop shape signals a change in the interfacial tension itself.

To be very precise, the drop density which should be applied in estimating the interfacial tension is the instantaneous density of the mixture in the drop phase. This density data can be obtained by hanging a drop at a capillary which is connected to a magnetic suspension balance (see Chapter 2.3.2). Using this method, the mass transfer into a drop can be tracked very well and the density change with time can be obtained. Here, the geometry of the interface is important. The diagram of density as a function of time is not the same whether a water drop is hung in the carbon dioxide environment or just a plane water surface is brought into touch with carbon dioxide. The final saturation density will be the same, but not the instantaneous one which is essential in estimating the precise instantaneous interfacial tension.

If the instantaneous drop density is applied, the degree of mass transfer is considered in the interfacial tension estimation. The interfacial tension diagram obtained will lie between both curves shown in Fig. 2-11. At the beginning, the drop density is closer to the pure water density. Shortly before the equilibrium state is reached, it will be very similar to the saturation density. Thus, the real interfacial tension will lie between these two diagrams. It starts from the interfacial tension diagram applying the pure drop phase density and ends in the diagram applying the saturation density of the drop phase.

The interfacial tension error appearing here due to the density used for the drop phase can be estimated by calculating the difference between the interfacial tension obtained using the pure and the saturated density. The mean difference between both interfacial tensions is 2.9 mN/m. That means, applying the interfacial tension either calculated by means of the pure drop density or by the saturated drop density causes an error in the interfacial tension of less than 2.9 mN/m.

The degree of importance in using the instantaneous drop mixture density depends on the solubility of carbon dioxide into the drop phase. For systems where the solubility between the phases is not that high (for example water-carbon dioxide system), it is less important to apply the instantaneous drop mixture density. However, once the solubility of carbon dioxide in the drop phase is high (for example systems containing alcohols or oil), the change in the instantaneous drop mixture density becomes higher. It is therefore more essential to apply the instantaneous drop density for such systems in order to minimize the imprecision in the interfacial tension estimation.

3 Wetting Characteristics of a Sessile Drop

A pessimist sees the difficulty in every opportunity, an optimist sees the opportunity in every difficulty.

Sir Winston Churchill

Basically, wetting is the contact between a fluid and a surface when the two meet each other. Wetting can be encountered in a large variety of phenomena in daily life as well as in industrial application. A few applications closely related to wetting are lubricating, coating, adhesion, detergency and lithographic printing. From the technological point of view, dealing with the wetting problem began, as far as we know, with people starting to write with inks.

Although the wetting problem itself is an old one and commonly known but little research has been done on the wetting under high pressure conditions especially when the miscibility between the phases coming into touch is not negligible. The study of wetting under high pressure conditions reported in the literature up to now is listed in Table 3-1.

Table 3-1: Review of past wetting research under high pressure conditions.

Source	Year	System	T [K]	p [MPa]
[17]	1997	water-aluminium-N ₂	298 - 443	0.8274
[194]	1997	water-Teflon-CO ₂	298-333	30
[194]	1997	water-stainless steel-CO ₂	298-333	30
[194]	1997	water-PVC- CO ₂	298-333	30
[194]	1997	water-sapphire- CO ₂	298-333	30
[194]	1997	water-glass- CO ₂	298-333	30
[92]	1998	water-stainles steel- CO ₂	293-313	25
[92]	1998	water-glass- CO ₂	293	25
[92]	1998	corn germ oil-stainless steel- CO ₂	313-353	30
[160]	2002	crude oil-brine-rock	301 - 468	25
[112]	2002	toluen-Teflon- N ₂	295.7	20
[112]	2002	ethandiol-Teflon- N ₂	295.7	20
[112]	2002	formamid-Teflon- N ₂	295.7	21
[112]	2002	water-Teflon- N ₂	295.7	20

The purpose of this chapter is to focus on the wetting properties of a sessile drop in dense carbon dioxide. To start with, the theoretical background of the wetting according to Young will be introduced, followed by the measurement methods and experimental setup used to measure the sessile drop contact angle surrounded by pressurized carbon dioxide. The difficulties encountered in the experiments are explained in Chapter 3.3. Finally the measurement results are reported in Chapter 3.4 and 3.5.

3.1 Theoretical Background

The Beginning

A strong debate on wetting phenomena among philosophers had begun in the time of Aristotle who observed that a piece of gold leaf or a chip of mahogany wood floats when laid on the surface of water. However, a century after Aristotle, Archimedes wrote a treatise on hydrostatics and invented the concept of specific gravity. The hydrostatics theory of Archimedes is contradictory to the observation made by Aristotle because the specific gravities of the floating solid materials are far larger than that of water and thus, hydrostatically seen, they cannot float on the water surface. Hereby, the debate between these two ideas started and lasted for about 1800 years before this conflict was settled by Galileo in 1612 [63]. He noticed that if the solid was denser than water, the flat, thin solid was floating on the water surface but the top of the solid was below the surface of the water (see Fig. 3-1). Thereby, he came to understand the wetting and spreading problem in modern terms. However, he could not measure the contact angle and did not have the concept of surface tension. Sulman [181] is the first to explicitly include contact angles in the relation with the floating-dense-solid phenomenon.

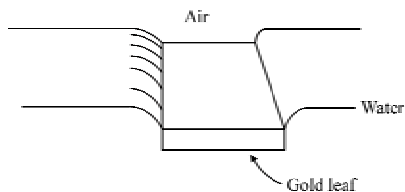


Figure 3-1: Galileo's explanation for the floating of thin sheets of gold or mahogany on water [75].

Contact Angle

The scientific investigation on the wetting phenomena started in earnest 200 years after Galileo. Thomas Young [204] was the first to explain the relationship between the interfacial tensions and the contact angle. Instead of formulating his concept mathematically, he expressed it clearly in words and therefore, the well known equation

$$\sigma_{sv} = \sigma_{sl} + \sigma_{lv} \cos \theta \quad (3-1)$$

is dedicated to him and referred to as the Young equation even though, strictly speaking, Eq. 3-1 is the formulation given by Bangham and Razouk [12]. In Eq. 3-1, the interfacial tensions are understood in terms of force vectors and considering the projection in the x-axis, the solid-vapour interfacial tension σ_{sv} is correlated with the solid-liquid σ_{sl} and the liquid-vapour interfacial tension σ_{lv} by means of the contact angle θ . By definition, the contact angle θ is the angle between the interfacial tension vectors of σ_{lv} and σ_{sl} . And therefore, it is clear, that contact angle θ is the reaction of the interfacial tension vector σ_{lv} to maintain the force balance [178] and thus, to reach the mechanical equilibrium when a drop rests on a horizontal surface.

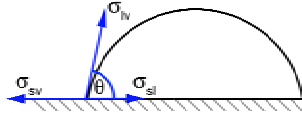


Figure 3-2: Force balance on the three-phase contact point according to Young [204]

The Young equation considers only the force balance in the x-axis. However, the inclination of the vector σ_{lv} presumed the existence of the force component of σ_{lv} in the y-axis and therefore, Bikerman [19] contended that the Young equation cannot be valid due to the fact that there is no opposite balancing force for the projection of σ_{lv} in the y-axis direction. Admittedly, Bikerman did not take the strain field in the solid below the three-phase line into account which furnishes the required balancing force [11,120].

Due to the contact angle hysteresis and the poor reproducibility of the contact angle in the experiments, there has been doubt about this property as a unique thermodynamic quantity which can be used to characterize the wettability of a given system [188]. However, Johnson [99] and Marmur [133] showed distinctively that this property is a thermodynamical one and can, even under consideration of gravity and adsorption, be derived using the method of Gibbs.

The contact angle is often roughly and wrongly understood solely as the property of a solid or a liquid. Actually, it is absolutely not a material property, but rather a system property. The contact angle is, as explained before, the result of the inclination of the interfacial tension σ_{lv} , as a reaction to the interfacial tensions σ_{sv} and σ_{sl} to maintain the force balance. And thus, the contact angle depends on the three interfacial tensions shown in Fig. 3-2 which also means, that the contact angle is a system, not a material property. In general, changing one of the three substances results in a new, from the previous one different contact angle mainly when the miscibility between the phases is not negligible.

According to the experimental results, there is a contact angle hysteresis which aggravates the reproducibility of this property. The Young equation is derived with the assumption of an ideal solid, namely chemically homogeneous, rigid and flat at an atomic scale. If this condition is not fulfilled, there will be an advancing θ_a and a receding contact angle θ_r . The advancing contact angle can be measured on an initially dry surface whereas the receding (also called the retreating) angle is found when the surface is pre-wetted. The difference between both shows the magnitude of the hysteresis itself. Although hysteresis up to 2° is regarded as negligible [186], it is common to find hysteresis in the range of 10° or even larger. The influence of surface heterogeneity on the contact angle is reported in the literature [28,91,100,122,126,145] and particularly on the influence of surface roughness on the contact angle in [27,49,87,98,143,150,172,193]. Some of the researchers believe that the drop size plays an important role in the contact angle [5,31,76,89,121,186] but this has not yet been fully explained.

From an engineering point of view, this hysteresis is seen as a challenge to access the real contact angle because the employed surface in the industrial application will neither be ideal nor homogeneous microscopically seen. In the experiments, this hysteresis problem is solved by measuring the contact angle repeatedly and on the whole area available as an attempt to obtain an average, representative value of the contact angle and to minimize the error happening during the measurement.

Some measurement methods of contact angle are the sessile drop, Wilhelmy plate and tilting plate methods. The sessile drop method is applied to measure both the static and the dynamic contact angles although only the static contact angle was used in later calculations. Measuring the dynamic angle, the liquid drop is introduced by means of a capillary which remains in the drop while additional liquid is added into the drop until the limited value of the advancing angle θ_a is reached. A further addition to such a drop causes a spontaneous spreading. To measure the retreating angle, liquid is withdrawn from the drop steadily. In the static angle measurement, a drop is detached from the capillary and when equilibrium is reached, the angle is measured.

The reproducibility of the dynamic angle is less when compared with the static angle because in the dynamic method, the drop is still pumped and pressed radially by the liquid added into it. The force inserted by the hand pump to introduce more liquid into the drop is not quantified and thus, the reproducibility of the angle is also not assured. Furthermore, the existence of the capillary held in a fixed position in the drop can under certain conditions, for instance when the drop is sufficiently small, distort the shape of the drop and falsify the measured angle. The force balance regarding the distorted angle is explained in 3.5.

In the literature, it is often reported that highly energetic surfaces have better wetting characteristics when compared with less energetic surfaces. Two concepts have to be more clearly explained: the energetic state of a surface and the quality of wetting. Starting from the latter one, the values 0° , 90° and 180° are often used as measures for the degree of wetting [2,140]. Total wetting is used to characterize a complete spreading of liquids on a solid surface where the contact angle is equal to 0° , whereas total non-wetting appears when the angle is 180° . If a system has a wetting angle below 90° , it is referred to as well wetted. Above 90° , the system is categorized as having a bad wetting characteristics. However, it should be emphasized that the wetting measure has not yet been standardized so the above mentioned categories are not generally accepted. To be more precise, it is better to use a qualitative expression for the wetting measure together with the absolute value of the angles.

Most of the materials made of polymers are referred to as low energetic surfaces with large contact angle, and thus, low wettability [55,57,207]. On the contrary, steel and glass are often categorized as high energetic with smaller contact angle and better wettability. The idea of classifying the material according to its energetic state goes back to the force balance at the three-phase contact point such as shown in Fig. 3-2. The quantity used to characterize a solid material is the solid-vapour interfacial tension σ_{sv} . A high σ_{sv} value forces the vector σ_{lv} to form a smaller inclination, and thus a smaller angle, in order to keep the force balance. As a result,

the wetting is good. On the contrary, a low value of σ_{sv} does not need a large contribution from the vector σ_{lv} to maintain the force balance. In such a case, the contact angle will be sufficiently large and thus, the wetting is rather poor. In extreme cases, the interfacial tension vector σ_{lv} is even tilted to the side of the interfacial tension vector σ_{sv} because the vector σ_{sv} is already smaller than the vector σ_{sl} . In this case, the wetting angle is larger than 90° .

The classification of a solid surface using its energetic state comes from the surface chemistry point of view where the quantity σ_{sv} or generally, the quantity σ is understood as energy. As explained in detail in Chapter 2.1, from the engineering point of view, the quantity σ is seen rather as a force. This concept is used in this whole work.

3.2 Experimental Setup

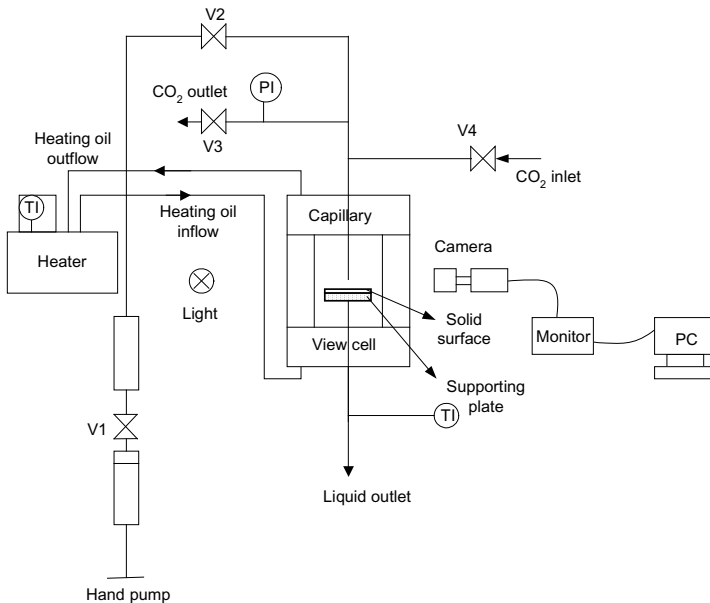


Figure 3-3: Experimental setup to measure the contact angle under high pressure conditions.

The experimental setup used to measure the contact angle under high pressure conditions is shown in Fig. 3-3. It is similar to that used to measure the interfacial tension (see 2.3.1). The view cell employed here is made of stainless steel with a volume of 88.5 ml. This view cell is designed for a maximal temperature of 393 K and a maximal pressure of 90 MPa. The same hand pump and liquid vessel as used in 2.3.1 for the interfacial tension measurement are employed here. The liquid is introduced onto the studied horizontal surface through a stainless

3.2 Experimental Setup

steel capillary whose outer diameter is equal to 1.59 mm (1/16"). The studied solid material is placed on a stainless steel plate with a diameter of 30 mm such as shown in Fig. 3-4.

The main difficulty in measuring the advancing angle is that at the beginning, the surface has to be clean and dry. It should not be prewetted by the liquid used as the drop phase. Therefore, to minimize the time- and energy-consuming procedure needed to release the pressure and clean the surface after each measurement, a view cell with a magnetic system is employed. This magnetic system enables the rotation and the vertical motion of the supporting plate (Fig. 3-4) on which the investigated solid surface is placed (see Fig. 3-3). Moving a magnet outside of the pressurized system, the solid surface in the view cell under the operating conditions can be turned and moved vertically in order to find a clean space to place a fresh drop. This magnetic construction permits the contact angle measurement of more than one drop before the whole system has to be depressurized to clean the surface.

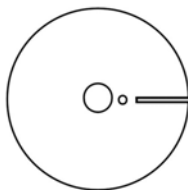


Figure 3-4: Stainless steel plate on which the investigated solid surface is placed.

Furthermore, it is often experienced that a small amount of the drop phase contains fluid bubbles and has therefore to be repelled at the beginning. This can be performed perfectly by moving the supporting plate upwards and placing the capillary in the slit (see Fig. 3-4). In this way, liquid can be thrown out without prewetting the solid material.

Table 3-2: Surface roughness of the investigated materials.

	R_a [μm]
Teflon	0.16
Glass	0.005
Smooth steel	0.241
Rough steel	2.557

In this work, the contact angles of water and ethanol on Teflon, steel and glass surfaces are measured according to the sessile drop method at temperatures up to 373 K and pressures up to 27 MPa. Both dynamic and static angles are measured and reported in 3.5 and 3.4 respectively. Normally, the surface of a steel is characterized by its surface roughness. The steel investigated here is 1.4305 and contains 70-wt% Fe, 9-wt% Ni, 18-wt% Cr, 1-wt% Si and 2-wt% Mn. In Table 3-2 the surface of each material used is characterized by its roughness R_a . The average roughness R_a is the arithmetic mean of the absolute distances of the surface points from the

mean plane. Here, steel with two different kinds of roughness are studied. The steel whose R_a equals $0.241\ \mu\text{m}$ is referred to as smooth steel in comparison to the rough one with R_a equal to $2.557\ \mu\text{m}$.

3.3 Some Remarks

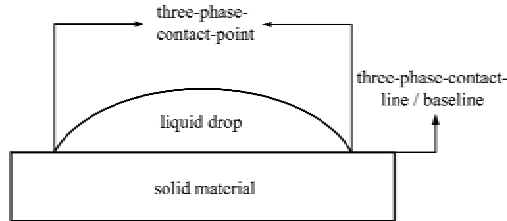


Figure 3-5: Contact angle measurement by means of the sessile drop method.

The contact angle of a sessile drop is measured by means of image processing software. This software makes use of the gray scale recognition to fit a mathematically defined curve to the drop shape. In this way, the tangent of the drop at the three-phase-contact-point can be estimated (see Fig. 3-2 and Fig. 3-5).

The main point in the measurement of the contact angle using this image processing software is the precise positioning of the baseline. The baseline is defined as the place where the drop touches the solid surface. The easiest way to place this line exactly at its position is by putting it across the two three-phase-contact-points (Fig. 3-5) so that the angle between this baseline and the tangent can be determined (see Fig. 3-2). This can be done if the precise identification of the three-phase-contact-points is possible.

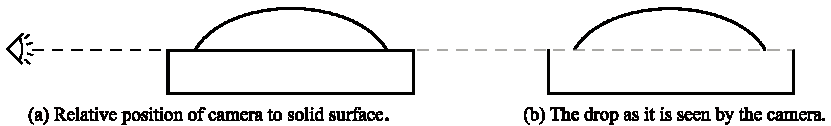


Figure 3-6: Relative position between the camera and the solid surface in order to obtain the correct contact angle.

Depending on the position of the camera relative to the solid surface (or the eye just as shown in Fig. 3-6, Fig. 3-7 and Fig. 3-9), there are three possible perspectives in measuring the contact angle. Theoretically, in order to get the correct contact angle, the camera axis has to be precisely at the same height as the solid surface (see Fig. 3-6). Only then can the exact contact angle be obtained.

3.3 Some Remarks

A precise measurement of the contact angle is therefore difficult, because a small inclination of the camera axis relatively to the solid surface leads to imprecision. If the camera axis is not positioned exactly at the same height as the solid surface but forms a negative inclination $-\alpha$ so that it looks at the surface from below (see Fig. 3-7) then the measured contact angle is always smaller than it actually is.

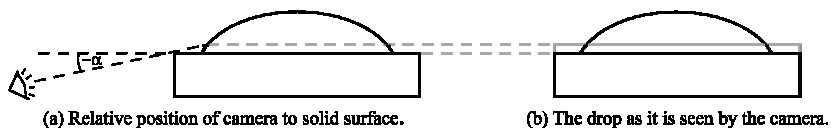


Figure 3-7: Optical error in the contact angle measurement. The drop is seen from a perspective below the solid surface.

This can be explained as follows. Looking at the border between the liquid and the solid phase from below causes the incorrect recognition of the baseline. The front border of the solid surface appears higher (due to the camera inclination). As a result, this border blocks one part of the drop (see Fig. 3-8). Only the upper part of the drop is still to be recognized while the part which comes directly into touch with the solid surface remains hidden. A visualization of the measured angle (θ_2) compared with the real one (θ_1) can be seen in Fig. 3-8. In such a case, the measured angle is erroneous. It is always less than it should be, regardless of whether the wetting is good (Fig. 3-8, right) or bad (Fig. 3-8, left).

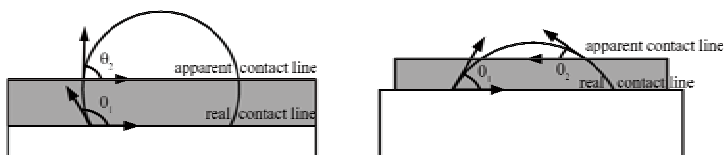


Figure 3-8: Erroneous identification of the solid surface leads to a smaller contact angle θ_2 regardless of whether the real contact angle θ_1 is larger (left) or smaller (right) than 90° .

If, on the contrary, the camera axis is put in such a position that the inclination is positive (the drop is recorded from above) then the angle measured is also not exactly like the original one. But the advantage of this measurement perspective is that the reflection of the drop on the solid surface can be recognized very well. And by means of this reflection method, the position of the three-phase-contact-points can be detected precisely. This is very important to be sure that the position of the baseline is correct.

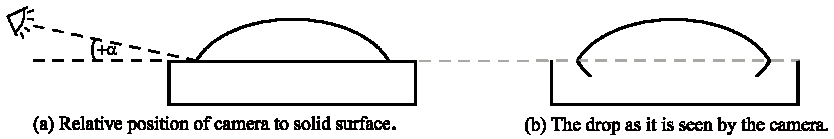


Figure 3-9: Reflection of the contact angle on the solid surface which can be seen only if the camera axis is inclined positively ($+α$) against the solid surface.

Theoretically seen, the correct method is to have zero inclination between the camera axis and the solid surface such as shown in Fig. 3-6. However, in reality, using such a drop image, no-one can ever be sure whether the inclination is really zero (Fig. 3-6) or if it is minus, such as shown in Fig. 3-7. Therefore, a compromise has to be made here. The aim is to measure an angle with a negligible deviation from the real angle. The method is to have a small positive inclination (Fig. 3-9) which allows the sight of the reflection of the drop on the solid surface. The inclination of the camera axis should not be too large because otherwise the angle measured is also not precise. Hereby, the baseline can be positioned comfortably by using the two three-phase-contact-points (compare with Fig. 3-10 and Fig. 3-12)

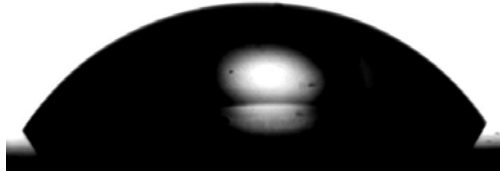


Figure 3-10: Reflection of the drop on the surface enables a precise optical identification of the baseline where the liquid touches the horizontal solid surface. System: water drop on a glass surface in CO_2 -environment at 333 K and 2 MPa.

For a contact angle near 90° , even using the reflection method is not of great help (see Fig. 3-11). The tangents of contact angles close to 90° are nearly vertical lines and thus the meeting point between the drop and the solid surface is not always clearly recognized. However, the error in measuring such an angle is negligible because one can be sure that the angle is around 90° .

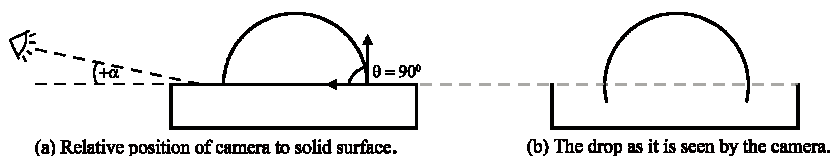


Figure 3-11: Drop reflection on the solid surface is not of a great help for the contact angle measurements in cases where the angles are very close to 90° .

To minimize the error of the measurement and to gain a representative, average value of the contact angle, the measurement is repeated around 7 times for both, the static and the dynamic angles. The values shown in Chapter 3.4 and Chapter 3.5 are the averaged ones.

3.4 Static Wetting Angles

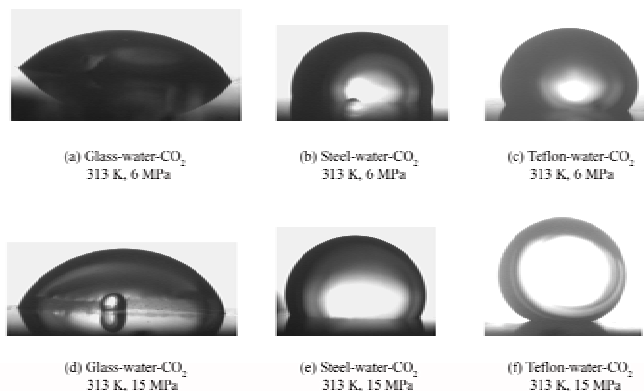


Figure 3-12: Static wetting angles of water on Teflon, glass and steel against carbon dioxide at 313 K.

The pictures of the static water drops on Teflon, glass and steel surfaces under the influence of gaseous as well as supercritical carbon dioxide can be seen in Fig. 3-12. The static, equilibrium contact angles of water drops on these surfaces are measured at temperatures up to 373 K and pressures up to 27 MPa.

The static contact angle values at 313 K presented in Fig. 3-13 and Fig. 3-14 are mean values. The measurements on those surfaces are repeated on average 7 times on different spaces of the material to minimize the experimental error and to obtain an average value of the contact angle where the hysteresis due to the surface heterogeneity is taken into account. The measured values

have a variability of 10° which is acceptable because here both, the measurement imprecision and the hysteresis are included.

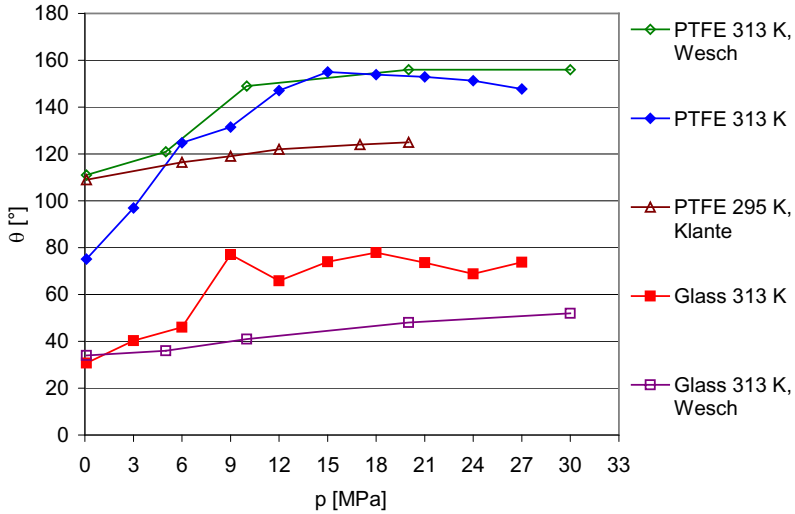


Figure 3-13: Contact angle of sessile water drop on Teflon and glass surfaces against carbon dioxide (except the data from Klante, they are measured against nitrogen).

In Fig. 3-13 the contact angles of water drops on Teflon and glass surfaces are shown. Water wets Teflon surface with a contact angle of between 75° and 155° at 313 K and in the pressure range up to 27 MPa. The wettability of water on Teflon surface becomes less as the pressure increases and in supercritical carbon dioxide the contact angle reaches a nearly constant, asymptotical value. Comparing the measured contact angle with the values reported in the literature, they coincide quite well except at 0.1 MPa and 3 MPa. Wesch [194] and Klante [112] reported an angle of around 110° for the contact angle of water on a Teflon surface at 0.1 MPa. Although the measurements were repeated several times, the contact angle obtained in this work is still far lower than the reported value in the literature.

Klante [112] measured the contact angle of a water drop on a Teflon surface against nitrogen. The miscibility between Klante's system is negligible and thus, the contact angle changes due to increasing pressure are not appreciable. At 295 K in the range of 20 MPa the contact angle increases just around 15° .

The contact angle of water on a glass surface at 313 K and up to 27 MPa lies between 31° and 78° . As mentioned before, the contact angle increases with increasing pressure only if carbon dioxide is still gaseous. In supercritical carbon dioxide the contact angle remains nearly constant. Except at ambient pressure, the contact angle reported in [194] by Wesch is always

3.4 Static Wetting Angles

lower than the measured one. The reason might lie in the different composition of the glass material employed in the experiment.

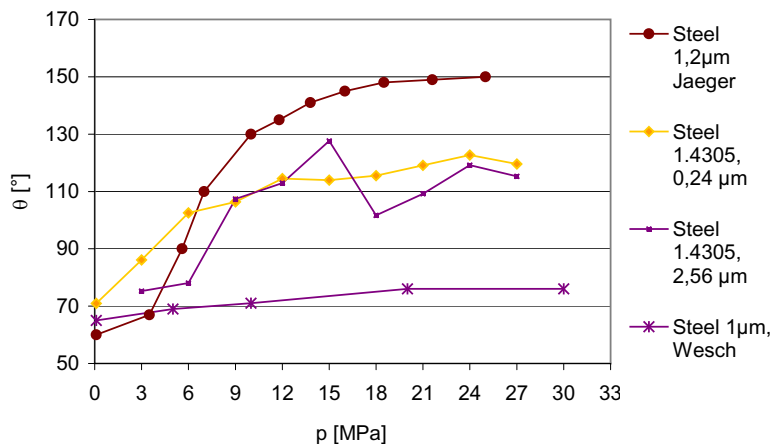


Figure 3-14: Contact angle of sessile water drop on steel surfaces against carbon dioxide at 313 K.

The contact angles of sessile water drops on steel surfaces are shown in Fig. 3-14. Two different kinds of steel roughness are investigated here, the smooth one has a roughness of R_a equals $0.24 \mu\text{m}$ and the rough steel $R_a = 2.56 \mu\text{m}$. The contact angle shown in Fig. 3-14 is measured at 313 K and up to 27 MPa. Steel can only be moderately wetted by a water drop under pressurized carbon dioxide. The contact angle on both steel surfaces ranges between 71° and 128° , the wetting angle increases generally with increasing pressure.

In [19] Bikerman talked about the rugosity effect on the contact angles. According to him, every groove, valley or scratch on a solid surface acts as a capillary tube in which the liquid rises in case of good wetting or descends if this angle is greater than 90° . Hence, a rough surface usually is better wetted than a smooth surface by a well-wetting liquid, while a poorly wetting liquid should spread on a smooth surface better than on a rough one.

In this work however, the influence of the surface roughness on the wetting characteristics can clearly be seen only when gaseous carbon dioxide is employed. At pressures below 9 MPa, the wetting angle of water drops on the smooth surface is larger than that on the rough surface. Wesch [194] also observed the same phenomenon and explained that at lower pressures where carbon dioxide is still gaseous, water molecules can fill the micro pores on the steel surface better than carbon dioxide molecules. As a result, the contact angle on a rough surface is smaller than on a smooth surface. However, once carbon dioxide turns supercritical, the roughness effect on the wetting behaviour cannot obviously be seen. The contact angles do not differ appreciably.

Only little contact angle data under high pressure conditions can be found in the literature and this aggravates the comparison of the obtained data here. Jaeger [92] and Wesch [194] reported their measurement results on the wetting characteristics of water on steel surfaces under elevated pressure of carbon dioxide. However, Jaeger employed the tilting plate method and Wesch, although he used the sessile drop method, did not specify which kind of steel he used. Obviously, the contact angle measured by Wesch is far lower than other values (see Fig. 3-14) and therefore, most possibly the steel he used has totally different wetting characteristics.

From the three investigated solid materials, glass can best be wetted by sessile water drops, followed by steel, both the smooth and the rough one. Teflon can be least wetted. This wetting behaviour under high pressure conditions is in accordance with other reports for wetting at atmospheric condition.

So far the wetting behaviour of liquids on solid surfaces has been reported and the influence of several factors such as the pressure and the surface roughness have been discussed. However, the real reason for the wetting behaviour of a system has not yet been explained because this cannot be understood solely by observing the change of the contact angle. The change of the contact angle itself is just the reaction to maintain the force balance. The root of the wetting behaviour itself can only be found and understood by observing the change of the three interfacial tension vectors σ_{sv} , σ_{lv} , and σ_{sl} which determine the inclination of the vector σ_{lv} and thus, the contact angle θ . This is the main objective of the next chapter.

In calculating the magnitude of the interfacial tension vectors σ_{sv} and σ_{sl} according to the Young equation, only the static contact angles are taken into account. During the measurement of the dynamic contact angle, liquid is added continuously into the drop until the maximum contact angle is found. The force exerted into the drop by pumping during the measurement is not considered in the Young equation. Therefore only the static contact angle is used in the calculation of the interfacial tension vectors σ_{sv} and σ_{sl} in the next chapter.

3.5 Dynamic Wetting Angles

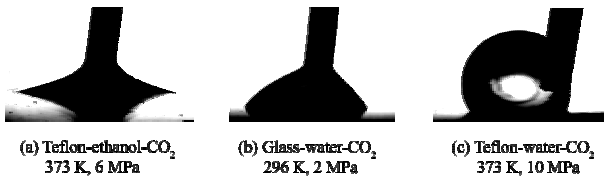


Figure 3-15: Dynamic wetting angles of water and ethanol on glass and Teflon surfaces.

The dynamic wetting angles of a sessile drop of water and ethanol are measured on glass and Teflon surfaces at temperatures up to 373 K and pressures up to 10 MPa. The drop figures can be seen in 3-15 and the measurement results in Fig. 3-17.

3.5 Dynamic Wetting Angles

As explained previously, the dynamic wetting is measured while additional liquid is added into the drop and the maximum angle is defined as the dynamic contact angle. The tip of the capillary remains during the measurement in the drop (see Fig. 3-15). This kind of measurement has some weaknesses such as poor reproducibility and drop shape distortion by the capillary. The first, commonly known weakness is caused by the difficulty in reproducing the exact conditions under which the measurement is performed, for instance the rate at which liquid is added into the drop. A pump with a defined flow rate can be used to assure the constancy of the liquid flow rate. However, this pump has to be a micro pump due to the small volume of the drop. A normal hand pump is far from ensuring a constant liquid flow rate. According to the experience gained in this work, the variability of the measured dynamic contact angles is quite large. At one operating condition, the maximum difference between the measured values is around 20° . An attempt to minimize this variability is to repeat the experiments several times in order to obtain a more representative average value at the end.

When the drop is sufficiently small, whereas the capillary-drop phase interfacial tension σ_{sl} is small and the capillary-continuous phase interfacial tension σ_{sv} is large, it is possible that the shape of the drop phase is distorted and the whole liquid is pulled vertically towards the capillary (see Fig. 3-16). There is an extra, vertical force component around the capillary which contributes to and strengthens the sinus-component of the liquid-fluid interfacial component σ_{lv} at the three-phase contact point between the drop, the fluid phase and the horizontal surface. In such cases, no drop shape in the conventional sense can be recognized. The drop phase is a triangular shape (seen two-dimensionally) or funnel-like body (observed three-dimensionally). This can be seen clearly in Fig. 3-15 when the dynamic contact angle of ethanol on a Teflon surface is measured.

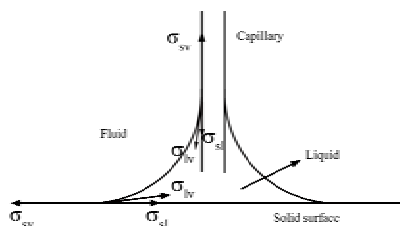


Figure 3-16: Force balance in dynamic wetting.

The dynamic contact angle of water and ethanol sessile drops on Teflon and glass surfaces can be seen in Fig. 3-17. The dynamic contact angle of the sessile water drop is measured at 313 K whereas for ethanol drop at 353 K (complete data of the measured dynamic angles at other operating conditions is listed in Appendix, Chapter 11).

For comparison purposes, the static contact angles of the liquid drops under the same operating conditions are given in the same diagram. A quick visual judgement permits a simple but

elementary conclusion that the dynamic contact angle is always greater than the static one. This meets the expectation very well that when the drop is still pressed and enlarged, it has to result in a larger contact angle than when the drop is in equilibrium. The maximal difference between both contact angles shown in Fig. 3-17 is as large as 25°.

The dynamic contact angle of a water drop on a Teflon surface at 313 K, up to 10 MPa ranges between 90° and 150°, on glass between 73° and 95°. Thus, as expected, glass can be far better wetted than Teflon, both under atmospheric conditions and under the influence of supercritical carbon dioxide. As can be clearly seen, the wetting behaviour of water on Teflon and glass surfaces becomes worse as the pressure increases. Contrary to this, the dynamic contact angle of ethanol on Teflon becomes less with increasing pressure. Ethanol wets Teflon at 353 K and atmospheric pressure with a dynamic contact angle of 32°. But at 10 MPa ethanol spreads already on a Teflon surface and thereby forms a contact angle of 0°. The ethanol drop also spreads spontaneously on glass surfaces at any conditions.

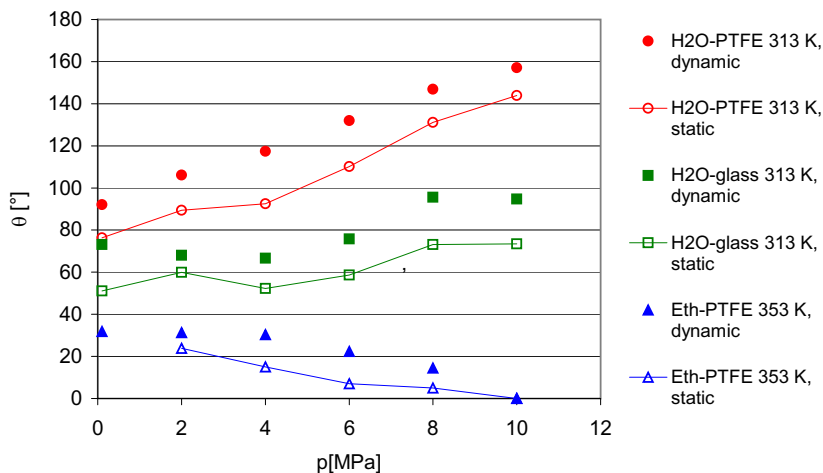


Figure 3-17: Dynamic and static contact angle of sessile-water and -ethanol drops on Teflon and glass surfaces.

4 On the Solid-Vapour Interfacial Tension

Only the wearer knows where the shoe pinches.

Two main properties of fluids, the interfacial tension σ_{lv} and the wettability θ , have been discussed theoretically and the results of the measurements of corresponding experiments are reported in Chapter 2 and 3 respectively. In the Young equation (Eq. 3-1), both of them are correlated in one single equation. Unfortunately, in that equation, only two of the four variables (the liquid-vapour σ_{lv} , the solid-vapour σ_{sv} , the solid-liquid interfacial tension σ_{sl} and the contact angle θ) are experimentally accessible. The first- and last-mentioned properties can be measured directly as can be seen in Chapter 2 and 3.

Some scientists provided another correlation which allows the solving of the Young equation and giving access to the solid-vapour interfacial tension σ_{sv} which enables the characterization of solid materials (or far better, the characterization of a solid material under the influence of a particular fluid or vapour). Some names to be mentioned in this field are Good and Girifalco, Fowkes, Zisman, Owens and Wendt, and finally Rabel. Zisman is one of the pioneer scientist who tried to gain a better understanding and correlation of both the liquid-vapour interfacial tension and the contact angle. A few years later, Good and Girifalco, followed by Fowkes, independently developed theories regarding the wettability of a system containing three phases, a fluid, a liquid and a solid material. And in this way, they began another era in surface chemistry by their attempt at estimating theoretically as well as empirically the magnitude of the solid-vapour interfacial tension σ_{sv} .

In this work, emphasis will only be given to the theory of Good and Girifalco since this belongs to the initial theory which later becomes the most widespread and, theoretically seen, seems to be the best-founded one. Since the beginning, the surface study was in the hands of surface chemists, thus, it is unavoidable that in some concepts, the interfacial tensions are handled and referred to as energy.

Although the theory developed by Good and Girifalco was designed for ambient conditions and not for high pressure conditions where appreciable miscibility between the phases has to be considered, an attempt is made—with some adjustments—to employ and verify the applicability of this theory under extreme pressure conditions and in the presence of carbon dioxide. The solid-vapour interfacial tension of Teflon, glass and steel surrounded by carbon dioxide at temperatures up to 373 K and pressures up to 27 MPa is estimated by means of the pairwise interaction parameter Φ_{sl} , the liquid-vapour interfacial tension and the contact angle. The estimated solid-vapour interfacial tension is, in turn, validated by using the calculated quantity to predict the contact angle of a liquid on that particular surface surrounded by carbon dioxide. The theoretically calculated value is compared with the experimental measured contact angle to allow a conclusion on the applicability of the estimated values of Φ_{sl} and σ_{sv} . The calculated values of Φ_{sl} and σ_{sv} at 313 K are reported in Chapter 4.2, the values at other temperatures

including the magnitude of the solid-liquid interfacial tension σ_{sl} are given in Chapter 11. At the end of this chapter, a brief overview of other theories in this field is given.

4.1 Theoretical Background according to Good and Girifalco

The main objective in all of the theories studying the surface and its wettability is to find another correlation which enables the solving of the Young equation. The same applies to the theory of Good and Girifalco which has its root in the free energy of adhesion and cohesion (Chapter 4.1.1). Here, the existence of a pairwise molecular interaction parameter Φ_{sl} is postulated. The magnitude of the free energy of adhesion and cohesion is estimated by means of the quasi continuum model, with help of the Lennard Jones potential in Chapter 4.1.2. The kinds and magnitude of the long range molecular interactions are explained in Chapter 4.1.3. Finally the pairwise molecular interaction parameter Φ_{sl} is formulated in terms of the energy ratio or attraction constant ratio A according to the Lennard Jones potential, as found in Chapter 4.1.2. The finding of an equation considering all of the molecular interactions between the phases in one single parameter Φ_{sl} permits a direct estimation of the solid-vapour interfacial tension σ_{sv} and thus, the solving of the Young equation.

4.1.1 Free Energy of Adhesion and Cohesion

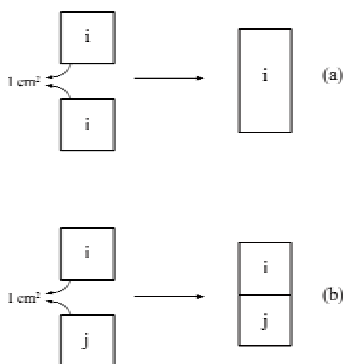


Figure 4-1: The process of forming a cohesive (a) and an adhesive (b) joint [73].

Following the suggestion of Harkins [80], the work required to bring two unlike bodies i and j with unit cross-sectional area reversibly together to form a continuous body is (see Fig. 4-1, b)

$$W_{ij}^{ad} = \sigma_i + \sigma_j - \sigma_{ij} \quad (4-1)$$

the work of adhesion. The free energy change per unit area, also known as the free energy of adhesion is the negative of the work of adhesion

$$-\Delta F_{ij}^{ad} = W_{ij}^{ad} = \sigma_i + \sigma_j - \sigma_{ij}. \quad (4-2)$$

By analogy to the work of adhesion, the work of cohesion for a body *i* (see Fig. 4-1, a)

$$W_i^{coh} = 2\sigma_i \quad (4-3)$$

and the free energy of cohesion can be written as

$$-\Delta F_i^{coh} = W_i^{coh} = 2\sigma_i. \quad (4-4)$$

It is assumed that the initial surfaces are destroyed in the cohesion process so that after joining the two bodies, no surface exists between them (Eq. 4-3 and 4-4). The symbol σ given in Eq. 4-1 to Eq. 4-4 denotes the pure interfacial tension of each phase against vacuum. In Eq. 4-2 and Eq. 4-4 the free energy of adhesion and cohesion are written in terms of the Helmholtz free energy *F* instead of the Gibbs free energy *G*. With respect to the surfaces, a distinction between both the Helmholtz *F* and the Gibbs free energy *G* is not necessary. In all rigorous derivations of the Gibbs adsorption equation [1,69], the volume of the reference system is, by definition, set equal to the sum of the volumes of the two phases in the real system and hence, the surface excess volume is equal to zero and both free energies are equal.

By analogy to the Berthelot geometric mean hypothesis [18], the van der Waals attractive constant between two unlike molecules 1 and 2 is

$$a_{12} = \sqrt{a_{11}a_{22}}. \quad (4-5)$$

In the Berthelot geometric mean hypothesis (Eq. 4-5), the character “*a*” denotes the van der Waals attractive constants between like (11 and 22) or unlike (12) molecules.

A proposal is made that the free energy of adhesion between two phases can be given by the geometric mean of the free energies of cohesion of each of the separate phases

$$|\Delta F_{ij}^{ad}| = \left(\Delta F_i^{coh} \Delta F_j^{coh} \right)^{\frac{1}{2}}. \quad (4-6)$$

Upon employing Eq. 4-2, 4-4 and 4-6 the following correlation can be written

$$\sigma_{ij} = \sigma_i + \sigma_j - 2\sqrt{\sigma_i\sigma_j}. \quad (4-7)$$

Equation 4-7 is found to be a good approximation for the fluorocarbon-hydrocarbon systems, but it does not have a general validity for many water-organic liquid systems [73,74].

The next improvement is to arrange Eq. 4-6 as quotient and call the result an empirical property of the interface

$$\Phi_{ij} \equiv \frac{-\Delta F_{ij}^{ad}}{\sqrt{\Delta F_i^{coh} \Delta F_j^{coh}}}. \quad (4-8)$$

Equations 4-7 and 4-8 are thermodynamic relationships having no greater physical content than the content of the definitions of free energy of adhesion and cohesion. The physical content is given later by the predictive evaluation of Φ as is explained further in 4.1.3.

The expression in Eq. 4-8 can also be written in terms of the total energy

4.1 Theoretical Background according to Good and Girifalco

$$\Phi_{ij} \equiv \frac{-\Delta U_{ij}^{ad}}{\sqrt{\Delta U_i^{coh} \Delta U_j^{coh}}}. \quad (4-9)$$

Considering that the ratio of the free energy of adhesion and cohesion is not necessarily equal to one (4-6), Eq. 4-7 turns to

$$\sigma_{ij} = \sigma_i + \sigma_j - 2\Phi_{ij}\sqrt{\sigma_i\sigma_j} \quad (4-10)$$

where Eq. 4-7 stands for particular cases with Φ_{sl} is equal to unity. For a three-phase system including a liquid l, a fluid v and a solid material s, Eq. 4-10 can be rewritten

$$\sigma_{sl} = \sigma_{sv} + \sigma_{lv} - 2\Phi_{sl}\sqrt{\sigma_{sv}\sigma_{lv}} \quad (4-11)$$

and together with the Young equation (3-1), the interfacial tension σ_{sl} can be eliminated and the interfacial tension σ_{sv} can be estimated

$$\sigma_{sv} = \sigma_{lv} \frac{(1 + \cos\theta)^2}{4\Phi_{sl}^2} \quad (4-12)$$

as long as the liquid-vapour interfacial tension σ_{lv} , the contact angle θ and the parameter Φ_{sl} are known. The first two properties are experimentally accessible, the last quantity Φ_{sl} is still unknown.

4.1.2 Quasi-continuum Model

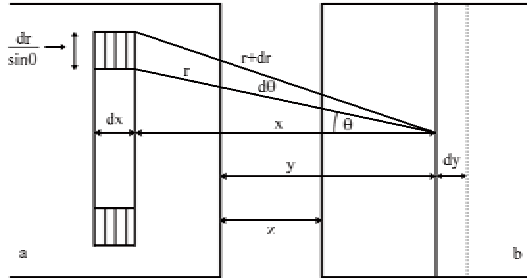


Figure 4-2: Interaction between two semi-infinite bodies, separated by distance z [73].

The quasi-continuum model describes the interaction between two semi-infinite bodies, e.g. two halves of a homogenous phase or two unlike materials, phase a and b as illustrated in Fig. 4-2 where the phases are considered to consist of symmetrical particles which are point-centers of force. The force of interaction F between two particles, one in the phase a and the other in the phase b, is given by the Lennard-Jones potential

$$U(r) = \frac{-A_{ab}}{r^6} + \frac{C_{ab}}{r^m}. \quad (4-13)$$

(Unfortunately F is required to denote both, force and free energy).

The Lennard-Jones potential is a simple mathematical model which represents the fact that neutral atoms or molecules are subject to two distinct forces within the limit of large distance (attractive force at long ranges) and short distance (a repulsive force at short ranges). In Eq. 4-13, the attractive constant is denoted by A whereas the repulsive constant is denoted by C with r as the intermolecular distance.

The force of interaction between two particles is

$$F(r) = \frac{\partial U(r)}{\partial r} = 6 \frac{A_{ab}}{r^7} - m \frac{C_{ab}}{r^{m+1}}. \quad (4-14)$$

This force can be summed over all the molecules in each body, the total force of interaction between the two phases separated by the distance z is hence

$$F(z) = 2\pi \int_z^\infty n_a n_b \int_y^\infty x dx \int_x^\infty n_b \frac{\partial U(r)}{\partial r} dr \quad (4-15)$$

with n_a and n_b as the density in phase a and b in molecules per unit volume.

The free energy of adhesion ΔF_{ab}^{ad} is the negative of the free energy required to transport the two phases from the equilibrium intermolecular distance r_0 to infinity without altering the structure or composition of both phases

$$-\Delta F_{ab}^{ad}(r_{0ab}) = 2\pi \int_{r_{0ab}}^\infty dz \int_z^\infty n_a n_b \int_y^\infty x dx \int_x^\infty n_b \frac{\partial U(r)}{\partial r} dr. \quad (4-16)$$

In analogy to the free energy of adhesion in Eq. 4-16, the free energy of cohesion can be written

$$-\Delta F_a^{coh}(r_{0a}) = 2\pi \int_{r_{0a}}^\infty dz \int_z^\infty n_a n_b \int_y^\infty x dx \int_x^\infty n_a \frac{\partial U(r)}{\partial r} dr. \quad (4-17)$$

Upon employing the Lennard-Jones potential in Eq. 4-13 and assuming the constancy of n_a and n_b and that the interface is sharp, Eq. 4-17 can be calculated

$$-\Delta F_{ab}^{ad} = 2\pi n_a n_b \left(\frac{-A_{ab}}{24z^2} - \frac{C_{ab}}{(-m+2)(-m+3)(-m+4)z^{-m+4}} \right). \quad (4-18)$$

When the separation between the two phases is the equilibrium intermolecular distance r_{0ab} , the total force between the two phases is equal to zero

$$F(z = r_{0ab}) = 0 \quad (4-19)$$

and hence, the repulsive constant C_{ab} can be written in terms of A_{ab}

$$C_{ab} = \frac{(m-2)(m-3)}{12r_{0ab}^{(m-6)}} A_{ab}. \quad (4-20)$$

Putting the expression for C_{ab} in Eq. 4-20 into Eq. 4-18, the free energy of adhesion becomes

$$-\Delta F_{ab}^{ad} = \frac{\pi n_a n_b A_{ab}}{6r_{0ab}^2} \left(\frac{-1}{2} + \frac{1}{(m-4)} \right) \quad (4-21)$$

and analogous to this, the free energy of cohesion for phase a

$$-\Delta F_a^{coh} = \frac{\pi n_a^2 A_a}{6r_{0a}^2} \left(\frac{-1}{2} + \frac{1}{(m-4)} \right) \quad (4-22)$$

and for phase b

$$-\Delta F_b^{coh} = \frac{\pi n_b^2 A_b}{6r_{0b}^2} \left(\frac{-1}{2} + \frac{1}{(m-4)} \right) \quad (4-23)$$

The parameter Φ_{sl} according to Eq. 4-8 by means of Eq. 4-21, 4-22, 4-23

$$\Phi_{ab} = \frac{A_{ab}}{\sqrt{A_a A_b}} \frac{r_{0a} r_{0b}}{r_{0ab}^2} = \Phi_A \Phi_r \quad (4-24)$$

The value of r_{0ab} can be set equal to the arithmetic mean of r_{0a} and r_{0b}

$$\Phi_r = \frac{r_{0a} r_{0b}}{\left(\frac{r_{0a} + r_{0b}}{2} \right)^2} \quad (4-25)$$

The parameter Φ_r which is made up by the square of the ratio of a geometric mean to an arithmetic mean differs seriously from unity only when the radii are drastically different from each other and hence, it is often acceptable to set Φ_r equal to unity.

The other component of Φ_{ab} , Φ_A can be evaluated from the parameters that determine the intermolecular interactions such as is done in the following section.

4.1.3 Intermolecular Potential Functions

In order to determine the parameter Φ_A , the intermolecular forces between molecules or atoms have to be evaluated. The fundamental long range physical forces controlling the non-chemical interactions among atoms and molecules are of two kinds, the coulombic or the electrostatic interactions and those lumped together under the general term of van der Waals forces. The coulombic interactions are by far the strongest of the physical interactions. However, they are not the most widely encountered type of interaction since they are present only in systems containing charged species.

The universal interaction type which can be encountered between every molecule or pair of atoms without the requirements of any particular properties is the van der Waals force. The name refers to the Dutch physicist and chemist Johannes Diderik van der Waals who first documented these types of forces. This type of interaction includes three separate types of atomic or molecular interactions, each of which has its own characteristics, its own theoretical basis and its own limitations. They are the Keesom interaction of permanent dipoles, Debye induced dipolar interaction and finally, the London dispersion interaction. The first two forces are reasonably easy to understand because they are based on relatively straightforward electrostatic principles similar to those used for the much stronger coulombic interactions. The last one is sometimes less clear because it is quantum mechanical in origin, and quantum

mechanics, even in its simplest form, seems to affect adversely the sanity of many who touch thereon.

In the following, the present ideas involved in the three interactions are discussed as simply as possible while still conveying the essence of the subject. The intention is to provide an understanding of the basis of the interactions leaving the fine points and complications to more advanced texts on the subject.

The discussion will be closed by – treating the intermolecular potentials as being additive – linking all of the interaction kinds and using the attraction constants required to go back to the formulation of the parameter Φ_{ab} in Eq. 4-24 explained in 4.1.2.

Permanent Dipole Interaction

If two polar molecules with dipole moments μ_a and μ_b approach in a vacuum there will develop a dipole-dipole interaction between the ends of the dipoles analogous to the interaction between the ends of two magnets. This kind of interaction is known as the interaction due to the orientation and thus, the magnitude of the interaction changes all the time depending on the relative orientation of the two molecules. The angle-averaged values of the interaction potential will never be equal to zero because there will always exist a Boltzmann weighting factor that gives priority to some angles or orientations more than to others. That is, those orientations which produce lower energy during the interaction will be favored over those with more energy. In 1921, Willem Hendrik Keesom [102,103], averaging over all positions, found as a result the magnitude of the total energy by orientation effect between two unlike molecules

$$U_{\mu,ab} = -\frac{2}{3} \frac{\mu_a^2 \mu_b^2}{kTr^6} \quad (4-26)$$

and between like molecules

$$U_{\mu,a} = -\frac{2}{3} \frac{\mu_a^4}{kTr^6} \quad (4-27)$$

with μ as the dipole moment, k the Boltzmann constant ($1.3806505 \cdot 10^{-23}$ Joule/Kelvin or $8.617343 \cdot 10^{-5}$ electron-volt/Kelvin), T the temperature and r the intermolecular center-to-center distance.

However, the initial Keesom expression in Eq. 4-26 and 4-27 is too large. Israelachvili [90] modified the Keesom expression as follows

$$U_{\mu,ab} = -\frac{1}{3} \frac{\mu_a^2 \mu_b^2}{kTr^6} \quad (4-28)$$

and between like molecules

$$U_{\mu,a} = -\frac{1}{3} \frac{\mu_a^4}{kTr^6} \quad (4-29)$$

(compare the initial formulation of Φ_{st} by Good et al. in [74,78] with the later improvement in [75,77]).

Dipole-induced Dipole Interaction

Debye and Falckenhagen [41,42,53] remarked that the dipoles interaction cannot be the only one that exists because this interaction is inversely proportional to the temperature and thus, should actually vanish with increasing temperature. But experience shows that the empirical van der Waals corrections do not vanish equally rapidly with high temperatures and Debye therefore concluded that there has to be, in addition, an interaction independent of temperature.

Debye suggested an interaction between a polar molecule and a nonpolar one where the force field inducing the dipole on the nonpolar molecules arises from the permanent polar molecule. Here, the interaction depends on the existence of one single polar molecule. The Debye induction effect on the total energy between unlike molecules takes the form

$$U_{ind,ab} = -\frac{\alpha_a \mu_b^2 + \alpha_b \mu_a^2}{r^6} \quad (4-30)$$

and between like molecules

$$U_{ind,a} = -\frac{2\alpha_a \mu_a^2}{r^6} \quad (4-31)$$

with α as the polarizability.

Later, van der Avoird and Hofelich [189] gave the terms in Eq. 4-30 and 4-31 a quantum mechanical treatment and found that the correct expression is smaller than the value given above. For two molecules of equal polarity and polarizability, the correction factor is 0.5. Although the correction factor depends on the relative magnitudes of the polarizability α and the dipole moment μ , the above-mentioned correction factor is taken as sufficiently accurate and thus

$$U_{ind,ab} = -\frac{0,5(\alpha_a \mu_b^2 + \alpha_b \mu_a^2)}{r^6} \quad (4-32)$$

and

$$U_{ind,a} = -\frac{\alpha_a \mu_a^2}{r^6}. \quad (4-33)$$

London Dispersion Interaction

The third interaction type, the London dispersion force—although it does not always make the largest contribution to the total van der Waals interaction—is often the most important one due to its universal nature, as contrasted to the dipolar and induced-dipolar forces which depend on the exact chemical natures of the species involved, and may or may not be significant in a particular given case. The London dispersion force is named after the German-American physicist Fritz London who published his work on this topic in 1937 [128].

The London dispersion interaction is a long range one, may be attractive or repulsive and is basically quantum mechanical in its nature because it involves interactions between rapidly fluctuating dipoles resulting from the movement of the electron cloud. This electron cloud is not always symmetrical with respect to the nucleus. The asymmetric charge distribution produces

an instantaneous dipole in the molecule. These very quickly varying dipoles, represented by the zero-point motion of a molecule, produce an electric field and act upon the polarizability of the other molecule and produce there induced dipoles, which are in interaction with the instantaneous dipoles producing them. The total energy coming from this kind of the interaction depends on the polarizability α , the frequency ν and the intermolecular center-to-center distance r and thus, between unlike molecules

$$U_{disp,ab} = -\frac{3\alpha_a\alpha_b}{4r^6} h \left(\frac{\nu_{0a}\nu_{0b}}{\nu_{0a} + \nu_{0b}} \right) \quad (4-34)$$

and between like molecules

$$U_{disp,a} = -\frac{3\alpha_a^2}{4r^6} h\nu_{0a} \quad (4-35)$$

with h as the Planck constant ($6.62 \cdot 10^{-34}$ Js). The multiplication of the characteristic frequency ν by the Planck constant h is, in all of the cases, nearly equal to the ionization energy I [128,151] and thus, between unlike molecules

$$U_{disp,ab} = -\frac{3\alpha_a\alpha_b}{4r^6} \left(\frac{I_a I_b}{I_a + I_b} \right) \quad (4-36)$$

and between like molecules

$$U_{disp,a} = -\frac{3\alpha_a^2}{4r^6} I_a \quad (4-37)$$

Quasi-Continuum Theory with Components of Energy of Interaction

Combining the dipolar, the dipole-induced dipole and the London interaction, the total energy of unlike molecules is given by

$$U_{ab} = U_{\mu,ab} + U_{ind,ab} + U_{disp,ab} \quad (4-38)$$

and between like molecules

$$U_a = U_{\mu,a} + U_{ind,a} + U_{disp,a} \quad (4-39)$$

The parameter Φ_{sl} can be formulated by means of Eq. 4-38 and 4-39 according to Eq. 4-9 or in terms of the attraction constants A

$$A_{ab} = A_{\mu,ab} + A_{ind,ab} + A_{disp,ab} \quad (4-40)$$

and

$$A_a = A_{\mu,a} + A_{ind,a} + A_{disp,a} \quad (4-41)$$

The attraction constant A of each kind of the molecular interaction is listed in Table 4-1 for both the interaction between like and unlike molecules.

4.1 Theoretical Background according to Good and Girifalco

Table 4-1: Attraction constant A derived from the permanent dipole, the dipole-induced dipole and the London interaction between unlike ab and like molecules a.

	ab	a
Dipole	$A_{\mu,ab} = -\frac{1}{3} \frac{\mu_a^2 \mu_b^2}{kT}$	$A_{\mu,a} = -\frac{1}{3} \frac{\mu_a^4}{kT}$
Dipole-induced dipole	$A_{ind,ab} = -0,5 \left(\alpha_a \mu_b^2 + \alpha_b \mu_a^2 \right)$	$A_{ind,a} = -\alpha_a \mu_a^2$
London dispersion	$A_{disp,ab} = -\frac{3}{4} \alpha_a \alpha_b \frac{2I_a I_b}{I_a + I_b}$	$A_{disp,a} = -\frac{3}{4} \alpha_a^2 I_a$

Upon employing Eq. 4-21, 4-22 and 4-23 for each type of interactions, the dipolar interaction (Eq. 4-28 and 4-29), the induced dipolar interaction (Eq. 4-32 and 4-33) and the London interaction (Eq. 4-36 and 4-37) according to Eq. 4-8 or Eq. 4-24, the molecular interaction parameter Φ is

$$\Phi_{ab} = \frac{\frac{3}{4} \alpha_a \alpha_b \frac{2I_a I_b}{I_a + I_b} + \frac{1}{2} \left(\alpha_a \mu_b^2 + \alpha_b \mu_a^2 \right) + \frac{1}{3} \frac{\mu_a^2 \mu_b^2}{kT}}{\left[\left(\frac{3}{4} \alpha_a^2 I_a + \alpha_a \mu_a^2 + \frac{1}{3} \frac{\mu_a^4}{kT} \right) \left(\frac{3}{4} \alpha_b^2 I_b + \alpha_b \mu_b^2 + \frac{1}{3} \frac{\mu_b^4}{kT} \right) \right]^{\frac{1}{2}}}. \quad (4-42)$$

Later on, in 1970 [74], the expression of the parameter Φ was improved and instead of the Lennard-Jones, the Kihara potential [109,110] was employed. Hereby, the molecules are treated as shells rather than point centers and instead of using the equilibrium intermolecular center-to-center distance r_0 , the equilibrium intermolecular distance between the shells ρ_0 is employed. The quotient of both is between 0.6 and 0.75

$$\frac{\rho_0}{r_0} = B \approx 0,6..0,75. \quad (4-43)$$

Additionally, Pitzer and Donath [156] showed that the ionization energy I should be replaced by a somewhat larger number. Thus, following the suggestion of Sinanoglu [174], the ionization energy is multiplied by δ with δ lies between 1 and 2

$$\Phi_{ab} = \frac{\frac{3}{4} \alpha_a \alpha_b \frac{2I_a \delta_a I_b \delta_b}{I_a \delta_a + I_b \delta_b} + \frac{1}{2} \left(\alpha_a \mu_b^2 + \alpha_b \mu_a^2 \right) B + \frac{1}{3} \frac{\mu_a^2 \mu_b^2}{kT} B^2}{\left[\left(\frac{3}{4} \alpha_a^2 I_a \delta_a + \alpha_a \mu_a^2 B + \frac{1}{3} \frac{\mu_a^4}{kT} B^2 \right) \left(\frac{3}{4} \alpha_b^2 I_b \delta_b + \alpha_b \mu_b^2 B + \frac{1}{3} \frac{\mu_b^4}{kT} B^2 \right) \right]^{\frac{1}{2}}}. \quad (4-44)$$

The correction factors or the adjustable parameters B and δ 's in Eq. 4-44 are not independent of each other. Two sets of the adjustable parameters are given in [74]. However, they are specific

for the systems water vs. organic liquids of various degrees of polarity. Since the systems investigated can be quite wide-ranging and these adjustable parameters can also well be seen as correction factor, the correction as suggested and included in Eq. 4-44 is neglected and instead of this equation, the former one (Eq. 4-42) is employed in the following calculations.

4.2 Solid-Vapour Interfacial Tension of Teflon, Glass and Steel Against Carbon Dioxide

4.2.1 First Attempt

In order to estimate the magnitude of the solid-vapour interfacial tension σ_{sv} of various solid surfaces (i.e. Teflon, glass and steel against carbon dioxide) the molecular interaction parameter Φ_{sl} has to be determined first. In the following, the molecular material properties of the employed fluids, (i.e. water, ethanol and carbon dioxide) and that of the investigated solid materials (i.e. Teflon, glass and steel) are given. These data are used to calculate the molecular interaction parameter Φ_{sl} . Knowing the value Φ_{sl} for each system (i.e. solid material-water-carbon dioxide and solid material-ethanol-carbon dioxide) the solid-vapour interfacial tension σ_{sv} of a solid material against carbon dioxide can be calculated. Two values σ_{sv} for each material or each system are obtained. They can be compared with each other. The absolute condition as a measure for the validity of these values is that both have to be close to each other. In turn, the calculated interfacial tensions σ_{sv} of the solid materials taken from the system solid material- ethanol-carbon dioxide, are put into the following equation

$$\cos \theta = 2\Phi_{sl} \sqrt{\frac{\sigma_{sv}}{\sigma_{lv}}} - 1 \quad (4-45)$$

and applied to the system of water with solid material and carbon dioxide. The index l in Eq. 4-45 denotes the liquid phase, in this case water. The aim is to predict the contact angle of a sessile water drop on the solid surface in the presence of carbon dioxide theoretically.

Later on, the theoretical estimated value of sessile water drop contact angle is compared with the measured angle in order to allow a conclusion about the ability of the theory to calculate the interfacial tension σ_{sv} . This is the sufficient condition which is necessary in order to provide a solid-vapour interfacial tension which can be employed in estimating the wettability of a system.

4.2 Solid-Vapour Interfacial Tension of Teflon, Glass and Steel Against Carbon Dioxide

Molecular Properties of the Employed Materials

The molecular properties of the studied fluids such as the dipole moment μ , the ionization energy I and the polarizability of a molecule α is given below in Table 4-2.

Table 4-2: Molecular properties of the fluids investigated.

	μ [D]	μ [1e-30*Cm]	I [eV]	I [1e-18*J]	α [1e-24*cm ³]	α [1e-40*Cm ² /V]
H ₂ O	1.8546	6.1863	12.6206	2.0193	1.45	1.6133
Ethanol	1.72	5.7373	10.43	1.6688	5.41	6.0194
CO ₂	0	0	13.773	2.2037	2.911	3.2389

The units conversions are as follows:

$$1 \text{ D} = 3.33564 \cdot 10^{-30} \text{ C} \cdot \text{m}$$

$$1 \text{ eV} = 1.6 \cdot 10^{-19} \text{ C} \cdot \text{V} \text{ (or } J \text{)}$$

$$1 \text{ cm}^3 = 1.11265 \cdot 10^{-16} \frac{\text{C} \cdot \text{m}^2}{V}$$

The molecular property Y of a phase i which is made up of more than one component, for instance when the miscibility between the coexisting phases is not negligible, can be estimated by taking the molecular property Y of both components 1 and 2 into account [74]

$$Y_i = x_{1,i} Y_1 + x_{2,i} Y_2 \quad (4-46)$$

x is the mole fraction of each component in the phase. This equation is used in estimating the molecular properties μ , I and α so that the solubility of carbon dioxide in water and ethanol can be considered. For this purpose, the solubility of carbon dioxide in water at 313 K is taken from [48]. For other operating conditions, the solubility data is reported in [70,164,169,195,196]. As the solubility of carbon dioxide in ethanol, data reported in [54,96,141,183] at 313 K is used here. For other operating conditions : [29,30,38,84,115,125,203].

As for the molecular properties of the solid materials, it is more complicated because the solid materials are often mixtures of more than two components (glass and steel) or even polymers (Teflon). In Table 4-3 the assumed material or assumed chemical bond which is important in the molecular interaction is listed and the value of each of the molecular properties along with the literature source from which the values are taken, are given.

Table 4-3: Molecular properties assumed for the solid materials. First attempt.

	Teflon		Glass		Steel	
μ [D]	1.2	C-F bond	0.5786	SiO ₂	3.88	CrO
		[78,175]		[36]		[124]
μ [1e-30*Cm]	4		1.93		12.9423	
I [eV]	10.12		11.49	SiO	7.7049	Mean value
		C ₂ F ₄ [124]		[124]		(mol ratio)
I [1e-18*J]	1.6192		1.8384		1.2328	[124]
α [1e-24*cm ³]	3.84		2.8411	Lorentz- Lorentz	8.885	Mean value
		CF ₄ [124]		Relation		(mol ratio)
α [1e-40*Cm ² /V]	4.2726		3.1611	SiO ₂ [77,78]	9.8859	[124]

Following the suggestion made by Good [78], for the computation of the Teflon interaction parameter against liquid Φ_{sl} , the group moment of C-F bond of 1.2 D [175] is employed, whereas for the ionization energy I and the polarizability α , the value of C₂F₄ and CF₄ from [124] are used respectively.

Although glass is made up of a mixture and the mixture of glass material can vary widely, initially SiO₂ is considered as the main component which actively takes part in the intermolecular interaction with the liquid lies on the material. As for the ionization energy, SiO is assumed. The data for the polarizability is not always given in the literature. However, this property can be estimated by means of the Lorentz-Lorentz relation as recommended by Good in [77,78]

$$\alpha = \frac{3V}{4\pi N_A} \left(\frac{n^2 - 1}{n^2 + 2} \right) \quad (4-47)$$

with V as the molar volume, n the refractive index and N_A the Avogadro number 6.02*10²³.

For steel, the dipole moment is taken from CrO. The ionization energy I and the polarizability α are mole fraction-averaged value according to Eq. 4-46. The composition of the steel 1.4305 investigated here is given in 3.2.

Interaction Parameter Φ_{sl}

The interaction parameter Φ_{sl} of six solid material-liquid systems (combination of three solid materials and two different liquids) at 313 K and pressures up to 27 MPa is given in Fig. 4-3. The pressure dependence of this value is due to the degree of solubility of carbon dioxide in the drop phase. The system of a solid material with water has less pressure dependence than a

system of a solid material with ethanol. This is as expected because the solubility of carbon dioxide in ethanol is far higher than that in water. However, the value is nearly constant over the whole pressure range. A larger pressure dependence is seen only in the system of glass with ethanol or steel with ethanol.

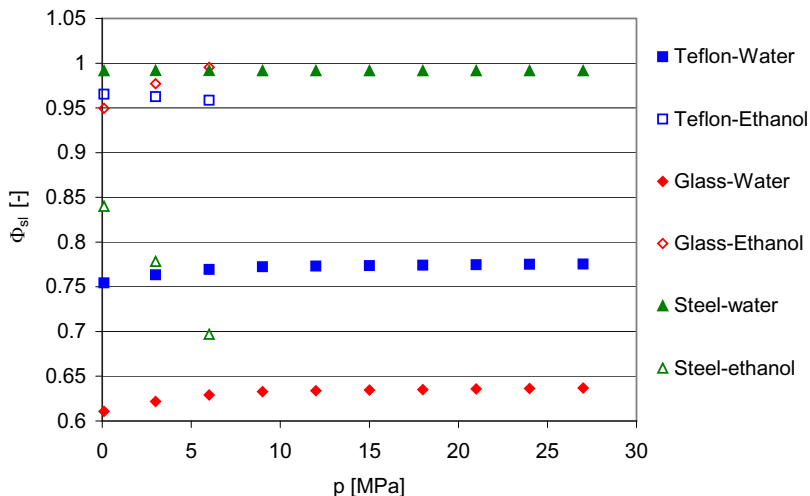


Figure 4-3: The value of the parameter Φ_{sl} at 313 K. The material properties are taken from tables 4-2 and 4-3.

Interfacial Tension σ_{sv}

The molecular interaction parameter Φ_{sl} calculated in Fig. 4-3 is used to calculate the solid-vapour interfacial tension σ_{sv} of Teflon, glass and steel embedded in carbon dioxide, at 313 K according to Eq. 4-12. The contact angle θ and the interfacial tension σ_{lv} are taken from 2.5.1 and 3.4. Some of the interfacial tension value σ_{lv} at higher pressures are taken from [92,194]. The result of the calculation is shown in Fig. 4-4.

The solid-vapour interfacial tension σ_{sv} is a system property which depends only on the nature of the solid material and the vapour or the fluid, in which the solid material is put. Therefore, calculating the value of this quantity twice by using the parameter Φ_{sl} obtained from the system of a solid material with water and the system of a solid material with ethanol provides a good chance to prove the validity of the calculated value σ_{sv} . Independence of the liquid used as the drop phase, the end results of σ_{sv} calculated has to be equal or nearly equal. This is an absolute condition which can be used as a criterion for the judgement whether the calculated value is right or absolutely wrong, since the value σ_{sv} is experimentally not accessible.

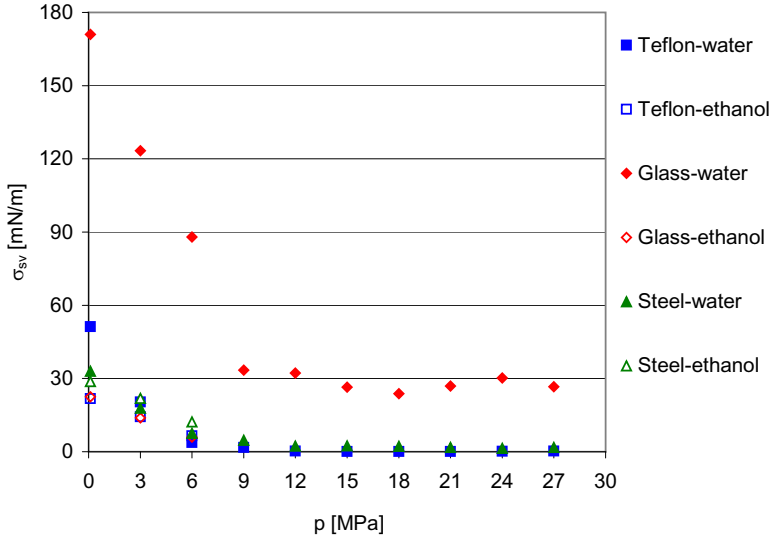


Figure 4-4: Interfacial tension σ_{sv} of Teflon, glass and steel against carbon dioxide at 313 K, calculated by means of the parameter Φ_{sl} as given in Fig. 4-3.

According to Fig. 4-4, the interfacial tension σ_{sv} falls drastically in gaseous carbon dioxide, but at higher pressure, there is no appreciable change in this value. This is as expected due to the effect of the pressure on the parameter Φ_{sl} , the interfacial tension σ_{lv} and the contact angle θ in supercritical carbon dioxide. Neither the interfacial tension σ_{lv} (see Chapter 2.5.1) nor the contact angle θ (see Chapter 3.4) change appreciably in supercritical carbon dioxide and the pressure effect on the parameter Φ_{sl} is also negligible.

The value σ_{sv} of Teflon against carbon dioxide is the same for both systems (Teflon with water and carbon dioxide, and Teflon with ethanol and carbon dioxide) except at 0.1 MPa. At ambient pressure, the solid-vapour interfacial tension σ_{sv} calculated from the system of Teflon with water in carbon dioxide environment is far too high compared with the one obtained from the system of Teflon with ethanol embedded in carbon dioxide. The value from the first system is around 51.5 mN/m whereas from the second system it is about 21.8 mN/m. As can be seen in Table 4-4, the first value is obviously much too high. The second value appears more plausible. This erroneous value can be the result of the deviating contact angle of water on Teflon measured in 3.4 which is far too low compared with other values reported in the literature (a confirmation of this assumption is also given when the calculated and measured contact angles are compared such as given in Fig. 4-5).

4.2 Solid-Vapour Interfacial Tension of Teflon, Glass and Steel Against Carbon Dioxide

Table 4-4: In the literature reported data of the interfacial tension σ_{sv} of Teflon at ambient condition.

Authors	Year	Source	$\sigma_{sv} \left[\frac{mN}{m} \right]$
Good & Girifalco	1960	[72]	28
Zisman	1963	[207]	18
Good	1964	[78]	24
Fowkes	1964	[57]	19.5
Owens & Wendt	1969	[149]	19.1
Rabel	1971	[159]	18.5
Kudra	1995	[117]	22.27
Janczuk	1999	[94]	20.24
Klante	2002	[112]	23.4

A good agreement between the value σ_{sv} obtained from the system of steel with water drop in carbon dioxide and the system of steel with ethanol in carbon dioxide can be observed in Fig. 4-4. Unfortunately, the solid-vapour interfacial tension σ_{sv} of glass against carbon dioxide obtained from water and ethanol systems are not in good agreement. The discrepancy is quite large, as can be seen in Fig. 4-4.

Hereby, using the solid material properties assumed in Table 4-3, by means of the absolute condition mentioned above, i.e. the interfacial tension σ_{sv} should be a system property independent of the liquid used as the drop phase, it can be said that most likely, the solid-vapour interfacial tension σ_{sv} found in Fig. 4-4 for the system of Teflon and carbon dioxide, and the system of steel and carbon dioxide is correct whereas for glass, the solid material properties still have to be reviewed.

Calculated and Experimental Measured Contact Angle θ

Beside the afore-mentioned absolute condition for the validity of the estimated solid-vapour interfacial tension σ_{sv} , another sufficient condition should also be fulfilled. The sufficient condition is related to the applicability of the value σ_{sv} to be employed for the prediction of the wetting behaviour of a particular liquid rests on the given solid surface surrounded by the fluid.

This is performed as follows. The value σ_{sv} obtained from the system of solid material with ethanol drop in carbon dioxide is employed to predict the contact angle of the sessile water drop on the particular solid materials. The interaction parameter of each system is taken from Fig. 4-3. The estimated contact angle on each solid material is compared with the measured values (Chapter 3.4), as shown in Fig. 4-5. If the measured and calculated values are exactly the same, the points should be located exactly on the line $x = y$ (diagonal bold line). The dashed lines show a discrepancy of $\pm 10^\circ$ between the measured and calculated values. This deviation is very reasonable regarding the contact angle hysteresis and the poor reproducibility of the contact

angle in the experiments. However, this kind of comparison can only be performed up to 6 MPa for each system because above this pressure, ethanol and carbon dioxide become one phase.

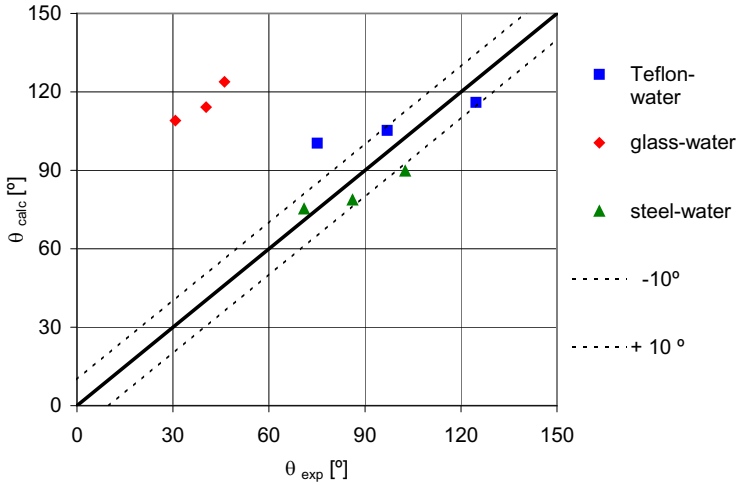


Figure 4-5: Comparison between the calculated and the measured water contact angle on Teflon, glass and steel against carbon dioxide at 313 K using the parameter Φ_d (Fig. 4-3) and the interfacial value σ_{sv} (Fig. 4-4) obtained from the three systems of solid material with ethanol in carbon dioxide.

If the theory applied is formulated accurately enough and the value of the material properties in Table 4-2, especially for the solid materials in Table 4-3, are precisely chosen, then the points should be located close to the bold line. Points falling between the dashed lines show a good agreement between the measured and the calculated values whereas which are far outside the dashed lines show a poor agreement between the experimental and the theoretical values.

As can be seen in Fig. 4-5, all three contact angles of water drop on steel lie in the limit given which means the agreement between the measured and the calculated values is very good. The same can be said for the results of the calculated contact angle values on Teflon. Except at 0.1 MPa (the most-left point), the accuracy of the estimated contact angles is within 10° . The measured contact angle of water on Teflon surrounded by carbon dioxide at 313 K and 0.1 MPa is equal to 75° whereas the calculated value is 101° . As has been explained in Chapter 3.4, the experimental value is quite different from the reported value in the literature. Wesch [194] and Klante [112] measured a sessile water drop angle of around 110° on a Teflon surface at the conditions mentioned above. And this value is obviously much nearer to the calculated value of 101° than to the experimental one. That means, due to an unknown reason and although the measurements were repeated several times, the experimental value is far below the one reported in the literature.

The result on the glass surface is, as expected, far outside the range given.

4.2.2 Subsequent Improvements

The molecular properties used to characterize the glass surface as suggested in Table 4-3 are not sufficient to describe the intermolecular interaction between the solid surface and the liquid on it. That is why, cautious evaluation and subsequent improvement are required.

As commonly known, glass is a mixture of several components. According to Zachariassen [190], the cations which form glass can be divided into network-former and network-modifier. Silicon (S), boron (B), germanium (Ge), phosphorus (P) and arsenic (As) belong to the network-former whereas the oxides of alkali metals and alkaline earth metals such as sodium (Na), potassium (K), calcium (Ca) and barium (Ba) belong to the network-modifier [62,154,161].

Normally, SiO_2 is taken to describe glass chemically. Apparently, this component does not play a major role in the dipolar interaction with the liquid (water and ethanol) rests on it. For the computation, barium oxide (BaO) is assumed as the component which actively takes part in the intermolecular interaction with the liquid which lies on the glass surface. The dipole moment of BaO (7.954 D) is used to substitute the initial value of SiO_2 (0.5786 D). The ionization energy and the polarizability remain the same as listed in Table 4-2.

Since the model used is highly polar, it is assumed that glass only interact with water and ethanol. Carbon dioxide is not polar at all and thus, the existence of carbon dioxide in the drop phase does not have to be taken into account in evaluating the intermolecular interaction between the drop phase and the solid material.

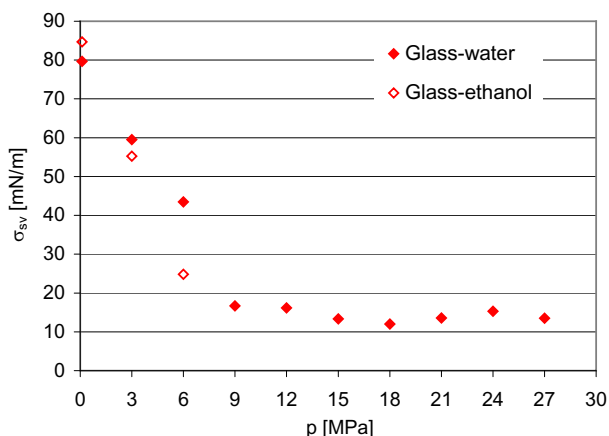


Figure 4-6: Interfacial tension σ_{sv} of glass at 313 K, calculated by means of BaO dipole moment value.

Neglecting the solubility of carbon dioxide in the drop phase, the interaction parameter Φ_{sl} of glass and ethanol becomes 0.49 whereas for the system of glass with water 0.895. Since the

miscibility between the phases is considered as negligible, the parameter Φ_{sl} depends solely on the temperature, not on the pressure. The interfacial tension of glass σ_{sv} calculated by means of the new interaction parameter values is given in Fig. 4-6. Apparently, the absolute condition for the validity of the value of σ_{sv} is quite well fulfilled. A larger discrepancy between both values of σ_{sv} is seen only at 6 MPa.

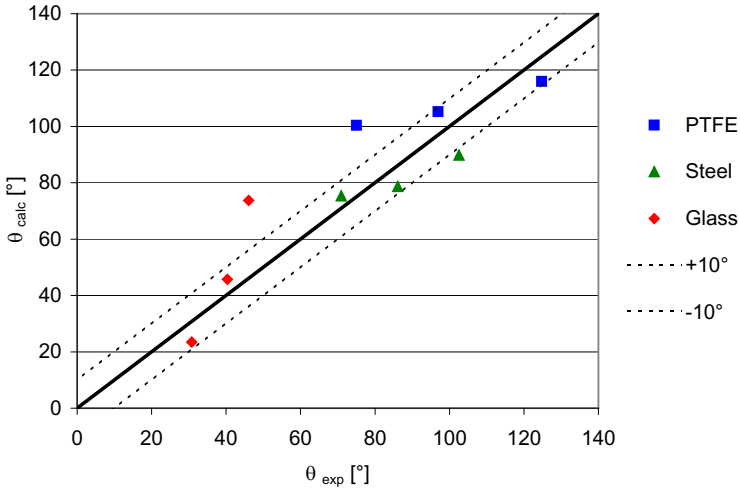


Figure 4-7: Comparison between the calculated and the measured water contact angle on Teflon, glass and steel against carbon dioxide at 313 K using the interfacial value σ_{sv} (Fig. 4-6) obtained from the system of ethanol with solid material in carbon dioxide.

The excellence and applicability of the calculated value of σ_{sv} is confirmed by comparing the calculated and measured sessile water drop contact angle on the glass surface as shown in Fig. 4-7. Here, the calculated and measured sessile water drop contact angles on all of the three materials against carbon dioxide are presented for the sake of completeness. The complete data of the calculated values of Φ_{sl} , σ_{sv} and σ_{sl} for all the systems (the combination of Teflon, steel and glass with water and ethanol against carbon dioxide) at temperatures up to 373 K is given in appendix (Ch. 11).

Finally, it can be concluded that the Quasi-continuum theory can be applied to estimate the molecular interaction parameter Φ_{sl} in order to estimate the magnitude of the solid-vapour interfacial tension σ_{sv} . However, extra attention has to be paid in choosing the molecular properties, the dipole moment μ , the ionization energy I and the polarizability α if the obtained interfacial tension σ_{sv} is to be as accurate as possible.

4.3 Some Remarks

Beside the theory explained in details above, there are some other scientists who worked in the surface chemistry field and tried to formulate an appropriate theory which allows an access to the interfacial tension σ_{sv} . Some to be mention are Zisman, Fowkes, Owens, Wendt and Rabel.

Fowkes' first report on the solid interfacial tension (he called it boundary energy of solid) is given in 1952 [59]. Later, he explained his idea about the additivity of the intermolecular forces at interfaces [56,58] which led to the determination of interfacial tensions, contact angles and also dispersion forces. Fowkes tried to estimate the magnitude of the solid interfacial tension by dividing the interfacial tension itself into two parts, the part due to the dispersion force and the part due to other interactions [57], also referred to as the rest part. The other interactions which are lumped together under the name "rest part" depend on the nature of the components involved. In addition to the dispersion force, the rest part can consist of the hydrogen bond, the metallic bond and dipole interactions [56]. The categorization into dispersion and rest part is determined according to the interatomic forces between the coexisting phases very similar to the basic idea of Good and Girifalco. However, in his work, Fowkes did not emphasize the theoretical derivation such as Good but paid more attention to the empirical method. Nevertheless, mathematically seen, the empirical method of Fowkes assumed that Good's interaction parameter Φ_{sl} is equal to unity. Fowkes tried to isolate and measure the dispersion interfacial tension of mercury, water and of some low energy surfaces such as Teflon, polystyrene, polyethylene [55,57].

Following the idea of Fowkes, Owens and Wendt [149] resolved the interfacial tension into contributions from dispersion and dipole-hydrogen bonding force whereas Rabel [159] suggested splitting the interfacial tension into polar and nonpolar contribution. All of the aforementioned theories are very similar.

Zisman and his coworkers tried to plot the liquid-vapour interfacial tension σ_{lv} directly against the cosine of the contact angle θ [60]. For homologous series of liquids on a given solid they found that the plot is generally a straight line and this led to the development of the concept of critical surface tension of wetting σ_c [207,208]. This empirical quantity is defined by the intercept of the horizontal line $\cos \theta = 1$ with the straight line plot of $\cos \theta$ vs. σ_{lv} . Finally, the conclusion is made that aqueous solutions will spread on a low-energy surface when the interfacial tension σ_{lv} is less than the value σ_c of the solid. This quantity is used as a solid surface characterizing parameter.

The method of Zisman has less importance, since it is known, that the correlation between the interfacial tension σ_{lv} and the cosine of the contact angle θ is more comprehensive than the mere linear correlation. That is why, the plot suggested by Zisman et al. does not always deliver one single straight-line [207,208]. When rectilinear bands are obtained, the intercept of the lower limb of the band at $\cos \theta = 1$ is chosen as the critical interfacial tension σ_c of the solid.

Moreover, in order to obtain the critical interfacial tension σ_c , a wide extrapolation of the plotted line is sometimes required [207]. And as commonly known, a wide extrapolation leads generally to a greater uncertainty in the result.

In the literature, there is also the acid-base theory based on the Lifschitz theory. This theory is a very chemical one and the discussion of this theory here is beyond the scope of this work.

5 Liquid Rivulet Geometry

The question is not what you look at, but what you see.

Henry David Thoreau

5.1 Introduction

In many chemical engineering processes, falling film apparatus is used to gain higher effectiveness regarding heat as well as mass transfer. Vertical condensers [139,166,167], horizontal-tube [68] and falling film evaporators [9,119,134] are some of the kinds of apparatus to be mentioned. They make use of the advantage of the wide covering falling film to optimize the heat exchange between the coexistence phases. Usually these kinds of apparatus are operated under ambient pressure condition. Examples of kinds of falling film apparatus which are operated at high pressure conditions using dense gases are wetted-wall absorbers and packed extraction columns. In many packed extraction columns, the benefit of the large exchange area of the falling film is combined with the advantage attained by using supercritical fluid, which is an alternative to conventional extraction using liquid organic solvents. Supercritical Fluid Extraction (SFE), which is of great interest for industrial use, is applied in many separation processes. Some examples of SFE performed in falling film extraction columns are the separation of free fatty acids from vegetable oil [206], decaffeination of high concentrated coffee solution by means of supercritical carbon dioxide [131], extraction of germ oil [199] and fractional extraction of paprika [3].

When discussing the falling film, one might imagine a wide-covering, continuous, thin film which flows down a vertical flat surface, driven by the gravitational force, and bounded by two other phases, the solid phase, on which the film flows, and the adjacent continuous phase. A rivulet, on the other hand, is a narrow stream of a liquid flowing down a solid surface, and is believed to be the unstable form of a wide covering falling film [106,187]. In contrast to the falling film, the thickness and the width of a rivulet are of the same magnitude [106]. This sharp distinction is not made for various reasons and both are investigated in this work. The first reason is regarding the availability of the apparatus for the falling film investigation. Due to the fact that the experiments are performed in a high pressure view cell under the presence of a dense fluid, the dimension of the produced liquid sheet is limited by the inner volume of the pressure chamber itself. Furthermore, in order to produce a wide covering film, a special distribution device is required, such as a distribution plate, which has the function of spreading the film phase properly onto the vertical solid. A bad covering of the solid surface area can be caused by fluid dynamics, system properties and bad wetting characteristics. However, this can also be triggered by a distribution device which is not properly designed. In order to concentrate on the most important issues and to avoid erroneous results due to the apparatus construction,

no special distribution device is included in the view cell used in this work. Thus, although the width of the liquid sheets formed in the experiments is nearly always larger than its thickness, (except in cases where the wettability is very low) it is also limited.

In contrast to the idea, which states that rivulets are the unstable form of the falling film, the reverse can also be seen as follows. A rivulet is the unit which forms a wide covering falling film. In order to attain adequate knowledge about the falling film, it is recommended to go back one step and to start with the single, smaller unit, i.e. the rivulet. This is the second reason for including rivulets in this work. And as is mentioned before, the investigation of a large falling film is done through studying a narrower sheet of liquid.

Even though attempts have been made to optimize chemical engineering processes by combining the geometry of falling film with the benefit of the advantageous material properties of supercritical fluid [86], the result attained is still not as expected [14]. Although the reasons have not yet been clarified completely, some of the possible causes can lie in the large axial back-mixing, the instability of falling film [200], where, instead of a large covering film, rivulets and drops are formed, and the wetting characteristics. The latter aspects regarding the instability and the wettability of liquid films or rivulets are the main topics of this chapter.

In the past, there has been little consideration of wetting characteristics as one factor which can lower the effectiveness of a chemical engineering process. In fact, using the Nusselt film condensation theory [146], the dimension of the film is predicted according to the hydrodynamics and the liquid properties [24,39,108,138,139,179]. This can be done if the whole available exchange area is covered perfectly by the film phase. Or in other words, the amount of liquid poured onto the solid surface is sufficient to produce a wide covering film.

As is known from the study described in Chapter 3, wetting characteristics are system properties, which means, they depend on the three phases which coexist and interact with each other. That is why, here, another approach is made in order to reach a better understanding of the fluid dynamics and wetting characteristics of falling film in the presence of gaseous and supercritical carbon dioxide.

The dimensions of the rivulet, which are obtained through experiments performed in this work, are used to find a universal parameter, which characterises the wettability of a system quantitatively, and in turn, allows a direct comparison between systems regarding their wetting characteristics. This universal parameter gained from the rivulet wetting characteristics study can be compared with the contact angle of a sessile drop reported in Chapter 3. Finally, a stability study of the rivulet is reported at the end of this chapter.

In Chapter 6 and 8 the fluid dynamics study is described for falling film surrounded by pressurized fluid. In contrast to the theories of the afore-mentioned authors, the rivulet fluid dynamics study in Chapter 7 is based on the wetting ability finding which is discussed in Chapter 5. Generally a wide-covering film thickness prediction is also made based on the fluid dynamics found in Chapter 6. Also in the last chapter, the extent of the shear stress exerted on the rivulet and the falling film is reported.

5.2 Experimental Setup

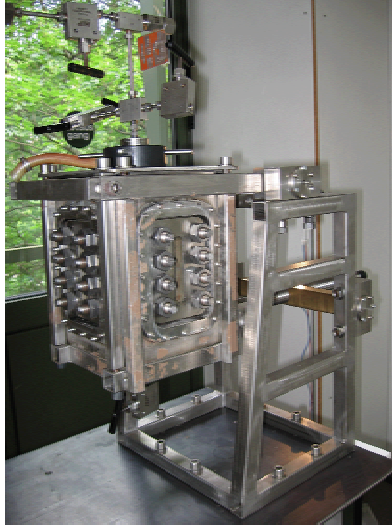


Figure 5-1: View cell with windows at three of its sides, used in the falling film experiments.

The experiments are performed in a pressure-resistant view cell made of stainless steel 1.4980 which is designed for a maximum temperature of 400 K and a maximum pressure of 50 MPa (see Fig. 5-1). The view cell used has a volume of 350 ml. The inner diameter is 40 mm and the effective height is approximately 160 mm. This view cell has glass windows on three of its sides which allow viewing into the pressure chamber while the experiment proceeds. The window has a length of 99 mm and a width of 18 mm.

At the beginning, the liquid, which is used as the film phase, is stored in a high pressure vessel made of stainless steel 1.4571. This liquid storage vessel is also designed for a maximum temperature of 400 K and a maximum pressure of 50 MPa.

A circulation pump can be used for saturation purposes if film phase presaturation by the fluid is desired (see saturation unit in Fig. 5-2). The circulation pump has the task of intensifying the contact between the liquid and the fluid phase in the storage vessel and, in this way, it enhances the dissolution of the fluid into the liquid phase until equilibrium is reached.

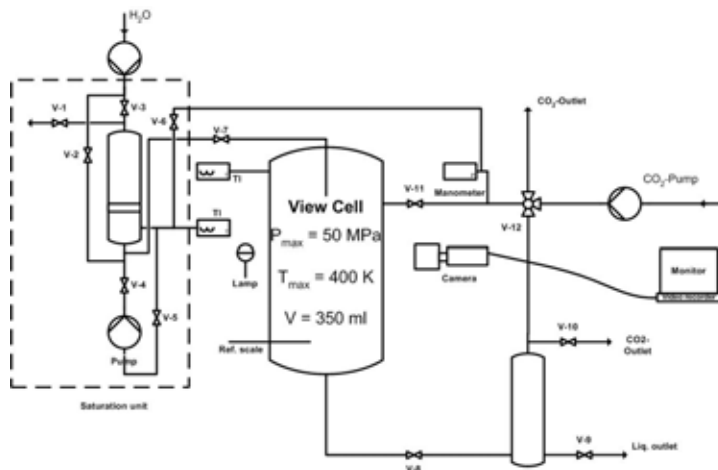


Figure 5-2: Falling film experimental setup.

To start with, the liquid in the storage vessel is introduced into the view cell by means of a pump. The liquid flows through a stainless steel capillary, whose outer diameter is $1/16''$. This capillary leans on a vertical surface in the view cell. The liquid covers the vertical solid surface and in this way forms a rivulet, which is driven down the surface by gravitational force. The solid surface placed in the view cell has the dimension $115 \times 15 \text{ mm}^2$ and is fixed in a solid surface holder made of stainless steel as can be seen in Fig. 5-3.



Figure 5-3: Solid surface holder in the view cell used in the experiments.

A buffer vessel, which is on the right hand side of the view cell, is used to avoid a large pressure drop in the view cell when liquid is released. A large, sudden pressure drop in the view cell damages the o-rings used for sealing purpose.

While the experiments proceed, images of the rivulet can be taken from two sides, the front as well as the side view. The recording of the images is not started until a steady flow of the liquid

is reached. For the dimension-measurement purpose later, the image taken is magnified. A larger picture is obtained, but as a consequence of the magnification, the recording area becomes smaller. The magnification used in the recording is a compromise. The picture taken has to be large enough that the dimensions, i.e. the thickness and the width of the film, can still be seen clearly, and they can later be measured by means of image processing software. At the same time, the recording area has to be large enough to get a representative average value of these dimensions. The magnification chosen for the film thickness allows an entire measurement length of 6 mm. For the width measurement, a length of 35 mm is available. The area recorded for the width measurement starts at a point 16 mm below the liquid inlet whereas for the thickness, the liquid flows 45 mm before the image is taken. As the picture taken is magnified, a reference scale is required to convert the dimensions back to the real sizes. The outer diameter of the stainless steel capillary, through which the liquid flows into the view cell, is one alternative for this purpose. Another possibility is to use a capillary installed at the bottom of the view cell (see Fig. 5-4, 2.a-2.e.).

In the experiments, the width and the thickness of water rivulet on steel (1.4305) as well as glass surfaces are measured. Pure water and water, which is presaturated with carbon dioxide, are used. The experiments are performed in dense carbon dioxide at 313 K, up to 27 MPa. The liquid phase flow rate varies up to 9 g/min.

5.3 Qualitative Results

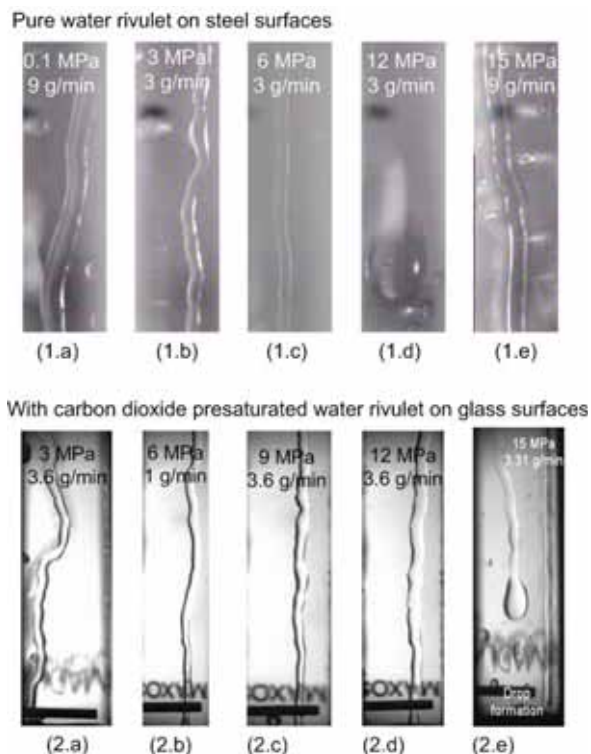


Figure 5-4: Water rivulet on solid surfaces

The images of the rivulet taken from the front side are shown in Fig. 5-4. As can be seen in the figure, the water rivulet does not always take the shortest path between two points on a vertical surface. Instead of flowing straight down the solid surface, it rather forms a sinuously structured path called a meander [34,105,107].

The difference in wetting can be seen qualitatively. For example on the steel surface, the water rivulet at 9 g/min and 0.1 MPa is wider than that at 15 MPa. A qualitative difference can also be observed when a glass surface is employed. At a flow rate of 3.6 g/min, the rivulet at 12 MPa appears wider than those at 3 and 6 MPa. The explanation for these different wetting characteristics lies in the operating conditions such as temperature, pressure and liquid mass flow, as well as in the wettability of the investigated system. More on this topic and the dimension measurement results can be found in 5.4, 5.6 and 5.7.

Due to the fact that the width of the rivulet is not constant as it flows down the vertical surface, it is averaged by dividing the whole wetting area by the length of the wetting path.

The qualitative form of the rivulet surface seen from the side projection is shown in Fig. 5-5. In general, the surface is not even, it is rather wavy [192]. The waviness depends on the operating conditions and the flow conditions of the rivulet as well as the continuous phase. According to the observation made in the experiments, at a constant liquid flow rate, the degree of rivulet-surface waviness increases with increasing pressure (Fig. 5-5 a-d) until a point is reached, where the whole rivulet becomes unstable. It breaks into drops which slide down the surface (Fig. 5-5 e). This is in line with the finding made by Kerst [108]. Moreover, Stockfleth [180] and Kerst found that, at a constant pressure, the waviness is intensified by an increase in the mass flow. When, for instance at 7 MPa, the mass flow is increased from 300 g/h up to 5000 g/h (this is an increase of approximately 5 g/min to 83 g/min), the initial flat film becomes not only wavy but the liquid also loosens itself from the surface [108]. There is a mixture of falling film on the vertical surface and liquid drops sprayed in the pressure chamber.

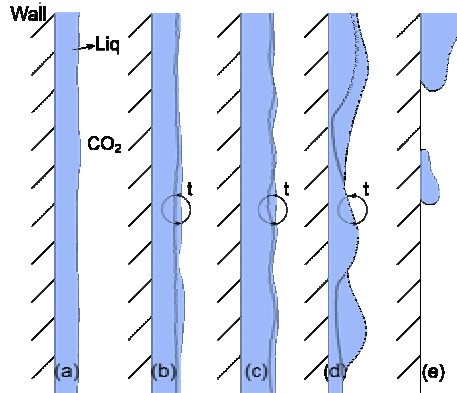


Figure 5-5: Rivulet surface seen from the side view.

This phenomenon can be explained as follows. On the one hand, the high mass flow of the liquid phase on the vertical wall ensures that there is always enough liquid on the vertical surface. However, on the other hand, the higher the mass flow is, the larger is the impulse inserted into the system. This impulse turns out to be a kind of form-destructing force which causes perturbation at the film surface and, when it is large enough, it splashes liquid into drops. Since the maximum liquid mass flow in this work is just one-tenth of that applied by Kerst, the influence of the mass flow at the film surface is contrariwise. Increasing the mass flow up to maximal 9 g/min weakens the waviness. An increase in the mass flow means that additional liquid is poured onto the surface. The velocity becomes larger due to the higher mass flow but at the same time, the inserted impulse is not large enough yet to perturb the film surface. A more even rivulet surface is reached when the liquid mass flow is increased.

5.4 Thickness and Width of Water Rivulet

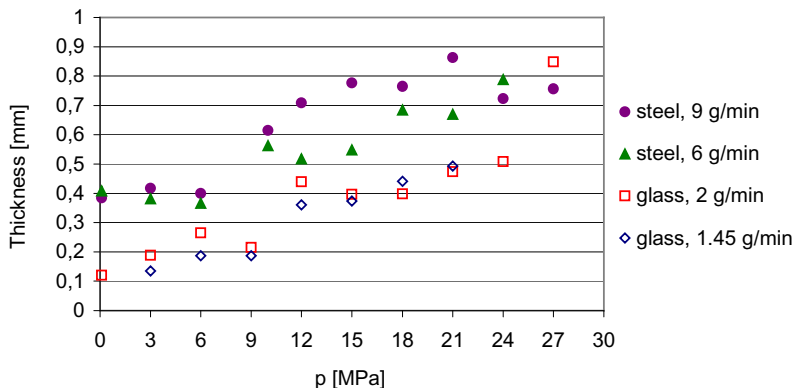


Figure 5-6: Measured water rivulet thickness on steel and glass surfaces at 313 K up to 27 MPa.

To obtain representative results, the dimensions of the rivulet, i.e. its width and thickness, are averaged across the whole recorded measurement length. The measured zone for thickness is 6 mm, whereas for the width, this zone is 35 mm. The thickness of water rivulet on steel and glass surfaces in dense carbon dioxide at 313 K is shown in Fig. 5-6. As shown in Chapter 3, in pressurized carbon dioxide, water wets glass better than steel. That is why higher water mass flow is required to form a stable rivulet on a steel surface. The maximum water mass flow applied on the glass surface is 3.6 g/min. This is the lowest water mass flow given on the steel surface. At this flow rate, a water rivulet on the steel surface remains stable only in gaseous carbon dioxide. As soon as carbon dioxide becomes supercritical, the water rivulet disintegrates into drops.

In Fig. 5-6 the rivulet thickness measurement results on both surfaces at two different mass flows are shown. The water rivulet on the steel is much thicker than on the glass. On the one hand, this might be the result of the higher mass flow on the steel surface, but on the other hand, the poorer water wettability on steel surfaces can also be responsible for the thicker rivulet. As might be expected, a higher rate of flow causes not only a faster flowing rivulet, but also an increase in its thickness. This can be seen on both surfaces.

The dependence of rivulet thickness on the pressure at a constant mass flow can be explained by means of the wetting characteristics (as will be done later) and the fluid dynamics. From fluid dynamics point of view, the density changes play an important role. The density of the liquid phase remains nearly the same as pressure increases. In contrast, at 313 K gaseous carbon dioxide becomes supercritical as soon as the critical pressure 7.4 MPa is exceeded. The transition to supercritical carbon dioxide causes a large rise in the density, so that the density difference between the phases becomes smaller as the pressure increases. This has the

consequence that the rivulet flows more slowly and becomes thicker. At 27 MPa, the rivulet on steel is twice as thick as the one at ambient pressure. On glass, the same pressure rise creates a rivulet which is approximately eight times thicker.

In order to gain a complete picture of the change in the wettability and thus, the dependence of the rivulet shape on the afore-mentioned factors, the width is also measured.

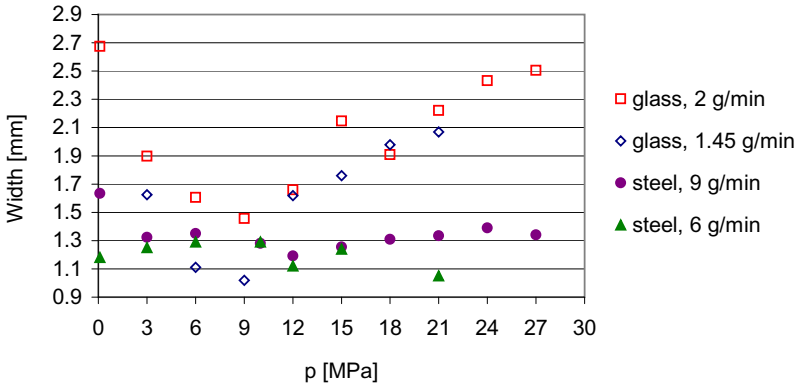


Figure 5-7: Measured width of water rivulet on steel and glass surfaces at 313 K up to 27 MPa.

As can be seen in Fig. 5-7, the rivulet width on the steel surface remains nearly the same in the whole pressure range. A rise in the mass flow from 6 g/min to 9 g/min does not change the width noticeably. Except at ambient pressure, the rivulet width on the steel surface varies from 1.2 mm to 1.4 mm.

In contrast, the width of water rivulet on the glass surface changes appreciably with the pressure. In gaseous carbon dioxide the rivulet becomes narrower as pressure increases until it reaches a minimum before the rivulet becomes wider with increasing pressure in the supercritical carbon dioxide. The width of the rivulet on the glass surface varies between 1.5 mm and 2.7 mm. A mass flow increase from 1.45 g/min to 2 g/min does not have a great impact on the wetting width.

Conclusions can be drawn based on the rivulet thickness and width measurement results on a steel surface as shown in Fig. 5-6 and 5-7. Qualitatively, it is easy to conclude that the wettability of a water rivulet on the steel surface becomes poorer at higher pressure. On the contrary, the conclusion on the wettability of a water rivulet on the glass surface is not that simple, because, although the thickness also increases with increasing pressure, the width of the rivulet does not change uniformly as pressure changes. In order to combine both dimensions and thus make a clear statement about the wettability of a liquid on a particular solid at given conditions, a universal parameter is required.

5.5 Theory on Rivulet-wetting Angle

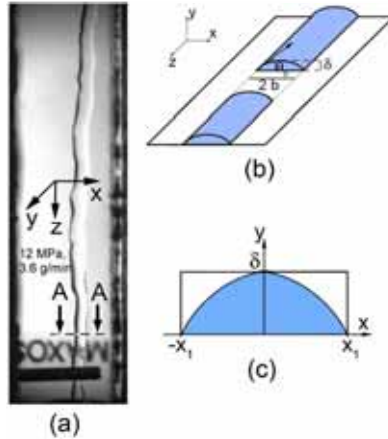


Figure 5-8: (a) The rivulet. (b) The rivulet cut perpendicular to its flow direction. (c) Enlarged view of cross-section of rivulet.

In order to obtain a universal parameter, which characterizes the wetting of a liquid on a vertical solid, the rivulet is, theoretically, cut perpendicular to its flow direction, as can be seen in Fig. 5-8(a). Adapting the idea of the sessile drop contact angle, a wetting angle θ_0 exists. The symbol θ_0 with index 0 is used here to distinguish rivulet-wetting angle from the sessile drop contact angle. Furthermore, in Chapter 7, θ characterizes the polar coordinate. This wetting angle cannot be measured directly.

If a circle with the radius R is cut horizontally at a particular point in y -axis (see Fig. 5-9(a)), a slice of circular segment is attained. The cross-section of the theoretically cut rivulet in Fig. 5-8(a) and (b) is assumed to have the shape of this circular segment slice (5-8(c)). The liquid-solid contact line (or the x -axis in Fig. 5-9(b) and (c)) and the tangent at the three-phase-contact-point between the solid, the continuous and the rivulet phase (see Fig. 5-8(b)) forms the rivulet-wetting angle. As can be seen in Fig. 5-9(a), this wetting angle ranges between 0° and 180° . The wetting angle is 0° if there is a total wetting. The opposite of this, is the non-wetting case, i.e. when the rivulet cross-section is a perfect circle. The wetting angle is 180° .

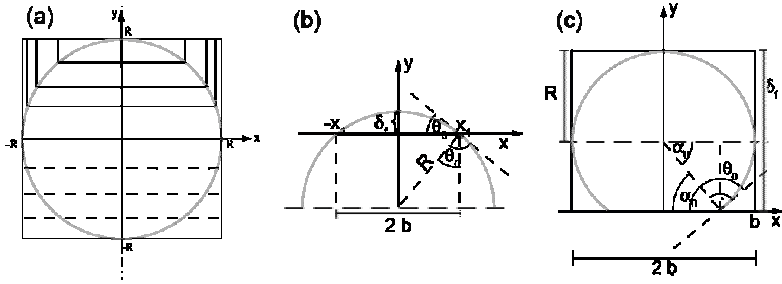


Figure 5-9: Assuming the cross-section of the rivulet to be a circular segment (a), the wetting angle can be less (b) or larger than 90° (c).

By means of the measured rivulet dimensions, the thickness δ_f and half of the rivulet width b , the wetting angle can be estimated with the help of the circle geometry in Fig. 5-9(b)

$$\theta_0 = \arcsin\left(\frac{2b\delta_f}{b^2 + \delta_f^2}\right) \quad (5-1)$$

if the angle is less than or equal 90° (generally, the index f refers to the film phase, which covers the vertical surface, regardless of the stage of covering, whether a rivulet or a wide film is formed on the solid surface). If the wetting angle is larger than 90° (Fig. 5-9(c)),

$$\theta_0 = \alpha_0 + \frac{\pi}{2} \quad (5-2)$$

with

$$\alpha_0 = \arcsin\left(\frac{\delta_f - b}{b}\right). \quad (5-3)$$

For the sake of completeness, the radius of the circle can be calculated according to Eq. 5-4

$$R = \frac{b^2 + \delta_f^2}{2\delta_f} \quad (5-4)$$

if the wetting angle is less than 90° . In a case where the wetting angle is equal to or larger than 90° , the radius of the circle is half of the rivulet width due to the fact that the measured rivulet width is the projection of the maximum width (see Fig. 5-9(c)).

5.6 Water Rivulet-wetting Angle

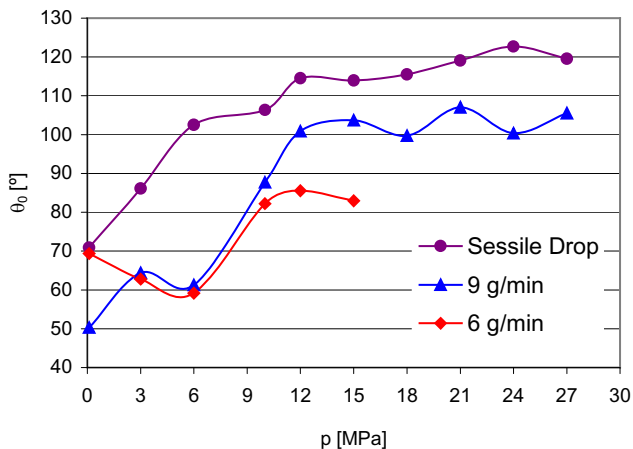


Figure 5-10: Pure sessile water drop contact angle and rivulet-wetting angle on a steel surface at 313 K.

In Fig. 5-10 the sessile water drop contact angle and the rivulet-wetting angle on a steel surface at 313 K are shown in terms of their dependency on the pressure. In general, the water rivulet does not wet the steel very well. The wetting angle increases from 50° at ambient pressure up to nearly 110° at 27 MPa.

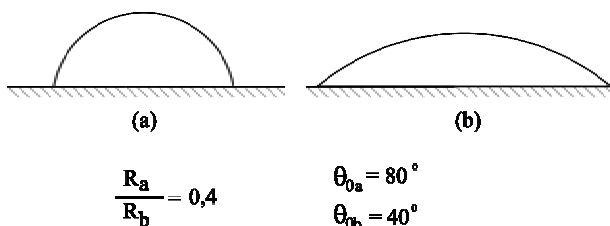


Figure 5-11: The change of rivulet cross-section shape due to spreading

In accordance with the sessile drop contact angle, the water rivulet wets the vertical steel surface less well as carbon dioxide pressure increases. A rise in the mass flow from 6 g/min to 9 g/min has the same effect on the wetting angle. In gaseous carbon dioxide, the increase in the wetting angle due to the increase in the mass flow is negligible. However, in supercritical carbon dioxide, this causes a wetting angle rise of about 15° . This clearly means, that through the increase in the mass flow, the extra amount of water added onto the vertical surface does not

spontaneously distribute itself sideways. It accumulates rather in thickness in the y-axis direction (see Fig. 5-8(c) and 5-9(b)) and results in a larger wetting angle.

The shape of the rivulet is held stable by the liquid interfacial tension σ_{lv} which acts around the circumference adjacent to the continuous phase. As long as the force provided by this interfacial tension is large enough, the increase in the mass flow causes a thicker rivulet with a larger wetting angle. When the mechanical equilibrium point is exceeded, the whole shape breaks. The collapse of the rivulet shape can be related to two aspects. The first factor is related to the impulse introduced by the pump. As the liquid mass flow increases, the impulse inserted into the system increases as well. In turn, this impulse acts as a form-destructing force and disturbs the whole rivulet in that way, so that the spreading is enhanced. Inherently, spreading itself—seen from the force point of view—is advantageous.

The spreading of a rivulet sideways gives a rise in the circumference, around which the liquid interfacial tension σ_{lv} acts (see Fig. 5-11). As a result, the total force which holds the whole geometry of the rivulet stable, increases as well. The spreading of the rivulet sideways can be seen as an alternative offered by the natural law, to change the rivulet shape to a more advantageous one and, thereby, to provide the required, higher force to maintain the stability of the whole geometry. In Fig. 5-11 the alteration of the rivulet cross-section through spreading is shown. For example, a drop in the wetting angle from 80° to just half, that is 40° , delivers—at a same cross-sectional area—a circle equivalent radius which is 2.5 times larger than the former one. Here, it is strictly assumed that the spreading does not bring any change in the cross-sectional area. In fact, it is conceivable that, through an increase in the mass flow, the cross-sectional area also becomes larger.

The spreading as shown in Fig. 5-11 gives a 22% increase in the circumference which also means a 22% additional force is available to hold the geometry stable. This is the second explanation for the spreading of the rivulet when mass flow increases.

Conversely, a decrease in the mass flow results in a smaller wetting angle, which means a better wetting behaviour. However, a consistent decrease in the mass flow ends in rivulet instability, such as discussed in 5.7.

The water rivulet-wetting angle on a glass surface at 313 K can be seen in Fig. 5-12. Here the wetting angle of the water rivulet at 1 g/min, 2 g/min and 3.1 g/min is compared with the sessile drop contact angle. On steel as well as glass surfaces, the sessile drop contact angle presents the upper limit of the possible angle value of the rivulet, so that, by rule of thumb, when respective data of the rivulet-wetting angle is not available, the contact angle of a sessile drop can be applied. And thus, one is at the safe side because according to the measurement results in Fig. 5-10 and 5-12, the rivulet-wetting angle is always smaller than the sessile drop contact angle. The difference ranges between 10° and 20° .

The explanation for the better wetting characteristics of rivulets compared with the sessile drops can be found in the dynamics involved. In the case of rivulets, liquid is pumped onto the vertical surface. It flows with a certain initial velocity, which is accelerated by the gravitational force

and decelerated by buoyancy, wall friction and shear stress exerted by the continuous phase (the existence of the shear stress depends on the material properties of the continuous phase and the velocity of the liquid phase). Although in a steady state, the liquid rivulet or liquid film is not accelerated anymore, it still contains a finite impulse which enhances the wetting on the vertical surface. The friction on the vertical wall helps the liquid to spread on the surface as well. This kind of impulse and the wall friction effect do not exist when a drop rests on a horizontal surface.

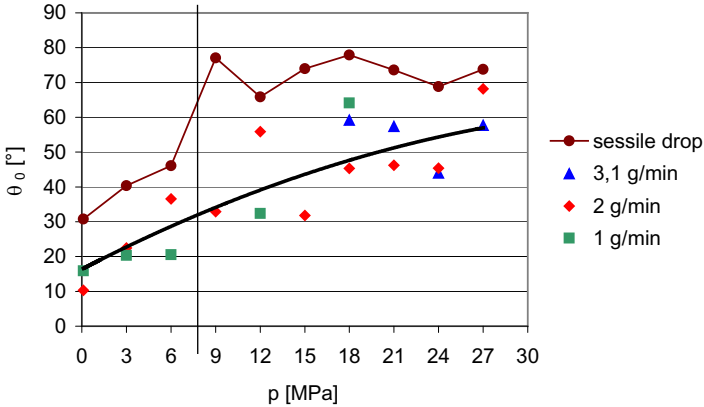


Figure 5-12: Sessile drop contact angle and pure water rivulet-wetting angle on a glass surface at 313 K.

In general, the rise of the rivulet-wetting angle on the glass surface due to the rise in the applied mass flow range is not appreciable. The wetting angle on the glass surface increases from 10° at ambient pressure up to nearly 70° at 27 MPa. Besides the wetting characteristics which becomes worse as the pressure increases, the fluid dynamics play also a major role. The density difference becomes smaller as pressure increases, and as a consequence, a water rivulet flows more slowly. The accumulation of the liquid can be seen in the wetting angle which becomes larger.

In accordance to the finding made on the sessile drop contact angle, a water rivulet can wet glass better than it can the steel surface. At the same operating conditions (but different water rate of flow), the wetting angle of the water rivulet on a glass surface varies between 10° and 70° , whereas on steel surface, the angle is larger. It is between 50° and 110° (Fig. 5-10).

The wetting angle results of the carbon dioxide presaturated water on steel and glass surfaces can be seen in Fig. 5-13. The presaturation does not affect the wetting characteristics markedly. The angle difference due to the presaturation varies between 1° and 5° . This discrepancy can also be caused by the errors occurring in the measurement.

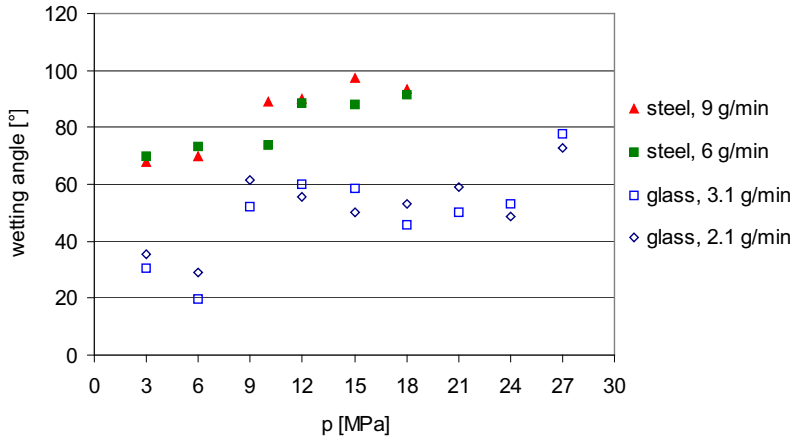


Figure 5-13: With carbon dioxide presaturated water rivulet-wetting angle on steel and glass surfaces at 313 K.

5.7 Rivulet Instability

As has been discussed before, a decrease in the rivulet phase mass flow enhances the wetting on both surfaces. However, one runs the risk of rivulet instability if the mass flow is decreased consistently.

If the amount of the rivulet phase poured onto the vertical solid is not sufficient to guarantee a homogenous, wide covering rivulet, this liquid accumulates and stagnates at certain points on the wall for a short period of time. When the gravitational force required to draw the liquid down the vertical surface is great enough, the deformed drops, which resemble a nose shape, slide down the solid surface (see Fig. 5-4, 1.d, 2.e). At this point, the gravitational force has exceeded the forces which prevent the liquid from flowing, i.e. the buoyancy, the wall friction, the shear stress exerted on the rivulet surface and the liquid interfacial tension.

At the beginning, there are both an unsteady flowing rivulet and liquid drops. A further decrease in the mass flow increases the unsteadiness of the rivulet flow and in this way enhances drop formation until only single drops slide down the vertical surface.

The measurement results of the minimum mass flow needed to guarantee a stable flowing water rivulet on steel and glass surfaces are shown in Fig. 5-14. Generally, the minimum amount of water or liquid needed to build a uniform rivulet becomes larger as the pressure increases. This is due to the fall in the density difference between the phases.

The good wetting characteristics of glass in comparison to steel can also be seen in the minimum liquid amount needed to form a rivulet. Less liquid is required to form a rivulet on a glass surface than on a steel surface.

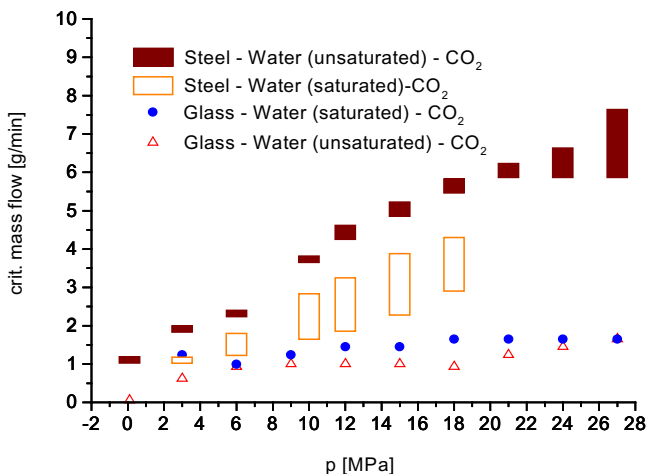


Figure 5-14: Critical mass flow of water rivulet on the steel and glass surfaces at 313 K.

Although water has a relatively high liquid interfacial tension, the wetting on the glass surface under pressurized carbon dioxide is excellent. In Fig. 5-14 the beginning of water rivulet disintegration on a glass surface is shown. On this surface, the water rivulet breaks up at 1.5 g/min at 313 K and 27 MPa. The wetting at ambient pressure is so good, that there is no disintegration down to a mass flow of nearly 0.05 g/min. As a result of the presaturation with carbon dioxide, more liquid is needed to avoid instability.

The bar diagram for a steel surface in Fig. 5-14 shows the transition zone of the rivulet regime to the drop regime. Above the bars the rivulet regime prevails, whereas below the bars there will be only single drops sliding down the vertical surface. Here the bars separate the rivulet and the drop regimes. The bar itself represents the transition zone where a mixture of both is expected.

On the steel surface, at ambient pressure and 313 K, a water rivulet becomes unstable at 1 g/min, whereas at 27 MPa the instability already begins at 8 g/min. According to the bar diagram shown in Fig. 5-14 water presaturation causes unexpectedly a better wetting on the steel surface. The amount of water needed to guarantee a stable rivulet becomes less. The explanation for this phenomenon might be found in the molecular interaction between the phases: water, carbon dioxide and steel material. Further discussion of this phenomenon exceeds the scope of the present work.

6 Fluid Dynamics of Falling Film

The state of mind which enables a man to do work of this kind ... is akin to that of the religious worshipper or the lover; the daily effort comes from no deliberate intention or programme, but straight from the heart.

Albert Einstein

The main objective of this chapter is to find a calculation model for the film velocity. The fluid dynamics of falling film will be discussed by means of three calculation models, the Nusselt, the wall and the tau models. The first two models present the extreme cases. A comparison of the calculated film mean velocity with the measured ones shows that both of them are suitable to describe the fluid dynamics of the falling film under particular conditions. But a general model, which is valid in a wide range of conditions, is required. In the third model, the tau model, a finite shear stress at the film surface is assumed. This shear stress is exerted by the continuous phase. Based on this assumption, the tau model is developed.

Assuming that the cross-section of a rivulet has the shape of a circular segment and the wetting angle of a rivulet can be smaller or larger than 90° , a distinction in the velocity equation regarding the wetting angle is made. This is an attempt to distinguish between the fluid dynamics of the liquid when a wall contact exists and the fluid dynamics of the liquid when it floats in the continuous phase and holds firmly by the rivulet just by means of the cohesion force.

To give an overview, the film phase velocity equations using three different shapes of cross-section are summarized in tabular form at the end of this chapter.

6.1 Nusselt Film Condensation Theory

In 1916 Nusselt [146] reported in his work on the subject of water steam film condensation on a vertical metal surface. He had already put forward a simple theory for the calculation of heat transfer in laminar film condensation in tubes and on vertical or inclined walls.

When a vapour condenses on a vertical surface and a liquid film develops, it flows along the surface under the influence of gravity. When the vapour velocity is low and the liquid film is sufficiently thin, a laminar flow in the film phase can be assumed. Along with gravity, buoyant force and shear stress also exist. Depending on the magnitude of these forces, they might have an appreciable influence on the film flow.

The film condensation theory can be explained as follows. When an infinitesimal volume element of the film phase is enlarged such as shown in Fig. 6-1, under the assumption of steady flow, the gravitational force F_G is balanced by the buoyant force F_B and the force exerted by the shear stress τ

$$F_G + \tau_{(y+dy)} dx dz = F_B + \tau_{(y)} dx dz . \quad (6-1)$$

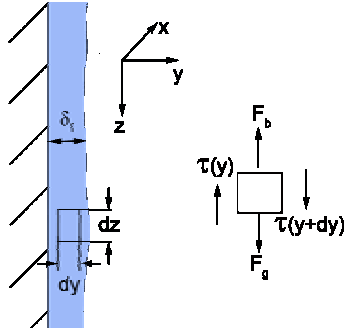


Figure 6-1: Force balance on an infinitesimal volume element in the film phase.

Putting the buoyant force on the left hand side and collecting the shear stress terms on the right hand side

$$F_G - F_B = -\left\{ \tau_{(y+dy)} - \tau_{(y)} \right\} dx dz, \quad (6-2)$$

substituting the gravitational and the buoyant force by the expressions in terms of the volume of the body and its density ρ , multiplied by the acceleration due to gravity, and expressing the change of the shear stress in differential terms, delivers Eq. 6-3

$$(\rho_f - \rho_c) g dx dy dz = -\frac{\partial \tau_y}{\partial y} dx dy dz \quad (6-3)$$

(the indices f and c stand for film and continuous phases respectively). For Newtonian fluid, Eq. 6-4 can be applied to describe the shear stress exerted on a surface

$$\tau = \pm \eta \left(\frac{\partial w}{\partial y} \right). \quad (6-4)$$

Shear stress is an internal force which can be understood as the friction between the molecules due to the gradient in the particle velocity vectors. Its magnitude is proportional to the velocity gradient perpendicular to the direction of the shear stress with the liquid viscosity η_f as the proportionality constant.

The algebraic signs in front of the right hand side term in Eq. 6-4 show the direction of the shear stress, whether it accelerates (positive sign) or decelerates (negative sign) the molecules. Due to the fact that shear stress is, by definition, a force per unit area, at the same time, the algebraic sign on the right hand side of Eq. 6-4 is also required to guarantee a positive force. In this context, a negative force does not make any sense (except to show the direction of the force and thus, whether it is an accelerating or decelerating force). For the absolute value, the algebraic sign in Eq. 6-4 is not required.

Equation 6-4 is differentiated with respect to the y-axis and put into Eq. 6-3

$$-\frac{\Delta\rho g}{\eta_f} = \frac{\partial^2 w}{\partial y^2} \quad (6-5)$$

where the density difference between the film and the continuous phase is expressed in $\Delta\rho$. The film velocity second order differential equation in 6-5 depends only on the material properties of both phases. To solve this equation, two boundary conditions are needed. Nusselt suggested the following boundary conditions:

- No-slip condition on the vertical wall: the outermost film phase molecules next to the vertical wall stick to the surface past which they flow. The velocity of the liquid on the wall is zero:

$$w(y=0) = 0. \quad (6-6)$$

- The shear stress exerted by the continuous phase at the film surface is negligible. Thus, the tangent of the velocity at the film surface is zero

$$\left(\frac{dw}{dy}\right)_{y=\delta_f} = 0. \quad (6-7)$$

Nusselt studied the case of film condensation on a vertical wall under ambient pressure without any appreciable shear stress at the film surface, and that is why the second boundary condition (Eq. 6-7) holds. The term of material properties ($\Delta\rho$ and η_f) multiplied by the gravitational acceleration constant g on the left hand side in Eq. 6-5 is collectively referred to as β_f

$$\beta_f = \frac{\Delta\rho g}{\eta_f}. \quad (6-8)$$

and the second order differential equation in Eq. 6-5 can be solved by means of the aforementioned boundary conditions:

$$w(y) = -\frac{\beta_f}{2}y^2 + \beta_f \delta_f y. \quad (6-9)$$

The gained equation in 6-9 is called the film velocity equation according to Nusselt model.

6.2 Wall Model

The Nusselt model describes one extreme condition where the shear stress at the film phase, exerted by the continuous phase, is negligible. In contrast to Nusselt, a second, possible extreme condition in a static continuous phase is when the shear stress exerted by the continuous phase is sufficiently large that the molecules on the film phase stick where they are

$$w(y = \delta_f) = 0 \quad (6-10)$$

as if the film flows between two walls. The velocity equation is given in 6-11

$$w(y) = -\frac{\beta_f}{2}y^2 + \frac{\beta_f \delta_f}{2}y. \quad (6-11)$$

The velocity equation according to the wall model (6-11) is similar to the one according to Nusselt (6-9). They are only different in the second term on the right hand side. This term in the wall equation is just one half of the one in the Nusselt equation.

6.3 A Comparison of Measured and Calculated Mean Velocity

In order to check the applicability of the calculation models explained in Chapter 6.1 and 6.2, the mean velocities according to these models are calculated, and compared with the measured ones. For the purpose of calculating average velocity, the cross-section of the rivulet is assumed to be circular (the details in the calculation of the mean velocity can be seen in Chapter 7). The results of the calculation according to the Nusselt and the wall models are given in Fig. 6-2. In this figure, the mean velocity of water film on a vertical steel surface at 313 K and a mass flow of 9 g/min under the presence of pressurized carbon dioxide is given. Here, the mass flow is held constant in the whole pressure range. The densities of the phases and the wetting behaviour change in accordance with increasing pressure so that the film thickness δ_f is not constant in the investigated pressure range (see Fig. 6-2).

At lower pressures, the experimental velocities are closer to the Nusselt model. Here, the deviation of the measured and calculated mean velocity according to the Nusselt model at 0.1 MPa is rather large. At this condition, Nusselt should be able to describe the fluid dynamics best. The possible reason for this discrepancy might lie in the measurement precision of the film thickness and the film width. The mass flow of the film is held constant at 9 g/min for the whole pressure range. Due to the fall in the density difference between the phases, the film becomes slower. At higher pressures, especially when gaseous carbon dioxide turns to supercritical, the experimental values come closer to the wall model. The described phenomenon is seen not only when film flows along a steel surface. When a glass surface is involved, the same run of the curves is obtained.

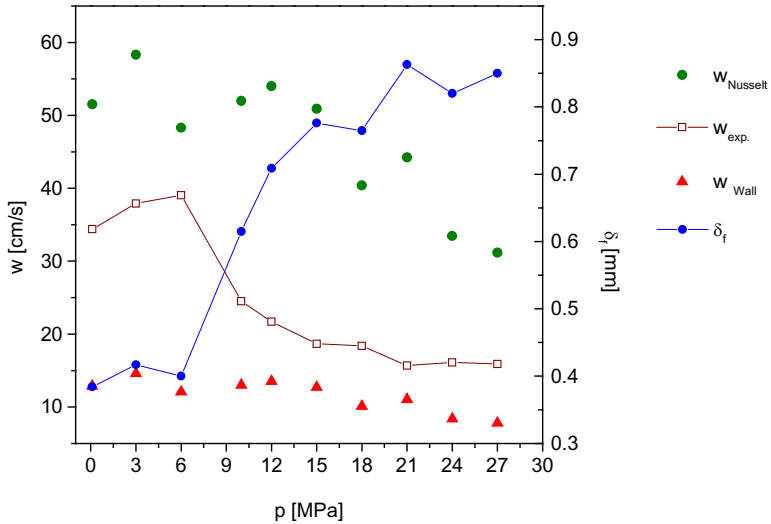


Figure 6-2: Measured and calculated film mean velocity according to the Nusselt and the wall model for water film on a vertical steel surface at 313 K and a mass flow of 9 g/min. The film thickness δ_f is given on the right-hand-side y-axis.

As can be seen in Fig. 6-2, the calculation results according to these models set the limits within which the measured mean velocity exists. Both models describe the extreme conditions, but the real one cannot be represented. Using the Nusselt model, the velocity at higher pressure range will always be overestimated whereas with the wall model, the velocity will be underestimated. The wall model is suitable to describe the fluid dynamics best when the assumed conditions are complied with, which occurs only at higher pressures. Thus, a universal model is needed to describe the fluid dynamics of the falling film.

6.4 Parabolic Velocity Profile

With the objective of developing a calculation model which can describe the fluid dynamics in the falling film better than the two former calculation models do, the parabolic profile in the film phase is observed more closely. In Fig. 6-3 (left) the possible parabolic profile of the film velocity can be seen. For the sake of completeness, two parabolic profiles with opposite algebraic signs are given.

6.4 Parabolic Velocity Profile

As has been explained before, the film flows down the vertical surface, driven by the gravitational force. This is described in the first part of the parabolic profile (see Fig. 6-3, left). When the continuous phase flows countercurrently, the second part where film flows oppositely to the gravitation exists. This means that the film does not flow downwards. A part of the film phase will be carried away by the countercurrent flow of the continuous phase. Since there is no countercurrent flow of the continuous phase in this work, the possibility of the second parabolic profile with a minus sign (positive sign of the velocity shows in the direction of the acceleration due to gravitation) can be ignored and the whole attention can be given to the first parabola, such as shown in Fig. 6-3 (right).

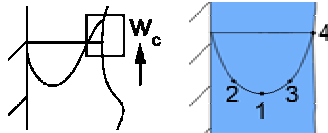


Figure 6-3: Possible parabolic velocity profile in the film phase. With (left) and without (right) countercurrent flow of continuous phase.

There are four possibilities for the form of the parabolic velocity profile in the film phase. They are numbered in Fig. 6-3 (right) consecutively from 1 to 4. It is assumed that the falling film has a thickness of δ_f . The four possible velocity profiles in the film phase δ_f are as follows (compare with the parabolic profile in the second column of Tab. 6-1 on page 92):

- Position 1: at the film surface, the maximum of the parabola or the maximum velocity is reached and thus, the tangent of the velocity on the surface is equal to zero. This is the Nusselt model.
- Position 2: at the film surface the highest velocity in the whole film phase is reached. But this is not the maximum of the parabola. The velocity increases steadily from the wall to the film surface but the vertex of the parabola has not been reached yet. This film behaviour is conceivable when for instance the continuous phase flows cocurrently. Since in this work the continuous phase does not flow at all, this possibility need not be considered (a solid mathematical explanation is given later).
- Position 3: at the film surface, a finite velocity is reached. The parabola reaches its vertex somewhere inside the film. The curve turns back and the velocity becomes smaller consistently until it reaches the film surface. This is possible when the shear stress exerted by the continuous phase is large enough to force the film slowing down its velocity.
- Position 4: the velocity at the film surface is equal to zero. The complete parabola is created in the film phase. This can occur when the continuous phase flows countercurrently and the velocity of the continuous phase is just sufficient to stop the film or when the shear stress exerted by the static continuous phase is large enough to brake the film and stops it exactly at the surface. This is the profile of the wall model.

In order to give a solid mathematical ground about which of the four possibilities describes the reality best, the parabolic equation

$$w(y) = -\frac{\beta_f}{2} \cdot y^2 + c_1 \cdot y + c_0 \quad (6-12)$$

is solved. In each single case, the no-slip boundary condition is employed. This is used as the first boundary condition and delivers the constant

$$c_0 = 0. \quad (6-13)$$

For position 1, the velocity ends at the vertex of the parabola

$$\left(\frac{dw}{dy} \right)_{y=\delta_f} = 0 \quad (6-14)$$

whereas positions 2 and 3 are caused by any arbitrary shear stress with positive and negative signs respectively. The positive sign means the velocity at the film surface is accelerated by this shear stress due to the fact that the shear stress acts in the same direction as the film flow. On the contrary, the negative sign shows that the film is decelerated. By means of the shear stress equation for Newtonian fluid, a second boundary condition for position 2 and 3 can be written

$$\left(\frac{dw}{dy} \right)_{y=\delta_f} = \pm \frac{\tau}{\eta_f}. \quad (6-15)$$

The magnitude of the shear stress τ in Eq. 6-15 is still unknown.

For the last one, position 4, the velocity at the film surface is equal to zero, such as is given in Eq. 6-10.

By means of these boundary conditions, the parabolic velocity profile in Eq. 6-12 can be solved. The results are given in Table 6-1. The figures of the parabolic velocity profile are also shown there. For comparison purposes, the same film thickness δ_f for every velocity profile is assumed. Due to the direction of the shear stress, position 2 is also called τ^+ model and position 3 is called as τ^- model. The same magnitude of the shear stress in τ^+ and τ^- model is assumed. The shear stress is finite but still unknown, whereas for the wall model, the shear stress can be estimated by means of Eq. 6-4 if the velocity equation is known.

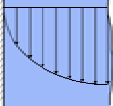
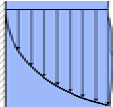
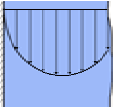
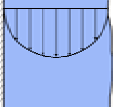
The mean velocity can be used to compare the models with each other. The velocity is averaged over its thickness

$$\bar{w} = \frac{1}{\delta_f} \int_0^{\delta_f} w(y) dy \quad (6-16)$$

using the velocity equations given in Table 6-1.

6.4 Parabolic Velocity Profile

Table 6-1: Possible parabolic velocity profile in the film phase with a thickness of δ_f . The film thickness can be obtained experimentally. The magnitude of the shear stress τ for τ^+ and τ^- model is still unknown.

Nr.	Parabolic profile	Shear stress	Boundary conditions	Velocity equation
1	Nusselt 	0	$w(y=0) = 0$ $\left. \frac{dw}{dy} \right _{y=\delta_f} = 0$	$w(y) = \beta_f \left(-\frac{y^2}{2} + \delta_f y \right)$
2	τ^+ 	finite	$w(y=0) = 0$ $\left. \frac{dw}{dy} \right _{y=\delta_f} = +\frac{\tau}{\eta_f}$	$w(y) = \beta_f \left(-\frac{y^2}{2} + \delta_f y \right) + \frac{\tau}{\eta_f} y$
3	τ^- 	finite	$w(y=0) = 0$ $\left. \frac{dw}{dy} \right _{y=\delta_f} = -\frac{\tau}{\eta_f}$	$w(y) = \beta_f \left(-\frac{y^2}{2} + \delta_f y \right) - \frac{\tau}{\eta_f} y$
4	Wall 	$\tau = \frac{\beta_f \eta_f}{2} \delta_f$	$w(y=0) = 0$ $w(y=\delta_f) = 0$	$w(y) = \beta_f \left(-\frac{y^2}{2} + \frac{\delta_f}{2} y \right)$

The mean velocity calculated according to Eq. 6-16 can be seen in Table 6-2. A direct comparison of the models regarding their mean velocity can be achieved. As it might have been expected, the mean velocity according to Nusselt is larger than the one according to the wall model. The mean velocity of the Nusselt model is four times as large as the one calculated according to the wall model. The mean velocity of the τ^+ model is larger than Nusselt, but the value of τ^- model is lower than Nusselt. The difference depends on the magnitude of the shear stress τ , which is still unknown. Going back to Fig. 6-2, only τ^- model applies to describe the fluid dynamics under high pressure conditions. On the contrary to τ^+ model, using this one, the mean velocity lies exactly between both extreme cases, the wall and the Nusselt model. When the shear stress is zero, the τ^- model is equal to the Nusselt model, whereas when the shear

stress is sufficiently large, the τ^- model describes exactly what the wall model expresses. For further discussion, the τ^+ model does not play any important role and thus, the τ^- model is referred to simply as the tau model.

Table 6-2: Mean, maximum and film surface velocity according to the Nusselt, the τ^+ , the τ^- and the wall model.

Parabolic profile	Velocity		
	Mean	Max.	Surface
Nusselt 	$\bar{w} = \frac{\beta_f}{3} \delta_f^2$	$w_{\max} = \frac{\beta_f}{2} \delta_f^2$ at $y = \delta_f$	$w_0 = \frac{\beta_f}{2} \delta_f^2$
τ^+ 	$\bar{w} = \frac{\beta_f}{3} \delta_f^2 + \frac{\tau}{2\eta_f} \delta_f$	$w_{\max} = \frac{\beta_f}{2} \delta_f^2 + \frac{\tau}{\eta_f} \left(\frac{\tau}{2\beta_f \eta_f} + \delta_f \right)$ at $y = \delta_f + \frac{\tau}{\beta_f \eta_f}$	$w_0 = \frac{\beta_f}{2} \delta_f^2 + \frac{\tau}{\eta_f} \delta_f$
τ^- 	$\bar{w} = \frac{\beta_f}{3} \delta_f^2 - \frac{\tau}{2\eta_f} \delta_f$	$w_{\max} = \frac{\beta_f}{2} \delta_f^2 + \frac{\tau}{\eta_f} \left(\frac{\tau}{2\beta_f \eta_f} - \delta_f \right)$ at $y = \delta_f - \frac{\tau}{\beta_f \eta_f}$	$w_0 = \frac{\beta_f}{2} \delta_f^2 - \frac{\tau}{\eta_f} \delta_f$
Wall 	$\bar{w} = \frac{\beta_f}{12} \delta_f^2$	$w_{\max} = \frac{\beta_f}{8} \delta_f^2$ at $y = \frac{\delta_f}{2}$	$w_0 = 0$

For the sake of completeness, the maximum and the surface velocity are also estimated. The maximum velocity is calculated according to Eq. 6-14. In Table 6-2 the position at which this maximum is reached is also given.

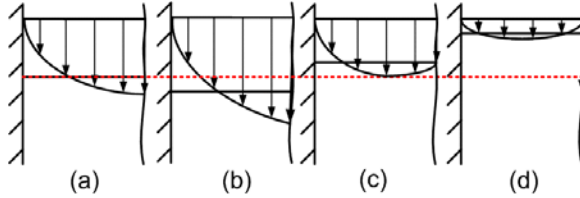


Figure 6-4: Possible velocity profiles in a film phase whose thickness δ_f is.

In Fig. 6-4 the different velocity profiles in the film phase with the thickness δ_f are shown. The mean velocity in each film phase is given as a horizontal line. The horizontal dashed line crossing the four film phases shows the Nusselt mean velocity which is used here as a reference. A direct comparison of the surface velocities can also be performed qualitatively.

6.5 Tau Model

In this section the tau model, which describes the fluid dynamics generally, will be presented. First of all, the tau model will be explained for a wetting angle up to 90° . To solve the problem with and without the wall contact—in case where the wetting angle is larger than 90° —an explanation is given in the last part of this section.

6.5.1 Wetting Angle up to 90°

The velocity equation according to the tau model (or previously referred to as τ model) with the applied boundary conditions (Eq. 6-6 and 6-15) is as follows

$$w(y) = -\frac{\beta_f}{2}y^2 + \left(\beta_f \delta_f - \frac{\tau}{\eta_f} \right)y. \tag{6-17}$$

The velocity profile as given in Eq. 6-17, where the shear stress between the phases at the surface is taken into account, had been considered by Nusselt. He extended the original model by including the influence of the fluid or vapour flow along the condensate film on the velocity profile in the film phase. He estimated the shear stress at the film surface by assuming the equality of the frictional and the pressure forces. In the calculation, he used the flow in a tube to solve the problem.

In this work, there is not flow of the continuous phase, which surrounds the film phase. The magnitude of the shear stress is calculated in another way, by assuming the existence of a velocity boundary layer.

Eq. 6-17 is derived from a one-dimensional force balance as shown in Fig. 6-1. The shear stress τ is calculated by means of the velocity gradient $\frac{\partial w}{\partial y}$ which is perpendicular to the film flow direction (see Fig. 6-5 arrow A). Observing the falling film two dimensionally, the cross-section has a circular-segment shape (see Fig. 5-8c). As a result, the velocity gradient necessary for the calculation of the shear stress τ is actually no longer proportional to $\frac{\partial w}{\partial y}$. It is the velocity gradient perpendicular to the curved-interface which should be taken into account (see Fig. 6-5 arrow B). However, from mathematical point of view, it is very complicated to consider the velocity gradient normal to the curved-interface. Therefore, the velocity gradient $\frac{\partial w}{\partial y}$ perpendicular to the film flow direction (Fig. 6-5 arrow A) should be regarded sufficient in calculating the shear stress.

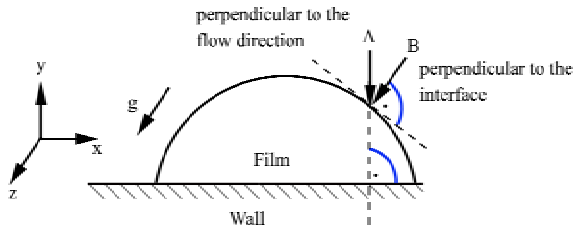


Figure 6-5: The direction of the velocity gradient used in calculating the shear stress.

In Eq. 6-17 the material properties in β_f , which contains the density of both phases and the dynamic viscosity of the film phase η_f , are known or can be measured. The film thickness δ_f can be measured as well. The only unknown in Eq. 6-17 is the magnitude of the shear stress τ .

Up to now attention has been given only to the film phase. If a finite shear stress exerted by the continuous phase is considered, this phase should also be taken into account and linked with the film phase to express the interaction between them.

The force balance between the gravitational force and the force resulted from the shear stress on a finite volume element in the continuous phase can be written as follows:

$$\rho_c g dy_c = \frac{\partial \tau_c}{\partial y_c} dy_c \quad (6-18)$$

the index c stands for the continuous phase. Making use of the shear stress relation of Newtonian fluid such as given in Eq. 6-4, Eq. 6-18 can be rewritten

$$\frac{\partial^2 w_c}{\partial y_c^2} = \frac{\rho_c g}{\eta_c} = \beta_c \quad (6-19)$$

where the ratio of the continuous phase properties ρ_c and η_c multiplied by the gravitational acceleration constant g are combined in one term called β_c . The second order velocity differential equation in 6-19 indicates the existence of a velocity boundary layer between both phases.

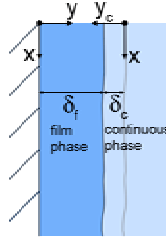


Figure 6-6: Film phase and continuous phase, with a velocity boundary layer, whose thickness δ_c is.

From the point of view of macromolecules, the continuous phase does not flow at all. In the vicinity of the film surface, molecules in the continuous phase are carried away by the flow of the film phase and in this way, the velocity boundary layer arises. The second order differential equation in 6-19 refers to the flow in this velocity boundary layer. The velocity in the boundary layer is maximum in the vicinity of the film surface where the molecules touch the film phase. The larger the distance from the film surface is, the lower is the velocity in this boundary layer. The thickness of the boundary layer is δ_c . Its magnitude is still unknown. At the distance δ_c from the film surface, the velocity reaches zero. Here the velocity boundary layer ends and from this point on, the velocity in the continuous phase is zero. For the sake of equation simplicity and convenience, a new axis y_c is defined. This axis has its initial at δ_c away from the film surface, such as seen in Fig. 6-6.

To solve Eq. 6-19 two boundary conditions are required, but only one is available at this moment

$$w_c(y_c = 0) = 0 \quad (6-20)$$

the velocity boundary layer ends at δ_c away from the film surface or the velocity is equal to zero at the initial point of the y_c axis. Integrating Eq. 6-19 twice and using the boundary condition in Eq. 6-20 results

$$w_c(y_c) = \frac{\beta_c}{2} y_c^2 + c_{1c} y_c \quad (6-21)$$

In equation 6-21 c_{1c} is still unknown. To solve both equations, the velocity equation in the film (Eq. 6-17) as well as in the continuous phase (Eq. 6-21), two boundary conditions are needed.

The velocity at the film surface w_0 has to be the same, whether it is approached from the film or the continuous phase. This is the first boundary condition

$$w_c(y_c = \delta_c) = w(y = \delta_f) = w_0. \quad (6-22)$$

The velocity at the film surface, approached from the continuous phase at $y_c = \delta_c$ can be calculated with help of Eq. 6-21 whereas from the film phase, this velocity can be calculated by means of Eq. 6-17. From Eq. 6-22

$$\tau = \frac{1}{2}\beta_f \delta_f \eta_f - \frac{1}{2}\beta_c \frac{\delta_c^2}{\delta_f} \eta_f - c_{1c} \frac{\delta_c}{\delta_f} \eta_f \quad (6-23)$$

or in term of c_{1c}

$$c_{1c} = \frac{1}{2}\beta_f \frac{\delta_f^2}{\delta_c} \frac{\tau}{\eta_f} - \frac{1}{2}\beta_c \delta_c. \quad (6-24)$$

In Eq. 6-24 the magnitude of δ_c and τ are still unknown.

At the film surface, the shear stress felt by the film phase is equal to that felt by the continuous phase. This complies with the Newton third law of reciprocal actions (for every action force there is an equal, but opposite, reaction force). This is the second boundary condition

$$\tau(y = \delta_f) = \tau_c(y_c = \delta_c). \quad (6-25)$$

The shear stress felt by the continuous phase τ_c can be estimated by differentiating Eq. 6-21 combined with the shear stress correlation for Newtonian fluid in 6-4. Putting the calculation result of this step equals the film phase shear stress (according to Eq. 6-25) gives

$$\tau = \beta_c \delta_c \eta_c + c_{1c} \eta_c \quad (6-26)$$

and solving Eq. 6-26 for c_{1c}

$$c_{1c} = \frac{\tau}{\eta_c} - \beta_c \delta_c. \quad (6-27)$$

Combining Eq. 6-24 with Eq. 6-27 gives

$$\tau = \frac{\eta_c \eta_f (\beta_c \delta_c^2 + \beta_f \delta_f^2)}{2(\delta_c \eta_f + \delta_f \eta_c)}. \quad (6-28)$$

If the magnitude of δ_c is known, Eq. 6-28 can be solved. In order to find this value, the geometrical consideration of the parabolic velocity profile in the film phase is made. As explained previously, the parabolic velocity profile reaches its vertex inside the film phase and is turning back as it reaches the film surface. At the film surface, the film velocity is finite but is not necessarily equal to zero as suggested in the wall model.

As mentioned before, the thickness of the velocity boundary layer is δ_c away from the film surface and from this point on, the velocity is equal to zero. With the aim of finding the value of δ_c , the film surface is moved theoretically towards the continuous phase so far, that at the new position, the film velocity at the surface is zero. Later, the distance between the real and the theoretically moved film surface $\Delta\delta$ is correlated with the thickness of the velocity boundary layer δ_c .

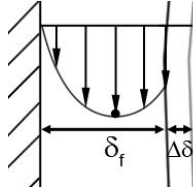


Figure 6-7: Velocity profile in the film phase δ_f according to the tau model. $\Delta\delta$ is the additional distance required to δ_f to obtain a complete parabola.

Mathematically, the distance between the real position of the film surface and the moved one to gain a complete velocity parabola is

$$\Delta\delta = 2y \Big|_{\frac{\partial w}{\partial y}=0} - \delta_f. \quad (6-29)$$

This is the distance gained when from the width of the whole parabola the film thickness δ_f is subtracted. The width of the whole parabola can be estimated by doubling the width of half of the parabola where the maximum is reached, such as is seen in Eq. 6-29.

Differentiating the velocity equation in 6-17 with respect to the y-axis and setting this equal to zero, the position of the vertex is found

$$y \Big|_{\frac{\partial w}{\partial y}=0} = \delta_f - \frac{\tau}{\beta_f \eta_f}. \quad (6-30)$$

The expression on the right hand side of Eq. 6-28 is used to substitute the shear stress term in Eq. 6-30. Due to the fact, that here, one deals with $\Delta\delta$ instead of δ_c , all terms in δ_c in Eq. 6-30 have to be replaced by $\Delta\delta$. Thus the position of the parabola vertex can be rewritten

$$y \Big|_{\frac{\partial w}{\partial y}=0} = \frac{\beta_f \delta_f^2 \eta_c + 2 \beta_f \delta_f \Delta\delta \eta_f - \beta_c \Delta\delta^2 \eta_c}{2 \beta_f (\delta_f \eta_c + \Delta\delta \eta_f)} \quad (6-31)$$

and putting this expression into Eq. 6-29, the magnitude of $\Delta\delta$ is found

$$\Delta\delta = \frac{\beta_f \delta_f (\eta_f - \eta_c)}{(\beta_c \eta_c + \beta_f \eta_f)}. \quad (6-32)$$

If a linearization of both parabolic velocity profiles in the boundary layer is allowed, the following correlation between $\Delta\delta$ and δ_c applies

$$\delta_c = \frac{\eta_c}{\eta_f} \Delta\delta \quad (6-33)$$

(for linearization details, please see Chapter 6.5.2). The thickness of the velocity boundary layer δ_c is proportional to $\Delta\delta$ and the proportionality constant is the ratio of the dynamic viscosities of both phases. Putting the expression of $\Delta\delta$ in Eq. 6-32 into Eq. 6-33 yields the thickness of velocity boundary layer

$$\delta_c = \frac{\eta_c}{\eta_f} \frac{\beta_f \delta_f (\eta_f - \eta_c)}{(\beta_c \eta_c + \beta_f \eta_f)}. \quad (6-34)$$

Knowing the magnitude of δ_c , Eq. 6-28 can be solved

$$\tau = \Phi \delta_f \quad (6-35)$$

with $\Phi = f(\beta_c, \beta_f, \eta_c, \eta_f)$ and can be estimated by

$$\Phi = \frac{\beta_f}{2\eta_f(\beta_c \eta_c + \beta_f \eta_f)}. \quad (6-36)$$

$$\frac{\beta_c \beta_f (\eta_c^2 \eta_f^2 - 2\eta_c^3 \eta_f + \eta_c^4 + 2\eta_c \eta_f^3) + \eta_f^2 (\beta_c^2 \eta_c^2 + \beta_f^2 \eta_f^2)}{2\beta_f \eta_f - \beta_f \eta_c + \beta_c \eta_c}$$

The shear stress is proportional to the film thickness, the proportionality constant is Φ . The parameter Φ considers the material properties of both phases and can be said to be the parameter which links the continuous phase with the film phase.

Hence, it is clear to be seen how the wetting properties are connected to the fluid dynamics. The film thickness which depends on the mass flow rate and the wetting properties, is brought into correlation with the shear stress of the film at its surface (see eq. 6-35). The shear stress determines, in turn, the fluid dynamics.

Now, the velocity equation according to tau model can be written as follows

$$w(y) = -\frac{\beta_f}{2} y^2 + \left(\beta_f - \frac{\Phi}{\eta_f} \right) \delta_f y. \quad (6-37)$$

The magnitude of the parameter Φ for the system water – carbon dioxide at 313 K can be seen in Fig. 6-8. In the investigated pressure range, the value of Φ varies between 0.5 and 2.5. The fall in Φ is caused mainly by the drop in the density difference between the phases when pressure increases. The pressure change does not affect the viscosity of the film phase in the system of water - carbon dioxide appreciably. If water is presaturated by carbon dioxide, the film phase density increases slightly [185] which causes a slight rise in the density difference too. The viscosity of the film phase does not change appreciably when it is presaturated by carbon dioxide [131]. The correction in the value of Φ caused by the presaturation of carbon dioxide can be seen in Fig. 6-8.

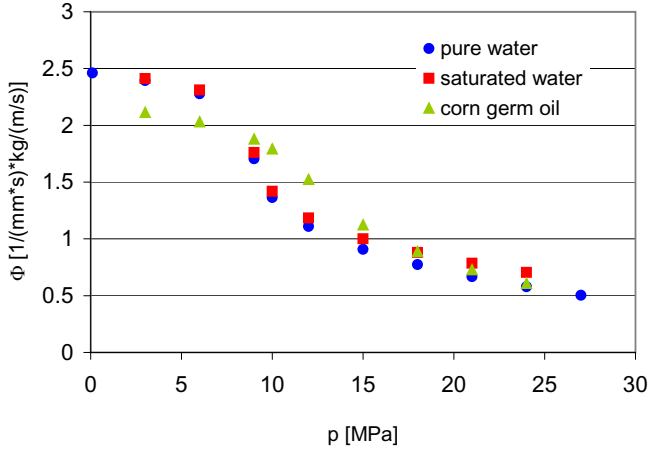


Figure 6-8: The magnitude of the parameter Φ for the system: water - carbon dioxide at 313 K and corn germ oil - carbon dioxide at 333 K.

In the same diagram, the magnitude of the parameter Φ for the system corn germ oil and carbon dioxide at 333 K is given (corn germ oil is presaturated with carbon dioxide). The material properties for corn germ oil are taken from the literature [92,185]. The parameter Φ for this system is calculated at 333 K, but due to the lack of data, the viscosity values at 338 K are applied here. As can be seen in Fig. 6-8, the values of Φ for the system corn germ oil-carbon dioxide lie in the same order of magnitude as the water-carbon dioxide system. In contrast to water, at the temperature investigated, the dynamic viscosity of corn germ oil at 24 MPa is just one fourth of the viscosity at 3 MPa. Despite this radical fall of the oil viscosity, the Φ value is not affected significantly.

6.5.2 Linearization of the Velocity Profiles

Equation 6-33 on page 98 shows the correlation between the thickness of the real velocity boundary layer δ_c and the width $\Delta\delta$. This is the result of the linearization of the parabolic velocity profiles in the velocity boundary layer. In this chapter, this linearization will be proved with the help of the assumptions made in the tau model.

According to the assumption that the shear stress at the film surface has the same magnitude, whether it is seen from the continuous or the film phase, the following equation is valid

$$\eta_f \left(\frac{\partial w}{\partial y} \right)_f = \eta_c \left(\frac{\partial w}{\partial y} \right)_c. \quad (6-38)$$

From this it follows that the ratio of the gradients of the film phase and the continuous phase velocity at the surface is equal to the ratio of the viscosities in both phases

$$\frac{\left(\frac{\partial w}{\partial y}\right)_f}{\left(\frac{\partial w}{\partial y}\right)_c} = \frac{\eta_c}{\eta_f} \quad (6-39)$$

In Fig. 6-9 the linearization of the film phase and the continuous phase profile is shown. The value $\Delta\delta_{\text{par}}$ is the width needed by the film phase to reach a velocity equal to zero at the film surface when the velocity profile remains parabolic. If the velocity profile is linearized, the distance needed is equal to $\Delta\delta_{\text{line}}$. The same logic applies for the continuous phase velocity profile. The width needed when the velocity profile is a parabolic one, is $\delta_{c, \text{par}}$, whereas through a linearization it becomes $\delta_{c, \text{line}}$.

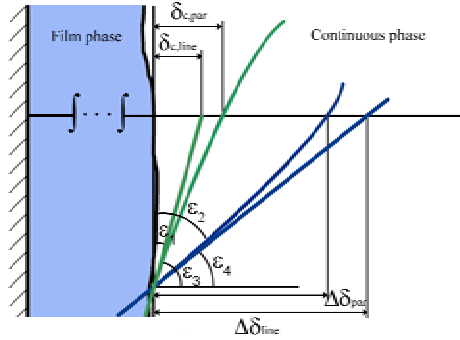


Figure 6-9: Linearization of the parabolic velocity profiles of the film $\Delta\delta$ and the continuous phase δ_c in the velocity boundary layer.

The angle between the linearized velocity profile $\delta_{c, \text{line}}$ and the vertical line is ε_1 with

$$\tan \varepsilon_1 = \frac{\delta_{c, \text{line}}}{w_0} \quad (6-40)$$

The complementary angle of ε_1 is ε_3 with

$$\tan \varepsilon_3 = \frac{1}{\tan \varepsilon_1} = \frac{w_0}{\delta_{c, \text{line}}} \quad (6-41)$$

The value of $\tan \varepsilon_3$ shows the gradient of the continuous phase velocity profile at the film surface

$$\tan \varepsilon_3 = \left. \left(\frac{\partial w_c}{\partial y_c} \right) \right|_{y_c = \delta_c} \quad (6-42)$$

The same applies for the film phase

$$\tan \varepsilon_2 = \frac{\Delta \delta_{line}}{w_0} \quad (6-43)$$

which is the complementary angle of ε_4

$$\tan \varepsilon_4 = \frac{1}{\tan \varepsilon_2} = \frac{w_0}{\Delta \delta_{line}}. \quad (6-44)$$

The gradient of the film phase velocity profile at the surface can be given in terms of $\tan \varepsilon_4$

$$\tan \varepsilon_4 = \left(\frac{\partial w}{\partial y} \right) \Big|_{y=\delta_f}. \quad (6-45)$$

The ratio of the film and continuous phase velocity gradient at the film surface according to Eq. 6-41 and 6-44 can be given in terms of the width ratio

$$\frac{\tan \varepsilon_3}{\tan \varepsilon_4} = \frac{\Delta \delta_{line}}{\delta_{c,line}}. \quad (6-46)$$

or in terms of the velocity gradient ratio according to Eq. 6-42 and 6-45, which in turn, represents the viscosity ratio of both phases, such as given in Eq. 6-39

$$\frac{\tan \varepsilon_3}{\tan \varepsilon_4} = \frac{\eta_f}{\eta_c}. \quad (6-47)$$

Upon employing Eq. 6-46 and Eq. 6-47 the ratio of the linearized width of $\delta_{c,line}$ and $\Delta \delta_{line}$ can be expressed in terms of the viscosity ratio of both phases

$$\frac{\delta_{c,line}}{\Delta \delta_{line}} = \frac{\eta_c}{\eta_f}. \quad (6-48)$$

If the difference between the linearized width and the parabolic one is negligible

$$\left| \delta_{c,line} - \delta_{c,par} \right| \rightarrow 0 \quad (6-49)$$

and

$$\left| \Delta \delta_{line} - \Delta \delta_{par} \right| \rightarrow 0 \quad (6-50)$$

Eq. 6-48 can be rewritten in terms of parabolic profiles (par) or in the initial symbols without any indices

$$\frac{\delta_c}{\Delta \delta} = \frac{\eta_c}{\eta_f}. \quad (6-51)$$

Hereby the correlation in Eq. 6-33 on page 98 is mathematically proved.

6.5.3 Wetting Angle above 90°

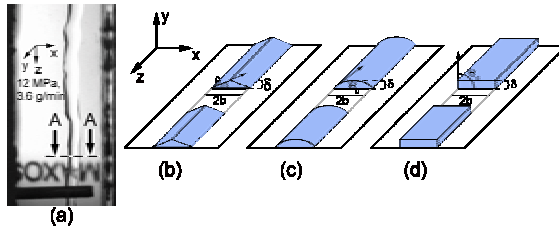


Figure 6-10: Possible film cross-section shapes.

In Fig. 6-10, three idealistic cross-section shapes are shown if the rivulet is cut perpendicular to its flow direction. By means of the measured rivulet width and the projection of its maximum thickness, a rectangle can be reconstructed (see Fig. 5-8 c). The real shape of the rivulet cross-section exists inside this rectangle. The smallest possible cross-sectional area has the shape of a triangle (Fig. 6-10 b), whereas the largest possible cross-section fills the whole bordered rectangular area given (Fig. 6-10 d). These shapes are two extreme cases. In reality, the cross-section is probably neither a triangle nor a rectangle. A circular shape such as shown in Fig. 6-10 c might best be used to describe the geometry of the cross-section. If the last one is assumed as the shape of the rivulet cross-section, two wetting cases regarding the fluid dynamics have to be distinguished, wetting with an angle smaller and larger than 90° . The fluid dynamics for the wetting with angle lower than or equal to 90° is discussed in 6.5.1. In this section, the fluid dynamics for the wetting with angles larger than 90° will be explained.

Symmetric Boundary Conditions

In Fig. 6-11 the circular cross-section of a rivulet which wets the vertical surface (x -axis) with an angle θ_0 larger than 90° is shown. When discussing the velocity profile, attention is focused only on one half of the whole rivulet cross-section $ABDG$ because the velocity profile is symmetrical with respect to the middle line AG .

In the area $ABFG$, the film phase has a direct contact with the vertical wall AB . On the contrary, the liquid in the area $BCDEF$ ($-\alpha_0 \leq \alpha < \alpha_0$) does not have direct contact with the wall. The liquid floats in the continuous phase, held firmly by the molecules of the film phase at the line BF . This floating is shown in Fig. 6-11 (right), where the side projection of the liquid slice CE is shown.

In the first part, the area $ABFG$, the initial tau model can be applied. In the second part where direct wall contact does not exist, the validity of the tau model with the no-slip boundary condition on the wall should be reexamined.

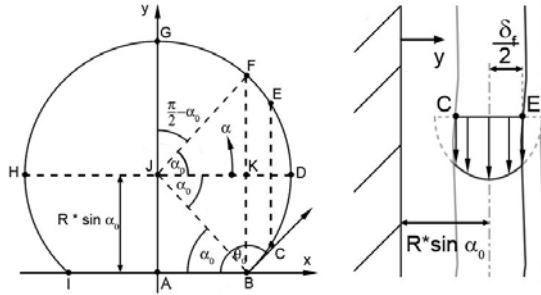


Figure 6-11: Film cross-section (left) and symmetric conditions (right) for wetting angle $\theta_0 > 90^\circ$.

In this section, symmetric boundary conditions used to describe the velocity profile in the area BCDEF will be introduced. For this purpose, the parabolic velocity equation with two unknowns such as given in Eq. 6-52

$$w(y) = -\frac{\beta_f}{2} y^2 + c_1 y + c_0 \quad (6-52)$$

is solved using a symmetric condition

$$\left. \frac{\partial w}{\partial y} \right|_{y=R \sin \alpha_0} = 0. \quad (6-53)$$

Due to the fact, that the liquid along the whole curvature BCDEF encounters the same carbon dioxide, the shear stress exerted by the continuous phase across the borderline DF has to be the same as that felt by the liquid across the arc BD. And that is why the velocity profile should be symmetrical with respect to the line DJ (see Fig. 6-11 right). This is expressed in the first boundary condition given in Eq. 6-53, in which it is stated that the parabolic velocity equation reaches its vertex at $y= R \sin \alpha_0$, which is also the position of the line DJ. The angle α_0 is the value gained if the right angle is subtracted from the rivulet-wetting angle θ_0 .

Differentiating the velocity equation in 6-52 and setting the tangent at $y= R \sin \alpha_0$ equals zero yields

$$c_1 = \beta_f R \sin \alpha_0. \quad (6-54)$$

Actually the main focus is not only to find an expression for the velocity equation in the second area, BCDEF, but also to link the velocity equations in a manner, in which the transition from one area to the next occurs smoothly. The second boundary condition which achieved the connection-function is given by

$$w_{F^-} = w_{F^+}. \quad (6-55)$$

This boundary condition assures that at point F, where the transition occurs, the velocity approached from the left hand side (minus sign) is the same as that approached from the right hand side (plus sign) of point F. The position of this point is

$$y = \delta_f = 2R \sin \alpha_0. \quad (6-56)$$

Upon employing Eq. 6-37 and Eq. 6-56

$$w(y_{F^-} = 2R \sin \alpha_0) = 2\beta_f R^2 \sin^2 \alpha_0 - 4R^2 \sin^2 \alpha_0 \frac{\Phi}{\eta_f} \quad (6-57)$$

and Eq. 6-52 for w_{F^+} ,

$$w(y_{F^+} = 2R \sin \alpha_0) = c_0 \quad (6-58)$$

the magnitude of c_0 can be written

$$c_0 = 2R^2 \sin^2 \alpha_0 \left(\beta_f - \frac{2\Phi}{\eta_f} \right). \quad (6-59)$$

By substituting c_0 (Eq. 6-59) and c_1 (Eq. 6-54) into Eq. 6-52

$$w(y) = -\frac{\beta_f}{2} y^2 + \beta_f R \sin \alpha_0 y + 2R^2 \sin^2 \alpha_0 \left(\beta_f - \frac{2\Phi}{\eta_f} \right) \quad (6-60)$$

the velocity equation in the area without any wall contact is introduced.

In order to discover how smooth the transition at line BF is, the discrepancy at this position is estimated by means of the Eq. 6-37 and Eq. 6-60

$$\Delta w(y) = w_{(BF)^-} - w_{(BF)^+} \quad (6-61)$$

the velocity jump at line BF depends on the position of y and the film thickness δ_f

$$\Delta w(y) = \left(\frac{\beta_f}{2} - \frac{\Phi}{\eta_f} \right) \delta_f y - \left(\frac{\beta_f}{2} - \frac{\Phi}{\eta_f} \right) \delta_f^2 \quad (6-62)$$

the magnitude of the film thickness δ_f at

$$x = R \cos \alpha_0 \quad (6-63)$$

is given in Eq. 6-56. The greatest velocity jump occurs at $y=0$

$$\Delta w_{\max}(y=0) = -\left(\frac{\beta_f}{2} - \frac{\Phi}{\eta_f} \right) \delta_f^2 \quad (6-64)$$

and the smoothest transition can be found at point F

$$\Delta w_{\min}(y = \delta_f = 2R \sin \alpha_0) = 0 \quad (6-65)$$

where the discrepancy is equal to zero.

Despite the attempt made in the second boundary condition (Eq. 6-55), there is still a velocity jump at line BF. The visualization and the magnitude of the velocity discrepancy can be found in 7.1.2.

Continuity Boundary Conditions

The second boundary condition set which solves Eq. 6-52 and at the same time links both areas is called the continuity boundary condition. To reach a smooth transition, not only is the velocity at point F from the left hand side (F⁻) equals that approached from the right hand side (F⁺)

$$w_{F^-} = w_{F^+} \quad (6-66)$$

but the shear stresses calculated from both sides are also equal

$$\tau_{F^-} = \tau_{F^+} \quad (6-67)$$

The velocity approached from the right hand side according to Eq.6-52 is

$$w_{F^+} = -2\beta_f R^2 \sin^2 \alpha_0 + 2R \sin \alpha_0 c_1 + c_0 \quad (6-68)$$

setting Eq. 6-68 equals the velocity at point F⁻ given in Eq. (6-57) leads to

$$c_0 = 4R^2 \sin^2 \alpha_0 \left(\beta_f - \frac{\Phi}{\eta_f} \right) - 2R \sin \alpha_0 c_1 \quad (6-69)$$

The expression for c_0 in Eq. 6-69 still contains c_1 which can be determined with the help of the second boundary condition at point F⁺

$$\tau_{F^+} = -\eta_f \left(-2R \sin \alpha_0 \beta_f + c_1 \right) \quad (6-70)$$

and F⁻

$$\tau_{F^-} = 2R \sin \alpha_0 \Phi \quad (6-71)$$

respectively.

Upon relating Eq. 6-70 and Eq.6-71, and solving it for c_1

$$c_1 = 2R \sin \alpha_0 \left(\beta_f - \frac{\Phi}{\eta_f} \right) \quad (6-72)$$

The value c_0 is thus

$$c_0 = 4R^2 \sin^2 \alpha_0 \left(\beta_f - \frac{\Phi}{\eta_f} \right) - (2R \sin \alpha_0)^2 \left(\beta_f - \frac{\Phi}{\eta_f} \right) \quad (6-73)$$

The velocity equation using continuity conditions is

$$w(y) = -\frac{\beta_f}{2} y^2 + \left(\beta_f - \frac{\Phi}{\eta_f} \right) 2R \sin \alpha_0 y \quad (6-74)$$

As has been done before, the velocity discrepancy at the line BF can be given according to Eq. 6-61 in order to find out whether the transition from the first to the second area happens smoothly

$$\Delta w(y) = \left(\beta_f - \frac{\Phi}{\eta_f} \right) (\delta_f - 2R \sin \alpha_0) y \quad (6-75)$$

The film thickness at point F is $2R \sin \alpha_0$ (Eq. 6-56) so that Δw in Eq. 6-75 is equal to zero. The applicability of this boundary condition set can be decided best by visualizing the velocity profile in the film phase and taking a careful look at the transition border BF.

Near-Wall Boundary Conditions

Although the velocity discrepancy at the border BF is equal to zero when the continuity conditions set is applied, which is a good sign that the boundary conditions are suitable to be used, a third boundary condition set will be explained here. In the symmetric boundary conditions, it is assumed that the liquid at the film surface along the borderline DF feels the same shear stress as it is felt by the liquid on BD due to the fact that the same continuous phase comes into touch with this liquid. As a result, the velocity profile is symmetric with respect to the middle line DJ. In contrast to this boundary condition set, here, using the near-wall boundary condition set, it is assumed that the shear stress exerted on the liquid along the borderline DF is not exactly the same as is felt by the liquid along the arc BD. This is caused by the wall existence which brakes the flow of the film phase in its vicinity. Even though in the area BCDEF there is no direct wall contact, the deceleration by the wall has an impact on the liquid flow in the vicinity of point B. Whereas on the opposite side, point F, there is no deceleration caused by the wall which needs to be taken into account. Therefore, attention should be paid to point B instead of point F. The first boundary condition is that the velocity on the right hand side of point B (B^+) is the same as that on the left hand side (B^-)

$$w_{B^+} = w_{B^-} \quad (6-76)$$

Due to the no-slip condition, the velocity at B^- is

$$w_{B^-} = 0 \quad (6-77)$$

and hereby, the constant c_0 in the parabolic velocity equation (6-52) is

$$c_0 = 0. \quad (6-78)$$

The shear stress along the borderline BF is the same, whether it is approached from the left or the right hand side

$$\tau_{(BF)^+} = \tau_{(BF)^-} \quad (6-79)$$

The shear stress on the left hand side of the borderline BF is

$$\tau_{(BF)^-} = (\pm) \eta_f \left(-\beta_f y + \left(\beta_f - \frac{\Phi}{\eta_f} \right) h(x) \right) \quad (6-80)$$

and on the right hand side

$$\tau_{(BF)^+} = (\pm) \eta_f (-\beta_f y + c_1). \quad (6-81)$$

The plus and minus signs in front of the right hand terms in Eq. 6-81 and 6-82 show the sign of the velocity gradient with respect to the y-axis. They are there to assure that the calculated shear stress is positive. Upon employing Eq. 6-81 and 6-82, and solving the equation for c_1

$$c_1 = \left(\beta_f - \frac{\Phi}{\eta_f} \right) h(x). \quad (6-82)$$

The velocity equation using the near-wall boundary condition set is

$$w(x, y) = -\frac{\beta_f}{2} y^2 + \left(\beta_f - \frac{\Phi}{\eta_f} \right) h(x) y. \quad (6-83)$$

Equation 6-83 is exactly the same as the equation used to describe the velocity profile in ABFG (6-37). That means this equation can be used to describe the velocity profile in the whole film phase regardless of the existence of the wall contact. Using this boundary condition set, a smooth transition is ensured.

6.6 List of Equations

In this section a brief overview is given of the calculation models explained in this chapter in combination with the geometrical assumptions of the rivulet cross-section. As explained in Chapter 6.5.3, there are three mathematical geometries which can be used to describe the shape of the rivulet cross-section. They are triangle, circle segment and rectangle. In Table 6-3 the interval of the rivulet-wetting angle is estimated by varying the rivulet thickness from nearly zero up to its width. This is the maximum thickness a rivulet can have when a circular cross-section is assumed. Only if the circular shape is assumed, can the rivulet-wetting angle exceed the value 90° . Otherwise the angle will always be smaller than or equal to 90° , as shown in Table 6-3.

In Table 6-4 the three calculation models according to the Nusselt, the tau and the wall models, assuming a rectangular cross-section, can be seen. The same calculation models using a circular (rivulet-wetting angle smaller than or equal to 90°) and a triangular cross-section are given in Tables 6-5 and 6-7 respectively. For rivulet-wetting angles which are larger than 90° , the tau model in combination with the symmetric, the continuity and the near wall boundary condition sets is given in Table 6-6.

To verify the validity of the calculation models introduced in this chapter, the velocity profiles in the film phase and the film mean velocity are shown and discussed in the next chapter.

Table 6-3: Interval of rivulet-wetting angle depending on the magnitude of the rivulet thickness and the assumed shape of the cross-section.

Shape of rivulet cross-section	$0 < \delta_f < b$	$\delta_f = b$	$b < \delta_f < 2b$	$\delta_f = 2b$
Triangle	$0 \dots 45^\circ$	45°	$45^\circ \dots 63.4^\circ$	63.4°
Circle segment	$0 \dots 90^\circ$	90°	$90^\circ \dots 180^\circ$	180°
Rectangle	90°	90°	90°	90°

Table 6-4: Film phase velocity equation assuming rectangular cross-section shape.

Calculation model and film cross-section shape	Boundary conditions	Velocity equation
<p><u>Nusselt</u></p>	$w(y=0) = 0$ $\left. \frac{dw}{dy} \right _{y=\delta_f} = 0$	$w(y) = -\frac{\beta_f}{2} y^2 + \beta_f \delta_f y$
<p><u>Tau</u></p>	$w(y=0) = 0$ $\left. \frac{dw}{dy} \right _{y=\delta_f} = -\frac{\tau}{\eta_f}$	$w(y) = -\frac{\beta_f}{2} y^2 + \left(\beta_f - \frac{\Phi}{\eta_f} \right) \delta_f y$
<p><u>Wall</u></p>	$w(y=0) = 0$ $w(y=\delta_f) = 0$	$w(y) = -\frac{\beta_f}{2} y^2 + \frac{\beta_f \delta_f}{2} y$

6.6 List of Equations

Table 6-5: Film phase velocity equation assuming circular cross-section shape. The rivulet-wetting angle is smaller than or equal to 90° .

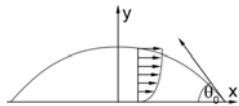
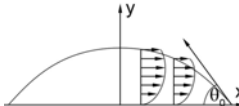
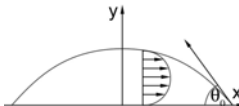
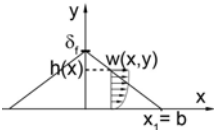
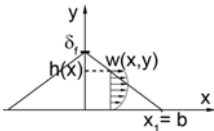
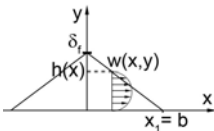
Calculation model and film cross-section shape	Boundary conditions	Velocity equation
<p><u>Nusselt</u></p> 	$w(y=0) = 0$ $\left. \frac{dw}{dy} \right _{y=h(x)} = 0$	$w(x, y) = -\frac{\beta_f}{2} y^2 + \beta_f h(x) y$
<p><u>Tau</u></p> 	$w(y=0) = 0$ $\left. \frac{dw}{dy} \right _{y=h(x)} = -\frac{\tau}{\eta_f}$	$w(x, y) = -\frac{\beta_f}{2} y^2 + \left(\beta_f - \frac{\Phi}{\eta_f} \right) h(x) y$
<p><u>Wall</u></p> 	$w(y=0) = 0$ $w(y=h(x)) = 0$	$w(x, y) = -\frac{\beta_f}{2} y^2 + \frac{\beta_f h(x)}{2} y$

Table 6-6: Film phase velocity equation assuming circular cross-section shape. The rivulet-wetting angle is larger than 90° .

Boundary conditions		Velocity equation	
		$-\alpha_0 \leq \alpha < \alpha_0$	$\alpha_0 \leq \alpha \leq \frac{\pi}{2}$
symmetric	$\left. \frac{\partial w}{\partial y} \right _{y=R \sin \alpha_0} = 0$ $w_{F^-} = w_{F^+}$	$w(x, y) = -\frac{\beta_f}{2} y^2 + \beta_f R \sin \alpha_0 y$ $+ 2R^2 \sin^2 \alpha_0 \left(\beta_f - \frac{2\Phi}{\eta_f} \right)$	$w(y) = -\frac{\beta_f}{2} y^2 + \left(\beta_f - \frac{\Phi}{\eta_f} \right) h(x) y$
continuity	$w_{F^-} = w_{F^+}$ $\tau_{F^-} = \tau_{F^+}$	$w(x, y) = -\frac{\beta_f}{2} y^2$ $+ \left(\beta_f - \frac{\Phi}{\eta_f} \right) 2R \sin \alpha_0 y$	
Near wall	$w_{B^+} = w_{B^-}$ $\tau_{(BF)^+} = \tau_{(BF)^-}$	$w(x, y) = -\frac{\beta_f}{2} y^2 + \left(\beta_f - \frac{\Phi}{\eta_f} \right) h(x) y$	

Table 6-7: Film phase velocity equation assuming triangular cross-section shape.

Calculation model and film cross-section shape	Boundary conditions	Velocity equation
<p><u>Nusselt</u></p> 	$w(y=0) = 0$ $\left. \frac{dw}{dy} \right _{y=\delta_f} = 0$	$w(x, y) = -\frac{\beta_f}{2} y^2 + \beta_f h(x) y$
<p><u>Tau</u></p> 	$w(y=0) = 0$ $\left. \frac{dw}{dy} \right _{y=h(x)} = -\frac{\tau}{\eta_f}$	$w(y) = -\frac{\beta_f}{2} y^2 + \left(\beta_f - \frac{\Phi}{\eta_f} \right) h(x) y$
<p><u>Wall</u></p> 	$w(y=0) = 0$ $w(y=h(x)) = 0$	$w(x, y) = -\frac{\beta_f}{2} y^2 + \frac{\beta_f h(x)}{2} y$

$$\beta_f = \frac{(\rho_f - \rho_c) g}{\eta_f} \tag{6-84}$$

$$\Phi = \frac{\beta_f}{2\eta_f (\beta_c \eta_c + \beta_f \eta_f)} \tag{6-85}$$

$$\frac{\beta_c \beta_f (\eta_c^2 \eta_f^2 - 2\eta_c^3 \eta_f + \eta_c^4 + 2\eta_c \eta_f^3) + \eta_f^2 (\beta_c^2 \eta_c^2 + \beta_f^2 \eta_f^2)}{2\beta_f \eta_f - \beta_f \eta_c + \beta_c \eta_c}$$

The borderline of the circular cross-section:

$$h(x) = R(\cos\theta - \cos\theta_0) \tag{6-86}$$

and triangular cross-section:

$$h(x) = -\frac{\delta_f}{b} x + \delta_f \tag{6-87}$$

7 Velocity Profile and Mean Film Velocity

I saw the angel in the marble and carved until I set him free.

Michelangelo

In the previous chapter it is stated and shown that the velocity profile in the film phase cannot be described solely by the commonly used Nusselt model nor is it to be forecast by the wall model. An attempt has been made to develop a calculation model which is based on the force balance according to the classic Nusselt model. The boundary conditions are adjusted to the requirements for processes to proceed at high pressure conditions where the miscibility and the friction between the phases are not negligible. The tau model, which assumed the existence of a finite shear stress at the film surface and, a velocity boundary layer lying between the film surface and the static continuous phase, is believed to be able to fulfill this task. However, the applicability of the last mentioned model has not been proved.

This chapter is divided into two large sections, the first one is about the velocity profile in the film phase and the second part discusses the film mean velocity.

In the first part of this chapter, the velocity profile in the film phase is shown. For wetting angles smaller than or equal to 90° , the velocity profile in the film phase which flows along a vertical glass surface is given according to the three calculation models, whereas for wetting angles larger than 90° , the film phase velocity profile on a steel surface is calculated according to the tau model, using three different sets of boundary conditions.

In Chapter 7.2 the mean velocities according to the three afore-mentioned models are formulated with the assumption that the cross-section area might have the shape of a rectangular segment (total wetting, also called one-dimensional problem), a circle segment (partial wetting, for instance a rivulet) and a triangle. For rivulets with a circular cross-section, a distinction of the mean velocity depending on the wetting angle is made. In cases where the wetting angle is larger than 90° , the mean velocity is calculated according to the tau model with three boundary condition sets introduced in Chapter 6.5.3. The calculated mean velocity is compared with the experimental one in Chapter 7.3 to allow a conclusion on the applicability of those models to describe the fluid dynamics.

The interdependency of the mass transfer and the film thickness is discussed in Chapter 7.4. An attempt is made to estimate the change of the film thickness as the mass transfer proceeds, if the miscibility between the adjacent phases is not negligible. This study is made based on the systems water-carbon dioxide and corn germ oil-carbon dioxide. Finally, the mean velocity equations are summarized in tabular form at the end of this chapter.

7.1 Velocity Profile in the Film Phase

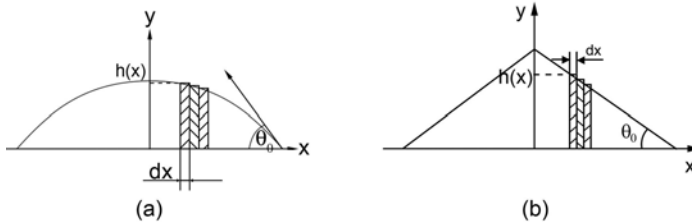


Figure 7-1: Assumed rivulet cross-section shape: (a) circular (b) triangular.

In this section, the visualization of the velocity profile in one half of the film phase will be shown. For wetting angles up to 90° , the velocity profiles of the water rivulet which flows along a glass surface surrounded by the supercritical carbon dioxide are calculated according to the Nusselt (Eq. 6-9), the tau (Eq. 6-37) and the wall models (Eq. 6-11). The experiment is performed at 313 K and 24 MPa. The film phase mass flow is 2.1 g/min. The rivulet-wetting angle θ_0 is 45° whereas the circle equivalent radius R is 1.71 mm.

For wetting angles larger than 90° , the water rivulet which flows along a vertical steel surface is taken as an example. The operating conditions are 313 K and 15 MPa, water flows at 9 g/min. The rivulet-wetting angle θ_0 is 104° and the circle equivalent radius R is 0.63 mm. The velocity profiles are calculated by means of the tau model. In the area where no direct wall contact exists, the afore-mentioned three different sets of boundary conditions (the symmetric boundary conditions according to Eq. 6-60, the continuity boundary conditions according to Eq. 6-74 and the near wall boundary conditions according to Eq. 6-83) are applied.

The equations used are developed for a one dimensional problem. Initially, they depend only on the y -axis, along which the thickness of the film expands. To draw the velocity profile in the cross-section, which means a two dimensional visualization, those equations are adapted. The shape of the film cross-section can, theoretically seen, be circular, triangular or rectangular, as explained in 6.5.3. The film thickness is constant if the rectangular shape is assumed, whereas if a circular or a triangular cross-section is applied, a mathematical expression is required to describe the change of the rivulet thickness along its width (see Fig. 7-1). The mathematical equations used to describe the borderline of the circular segment and the side of the triangle can be found in Chapter 6.6.

To draw the two-dimensional velocity profile, the film cross-section is divided into several thin slices of equal width dx such as seen in Fig. 7-1. The afore-mentioned one-dimensional equations are applied in each thin slices. It is therefore assumed that the velocity profile in each

slice of width dx and thickness $h(x)$ is that of a uniform draining film of the same thickness. Hereby, the two-dimensional velocity profile is created. The adapted two-dimensional equations which describe the velocity equations in terms of their dependency on the x - and the y -axes are given in Chapter 6.6.

In this chapter, the visualization of the two dimensional velocity profiles is given based on the well-established conception that the cross-section has a circular shape. All colored diagrams can be observed in online dissertation at: <http://doku.b.tu-harburg.de/volltexte/2007/355/> or <http://nbn-resolving.de/urn/resolver.pl?urn=urn:nbn:de:gbv:830-tubdok-3556>, the URN: urn:nbn:de:gbv:830-tubdok-3556.

7.1.1 Wetting Angle up to 90°

Nusselt Model

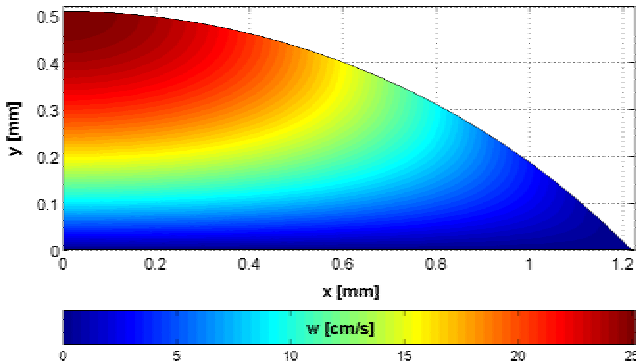


Figure 7-2: Velocity profile according to the Nusselt model. The water film phase flows along a vertical glass surface at 313 K and 24 MPa. The water mass flow is 2.1 g/min.

According to the Nusselt model, the film velocity at the wall is equal to zero. This increases consistently with increasing distance to the wall until the local maximum in the velocity is reached. This happens at the film surface. In Fig. 7-2 the velocity profile in one half of the film phase according to the Nusselt model can be seen. The velocity varies from zero to 25 cm/s and the maximum velocity in the whole film phase is reached at the top, in the middle of the film width (the coloured diagrams is accessible in the electronical thesis).

Tau Model

The film velocity profile according to the tau model can be seen in Fig. 7-3. The same water rivulet as in the previous model is shown here. However, the local velocity varies only in the range between zero and 7.5 g/min. There is a great velocity difference in the result gained using

7.1 Velocity Profile in the Film Phase

the tau and the Nusselt model (this can be seen more clearly later when the mean velocities are calculated and compared in Chapter 7.3).

According to the tau model, at the beginning, the film velocity increases with increasing distance from the vertical wall until the maximum of the parabola is reached. In the example given here, the maximum is reached nearly in the middle of the local film thickness $h(x)$. Going further, the parabola turns back and the velocity decreases consistently up to the film surface. At the film surface, a finite velocity, which is, in general, different from zero, is reached. The velocity profile in the film phase according to the tau model resembles the annular flow in a tube.

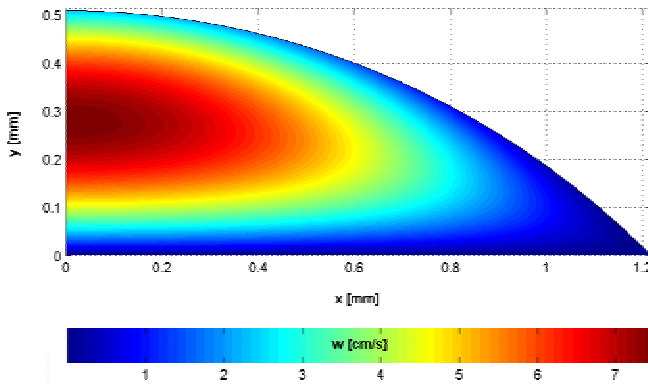


Figure 7-3: Velocity profile according to the tau model. The water film phase flows along a vertical glass surface at 313 K and 24 MPa. The water mass flow is 2.1 g/min.

Wall Model

In Fig. 7-4 the velocity profile in the film phase is calculated according to the wall model. In this model, besides that at the wall the no-slip condition is assumed, the shear stress at the film surface is estimated as sufficient to prevent the molecules from flowing. The local velocity varies from zero to approximately 6.5 cm/s, which does not differ very much from the one calculated according to tau model (this will be explained later in details in Chapter 7.3).

The local maximum in the velocity is reached exactly in the middle of the local film thickness $h(x)$. The highest velocity is reached in the middle of the film width, exactly in the middle of the film thickness at $x=0$.

At the given conditions, the velocity profile according to the wall model is very similar to that estimated by means of the tau model. This is a good proof that the tau model describes the velocity generally, but once the conditions become extreme, the results gained using tau model resemble the ones delivered by the wall model. At higher pressures, the assumption that the

molecules near the film phase surface do not flow, is plausible and therefore the wall model can better be applied at these conditions.

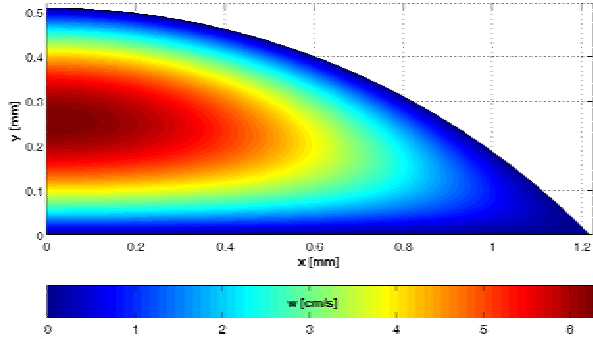


Figure 7-4: Velocity profile according to the wall model. The water film phase flows along a vertical glass surface at 313 K and 24 MPa. The water mass flow is 2.1 g/min.

7.1.2 Wetting Angle above 90°

Symmetric Boundary Conditions

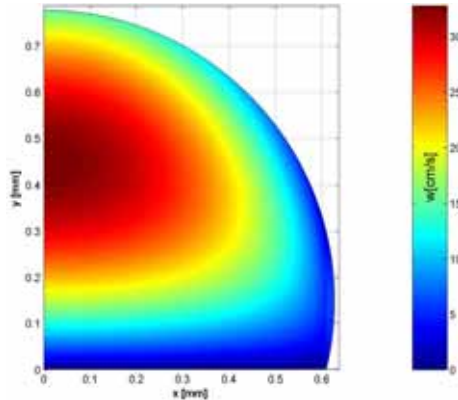


Figure 7-5: Velocity profile according to the tau model using symmetric boundary conditions. The water film phase flows along a vertical steel surface at 313 K and 15 MPa. The water mass flow is 9 g/min.

If a rivulet wets a vertical surface with a wetting angle larger than 90° , which means a circular shape of the cross-section is assumed, one part of the liquid along the wall (in x-axis) is supported directly by the wall through its wall contact whereas the other part is bound to the rivulet just by the cohesion force between the liquid molecules while it floats in the continuous

7.1 Velocity Profile in the Film Phase

phase. The visualization of such a velocity profile can be seen in Fig. 7-5. Here, the symmetric boundary conditions are used. That means, in the area without any direct wall contact, the velocities of the opposite points are equal. The velocity profile in the area where the liquid is supported directly through the wall contact appears as expected. However, great attention should be paid to the borderline where the transition from the first to the second area occurs. This is approximately at $x = 0.6$ mm and $x = 0.61$ mm (see Fig. 7-6).

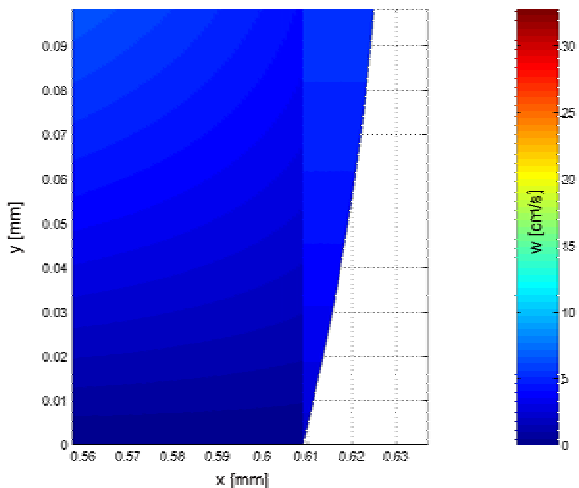


Figure 7-6: Enlarged velocity profile according to the tau model using symmetric boundary conditions. The water film phase flows along a vertical steel surface at 313 K and 15 MPa. The water mass flow is 9 g/min.

To observe the transition better, the spot is enlarged such as seen in Fig. 7-6. It can be seen very clearly that due to the change in the velocity equation used, there is an unexpected jump in the velocity (observable through the abrupt color change in the color diagram). The jump seen here is not caused by the picture resolution.

The incontinuity in the velocity was forecast in Eq. (6-62). The maximum velocity jump can be found at $y = 0$, as can be obviously seen in the color difference in Fig. 7-6. At this position, the velocity difference between the adjacent molecules is approximately 2 cm/s, which is very large.

Continuity Boundary Conditions

The velocity profile calculated by means of the tau model using the continuity boundary condition set can be seen in Fig. 7-7. Such as predicted in Eq. 6-75, there is no velocity jump from one area to the other. The transition occurs more smoothly when compared with the one using the symmetric conditions. However, the isotach lines (lines with constant speed, color-coded for velocity) in the film phase show a sharp break which is not expected. According to its name, the continuity conditions provide a continuous but, at the point where the transition occurs, not differentiable velocity profile, which means, there is an edge in the isotach lines.

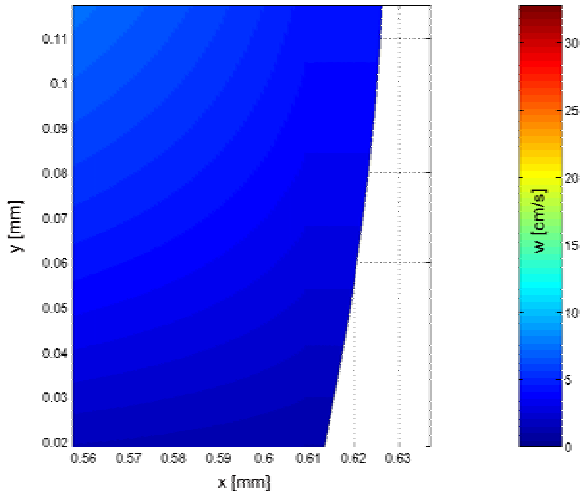


Figure 7-7: Enlarged velocity profile according to the tau model using continuity boundary conditions. The water film phase flows along a vertical steel surface at 313 K and 15 MPa. The water mass flow is 9 g/min.

Near-Wall Boundary Conditions

In Fig. 7-8 the velocity profile in the film phase according to the tau model using near wall boundary condition set is shown. The isotach lines are continuous in the whole phase and there are no edges in the lines. The no-slip effect on the molecules near the wall is also shown there. This boundary condition set can be best applied to show the velocity profile in the film phase.

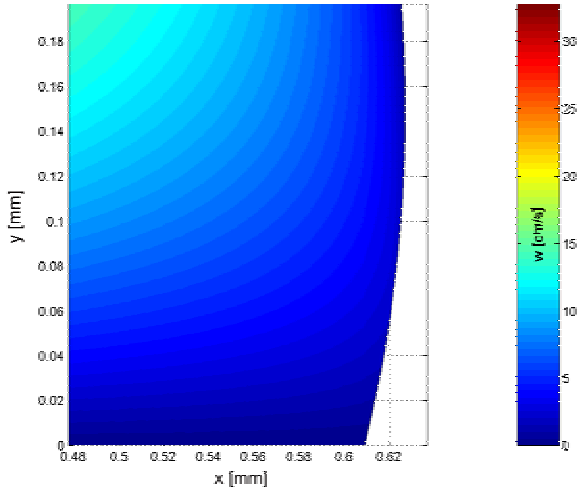


Figure 7-8: Velocity profile according to the tau model using near wall boundary conditions. The water film phase flows along a vertical steel surface at 313 K and 15 MPa. The water mass flow is 9 g/min.

7.2 Mean Film Velocity: Theoretical Background

7.2.1 Wetting Angle up to 90°

The main idea in calculating the mean velocity in the film phase is to sum up the product of the local velocity with the infinitesimal area in which the velocity is taken as constant and divide it by the area itself

$$\bar{w} = \frac{\int_0^x \int_0^y w(x, y) dy dx}{\int_0^x \int_0^y dy dx} \quad (7-1)$$

The calculation using the infinitesimal term of dx and dy in Eq. 7-1 is required here due to the velocity distribution in the whole film phase. For this purpose, the whole film width is divided into a large number of thin slices of equal width dx. Furthermore this slice is cut again into several small pieces with the dimension dx*dy which is sufficiently small that the velocity in it can be taken as constant (see Fig. 7-9 and 7-10) and thus, the mean velocity can be calculated provided that the shape of the cross-section is known.

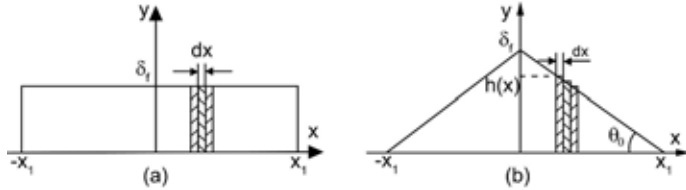


Figure 7-9: Film mean velocity averaged over the whole rivulet area by assuming a rectangular (a) or a triangular (b) film cross-section shape .

In the following, only brief explanation is given regarding the integration limits and the function $h(x)$ which describes the borderline of the three possible cross-sections. The equations of the mean velocity are given at the end of this chapter in Section 7.5.

Rectangular Cross-section Shape

If a rectangular cross-section is assumed, the calculation in Eq. 7-1 becomes simpler since it has to be carried out only in one direction

$$\bar{w} = \frac{\int_0^{\delta_f} w(y) dy}{\int_0^{\delta_f} dy} \quad (7-2)$$

due to the fact that in a rectangular cross-section the film thickness δ_f is constant over the whole width and thus, only a one-dimensional problem needs to be solved here.

Triangular Cross-section Shape

For a triangular cross-section, in y -axis, the equation in 7-1 has to be summed up from zero to $h(x)$ and in x -axis from zero to half of the rivulet width b at the position $x=x_1$ (the mean velocity is averaged in just one half of the film phase as the velocity profile is symmetrical with respect to the middle line or the y -axis)

$$\int_0^{x_1} \int_0^{h(x)} w(x, y) dy dx \quad (7-3)$$

The borderline of the film phase is described by the function

$$h(x) = -\frac{\delta_f}{b} x + \delta_f \quad (7-4)$$

and the area of half of the rivulet is

$$\int_0^{x_1} \int_0^{h(x)} dy dx = \frac{b \delta_f}{2} \quad (7-5)$$

Circular Cross-section Shape

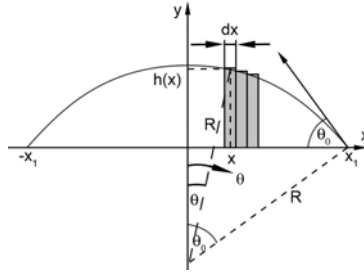


Figure 7-10: Film mean velocity averaged over the whole rivulet area by assuming a circular cross-section shape.

The same idea is employed if the rivulet is assumed to have a circular cross-section such as shown in Fig. 7-10. The integration of the numerator in Eq. 7-1 in the y-axis is from zero (wall surface) up to the rivulet surface $h(x)$ and from the film middle line $x=0$ up to half of the rivulet width b , also called x_1

$$\int_0^{x_1} \int_0^{h(x)} w(x, y) dy dx \quad (7-6)$$

The rivulet surface is described by the function

$$h(x) = R(\cos \theta - \cos \theta_0) \quad (7-7)$$

with

$$x = R \sin \theta \quad (7-8)$$

and thus

$$x_1 = R \sin \theta_0 \quad (7-9)$$

$$dx = R \cos \theta d\theta \quad (7-10)$$

Half of the rivulet area which is seen in the denominator in Eq. 7-1 can be written in the term of its dependency on the circle equivalent radius R and the wetting angle θ_0

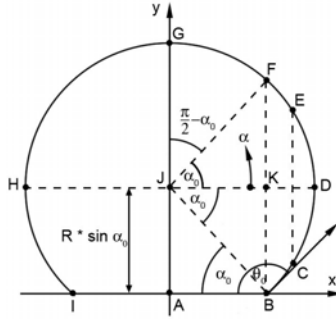
$$\int_0^{x_1} \int_0^{h(x)} dy dx = R^2 a_1(\theta_0) \quad (7-11)$$

where

$$\begin{aligned} a_1 &= \int_0^{\theta_0} \cos \theta (\cos \theta - \cos \theta_0) d\theta \\ &= \frac{1}{2}(\theta_0 - \sin \theta_0 \cos \theta_0) \end{aligned} \quad (7-12)$$

The term $w(x,y)$ can be substituted by the velocity equations given in 6.6 for all three calculation models.

7.2.2 Wetting Angle Above 90°

Figure 7-11: Film cross-section with the wetting angle θ_0 larger than 90° .

If a circular cross-section is assumed and the wetting angle is larger than 90° , generally two velocity equations are used to describe the fluid dynamics in the film phase. The first one is for the area ABFG where a direct wall contact exists and the second one is used to describe the velocity profile in the area BDF where no direct wall contact exists. Besides that, the integration limits along the y -axis are not the same as well. For ABFG, integration is carried out from the wall $y=0$ up to the rivulet surface $h(x)$ whereas in BDF the calculation is from $h_2(x)$ up to $h(x)$. The function $h(x)$ refers to the borderline DG whereas $h_2(x)$ describes exactly the opposite points of the arc DF, that is, the border line BD (see Fig. 7-11 and Fig. 8-3).

That is why the calculation of the mean velocity is also performed in two steps too

$$\bar{w} = \frac{1}{A_{ABDFG}} \left(\int_0^{A_{ABFG}} w_{ABFG}(x, y) dA + \int_0^{A_{BDF}} w_{BDF}(x, y) dA \right). \quad (7-13)$$

Equation 7-13 is written generally in terms of the product of the velocity and the infinitesimal area dA . The first term refers to the area ABFG whereas the second one refers to the area BDF.

The whole area ABDFG is therefore the sum of both

$$A_{ABDFG} = A_{BJGD} + A_{ABJ} \quad (7-14)$$

with

$$A_{BJGD} = \frac{R^2}{4} (\pi + 2\alpha_0) \quad (7-15)$$

and

$$A_{ABJ} = \frac{R^2}{4} \sin(2\alpha_0) \quad (7-16)$$

and the whole area can be written in terms of its dependency on the circle equivalent radius R and the angle α_0 (the polar coordinate system α has its initial on the line DJ)

$$A_{ABDFG} = \frac{R^2}{4} (\pi + 2\alpha_0 + \sin(2\alpha_0)). \quad (7-17)$$

7.2 Mean Film Velocity: Theoretical Background

In ABFG the velocity is averaged from the wall ($y=0$) up to the film surface $h(x)$ whereas in BDF, it is calculated from $h_2(x)$ up to $h(x)$ and from $x=x_1$ (exactly at point B) up to R

$$\bar{w} = \frac{1}{A_{ABDFG}} \left[\int_0^{x_1} \int_0^{h(x)} w(x, y) dy dx + \int_{x_1}^R \int_{h(x)-\delta_f(x)}^{h(x)} w(x, y) dy dx \right] \quad (7-18)$$

(instead of $h_2(x)$, the lower limit of the integration in second term can also be expressed in the term of $h(x)-\delta_f(x)$ with $\delta_f(x)$ as the rivulet thickness which depends on the x -axis). The borderlines can be expressed

$$h(x) = h_2(x) = R(\sin \alpha_0 + \sin \alpha) \quad (7-19)$$

with

- $0 \leq \alpha \leq \frac{\pi}{2}$ for $h(x)$
- $-\alpha_0 \leq \alpha < 0$ for $h_2(x)$.

The term in x can be expressed in the polar coordinate system

$$x = R \cos \alpha \quad (7-20)$$

and thus

$$x_1 = R \cos \alpha_0 \quad (7-21)$$

with

$$dx = -R \sin \alpha d\alpha. \quad (7-22)$$

Hereby the integration in Eq. 7-18 is performed from $\pi/2$ to α_0 (ABFG) and from α_0 to 0 for the area BDF. The magnitude of the film thickness itself can be calculated by means of Eq. 7-23 and Eq. 7-24 such as listed in Table 7-1.

Table 7-1: Film thickness in term of its dependency on the angle α .

Area	$\delta_f(x)$	α
ABFG	$\delta_f(x) = h(x) \quad (7-23)$	$\alpha_0 \leq \alpha \leq \frac{\pi}{2}$
BDF	$\delta_f(x) = 2R \sin \alpha \quad (7-24)$	$0 \leq \alpha < \alpha_0$

The integration result of the first term of Eq. 7-18 (the area ABFG) if the tau model is employed, can be seen in Eq. 7-25

$$\int_0^{x_1} \int_0^{h(x)} w(x, y) dy dx = R^4 \left(\frac{\beta_f}{3} - \frac{\Phi}{2\eta_f} \right) \left(\frac{15}{16}\pi - \frac{3}{4}\pi \cos^2 \alpha_0 + \frac{15}{4}\sin^3 \alpha_0 \cos \alpha_0 \right) \left(-\frac{3}{2}\alpha_0 \sin^2 \alpha_0 + \frac{19}{8}\cos \alpha_0 \sin \alpha_0 - \frac{3}{8}\alpha_0 \right) \quad (7-25)$$

and if the wall model is taken

$$\int_0^{x_i} \int_0^{h(x)} w(x, y) dy dx = \frac{\beta_f}{12} R^4 \left(\frac{15}{16} \pi - \frac{3}{4} \pi \cos^2 \alpha_0 + \frac{15}{4} \sin^3 \alpha_0 \cos \alpha_0 - \frac{3}{2} \alpha_0 \sin^2 \alpha_0 + \frac{19}{8} \cos \alpha_0 \sin \alpha_0 - \frac{3}{8} \alpha_0 \right) \quad (7-26)$$

The wall model calculation equation is valid for the whole area whereas when the tau model is applied, there are three different possible equations in BDF, which are obtained using three different boundary condition sets. The mean velocity equations obtained are listed in tables 7-2 and 7-3.

7.3 Experimental and Calculated Mean Velocity

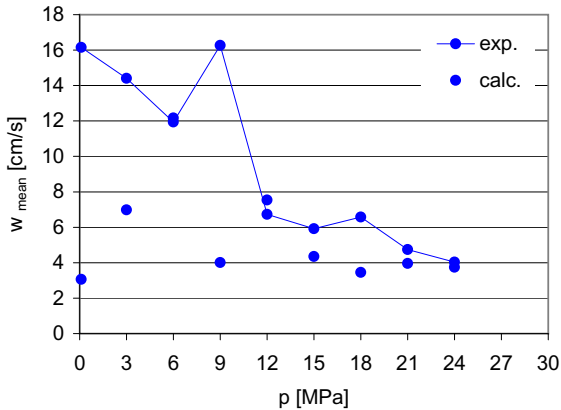


Figure 7-12: Experimental and calculated mean velocity according to the tau model by assuming a circular cross-section. System: water rivulet flowing along a vertical glass surface at 313 K and a flow rate of 2.1 g/min.

The calculated mean velocity can be compared with the experimental one to allow a conclusion about the applicability of each model to describe the fluid dynamics. In Fig. 7-12 the mean velocity of the water rivulet which flows along a vertical glass surface at 313 K and a constant flow rate of 2.1 g/min is shown. Here, a circular cross-section shape is assumed. In the experimental values, there is a sudden jump of the mean velocity at 9 MPa. This is probably caused by the imprecise measurement carried out in the vicinity of the critical pressure of carbon dioxide. The uncertainty of the measurement in this pressure range is even enhanced by the large density gradient caused by a small pressure or temperature gradient. The schlieren of the continuous phase aggravates the optical measurement and thus, leads to imprecision. The mean velocity of the rivulet at a constant rate of flow in Fig. 7-12 decreases as pressure

7.3 Experimental and Calculated Mean Velocity

increases. This is caused by the density difference which becomes smaller and the buoyant force which increases. As a consequence, the rivulet is decelerated and the velocity falls.

In Fig. 7-12 the tau model is applied under the assumption that the rivulet has a circular cross-section. As has been explained, there are three calculation models which can be combined with three cross-section shapes. The result shown in Fig. 7-12 is just one example of the nine theoretically possible combinations. In the study carried out to prove the applicability of these models, all nine possibilities are compared with the mean values. The result shows that the tau model, in combination with the circular cross-section, coincides best with the measured values. However, there are some exceptional points, where the discrepancy between these points is rather large, such as seen in Fig. 7-12. In supercritical carbon dioxide, except at 9 MPa, the calculated values comply with the measured ones. Whereas in gaseous carbon dioxide, the discrepancy is rather large.

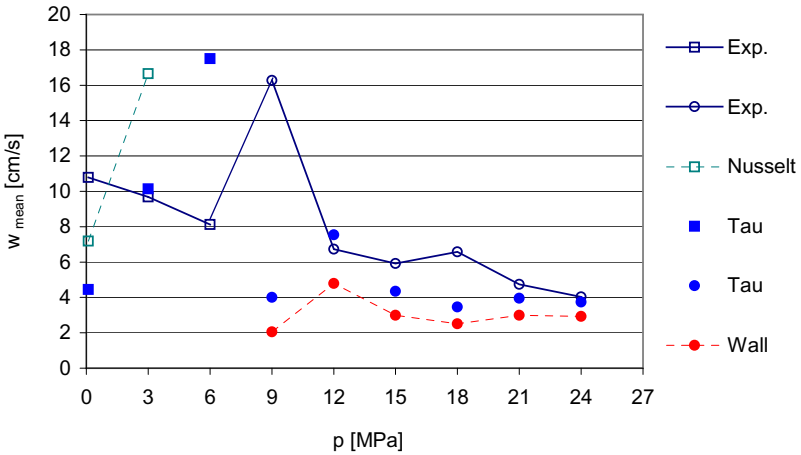


Figure 7-13: Experimental and calculated mean velocity of the water rivulet flowing along a vertical glass surface at 313 K and at a constant flow rate of 2.1 g/min.

A further analysis of the data according to the nine combination possibilities available to forecast the mean velocity yields the diagram seen in Fig. 7-13. Here, all three calculation models can be found in one diagram. As can be seen, at atmospheric pressure, the Nusselt model approaches the mean value better than the tau model. This is as expected since at atmospheric pressure the shear stress exerted at the film surface is negligible and the Nusselt model is the one which should be able to describe the fluid dynamics best. If the Nusselt model is applied at higher pressure, the mean velocity is overestimated strongly because, in contrast to reality, no shear stress is taken into account there. This can be seen at 3 MPa where the calculated mean velocity according to the Nusselt model is far higher than the measured one.

The tau model can, except at 0.1 MPa, describe the fluid dynamics of the water rivulet very well. The discrepancy at 6 MPa and 9 MPa is rather large. But this is probably due to the imprecision of the measurement in the vicinity of the carbon dioxide critical pressure.

The calculation result of the wall model is also shown at higher pressure. The wall model underestimates the mean velocity by a large amount if this is applied at lower pressures due to the fact, that the shear stress assumed is too large. But in supercritical carbon dioxide, the results are in accordance with the tau model and thus, with the measured values.

The shape of the symbols in Fig. 7-13 gives a hint about the assumed cross-section shape employed in the calculation. As can be seen, at the glass surface, due to its good wetting characteristics, a relatively thin and wide covering rivulet is formed at lower pressure. That is why in gaseous carbon dioxide the rectangular shape can be assumed. The wetting characteristics becomes poorer as the pressure increases and in supercritical carbon dioxide the circular cross-section has to be taken into account.

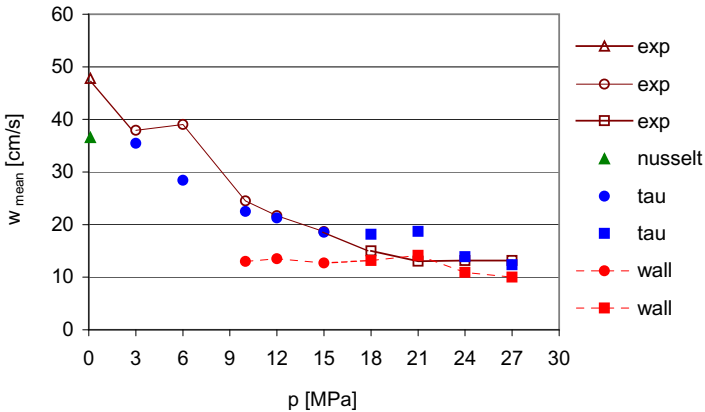


Figure 7-14: Experimental and calculated mean velocity of the water rivulet flowing along a vertical steel surface at 313 K and a flow rate of 9 g/min.

The mean velocity of the water rivulet drains along a vertical steel surface at 313 K and a flow rate of 9 g/min is calculated and compared with the measured value as well. The comparison and analysis of the data show nearly the same results as explained before. At atmospheric pressure, the Nusselt model delivers the best result. The tau model can be applied in the whole pressure range except at atmospheric pressure and the wall model is valid at higher pressure such as seen in Fig. 7-14. The mean velocity estimated by means of the wall model always lies below the value calculated using the tau model. This is understandable since the wall model presents the lower limit of the tau model where the shear stress is maximum.

The wetting characteristics of steel surrounded by carbon dioxide are not the same as the ones of glass. Steel is wetted poorly when compared with glass. As can be seen through the shape of

the symbols in Fig. 7-14, at atmospheric pressure, the rivulet cross-section approaches a triangular shape. Up to 15 MPa a circular cross-section can be assumed but afterwards, due to the poor wettability of the steel, instead of spreading spontaneously, liquid augments itself in the thickness direction causing a thick rivulet with a near-rectangular cross-section.

If at higher pressure circular cross-section is assumed, the mean velocity using the tau model has to be calculated in two steps by means of the three different boundary condition sets because the wetting angle θ_0 exceeds 90° . A conclusion about the applicability of these boundary condition sets by means of the resulted mean velocity cannot be made since the values are simply very similar to each other. This is partly caused by the small area of BDF (the largest wetting angle is 107°). As a comparison, the wetting angle of the water rivulet draining along the steel surface in Fig. 7-5 is 104°). However, as explained in 7.1.2 a conclusion about the usability of these boundary conditions is made based on the velocity profile in the film phase, especially at the transition line BF. The wetting angle of the water rivulet at pressures above 10 MPa is larger than 90° . The mean velocity above this pressure is calculated by means of the tau model with the near-wall boundary condition set (see Fig. 7-14).

A discussion about the shape of the cross-section is needed here because the mean velocity of the rivulet has to be compared with the measured one to give a conclusion about the applicability of each model at the given operating conditions. If a total wetting of a wide covering film can be assured, the discussion about the cross-section shape is not interesting any more since the film can only have a rectangular cross-section. This is fulfilled either when the wettability of the system at the given operating conditions is very good or when the rate of flow of the film phase is adjusted in such a way that a total wetting of the available vertical surface is consistently guaranteed.

As for the wall model, at and above 18 MPa the mean velocity can be predicted quite well by means of this model. Here, like in the tau model, a rectangular shape is assumed. Below 18 MPa the wall model underestimate the mean velocity. This is a consequence of the overestimation of the shear stress at the film surface.

In the following, the tau model is compared with the wall model by means of its mean velocity to allow a prediction of the operating conditions at which the latter approaches the first one. Under the assumption of the equality of the mean velocity of both models, the wall model is equal to the tau model when

$$\Phi = \frac{1}{2} \beta_f \eta_f . \quad (7-27)$$

In Fig. 7-15 the right-hand term of Eq. 7-27 ($1/2 * \beta_f * \eta_f$) is plotted against Φ for the system water-CO₂ at 313 K and corn germ oil-CO₂ at 333 K in the pressure range up to 30 MPa. If Eq. 7-27 is fulfilled, the points would lie on the diagonal line seen in Fig. 7-15, where the term ($1/2 * \beta_f * \eta_f$) complies exactly with the value of Φ . At lower pressures the difference between both terms is apparently large (observable through the distance of the points to the diagonal line). As pressure increases (see the direction of the pressure-axis in Fig. 7-15), the points draw

near the diagonal line. At sufficiently high pressure, the points lie exactly on this diagonal line, which indicates that there is no difference between the mean velocity calculated by means of the tau and the wall model. This is in line with the findings shown in Fig. 7-13 and 7-14.

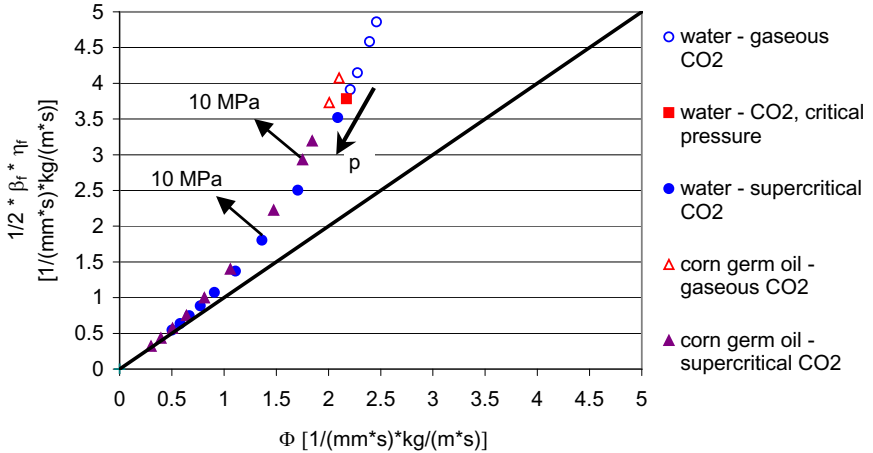


Figure 7-15: If the term $(\frac{1}{2} \beta_f \eta_f)$ is equal to Φ then the wall model approaches the tau model. Investigated systems: water-CO₂ at 313 K and corn germ oil- CO₂ at 333 K in the pressure range up to 30 MPa.

7.4 Interdependency of Mass Transfer and Falling Film Thickness

According to the continuity equation, if the mass flow

$$\dot{m} = \rho_f \bar{w} A \quad (7-28)$$

is kept constant, a theoretical comparison of the film thickness at these conditions can be performed

$$\frac{\delta_{f,2}}{\delta_{f,1}} = \sqrt[3]{\frac{(\rho_f \beta_f)_1}{(\rho_f \beta_f)_2}} \quad (7-29)$$

Here, it is assumed that the liquid covers the available vertical surface very well and thus, a thin film with a rectangular cross-section and a constant film width can be assumed. The ratio of the film thickness in Eq. 7-29 is estimated by means of the Nusselt and the wall models. If the tau model is applied

$$\frac{\delta_{f,2}}{\delta_{f,1}} = \sqrt[3]{\frac{\rho_{f,1} \left(\frac{\beta_f}{3} - \frac{\Phi}{2\eta_f} \right)_1}{\rho_{f,2} \left(\frac{\beta_f}{3} - \frac{\Phi}{2\eta_f} \right)_2}} \quad (7-30)$$

In Eq. 7-29 and 7-30 it can obviously be seen that the film thickness ratio depends, at the same mass flow rate, only on the material properties η_c , η_f , ρ_c and ρ_f .

This kind of film thickness comparison can be carried out for:

- two different systems at the same operating conditions
- one same system at different operating conditions
- one same system at the constant operating conditions but different degree of saturation.

The first alternative to compare the film thickness of two different systems provides a basis to predict the effectiveness of a hitherto unknown process regarding the mass transfer between the phases, for instance when an extraction column should be used for a process including a new material system. The available data of a system can be used to forecast the effectiveness of the unknown system by means of the film thickness ratio.

Varying the operating conditions means an alteration in the material properties as well. This is well known and is not astonishing if, due to the change in the material properties, the film thickness changes as well. This change of the film thickness can as well be predicted according to the given equations above.

When at the constant operating conditions the material properties change as the saturation process or the dissolution proceeds, it is interesting to discover, how the film thickness is affected. Upon employing Eq. 7-29 for the Nusselt and the wall model, and Eq. 7-30 for the tau model (1: pure, 2: saturated film phase) the film thickness ratio is calculated. The result for the system water-carbon dioxide at 313 K is given in Fig. 7-16. The mixture properties such as the viscosity η_f and the density ρ_f of the water saturated with carbon dioxide are taken from [131,185]. At 6 MPa the film thickness of the saturated water is 1% higher than the initial film. However the value of the ratio decreases with increasing pressure so that at 30 MPa it becomes 0.91 (tau model) or 0.93 (Nusselt and wall model).

The fall of the film thickness ratio is even more radical when corn germ oil is brought in touch with pressurized carbon dioxide. The ratio of the film thickness at 333 K calculated by means of the Nusselt, the wall and the tau model can be seen in Fig. 7-17. In [185] the density of corn germ oil against pressurized nitrogen at 335 K is reported. The viscosity of pure corn germ oil at 338 K [92] is assumed as constant in the whole pressure range and applied for the calculation of the thickness ratio at 333 K. The density of the carbon dioxide saturated corn germ oil is reported also in [185] and the influence of the dissolved carbon dioxide on the viscosity of corn germ oil at 338 K is taken from [92].

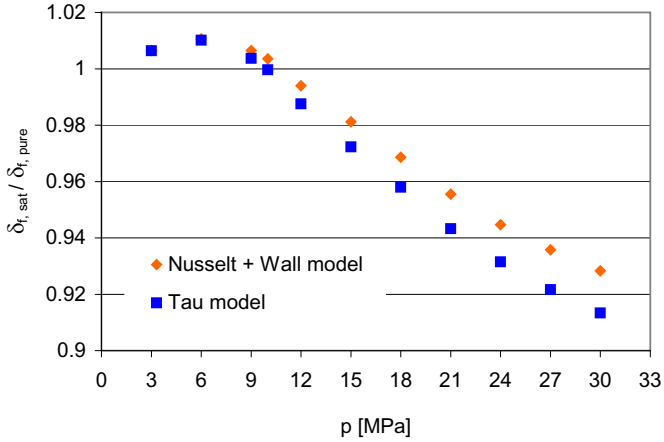


Figure 7-16: Theoretically predicted film thickness ratio between the pure and with carbon dioxide saturated water film at 313 K.

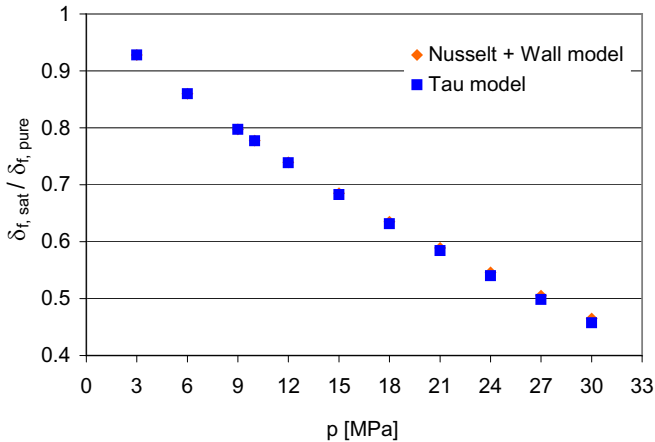


Figure 7-17: Theoretically predicted film thickness ratio between the pure and with carbon dioxide saturated corn germ oil film at 333 K.

At 3 MPa and 333 K, the saturated film thickness becomes only 92.8% of the initial thickness where no carbon dioxide is mixed in the oil phase. The ratio falls consistently and at 30 MPa it reaches the value 0.45. At the end of the saturation process, that is when equilibrium is reached, the film becomes just one half of its initial thickness. Since the equilibrium process is time-dependent, the change in the film thickness does not happen suddenly too. As the amount of the

dissolved carbon dioxide in the oil phase increases, the film becomes thinner. This, in turn, gives the carbon dioxide a better chance to be transferred into the bulk phase of the film. Other molecules can thus be dissolved at the film surface which causes a further alteration of the material properties, the film becomes thinner and so on. This is a snow ball effect which enhances and thus from advantage for the mass transfer.

The difference in the thickness ratio calculated with help of the Nusselt and the wall model compared with the tau model shown in Fig. 7-16 and Fig. 7-17 is not appreciable. The solubility of carbon dioxide in the oil phase is much higher than that in the water phase. As a consequence, the material properties of the oil phase are affected more strongly too. That is why the fall in the ratio thickness can be seen more clearly in corn germ oil-carbon dioxide than in water-carbon dioxide system.

7.5 List of Equations

Table 7-2: Film phase mean velocity for θ_0 up to 90° .

	Rectangle	Circle	Triangle
Nusselt	$\bar{w} = \frac{\beta_f}{3} \delta_f^2$	$\bar{w} = \frac{\beta_f}{3} R^2 \frac{a_3(\theta_0)}{a_1(\theta_0)}$	$\bar{w} = \frac{\beta_f}{6} \delta_f^2$
Tau	$\bar{w} = \left(\frac{\beta_f}{3} - \frac{\Phi}{2\eta_f} \right) \delta_f^2$	$\bar{w} = \left(\frac{\beta_f}{3} - \frac{\Phi}{2\eta_f} \right) R^2 \frac{a_3(\theta_0)}{a_1(\theta_0)}$	$\bar{w} = \left(\frac{\beta_f}{3} - \frac{\Phi}{2\eta_f} \right) \frac{\delta_f^2}{2}$
Wall	$\bar{w} = \frac{\beta_f}{12} \delta_f^2$	$\bar{w} = \frac{\beta_f}{12} R^2 \frac{a_3(\theta_0)}{a_1(\theta_0)}$	$\bar{w} = \frac{\beta_f}{24} \delta_f^2$

The equations for β_f and Φ are given in Eq. 6-84 and 6-85 on page 112 whereas the circle equivalent radius R is given in Eq. 5-4 on page 79. The integration results a_i as a function of the wetting angle θ from zero to θ_0

$$a_i = \int_0^{\theta_0} (\cos \theta - \cos \theta_0)^i \cos \theta d\theta \tag{7-31}$$

for $i=1$ and $i=3$ are:

- $i=1$:

$$\frac{1}{2}(\theta_0 - \sin \theta_0 \cos \theta_0) \tag{7-32}$$

- $i=3$:

$$-\frac{1}{4}\cos(\theta_0)^3 \sin(\theta_0) - \frac{13}{8}\sin(\theta_0) \cos(\theta_0) + \frac{3}{8}\theta_0 + \frac{3}{2}\cos(\theta_0)^2 \theta_0 \quad (7-33)$$

The relation between the angle θ_0 and α_0 can be seen in Eq. 5-2 on page 79.

Table 7-3: Film phase mean velocity for θ_0 above 90° .

Tau	Mean Velocity
Symmetric	$\frac{R^2}{24(\pi + 2\alpha_0 + \sin(2\alpha_0))} \left[\begin{aligned} &\beta_f \left(\begin{aligned} &112 \cos^3 \alpha_0 \sin \alpha_0 - 24 \cos \alpha_0 \sin \alpha_0 + 30\pi \\ &-24\pi \cos^2 \alpha_0 - 192 \cos^2 \alpha_0 \alpha_0 + 168\alpha_0 \end{aligned} \right) \\ &+ \frac{\Phi}{\eta_f} \left(\begin{aligned} &-204 \cos^3 \alpha_0 \sin \alpha_0 + 90 \cos \alpha_0 \sin \alpha_0 - 45\pi \\ &-294\alpha_0 + 36\pi \cos^2 \alpha_0 + 312 \alpha_0 \cos^2 \alpha_0 \end{aligned} \right) \end{aligned} \right]$
Continuity	$\frac{R^2}{24(\pi + 2\alpha_0 + \sin(2\alpha_0))} \left[\begin{aligned} &\beta_f \left(\begin{aligned} &16 \cos^3 \alpha_0 \sin \alpha_0 + 72 \cos \alpha_0 \sin \alpha_0 + 30\pi \\ &-96 \alpha_0 \cos^2 \alpha_0 - 24\pi \cos^2 \alpha_0 + 72\alpha_0 \end{aligned} \right) \\ &+ \frac{\Phi}{\eta_f} \left(\begin{aligned} &-12 \cos^3 \alpha_0 \sin \alpha_0 - 102 \cos \alpha_0 \sin \alpha_0 - 102\alpha_0 \\ &-45\pi + 120 \alpha_0 \cos^2 \alpha_0 + 36\pi \cos^2 \alpha_0 \end{aligned} \right) \end{aligned} \right]$
Near-wall	$\frac{R^2}{24(\pi + 2\alpha_0 + \sin(2\alpha_0))} \left[\begin{aligned} &\beta_f \left(\begin{aligned} &128 \sin \alpha_0 - 16 \sin \alpha_0 \cos^3 \alpha_0 - 24 \sin \alpha_0 \cos \alpha_0 \\ &-24\pi \cos^2 \alpha_0 + 30\pi - 24\alpha_0 \end{aligned} \right) \\ &+ \frac{\Phi}{\eta_f} \left(\begin{aligned} &-128 \sin \alpha_0 - 6 \sin \alpha_0 \cos \alpha_0 + 20 \sin \alpha_0 \cos^3 \alpha_0 \\ &+36\pi \cos^2 \alpha_0 - 6\alpha_0 - 45\pi + 24\alpha_0 \cos^2 \alpha_0 \end{aligned} \right) \end{aligned} \right]$
Wall	Mean Velocity
	$\frac{4\beta_f R^2}{(\pi + 2\alpha_0 + \sin(2\alpha_0))} \left(\begin{aligned} &\frac{5}{64}\pi - \frac{1}{16}\pi \cos^2 \alpha_0 + \frac{11}{96}\sin^2 \alpha_0 \sin(2\alpha_0) \\ &-\frac{5}{8}\alpha_0 \sin^2 \alpha_0 - \frac{97}{192}\sin(2\alpha_0) - \frac{5}{32}\alpha_0 + \frac{4}{3}\sin \alpha_0 \end{aligned} \right)$

8 Velocity Boundary Layer

Logic will get you from A to B. Imagination will take you everywhere.

Albert Einstein

This chapter discusses the thickness and velocity profile in the boundary layer which lies between the flowing film phase and the static continuous phase. To give an idea of the magnitude of the boundary layer thickness, this is calculated according to the equation given in Chapter 6.5.1 on page 99 by means of the measured rivulet thickness. In Chapter 8.2 the general theoretical background concerning the fluid dynamics in the boundary layer is explained. Regarding rivulets, the fluid dynamics in this boundary layer is distinguished according to its wetting angle, whether the angle is smaller than 90° or above 90°. In the theoretical part, the equation used to estimate the magnitude of the boundary layer thickness when the wetting is poor, is given. A visualization of the velocity profiles in the boundary layer of a water rivulet is shown in Chapter 8.3. The boundary layer around a water rivulet flowing along a glass surface is taken as an example of the wetting with angles smaller than 90°. For angles above 90° the boundary layer around the water rivulet draining along a steel surface is shown. In the last section the influence of fluid dynamics and material properties, which depend solely on the operating conditions, on the boundary layer thickness is discussed upon the assumption that, either the film thickness or the mean film velocity is held constant. A summary of the important equations employed in the calculation of the boundary layer thickness and the velocity profile can be found at the end of this chapter in tabular form.

8.1 The Thickness

The thickness of the velocity boundary layer between static carbon dioxide and the water falling film which flows at the rates 2 g/min (along a glass surface) and 9 g/min (along a steel surface) at 313 K is shown in Fig. 8-1. This is calculated by means of the material properties and the film thickness according to Eq. 8-1 (taken from Eq. 6-34 on page 99)

$$\delta_c = \frac{\eta_c}{\eta_f} \frac{\beta_f \delta_f (\eta_f - \eta_c)}{(\beta_c \eta_c + \beta_f \eta_f)}. \quad (8-1)$$

For the estimation of the boundary layer thickness, the measured projection of the rivulet maximum thickness in Chapter 5.4 is used as the film thickness (assumption of a one-dimensional problem).

On the basis of Eq. 8-1, it seems as if the thickness of the boundary layer depends solely on the material properties. A direct influence of the fluid dynamics cannot be found in the equation. Indeed, this factor is considered and taken into account indirectly through the film thickness δ_f . This is also clearly seen in Fig. 8-1 where the thickness of the boundary layer depends additionally on the rivulet mass flow.

Even though according to Chapter 5.4, at a constant film phase mass flow, the rivulet thickness increases consistently with increasing pressure, the thickness of the boundary layer depends also on the change of the material properties. The combination of both delivers a boundary layer thickness such as seen in Fig. 8-1.

A further discussion regarding the influence of the fluid dynamics and the material properties on the boundary layer thickness can be found in details in Chapter 8.4.

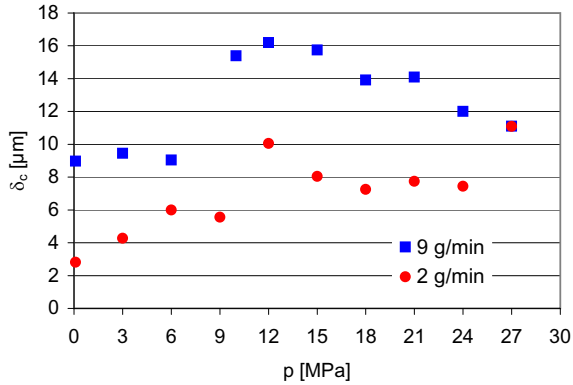


Figure 8-1: Estimation of the boundary layer thickness around a falling film at 313 K by means of the measured rivulet thickness.

8.2 Fluid Dynamics

In this section, the velocity profiles in the boundary layer for a wetting angle up to and above 90° are derived. Additionally, the boundary layer thickness in cases where the rivulet wets the vertical surface poorly is also given. As explained in Chapter 6.5.3, the velocity profile in the boundary layer is calculated and visualized only around one half of the rivulet or film cross-section because the film and thus the boundary layer velocity profile are symmetrical with respect to the y -axis.

8.2.1 Wetting Angle up to 90°

As explained in 6.5.1 the parabolic velocity equation in the boundary layer is

$$w_c(y_c) = \frac{\beta_c}{2} y_c^2 + c_{1c} y_c \quad (8-2)$$

when a new coordinate system y_c is employed in order to let the calculation be as simple as possible. It is assumed that the velocity w_c is equal to zero at $y_c = 0$. And as a result, the second constant c_{0c} is zero. Upon employing Eq. 6-23 on page 97 and Eq.6-26 on page 97, the constant c_{1c} can be written as

$$c_{1c} = \frac{\frac{1}{2}\beta_f \delta_f^2 \eta_f - \frac{1}{2}\beta_c \delta_c^2 \eta_f - \beta_c \delta_c \delta_f \eta_c}{\delta_c \eta_f + \delta_f \eta_c}. \quad (8-3)$$

When the thickness of the boundary layer δ_c in Eq. 8-3 is substituted by the right-hand term in Eq. 8-1, the constant c_{1c} depends only on the film thickness δ_f and the material properties which are summarized in terms of the parameter Ξ

$$c_{1c} = \Xi \delta_f. \quad (8-4)$$

The parameter Ξ in Eq. 8-4 is a function of the densities and the viscosities of both phases

$$\Xi = f(\beta_c, \beta_f, \eta_c, \eta_f) \quad (8-5)$$

and can be calculated according to

$$\Xi = \frac{\beta_f \left[\beta_f \eta_f^2 (3\beta_c \eta_c^2 - \beta_f \eta_f^2 - 2\beta_c \eta_c \eta_f) - \beta_c \eta_c^2 \eta_f (\beta_c \eta_f + 4\beta_f \eta_c) \right] + \beta_c \eta_c^3 (\beta_f \eta_c + 2\beta_c \eta_f - 2\beta_c \eta_c)}{2\eta_c \eta_f (\beta_c \eta_c + \beta_f \eta_f) (\beta_f \eta_c - \beta_c \eta_c - 2\beta_f \eta_f)}. \quad (8-6)$$

The parabolic velocity equation in the boundary layer according to Eq. 8-2 can be written in terms of y_c or transformed back to the coordinate system y , so that only one universal coordinate system is needed. Both coordinate systems are related by

$$y = (\delta_f + \delta_c) - y_c \quad (8-7)$$

or

$$y_c = (\delta_f + \delta_c) - y \quad (8-8)$$

so that

$$w_c(y) = \frac{\beta_c}{2} (\delta_c + \delta_f - y)^2 + c_1 (\delta_c + \delta_f - y). \quad (8-9)$$

Upon employing Eq. 8-4

$$w_c(y) = \frac{\beta_c}{2} y^2 - (\beta_c (\delta_c + \delta_f) + \Xi \delta_f) y + (\delta_c + \delta_f) (\beta_c (\delta_c + \delta_f) + \Xi \delta_f) \quad (8-10)$$

or in terms of $h(x)$

$$w_c(y) = \frac{\beta_c}{2} y^2 - (\beta_c (\delta_c(x) + h(x)) + \Xi h(x)) y + (\delta_c(x) + h(x)) (\beta_c (\delta_c(x) + h(x)) + \Xi h(x)) \quad (8-11)$$

where the rivulet thickness is written in terms of its dependency on the coordinate system x , with $h(x)$ according to Eq. 6-86 for a circular cross-section or Eq. 6-87 for a triangular cross-

section (see page 112). For a wide covering thin falling film, where the cross-section is assumed to have a rectangular shape, the film thickness is a constant and Eq. 8-10 is valid.

8.2.2 Wetting Angle above 90°

The velocity profile such as given in Eq. 8-11 is valid for the boundary layer around the borderline DG or in terms of the angle $0^\circ \leq \alpha \leq 90^\circ$. An equation which describes the velocity around the borderline BD expressed by $-\alpha_0 \leq \alpha < 0^\circ$ is still unknown.

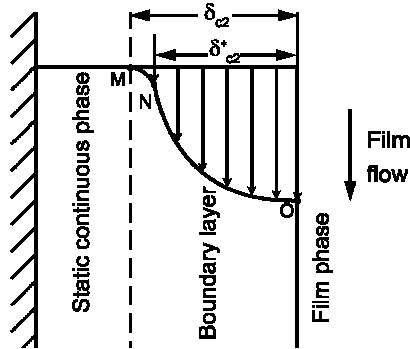


Figure 8-2: A sigmoidal function approximated by two parabolas describes the velocity profile in the boundary layer precisely.

Two simplifications in calculating the velocity profile around the borderline BD are made. The first being the velocity profile in the boundary layer. The second is related to the velocity gradient taken into account for the calculation of the shear stress τ .

The velocity profile in the boundary layer is a sigmoidal function as can be seen in Fig. 8-2. The precise velocity profile in the boundary layer has a s-shape. The sigmoidal curve MNO can be approximated by two parabolas which follow the model $y = ax^2 + bx + c$, or here $w = ay^2 + by + c$ with $a > 0$ from point M to point N and $a < 0$ from point N to point O. At point M, there is a transition from the boundary layer to the static continuous phase. At this point, the curve is continuously differentiable and has a velocity of zero. At point N, the second derivation of the velocity with respect to y-axis $\frac{\partial^2 w}{\partial y^2}$ is equal to zero. It is the inflection point

of the sigmoidal function. From the mathematical point of view, it is highly complicated to perform an analytical solution of the velocity profile having a sigmoidal shape. In addition, if the distance MN and the velocity at point N are too small to be significant (see Fig. 8-2), point N instead of point M can be considered as the starting point of the function. In other words, as long as the width of the real boundary layer δ_{c2} is approximately equal to the width δ_{c2}^* of the

section NO of the sigmoidal curve ($\delta_{c2} \approx \delta_{c2}^*$, see Fig. 8-2), the sigmoidal function can be approximated by a parabola to calculate the velocity profile. This mathematical solution is accurate enough although the real profile of the velocity in the boundary layer is not parabolic. As for the second simplification, it is stressed once again that the shear stress τ is derived from the velocity gradient $\frac{\partial w}{\partial y}$ which is perpendicular to the film flow direction but not to the film interface (see explanation in Section 6.5.1, Fig. 6-5).

In the next step, a force balance on an infinitesimal volume element in the boundary layer between the gravitational force and the forces result from the shear stress can be written

$$\rho_c g dx dy dz = (-\tau(y+dy) + \tau(y)) dx dz. \tag{8-12}$$

Assuming a flow behaviour of Newtonian fluid

$$\frac{\partial^2 w}{\partial y_c^2} = -\frac{\rho_c g}{\eta_c} = -\beta_c \tag{8-13}$$

where the product of the continuous phase density ρ_c and the acceleration due to the gravitation g divided by the viscosity η_c is collected in a single term called β_c . Thus, the typical parabolic velocity equation around the borderline BD is found

$$w_c(y) = -\frac{\beta_c}{2} y^2 + c_1 y + c_2 \tag{8-14}$$

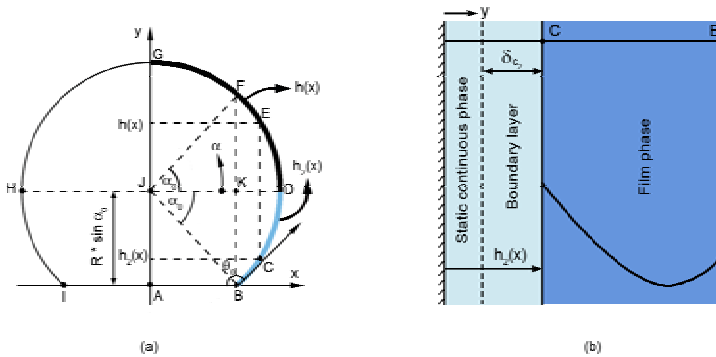


Figure 8-3: Estimation of the velocity boundary layer thickness around the borderline BD.

The velocity profile in the film phase BDF (without any wall contact) along the y-axis is reported in 6.5.3 on page 108 . The main idea in solving Eq. 8-14 is to make use of the already known velocity profile in the film phase according to the tau model with near-wall boundary conditions. To comply with the requirements already made in 6.5.3 for the velocity profile around DG, the shear stresses and the velocities in both phases have to be mathematically linked.

The first boundary condition is regarding the equality of the velocities in both phases at the borderline

$$w_c(y = h_2(x)) = w_f(y = h_2(x)) \quad (8-15)$$

$h_2(x)$ is a function which describes the curvature and thus, the position of the borderline BD relative to the vertical wall ($y=0$). This function is given in Section 8.5. The thickness of the boundary layer around the borderline BD is referred to as δ_{c_2} (see Fig. 8-3).

Upon employing Eq. 8-14 for the calculation of the velocity profile in the boundary layer

$$w_c(y = h_2(x)) = -\frac{\beta_c}{2} h_2(x)^2 + c_1 h_2(x) + c_2 \quad (8-16)$$

and Eq. 6-83 for the film phase

$$w_f(y = h_2(x)) = -\frac{\beta_f}{2} h_2(x)^2 + \left(\beta_f - \frac{\Phi}{\eta_f} \right) h(x) h_2(x) \quad (8-17)$$

and putting them into Eq. 8-15 and solved for the constant c_2

$$c_2 = h_2(x)^2 \left(\frac{\beta_c}{2} - \frac{\beta_f}{2} \right) + \left(\beta_f - \frac{\Phi}{\eta_f} \right) h(x) h_2(x) - c_1 h_2(x) \quad (8-18)$$

The constant c_2 in Eq. 8-18 contains c_1 which is still unknown. The boundary layer ends at the distance δ_{c_2} away from the film phase or from the borderline (see Fig. 8-3b). This is used as the second boundary condition

$$w_c(y = h_2(x) - \delta_{c_2}(x)) = 0 \quad (8-19)$$

upon employing Eq. 8-14

$$w_c(y = h_2(x) - \delta_{c_2}(x)) = -\frac{\beta_c}{2} \left(h_2(x) - \delta_{c_2}(x) \right)^2 + c_1 \left(h_2(x) - \delta_{c_2}(x) \right) + c_2 = 0 \quad (8-20)$$

Equation 8-20 contains the local thickness of the boundary layer δ_{c_2} whose magnitude is not known. Therefore the equality of the shear stresses at the surface is

$$\tau_c(y = h_2(x)) = \tau_f(y = h_2(x)) \quad (8-21)$$

with the magnitude of the shear stress approached from the continuous phase

$$\tau_c = \eta_c \left(-\beta_c h_2(x) + c_1 \right) \quad (8-22)$$

and approached from the film phase

$$\tau_f(y = h_2(x)) = \eta_f \left(-\beta_f h_2(x) + \left(\beta_f - \frac{\Phi}{\eta_f} \right) h(x) \right) \quad (8-23)$$

delivers the constant c_1

$$c_1 = \frac{\eta_f}{\eta_c} \left(-\beta_f h_2(x) + \left(\beta_f - \frac{\Phi}{\eta_f} \right) h(x) \right) + \beta_c h_2(x) \quad (8-24)$$

and c_2 upon employing Eq. 8-18 and Eq. 8-24

$$c_2 = \frac{h_2(x)}{2 \eta_c \eta_f} \left(\begin{array}{l} -\beta_c h_2(x) \eta_c \eta_f - h_2(x) \eta_c \eta_f \beta_f \\ +2 h(x) \eta_c \beta_f \eta_f - 2 h(x) \eta_c \Phi \\ +2 \beta_f h_2(x) \eta_f^2 - 2 h(x) \beta_f \eta_f^2 + 2 \eta_f h(x) \Phi \end{array} \right) \quad (8-25)$$

Substituting c_1 and c_2 in Eq. 8-20 by the expressions in Eq. 8-24 and Eq. 8-25 respectively, and factoring the second degree polynomial for the thickness of the boundary layer δ_{c_2}

$$\delta_{c_2} = \frac{1}{\beta_c \eta_c} + \frac{k_1}{\sqrt{\eta_f}} \left[\begin{array}{l} \beta_f \eta_f h_2(x) - (\beta_f \eta_f - \Phi) h(x) \\ \left(\begin{array}{l} \eta_f h(x)^2 \Phi^2 + 2 \eta_f^2 h(x) \Phi \beta_f h_2(x) \\ -2 \eta_f^2 h(x)^2 \Phi \beta_f + \beta_f^2 h_2(x)^2 \eta_f^3 \\ -2 \beta_f^2 h_2(x) \eta_f^3 h(x) + h(x)^2 \beta_f^2 \eta_f^3 \\ -\beta_c \eta_c^2 \eta_f h_2(x)^2 \beta_f - 2 \beta_c \eta_c^2 h_2(x) h(x) \Phi \\ +2 \beta_c \eta_c^2 \eta_f h_2(x) h(x) \beta_f \end{array} \right)^{\frac{1}{2}} \end{array} \right] \quad (8-26)$$

The solution of the second order polynomial in δ_{c_2} delivers two possibilities for the magnitude of δ_{c_2} due to the fact that the result of a square root can be positive or negative. The possible algebraic signs of the square root are written in terms of k_1 which is either +1 or -1 and thus, the term in the brackets behind k_1 contains only the absolute value.

At the wall the film phase does not flow, the film velocity at the surface is zero and thus, no boundary layer exists there. This can be used as a condition to solve the above mentioned mathematical problem.

At point B (see Fig.8-3a) with

$$h_2(x) = 0 \quad (8-27)$$

the film touches the wall already and due to the no-slip condition at the wall surface, the molecules of the film stick on the wall. No film flow means logically there exists no velocity boundary layer as well

$$\delta_{c_2} = 0 \quad (8-28)$$

and thus at $y=0$

$$\delta_{c_2} = \frac{1}{\beta_c \eta_c} \left[-(\beta_f \eta_f - \Phi) h(x) + \frac{k_1}{\eta_f} \left(\eta_f^2 h(x)^2 (\Phi^2 - 2 \beta_f \eta_f \Phi - \beta_f^2 \eta_f^2) \right)^{\frac{1}{2}} \right] \quad (8-29)$$

There are two possibilities in factoring the second order polynomial in the last term in the brackets of Eq. 8-29. The first one is in terms of $(\Phi - \beta_f \eta_f)^2$

$$\delta_{c_2} = \frac{1}{\beta_c \eta_c} \left[-(\beta_f \eta_f - \Phi) h(x) + \frac{k_1}{\eta_f} \left(\eta_f^2 h(x)^2 (\Phi - \beta_f \eta_f)^2 \right)^{\frac{1}{2}} \right] \quad (8-30)$$

and the second possibility is in terms of $(\beta_f \eta_f - \Phi)^2$

$$\delta_{c_2} = \frac{1}{\beta_c \eta_c} \left[-(\beta_f \eta_f - \Phi) h(x) + \frac{k_1}{\eta_f} \left(\eta_f^2 h(x)^2 (\beta_f \eta_f - \Phi)^2 \right)^{\frac{1}{2}} \right] \quad (8-31)$$

The afore-mentioned condition can be used as an orientation to decide whether Eq. 8-30 or 8-31 should be taken, i.e. the square root terms behind k_1 comprise now only the absolute value and thus, taking the product of the three quadratic terms of Eq. 8-30 out of its square root yields

$$\delta_{c_2} = \frac{1}{\beta_c \eta_c} \left[(\Phi - \beta_f \eta_f) h(x) + k_1 h(x) \underbrace{(\Phi - \beta_f \eta_f)}_{>0} \right] \quad (8-32)$$

Equation 8-32 is valid if $(\Phi - \beta_f \eta_f) > 0$. Otherwise

$$\delta_{c_2} = \frac{1}{\beta_c \eta_c} \left[(\Phi - \beta_f \eta_f) h(x) + k_1 h(x) \underbrace{(\beta_f \eta_f - \Phi)}_{>0} \right] \quad (8-33)$$

Equation 8-33 is derived from Eq.8-31.

Considering these two possibilities, the condition in Eq. 8-28– δ_{c_2} is equal to zero—can only be fulfilled with the following criteria for k_1 :

- $k_1 = -1$ when $(\Phi - \beta_f \eta_f) > 0$
- $k_1 = 1$ when $(\Phi - \beta_f \eta_f) < 0$

That means, depending on the magnitude of Φ and $(\beta_f \eta_f)$ the value of k_1 is either equal to 1 or -1 and the magnitude of δ_{c_2} in Eq. 8-26 can be estimated.

8.3 Velocity Profile

8.3.1 Wetting Angle up to 90°

One half of the velocity boundary layer which exists between the flowing film phase and the static continuous phase is shown in Fig. 8-4. This is the boundary layer around a water rivulet draining along a glass surface at 313 K and 21 MPa. The flow rate of the rivulet in supercritical carbon dioxide is 1.65 g/min. The rivulet wets the vertical surface with an angle of 63.5° , the circle equivalent radius is 1.07 mm.

The thickness of the boundary layer varies between $9.6 \mu\text{m}$ (at $x = 0$) and zero where the molecules of the film phase stick on the wall (at the three-phase-contact-line between the solid, the liquid and the fluid phase).

The maximal velocity $w = 4.2 \text{ cm/s}$ is reached exactly at the film surface at $x = 0$. The enlarged velocity profile can be seen clearly in Fig. 8-5.

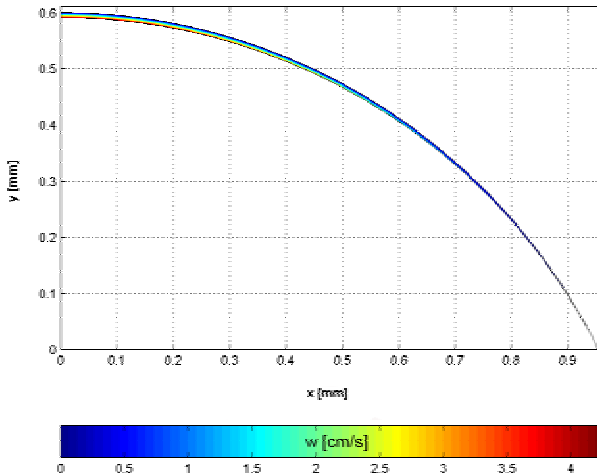


Figure 8-4: Velocity profile in the boundary layer between carbon dioxide and a water rivulet flowing along a glass surface at 313 K, 21 MPa and a water mass flow of 1.65 g/min.

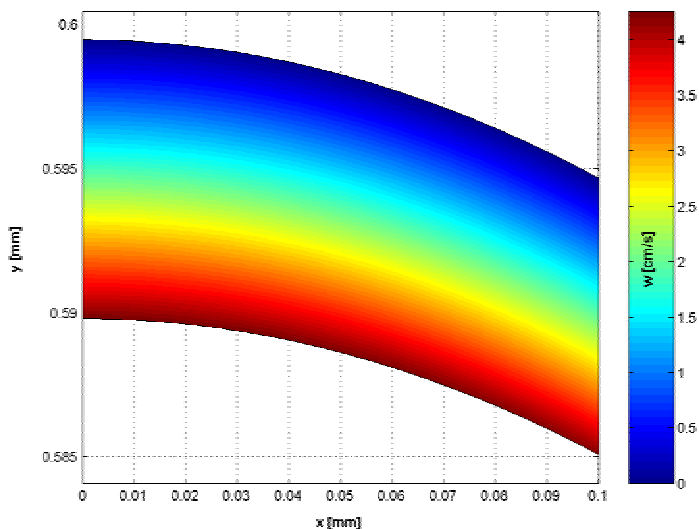


Figure 8-5: Enlarged velocity profile in the boundary layer between carbon dioxide and a water rivulet flowing along a glass surface at 313 K, 21 MPa and a water mass flow of 1.65 g/min.

8.3.2 Wetting Angle above 90°

The velocity profile in the boundary layer lying between the water rivulet flowing along a steel surface and supercritical carbon dioxide can be found in Fig. 8-6. The water rivulet flows with a rate of 9 g/min at 313 K and 21 MPa. The rivulet wets the vertical surface with an angle of 107° whereas the circle equivalent radius is 0.67 mm. The magnitude of the boundary layer thickness δ_c in the middle of the rivulet width at $x = 0$ is 14 μm and the maximal velocity is 9.1 cm/s. The enlarged boundary layer can be seen in Fig. 8-7.

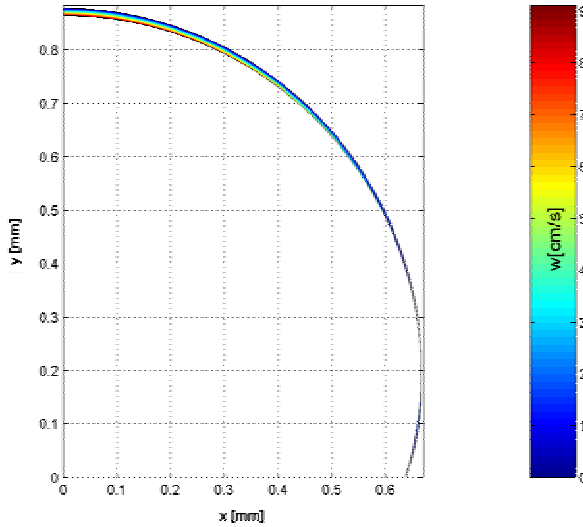


Figure 8-6: Velocity profile in the boundary layer between carbon dioxide and a water rivulet flowing along a steel surface at 313 K, 21 MPa. Water mass flow: 9 g/min.

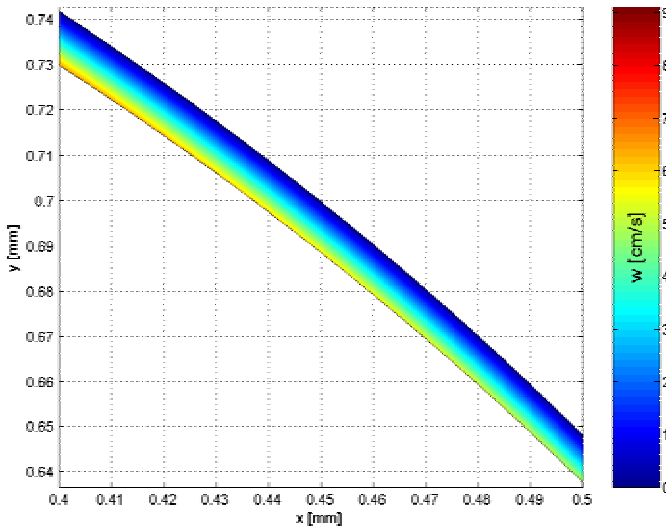


Figure 8-7: Enlarged velocity profile in the boundary layer between carbon dioxide and a water rivulet flowing along a steel surface at 313 K, 21 MPa. Water mass flow: 9 g/min.

8.4 The Influence of Fluid Dynamics and Material Properties

The most important equations regarding the calculation of the boundary layer thickness and the velocity profile in this boundary layer have been introduced. Thus, the discussion which is focused on the dependency of the boundary layer thickness on the fluid dynamics and the material properties such as density and viscosity can be held.

If the discussion is focused on a wide covering falling film with an approximately constant thickness in its whole width (a one dimensional problem), then the ratio of the boundary layer and the falling film thickness can be estimated with help of Eq. 8-1 on page 135. The magnitude of this ratio for the system water-CO₂ and corn germ oil-CO₂ at 313 K and 333 K respectively is calculated theoretically and can be seen in Fig. 8-8. The material properties needed for the estimation are taken from the literature [92,185]. Due to the lack of data, the dynamic viscosity of with carbon dioxide saturated corn germ oil at 338 K is used here. In the calculation, it is assumed that the film phase is saturated by the continuous phase.

The thickness ratio of the boundary layer and the falling film depends solely on the material properties, which are, in turn, a function of the operating conditions. The influence of the operating conditions on the ratio is seen clearly in Fig. 8-8. The dependency of the thickness ratio on the system pressure for the system water-CO₂ is different than the one observed when corn germ oil is used.

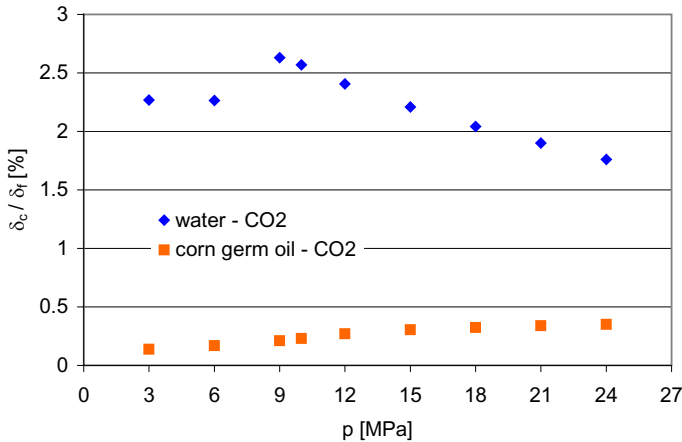


Figure 8-8: The thickness ratio of the velocity boundary layer and the falling film for the system water-CO₂ at 313 K and for corn germ oil-CO₂ at 333 K.

As is commonly known, water density does not change appreciably with pressure whereas the density of carbon dioxide does. As a result, the density difference between the phases becomes smaller with increasing pressure while the liquid viscosity remains nearly constant. That is why,

the value of β_f decreases consistently if the pressure is raised. This is also reflected in the thickness ratio such as given in Fig. 8-8. In supercritical carbon dioxide, the ratio decreases markedly with increasing pressure. However, it remains nearly constant at lower pressure where the carbon dioxide is still gaseous. The appreciable jump in the thickness ratio to a higher value between 6 MPa and 9 MPa can be explained through the change in the dynamic viscosity of carbon dioxide which becomes noticeably larger when it becomes supercritical (it becomes twice as large as before when the pressure is raised from 6 MPa to 9 MPa).

In contrast to the water-CO₂ system, the thickness ratio of the corn germ oil increases with increasing pressure. This can be understood by observing the dependency of the corn germ oil material properties on the amount of dissolved carbon dioxide in it. As pressure increases, which means, the dissolved amount of carbon dioxide rises too, the density of the oil increases a little bit while the dynamic viscosity drops appreciably. As an example: if the pressure is increased at 313 K from 3 MPa to 24 MPa, the oil dynamic viscosity at the higher pressure falls to just one fourth of the initial value.

Although the density difference $\Delta\rho$ decreases as pressure increases, the effect of the fall in the oil viscosity on the thickness ratio is stronger

$$\frac{\delta_c}{\delta_f} = \frac{\eta_c}{\eta_f^2} (\eta_f - \eta_c) \frac{\Delta\rho}{(\Delta\rho + \rho_c)}. \quad (8-34)$$

This is even enhanced by the rise in the carbon dioxide viscosity and results in an increase in the thickness ratio as pressure increases, as can be seen in Eq. 8-34 where the thickness ratio is written in terms of the densities and the viscosities instead of the viscosities and the β 's.

Physically, the whole phenomenon can be very well explained by focusing on the drop in the oil viscosity and the rise in the carbon dioxide viscosity. A lower liquid viscosity allows a better flow behaviour and thus, at the same operating condition and the same liquid rate of flow, a lower viscosity lets the liquid drain faster along the vertical solid surface. And therefore, the local film velocity at the surface is also larger, which means a thicker boundary layer is required to reduce the velocity down to zero. If at the same time the continuous phase viscosity increases, the space needed to hold down the velocity is even greater until the value of zero is reached.

Up to now, the discussion about the thickness ratio in terms of its dependency on the operating condition has been carried out. However, the absolute value of the boundary layer thickness itself depends not only on the material properties but, as one might expect, it is also affected by the fluid dynamics. In order to take both into consideration, either the film thickness or the mean velocity is held constant in the whole pressure range. When the film thickness is kept constant, the influence of the fluid dynamics and the material properties are considered, whereas when the mean velocity remains the same, only the influence of the material properties is investigated. In this case, the fluid dynamics are not considered.

8.4.1 Constant Film Thickness

By assuming a constant film thickness of 1 mm over the whole pressure range from 3 MPa up to 24 MPa, the thickness ratio calculated for the systems water and corn germ oil films embedded in pressurized carbon dioxide at 313 K and 333 K respectively (Fig. 8-8) can be employed to estimate the absolute thickness of the velocity boundary layer. The thickness of the velocity boundary layer of both systems does not change uniformly as the pressure increases.

In gaseous carbon dioxide, the thickness of the water film velocity boundary layer remains nearly constant. A decrease of the thickness with increasing pressure is seen clearly in supercritical carbon dioxide. The explanation for this behaviour can be found in the change of the material properties which at the same time affect the fluid dynamics too.

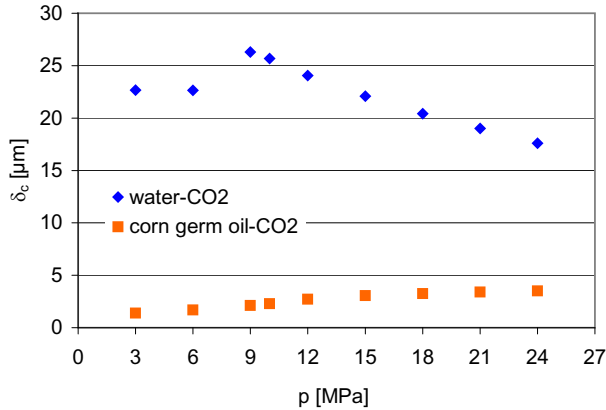


Figure 8-9: The thickness of the velocity boundary layer estimated by assuming the film thickness $\delta_f = 1$ mm.

The water film thickness can be held constant over the whole pressure range by adjusting the film velocity. According to the equation given in 7.5, the mean velocity of a wide covering thin

film calculated by means of the tau model is a product of $\left(\frac{\beta_f}{3} - \frac{\Phi}{2\eta_f}\right)$ and the square of the

film thickness. The dependency of the term $\left(\frac{\beta_f}{3} - \frac{\Phi}{2\eta_f}\right)$ on the pressure is shown in Fig. 8-10.

For the system water-carbon dioxide, the value of $\left(\frac{\beta_f}{3} - \frac{\Phi}{2\eta_f}\right)$ decreases from $2850 \frac{1}{\text{mm s}}$ at

3 MPa down to $270 \frac{1}{\text{mm s}}$ at 24 MPa which means that if the film thickness is to be kept

constant in the whole pressure range, the film phase velocity has to be lowered as the pressure is increasing. A constant film phase velocity at increasing pressure causes, purely theoretically, a thicker film which is not desired here. According to the mass continuity equation, at a constant flow cross-section the mass flow has to be lowered if the mean liquid velocity is to be decreased (the rise in the liquid density with increasing pressure is negligible). A fall in the rate of flow and thus a fall in the mean velocity is responsible for a thinner velocity boundary layer because less distance is needed to hold down the velocity which is already sufficiently low. This is the explanation for the fall in the boundary layer thickness as the pressure increases.

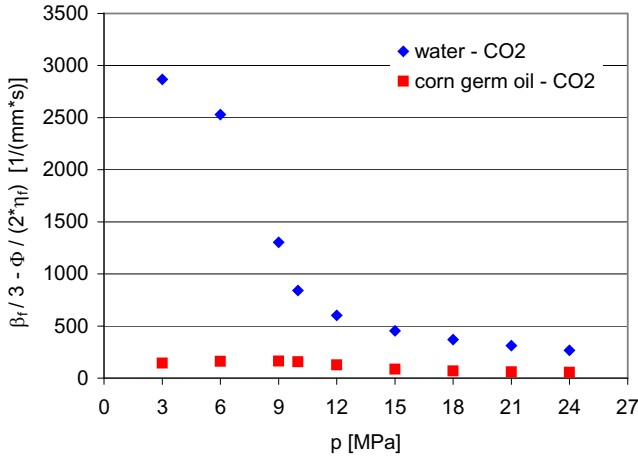


Figure 8-10: The dependency of $\left(\frac{\beta_f}{3} - \frac{\Phi}{2\eta_f}\right)$ on the pressure for the systems water-carbon dioxide at 313 K and corn germ oil-carbon dioxide at 333 K.

In contrast to the system water-CO₂, the value of $\left(\frac{\beta_f}{3} - \frac{\Phi}{2\eta_f}\right)$ for the system corn germ oil-carbon dioxide does not change uniformly as the pressure increases. The diagram resembles a parabolic curve with a maximum in the vicinity of the carbon dioxide critical pressure, which means this parameter increases first with increasing pressure. After the maximum has been reached, the parameter falls as the pressure increases (this is to be seen vaguely in Fig. 8-10 due to the scaling of y-axis). The value of $\left(\frac{\beta_f}{3} - \frac{\Phi}{2\eta_f}\right)$ in Fig. 8-10 for the system corn germ oil-CO₂ varies from $55 \frac{1}{mm \cdot s}$ to $160 \frac{1}{mm \cdot s}$. The slight increase in $\left(\frac{\beta_f}{3} - \frac{\Phi}{2\eta_f}\right)$ in the lower pressure range forces an increase in the mean film velocity if the film thickness of corn germ oil

is to be kept constant. This is reached by increasing the liquid mass flow which has a consequence that the force (inserted by the liquid film) which sweeps the molecules in the continuous phase to flow in the direction of gravitation, becomes higher. And a larger boundary layer thickness is required to obtain a velocity of zero.

Although at higher pressure range the mass flow of the film phase has to be decreased in order to keep the film thickness constant, the influence of the dynamic viscosity of both phases becomes more dominant. The increase of the carbon dioxide viscosity, enhanced by the decrease in the oil viscosity, is responsible for the rise of the boundary layer thickness even when the mass flow is decreased.

Comparing the boundary layer thickness around both films, water as well as corn germ oil, the thickness of the boundary layer around the water film is apparently larger than the corn germ oil film (see Fig. 8-9). The boundary layer around the water film ranges between 13 μm and 23 μm whereas around the corn germ oil film, it has a thickness of 1.5 μm -3.5 μm . The reason that the boundary layer around the water film is, at exactly the same operating conditions and the same film thickness, nearly eight times thicker than the one around oil film, lies in the different order of magnitude of the liquid viscosities. At 338 K, the viscosity of corn germ oil at 3 MPa is 27 times that of water, while at 24 MPa the previous one has a viscosity which is 7 times as large as the latter one. The high oil viscosity is responsible for the narrower velocity boundary layer due to the fact that the high viscosity prevents the film from flowing and thus, less distance is needed to stop the molecules flow totally.

8.4.2 Constant Mean Velocity

Keeping the mean velocity of the film constant means taking the fluid dynamics out of consideration and concentrating only on the effect of the material properties which in turn, depend on the operating conditions. If the mean velocity of the film is to be kept constant as the pressure increases, the mass flow has to be raised due to the fall in the density difference which slows the film and inhibits it from flowing. At the same time the film thickness becomes larger

and thus, compensates for the fall in $\left(\frac{\beta_f}{3} - \frac{\Phi}{2\eta_f} \right)$ with increasing pressure (see Fig. 8-10). The

dependency of the film thickness on the pressure at a constant film mean velocity is given in Fig. 8-11. In contrast to the water film thickness, which increases consistently with the pressure, the oil film first decreases slightly before it increases with the pressure. This is due to the

parabolic shaped curve when the value $\left(\frac{\beta_f}{3} - \frac{\Phi}{2\eta_f} \right)$ is plotted against the pressure (Fig. 8-10).

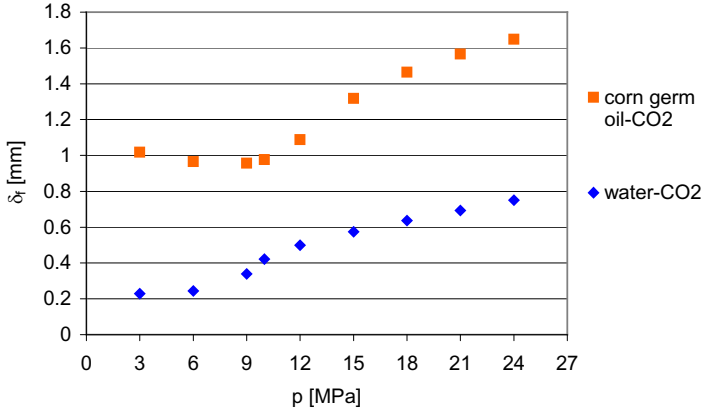


Figure 8-11: The estimated film thickness by assuming a constant mean film velocity of 15 cm/s in the whole pressure range.

Despite the commonly known excellent wetting characteristics of oil, the film thickness of water in Fig. 8-11 varies between 0.23 mm and 0.75 mm which is very thin when compared with the oil film which ranges between 0.96 mm and 1.65 mm. However, it has to be kept in mind that the film thickness is theoretically calculated by assuming a constant liquid velocity

and that the value of $\left(\frac{\beta_f}{3} - \frac{\Phi}{2\eta_f}\right)$ —which plays the role of a kind of proportionality constant in

the equation of the mean velocity—for oil is far lower than that of water. And as a consequence, the film thickness of the oil becomes far larger than that of water. The excellent wettability of oil when compared with water is of no importance, because here a perfect wetting of the thin, wide covering continuous film is assumed regardless of the liquid or the vertical surface employed.

By combining the film thickness obtained with the ratio of the film and the boundary layer thickness such as shown in Fig. 8-8, the thickness of the boundary layer at a constant film mean velocity can be calculated. The result can be seen in Fig. 8-12.

Regardless of the liquid material, the boundary layer thickness δ_c increases with increasing pressure. The sharp rise in the water film thickness above 12 MPa (Fig. 8-11) is compensated for the fall in the thickness ratio (see Fig. 8-8) which can be seen in the leveling off of the thickness of the water velocity boundary layer in Fig. 8-12.

As for corn germ oil, the slight decrease in the film thickness in the lower pressure range does not affect the thickness of the boundary layer appreciably. The boundary layer thickness increases consistently with increasing pressure.

Even though at the same mean velocity the oil film is far thicker than the water film, the boundary layer around the oil film is still thinner than that around the water film. According to the calculation made and shown in Fig. 8-12, the boundary layer around the corn germ oil film has a thickness of between 1.4 μm and 5.8 μm , while the thickness of the water boundary layer ranges between 5.2 μm and 13.2 μm . The explanation for the thin boundary layer around the oil film lies in the magnitude of the thickness ratio given in Fig. 8-8. The thickness ratio of the boundary layer and the water film lies between 1.7 % and 2.7 %. For oil film, this value ranges only between 0.14 % and 0.35 %.

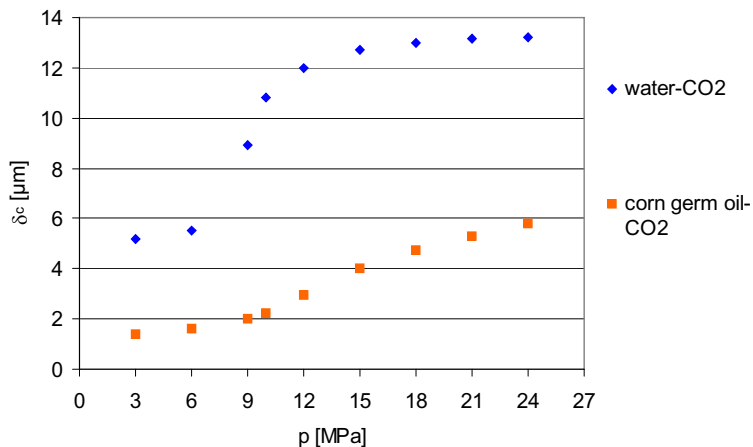


Figure 8-12: The estimated boundary layer thickness by assuming a constant mean film velocity of 15 cm/s in the whole pressure range.

8.5 List of Equations

Table 8-1: Thickness and velocity profile in the boundary layer for $0 \leq \alpha \leq \pi/2$.

	$0 \leq \alpha \leq \frac{\pi}{2}$ (around the borderline DG, see Fig.8-3 on page 139)
Thickness	$\delta_c = \frac{\eta_c}{\eta_f} \frac{\beta_f \delta_f (\eta_f - \eta_c)}{(\beta_c \eta_c + \beta_f \eta_f)}$
Velocity	$w_c(y) = \frac{\beta_c}{2} y^2 - (\beta_c (\delta_c(x) + h(x)) + \Xi h(x)) y$ $+ (\delta_c(x) + h(x)) \left(\frac{\beta_c}{2} (\delta_c(x) + h(x)) + \Xi h(x) \right)$ <p>with</p> $\Xi = \frac{\beta_f \left[\beta_f \eta_f^2 (3\beta_c \eta_c^2 - \beta_f \eta_f^2 - 2\beta_c \eta_c \eta_f) - \beta_c \eta_c^2 \eta_f (\beta_c \eta_f + 4\beta_f \eta_c) \right] + \beta_c \eta_c^3 (\beta_f \eta_c + 2\beta_c \eta_f - 2\beta_c \eta_c)}{2\eta_c \eta_f (\beta_c \eta_c + \beta_f \eta_f) (\beta_f \eta_c - \beta_c \eta_c - 2\beta_f \eta_f)}$ <p>for rectangular cross-section (one dimension problem): $h(x) = \delta_f$.</p> <p>for circular and triangular cross-section: $h(x)$ see Eq. 6-86 and Eq. 6-87 in 6.6 on page 112.</p>

Table 8-2: Thickness and velocity profile in the boundary layer for $-\alpha_0 \leq \alpha < 0$.

	$-\alpha_0 \leq \alpha < 0$ (around the borderline BD, see Fig.8-3 on page 139)
Thickness	$\delta_{c_2} = \frac{1}{\beta_c \eta_c} + \frac{k_1}{\sqrt{\eta_f}} \left[\begin{array}{l} \beta_f \eta_f h_2(x) - (\beta_f \eta_f - \Phi) h(x) \\ \eta_f h(x)^2 \Phi^2 + 2 \eta_f^2 h(x) \Phi \beta_f h_2(x) \\ -2 \eta_f^2 h(x)^2 \Phi \beta_f + \beta_f^2 h_2(x)^2 \eta_f^3 \\ -2 \beta_f^2 h_2(x) \eta_f^3 h(x) + h(x)^2 \beta_f^2 \eta_f^3 \\ -\beta_c \eta_c^2 \eta_f h_2(x)^2 \beta_f - 2 \beta_c \eta_c^2 h_2(x) h(x) \Phi \\ +2 \beta_c \eta_c^2 \eta_f h_2(x) h(x) \beta_f \end{array} \right]^{\frac{1}{2}}$ <p>with</p> $k_1 = -1 \quad \text{if } (\Phi - \beta_f \eta_f) > 0$ $k_1 = 1 \quad \text{if } (\beta_f \eta_f - \Phi) > 0$
Velocity	$w_c(y) = -\frac{\beta_c}{2} y^2 + c_1 y + c_2$ <p>with</p> $c_1 = \frac{\eta_f}{\eta_c} \left(-\beta_f h_2(x) + \left(\beta_f - \frac{\Phi}{\eta_f} \right) h(x) \right) + \beta_c h_2(x)$ $c_2 = \frac{h_2(x)}{2 \eta_c \eta_f} \left(\begin{array}{l} -\beta_c h_2(x) \eta_c \eta_f - h_2(x) \eta_c \eta_f \beta_f \\ +2 h(x) \eta_c \beta_f \eta_f - 2 h(x) \eta_c \Phi \\ +2 \beta_f h_2(x) \eta_f^2 - 2 h(x) \beta_f \eta_f^2 + 2 \eta_f h(x) \Phi \end{array} \right)$ <p>with</p> $h_2(x) = R(\sin \alpha_0 - \sin \alpha)$

9 Shear Stress Exerted at Rivulet and Film Surface

Genius is eternal patience.

Michaelangelo

Seen in one dimension, the surface shear stress is a product of the parameter Φ and the film thickness itself (see Eq. 6-35 on page 99). However, it can also be written in terms of its dependency on the x-axis

$$\tau_0 = \Phi h(x). \quad (9-1)$$

This is the local shear stress at the interphase between the film and the continuous phase at a point $(x, h(x))$. If it is required, the friction between the adjacent molecules in the film phase can be estimated with the help of the above mentioned equation so that the shear stress at each point (x,y) is known. Depending on the local film thickness $h(x)$, the magnitude of the shear stress is not in general homogenous along the whole borderline. In order to give an idea of the magnitude of the shear stress, this value is averaged over the whole length of the boundary layer. In this chapter, the integration and its limits to obtain the mean shear stress are introduced briefly. The theoretical calculation is divided into two parts. One is the wetting angle which is smaller than or equal to 90° and the other one is the wetting angle above 90° . For the wetting angle up to 90° the three geometrical shapes of the cross-section are applied for the tau and the wall model (in the Nusselt model no surface shear stress exists). And for wetting angles above 90° , the wall model and the tau model in combination with the three different sets of boundary conditions are employed. The results of the calculation are compared with the reference shear stress value in the second section. And the equations used to estimate the shear stress are given in Section 9.3.

9.1 Theoretical Background

9.1.1 Wetting Angle up to 90°

Usually if a theory is developed in order to estimate a measurable quantity, the theory is, in turn, proved by means of a comparison between the predicted value and the actual measurement. In cases where shear stress is concerned, such a direct comparison is not possible due to the fact that the surface shear stress cannot be measured directly. However, a reference quantity is required—even though the validity of this value to be used as a reference might still need to be proved—to be certain whether the forecast value is reasonable and whether the theory developed is applicable or not. For this purpose, this section starts with an attempt to estimate the magnitude of the shear stress by using the measured values and is then followed by the calculations of the shear stress with the help of the already known theory. Although the

estimated value which is used later as a reference is not the experimental value in the sense that it is measured directly, this quantity is referred to as the experimental value for practical purposes.

Experimental Value

To obtain a reference quantity which can be used later as a comparison for the calculated values, the surface velocity equation in Chapter 6.4, Table 6-1 on page 92 (also referred to as τ^- -Model)

$$w(y) = \beta_f \left(-\frac{y^2}{2} + h(x)y \right) - \frac{\bar{\tau}_0}{\eta_f} y \tag{9-2}$$

is integrated along the borderline at $y=h(x)$

$$\bar{w} = \frac{\int_0^b w(x, y) dx}{\int_0^b dx} . \tag{9-3}$$

Instead of treating the shear stress τ as a function of the x- and y-axes, it is taken as a constant here in order to enable an integration over the x-axis. Therefore, the shear stress found in Eq. 9-2 is written as $\bar{\tau}_0$ which means the averaged surface (symbolized by the index 0) shear stress. The mean velocity calculated in this way is solved for the shear stress $\bar{\tau}_0$ and this quantity is referred to as the experimental value of shear stress, in the sense that this value is estimated by means of the measured mean velocity and the film thickness. Depending on the cross-section shape assumed, there are three experimental values of the shear stress, as an example

$$\bar{\tau}_0 = \frac{1}{3} \beta_f \delta_f \eta_f - \frac{2 \eta_f \bar{w} \sqrt{b^2 + \delta_f^2}}{b \delta_f} \tag{9-4}$$

if the cross-section is taken as triangle. The equations for all other shapes are listed in Table 9-1 on page 161. This is the only reference value which can be used to prove the theory used for the shear stress estimation. Nevertheless, this quantity has to be treated carefully in practice for comparative purposes because the assumption that the shear stress term in Eq. 9-2 does not depend on the x- and y-axis is an oversimplification which is required to enable the integration.

Calculated Shear Stress: Tau Model

Actually, the equation needed to calculate the local shear stress is already introduced in Chapter 6.5.1. This shear stress has to be averaged over the borderline by means of integration. The local shear stress is multiplied with an infinitesimal arc length of dx, along which the shear stress is assumed as constant, and later divided by the arc length s itself

$$\bar{\tau}_0 = \frac{\int_0^b \tau_0(x) dx}{\int_0^b dx} \quad (9-5)$$

The arc length of a circular segment

$$s = \theta_0 r \quad (9-6)$$

and of a triangle side

$$s = \sqrt{\delta_f^2 + b^2} \quad (9-7)$$

Calculated Shear Stress: Wall Model

The same integration as written in Eq. 9-5 can be applied with

$$\tau_0(x) = \frac{1}{2} \beta_f \eta_f h(x) \quad (9-8)$$

if the wall model is concerned.

9.1.2 Wetting Angle above 90°

Experimental Value

For the calculation of the experimental value when the wetting angle is above 90°, the integration has to be carried out twice

$$\bar{w} = \frac{1}{\left(\int_0^R dx + \int_{x_1}^R dx \right)} \left(\int_0^R w(x, y) dx + \int_{x_1}^R w(x, y) dx \right) \quad (9-9)$$

The first term concerns the multiplication of the velocity with the infinitesimal arc length dx in DFG (see Fig. 7-11 and 8-3) while the second term is the same product of the velocity and the arc length dx in BD. This can be seen more clearly in the term of the polar coordinate system

$$\bar{w} = \frac{1}{R \theta_0} \left(\int_{\pi/2}^0 w(x, y) (-R \sin \alpha) d\alpha + \int_{-\alpha_0}^0 w(x, y) (-R \sin \alpha) d\alpha \right) \quad (9-10)$$

The integration has to be split due to the fact that

$$h(x) = R(\sin \alpha_0 + \sin |\alpha|) \quad (9-11)$$

and thus, for $0 \leq \alpha_0 \leq \pi/2$

$$h(x) = R(\sin \alpha_0 + \sin \alpha) \quad (9-12)$$

whereas for $-\alpha \leq \alpha_0 < 0$

$$h(x) = R(\sin \alpha_0 - \sin \alpha) \quad (9-13)$$

9.1 Theoretical Background

As explained before, the calculated mean velocity from Eq. 9-10 is solved for the shear stress $\bar{\tau}_0$ and referred to as the experimental value of the shear stress.

Calculated by Means of the Tau Model: Symmetric Boundary Conditions

Depending on the velocity equations and the integration limits used, the mean calculated shear stress can be split in several terms. Generally written, the whole borderline BDFG is divided into three parts BD, DF and FG

$$\bar{\tau}_0 = \frac{1}{S_{BDFG}} \left(\int_0^{s_{BD}} \tau_0(x) dx + \int_0^{s_{DF}} \tau_0(x) dx + \int_0^{s_{FG}} \tau_0(x) dx \right). \quad (9-14)$$

In fact, due to several factors, the terms needed in the calculation might be less than three, such as mentioned in Eq. 9-14. For the tau model with its set of symmetrical boundary conditions, only two integration terms are required

$$\bar{\tau}_0 = \frac{1}{S_{BDF}} \left(\int_0^{x_1} \tau_0(x) dx + \int_{x_1}^R \tau_0(x) dx \right) \quad (9-15)$$

because the shear stress exerted at DF is exactly the same as that exerted at BD (symmetrical conditions) and thus, it is sufficient to average the shear stress along DFG, with

$$\tau_{0,DF}(\alpha) = \beta_f \eta_f R \sin \alpha. \quad (9-16)$$

Calculated by Means of the Tau Model: Continuity Boundary Conditions

The calculation of the averaged shear stress for the tau model with its set of continuity boundary conditions needs to be split in three terms

$$\bar{\tau}_0 = \frac{1}{S_{BDFG}} \left(\int_0^{x_1} \tau_0(x) dx + \int_{x_1}^R \tau_0(x) dx + \int_{x_1}^R \tau_0(x) dx \right) \quad (9-17)$$

because the shear stress at DF is not the same as that at BD. The same reason applies for the tau model with its set of near-wall boundary conditions (Eq. 9-18). As for the arc DFG, the integration can be performed in one term because the equations employed are the same.

Calculated by Means of the Tau Model: Near-wall Boundary Conditions

$$\bar{\tau}_0 = \frac{1}{S_{BDFG}} \left(\int_0^R \tau_0(x) dx + \int_{x_1}^R \tau_0(x) dx \right) \quad (9-18)$$

Calculated by Means of the Wall Model

The shear stress along the arc DF and BD is also the same if the wall model is applied. The velocity profile in BDF is symmetrical with respect to the line DK and at the interphase, the velocity is equal to zero. Due to this symmetrical condition, the integration can be performed in just two steps

$$\bar{\tau}_0 = \frac{1}{S_{DFG}} \left(\int_0^{x_1} \tau_0(x) dx + \int_{x_1}^R \tau_0(x) dx \right) \quad (9-19)$$

and the calculated mean shear stress according to the wall model is

$$\bar{\tau}_0 = \frac{\beta_f \eta_f R}{\pi} \left(\frac{\pi}{4} + \frac{1}{4} \sin(2\alpha_0) + \frac{\alpha_0}{2} \right) \quad (9-20)$$

9.2 Mean Surface Shear Stress

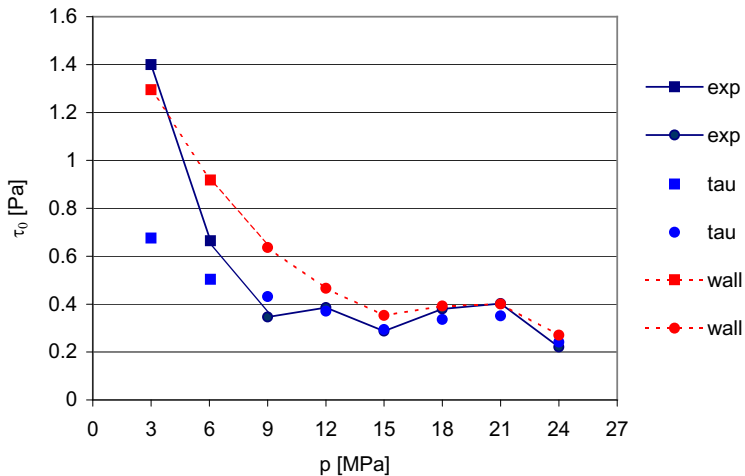


Figure 9-1: Experimental and calculated mean shear stress. System: water rivulet flowing along a vertical glass surface at 313 K and a flow rate of 2.1 g/min.

In Fig. 9-1 the mean shear stresses of the water rivulet which flow along the vertical glass surface at a mass flow rate of 2.1 g/min according to the tau and the wall model are compared with the experimental value. The symbols give information about the assumption of the cross-section shape, which is made according to the findings in Chapter 7.3.

Generally, as expected, the mean shear stress according to the wall model is higher than the one calculated according to the tau model. As the pressure increases, the experimental as well as the calculated shear stress decrease. This does not mean that the shear stress at higher pressure is lower than the shear stress at lower pressure. According to the figure shown in Chapter 7.3, the mean velocity is decreasing with increasing pressure due to the fact that the mass flow of the film phase is kept constant in the whole pressure range. However, the density difference between the phases is decreasing, and thus, the mean velocity is also decreasing. It decreases

9.2 Mean Surface Shear Stress

from approximately 14 cm/s at 3 MPa down to 4 cm/s at 24 MPa. And a decrease in the mean velocity means at the same time a lower shear stress between the phases. At a same flow velocity, the shear stress at higher pressure is expected to be larger than the one at a lower pressure due to the fact that carbon dioxide becomes more viscous when it changes its gaseous form to the supercritical one. A higher viscosity means that the friction between the phases should increase too.

The experimental shear stress at 3 MPa seems to be erroneous. The value is far too high, it exceeds even the predicted value by means of the wall model. Except at this point, the calculated shear stress according to the tau model is in accordance with the experimental value. At high pressure, the result of the wall model coincides very well with both the experimental and the calculated value according to the tau model.

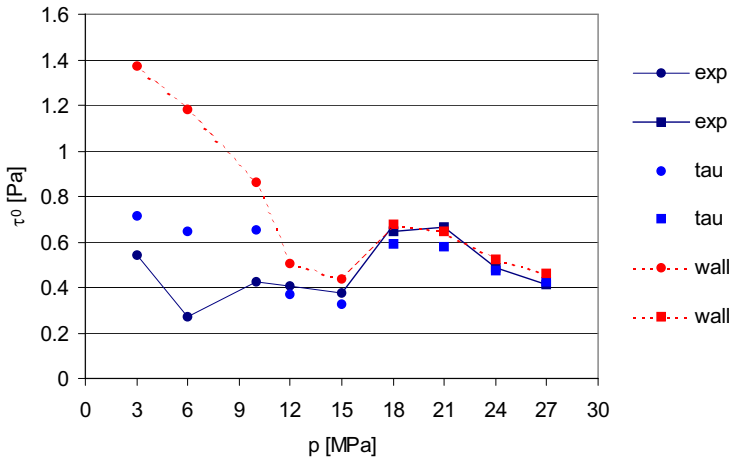


Figure 9-2: Experimental and calculated mean shear stress. System: water rivulet flowing along a vertical steel surface at 313 K and a flow rate of 9 g/min.

In Fig. 9-2 the shear stress between the water rivulet and pressurized carbon dioxide at 313 K and a mass flow of 9 g/min is shown. Here, the same shear stress behavior as explained before can be observed. The shear stress according to the wall model is far higher than the one according to the tau model. Except at 6 MPa, the estimated shear stress by means of the tau model complies with the experimental value. The wall model can predict the shear stress better when carbon dioxide becomes supercritical.

At higher pressure where the wetting angle becomes larger than 90° , the mean shear stress according to the tau model is calculated with the help of all three sets of boundary conditions. The calculations resulting from different boundary conditions are nearly the same. This is probably due to the shorter arc of BDF in comparison to the arc FG (the maximal wetting angle

is 107°). The mean shear stress according to the tau model presented in Fig. 9-2 is calculated by means of the set of near-wall boundary conditions.

9.3 List of Equations

Table 9-1: Shear stress calculated by means of experimental values.

$\theta_0 \leq 90^\circ$		$\theta_0 > 90^\circ$
	$\frac{2}{3} \beta_f \eta_f \delta_f - 2 \frac{\eta_f}{\delta_f} \bar{w}$	$\frac{-\eta_f \left(\begin{array}{l} \bar{w}(-6\pi - 12\alpha_0) \\ + \beta_f R^2 \begin{pmatrix} 3\pi \sin \alpha_0 + 6\alpha_0 \sin \alpha_0 \\ + 4 + 6 \cos \alpha_0 \\ - 12 \cos^2 \alpha_0 + 6 \cos^3 \alpha_0 \end{pmatrix} \end{array} \right)}{3R(-8 \sin \alpha_0 + 2 \sin \alpha_0 \cos \alpha_0 - \pi + 2\alpha_0)}$
	$\frac{-\eta_f \left(\begin{array}{l} 6\bar{w} \theta_0 \\ - \beta_f R^2 \begin{pmatrix} \cos^2 \theta_0 \sin \theta_0 \\ + 2 \sin \theta_0 - 3\theta_0 \cos \theta_0 \end{pmatrix} \end{array} \right)}{3R(\theta_0 - \cos \theta_0 \sin \theta_0)}$	
	$\frac{1}{3} \beta_f \delta_f \eta_f - \frac{2\eta_f \bar{w} \sqrt{b^2 + \delta_f^2}}{b \delta_f}$	

Table 9-2: Local and mean surface shear stress for the wetting angle θ_0 smaller than or equals 90°.

Tau model $\tau_0(x) = \Phi h(x)$		Wall model $\tau_0(x) = \frac{1}{2} \beta_f \eta_f h(x)$	
Shape	Mean surface shear stress $\bar{\tau}_0$	Shape	Mean surface shear stress $\bar{\tau}_0$
	$\Phi \delta_f$		$\frac{1}{2} \beta_f \eta_f \delta_f$
	$\Phi R \frac{a_1(\theta_0)}{\sin \theta_0}$		$\frac{1}{2} \beta_f \eta_f R \frac{a_1(\theta_0)}{\sin(\theta_0)}$
	$\frac{\Phi}{2} \delta_f$		$\frac{1}{4} \beta_f \eta_f \delta_f$

9.3 List of Equations

Table 9-3: Local and mean surface shear stress for the wetting angle θ_0 larger than 90° .

Tau		$\tau_0(x, y)$ also $\tau_0(\alpha)$	$\bar{\tau}_0$
Symmetrical	DF	$\beta_f \eta_f R \sin \alpha$	$\frac{R}{\pi} \left(\Phi \left(\frac{\pi}{2} + \frac{3}{2} \sin(2\alpha_0) - \alpha_0 \right) + \beta_f \eta_f \left(\alpha_0 - \frac{1}{2} \sin(2\alpha_0) \right) \right)$
	BD	$\beta_f \eta_f R \sin \alpha$	
Continuity	DF	$-\eta_f \left(-\beta_f h(x) + \left(\beta_f - \frac{\Phi}{\eta_f} \right) 2R \sin \alpha_0 \right)$	$\frac{R}{\frac{\pi}{2} + \alpha_0} \left(\frac{\Phi}{4} \left(\pi + 6 \sin \alpha_0 \cos \alpha_0 \right) - 2\alpha_0 \right) + \beta_f \eta_f \left(-\sin \alpha_0 \cos \alpha_0 \right) + \alpha_0$
	BD	$\eta_f \left(-\beta_f (h(x) - \delta_f(x)) + \left(\beta_f - \frac{\Phi}{\eta_f} \right) 2R \sin \alpha_0 \right)$	
Near-wall	DFG	$\Phi R (\sin \alpha_0 + \sin \alpha)$	$\frac{R}{2(\pi + 2\alpha_0)} \left(4\beta_f \eta_f (\alpha_0 - \cos \alpha_0 \sin \alpha_0) + \Phi \left(\pi + 6 \sin \alpha_0 \cos \alpha_0 \right) - 2\alpha_0 \right)$
	BD	$\eta_f R \left(-2\beta_f \sin \alpha - \frac{\Phi}{\eta_f} (\sin \alpha_0 - \sin \alpha) \right)$	
Wall		$\tau_0(x, y)$ also $\tau_0(\alpha)$	$\bar{\tau}_0$
		$\frac{1}{2} \beta_f \eta_f \delta_f(x)$	$\frac{\beta_f \eta_f R}{\pi} \left(\frac{\pi}{4} + \frac{1}{4} \sin(2\alpha_0) + \frac{\alpha_0}{2} \right)$

The angle α in Table 9-3 is the absolute value of the angle. The algebraic sign has been taken into account in the equations. The equation for the film thickness $\delta_f(x)$ is listed in Table 7-1 on page 124.

10 Bibliography

- [1] Adam, N. K., *The Physics and Chemistry of Surfaces*, third ed., Oxford University Press, London, New York, 1941.
- [2] Adamson, A. W., *Physical Chemistry of Surfaces*, sixth ed., Wiley, New York, 1990.
- [3] Ambrogi, A., Cardarelli, D.A., Eggers, R., Fractional Extraction of Paprika using Supercritical Carbon Dioxide and On-line Determination of Carotenoids, *J. Food. Sci.* 67 (2002) 3236-3241.
- [4] Ambwani, D.S., Fort Jr., T., Pendant Drop Technique for Measuring Liquid Boundary Tensions, *Surf. Colloid Sci.* 11 (1979) 93-119.
- [5] Amirfazli, A., Haenig, S., Mueller, A., Neumann, A.W., Measurements of Line Tension for Solid-Vapor Systems Using Drop Size of Dependence of Contact Angles and its Correlation with Solid-Liquid Interfacial Tension, *Langmuir* 16 (2000) (4) 2024-2031.
- [6] Anastasiadis, S.H., Chen, J.-K., Koberstein, J.T., Siegel, A.F., Sohn, J.E., Emerson, J.A., The Determination of Interfacial Tension by Video Image Processing of Pendant Fluid Drops, *J. Phys. Chem.* 119 (1987) (1) 55-66.
- [7] Andreas, J.M., Hauser, E.A., Tucker, W.B., Boundary Tension by Pendant Drops, *J. Phys. Chem.* 42 (1938) 1001-1019.
- [8] Arendt, B., Dittmar, D., Eggers, R., Interaction of Interfacial Convection and Mass Transfer Effects in the System CO₂-Water, *Int. J. Heat Mass Transfer* 47 (2004) 3649-3657.
- [9] Asblad, A., Berntsson, T., Surface Evaporative Heat Transfer Coefficient in Turbulent Free-Falling Liquid Films, *Int. J. Heat Mass Transfer* 34 (1991) 834-841.
- [10] Backes, H.M., *Messung und Korrelation der Grenzflächenspannung zwischen zwei flüssigen Phasen*, PhD thesis, Universität Kaiserslautern, 1984.
- [11] Bailey, A.I., *Proc. 3rd Int. Conf. Surface Activity*, Cologne 1960.
- [12] Bangham, D.H.; Razouk, R.I., *Trans Faraday Soc.* 33 (1937) 1459, 1493, *Proc. R. Soc. London, Ser. A.* 166 (1938) 572.
- [13] Bankoff, S. G., Minimum Thickness of a Draining Liquid Film, *Int. J. Heat Mass Transfer* 14 (1971) 2143-2146.
- [14] Bänziger, G., *Untersuchung des Fluidverhaltens in geordneten Packungen unter Hochdruck*, PhD thesis, ETH Zürich, 1995.
- [15] Bashforth, F., Adams, J.C., *An Attempt to Test the Theories of Capillary Action by Comparing the Theoretical and Measured Forms of Drops of Liquid. With an Explanation of the Method of Integration Employed in Constructing the Tables which Give the Theoretical Forms of Such Drops*, Cambridge, 1883.

- [16] Berg, T. A., Deye, J. F., Composition and Density Effects Using Methanol/Carbon Dioxide in Packed Column Supercritical Fluid Chromatography, *Anal. Chem.* 62 (1990) 1181-1185.
- [17] Bernardin, J.D., Mudawar, I., Walsh, C.B., Franses, E.I., Contact Angle Temperature Dependence for Water Droplets on Practical Aluminum Surfaces, *Int. J. Heat Mass Transfer* 40 (1997) (5) 1017-1033.
- [18] Berthelot, D., *Compt. Rend.* 126 (1898) (1703) 1703, 1857.
- [19] Bikerman, J.J., *Surface Chemistry*, second ed., Academic Press, New York (1958).
- [20] Bosch, K., *Mathematik - Lexikon : Nachschlagewerk und Formelsammlung für Anwender*, fourth ed., Oldenbourg, München, 2000.
- [21] Brauer, E.B., Hough, E.W., Interfacial Tension of the Normal Butane-Carbon Dioxide System, *Producers Monthly* 29 (1965) 13.
- [22] Bravo, J. L., Rocha, J. A., Fair, J. R., Mass Transfer in Gauze Packings, *Hydrocarbon Processing*, January (1985) 91-95.
- [23] Bronstein, Semendjajew, Musiol, Mühlig, *Taschenbuch der Mathematik*, fifth ed., Thun, Frankfurt am Main, 2000.
- [24] Brötz, W., Über die Vorausberechnung der Absorptions Geschwindigkeit von Gasen in strömenden Flüssigkeitsschichten, *Chem. Ing. Tech.* 26 (1954) (8-9) 470-478.
- [25] Bruce, J.W., Giblin, P.J., *Curves and Singularities*, second ed., Cambridge Univ. Press, Cambridge, 1992.
- [26] Budich, M., Countercurrent Extraction of Citrus Aroma from Aqueous and Nonaqueous Solutions Using Supercritical Carbon Dioxide, PhD thesis, Technische Universität Hamburg Harburg, 1999.
- [27] Cassie, A.B.D., Baxter, S., *Trans. Faraday Soc.*, 40 (1944) 546.
- [28] Cassie, A.B.D., Contact Angles, *Discuss. Faraday Soc.* 3 (1948) 11-15.
- [29] Chang, C., Chiu, K-L, Day, C-Y, A New Apparatus for the Determination of P-x-y-Diagrams and Henry's Constants in High Pressure Alcohols with Critical Carbon Dioxide, *J. Supercrit. Fluids* 12 (1998) 223-237.
- [30] Chang, C.J., Day, C-Y, Ko, C.-M., Chiu, K.-L., Densities and P-x-y- diagrams for Carbon Dioxide Disolution in Methanol, Ethanol and Acetone Mixtures, *Fluid Phase Equilib.* 131 (1997) 243-258.
- [31] Chiu, N.C., Master thesis, State University of New York at Buffalo, 1991.
- [32] Chun, B.S., Wilkinson, G.T., Interfacial Tension in High-Pressure Carbon Dioxide Mixtures, *Industrial and Engineering Chemistry Research* 34 (1995) 4371-4377.
- [33] Cibulka, I., Ziková M., Liquid Densities at Elevated Pressures on Alkanols from C1 to C10: A Critical Evaluation of Experimental Data, *J. Chem. Eng. Data* 39 (1994) (4) 876-886.

-
- [34] Culkin, J.B., Davis, S.H., Meandering of Water Rivulets, *AIChE Journal* 30 (2) (1984) 263-267.
- [35] Czerwonatis, N., Zerfall flüssiger Strahlen und Widerstand von Tropfen in verdichteten Gasen am Beispiel des Verfahrens der Hochdruck-Sprüh-Extraktion, PhD thesis, Technische Universität Hamburg Harburg, 2002.
- [36] Daubert, T.E., Danner, R.P., Sibul, H.M., Stebbins, C.C., Rowley, R.L., Wilding, W.V., Oscarson, J.L., Adams, M.E., Marshall, T.L., *Physical and Thermodynamic Properties of Pure Chemicals. Evaluated Process Design Data. American Institute of Chemical Engineers. Design Institute for Physical Property Data.* Greyden Press, Columbus, OH, 1999.
- [37] Davies, J. T., Rideal, E. K., *Interfacial Phenomena*, Academic Press, New York, 1961.
- [38] Day, C-Y, Chang, C.J., Chen, C.-Y., Phase Equilibrium of Ethanol + CO₂ and Acetone + CO₂ at Elevated Pressures, *J. Chem. Eng. Data* 41 (1996) (4) 839-843.
- [39] de Haan, A.B., de Graauw, Jan, Mass Transfer in Supercritical Extraction Columns with Structured Packings for Hydrocarbon Processing, *Ind. Eng. Chem. Res.* 30 (1991) 2463-2470.
- [40] de Laplace P.S., *Mechanique Celeste*, Supplement to Book 10, 1806.
- [41] Debye, P., Die van der Waalsschen Kohäsionskräfte, *Phys. Z.* 21 (1920) 178-192.
- [42] Debye, P., Molekularkräfte und ihre elektrische Deutung, *Phys. Z.* 22 (1921) 302-308.
- [43] Demarquette, N.R., Kamal, M.R., *Interfacial Tension in Polymer Melts I: An Improved Pendant Drop Apparatus*, *Polym. Eng. And Sci.* 34 (1994) (24) 1823-1833.
- [44] Dimitrov, K., Boyadzhiev, L., Tufeu, R., Properties of Supercritical CO₂ saturated poly(ethylene glycol) nonylphenyl ether, *Macromolecular Chemistry and Physics*, 200 (1999) 1626-1629.
- [45] Dittmar, D., Eggers, R., Kahl, H., Enders, S., Measurement and Modelling of the Interfacial Tension of Triglyceride Mixtures in Contact with Dense Gases, *Chem. Eng. Sci.* 57 (2002) 355-363.
- [46] Dittmar, D., Fredenhagen, A., Oei, S. B., Eggers, R., Interfacial Tensions of Ethanol-Carbon Dioxide and Ethanol-Nitrogen. Dependence of the Interfacial Tension on the Fluid Density-Prerequisites and Physical Reasoning, *Chem. Eng. Sci.*, 58 (2003) 1223-1233.
- [47] Docter, A., Lösch, H.-W., Wagner, W., Entwicklung und Aufbau einer Anlage zur simultanen Messung der Viskosität und der Dichte fluider Stoffe, *Fortschritt-Berichte der VDI-Zeitschriften*, Reihe 3, Nr. 494 VDI-Verlag, Düsseldorf, 1997.
- [48] Dodds, W.S., Stutzman, L.F., Sollami, B.J., Carbon Dioxide Solubility in Water, *Ind. Eng. Chem.* 1 (1956) (1) 92-95.
- [49] Drelich, J., Wilbur, L., Miller, J. D., *Langmuir* 12 (1996) 1913.

- [50] Dukhin, S.S., Kretzschmar, G., Miller, R., Dynamics of Adsorption at Liquid Interfaces, Möbius, D., Miller, R.(Eds.), Elsevier, Amsterdam, 1995.
- [51] Eggers, J., Theory of Drop Formation, *Phys. Fluids* 7 (5) (1995) 941-953.
- [52] Eggers, R., Jaeger, P.T., Der Einfluß von Grenzflächenerscheinungen auf den Sotffübergang und die Prozeßführung in Gegenstromkolonnen mit überkritischem CO₂, *Wärme- und Stoffübertragung* 29 (1994) 373-377.
- [53] Falckenhagen, H., Kohäsion und Zustandsgleichung bei Dipolgasen, *Physik. Zeitschr.* 23 (1922) 87-95.
- [54] Feng, Y.S., Du, X.Y., Li, C.F., Hou, Y.J., An Apparatus for Determining High Pressure Fluid Phase Equilibria and its Applications to Supercritical Carbon Dioxide Mixtures, *Proceedings of the International Symposium on Supercritical Fluids* (1988) 75-84.
- [55] Fowkes, F. M., Predicting Attractive Forces at Interfaces Analogy to Solubility Parameter, *Chemistry & Physics of Interfaces 2. Symposium on Chemistry and Physics of Interfaces I.* Amer. Chem. Soc. 1971. Based on the 5th Annual State of the Art Symposium sponsored by Industrial and Engineering Chemistry and the Division of Industrial and Engineering Chemistry of the American Chemical Society, Washington DC (1968) 154-166.
- [56] Fowkes, F.M., Additivity of Intermolecular Forces at Interfaces, *J. Phys. Chem.* 67 (1963) 2538-2541.
- [57] Fowkes, F.M., Attractive Forces at Interfaces, *Ind. Eng. Chem.* 56 (1964) (12) 40-53.
- [58] Fowkes, F.M., Determination of Interfacial Tensions, Contact Angles, and Dispersion Forces in Surfaces by Assuming Additivity of Intermolecular Interactions in Surfaces, *J. Phys. Chem.* 66 (1962) 382-383.
- [59] Fowkes, F.M.; Sawyer, W.M., Contact Angles and Boundary Energies of a Low Energy Solid, *J. Chem. Phys.*, 20 (1952) 1650.
- [60] Fox, H. W., Zisman, W. A., The Spreading of Liquids on Low-Energy Surfaces. III. Hydrocarbon Surfaces, *Journal of Colloid Science* 4 (1952) 428-442.
- [61] Fredenhagen, A., Grenzflächenspannung und Gemischdichten unter erhöhten Drücken, Ms. Thesis, Technische Universität Hamburg Harburg, 1996.
- [62] Fröhler, A.W., *Glas und Glasprodukte*, second ed., J- Agst. Moers, 1997.
- [63] Galileo, G., Bodies that Stay Atop Water, or Move in It (1612). Drake, S., Cause, Experiment and Science: A Galilean Dialogue Incorporating a New Translation of Galileo's Bodies that Stay Atop Water, University of Chicago Press 1981.
- [64] Garthe, D., Fluidynamics and Mass Transfer of Single Particles and Swarms of Particles in Extraction Columns, PhD thesis, Technische Universität München, 2006.

-
- [65] Gasem, K.A.M., Dickson, K.B., Dulcamara, P.B., Nagarajan, N., Robinson Jr., R.L., Equilibrium Phase Compositions, Phase Densities, and Interfacial Tensions for CO₂ + Hydrocarbon Systems. 5. CO₂ + n-Tetradecane, *J. Chem. Eng. Data* 34 (1989) (2) 191-195.
- [66] Gasem, K.A.M., Dickson, K.B., Shaver, R.D., Robinson Jr., R.L., Experimental Phase Densities and Interfacial Tensions for a CO₂/Synthetic Oil and a CO₂/reservoir-oil system, *SPE Reservoir Engineering* 8 (1993) 170-174.
- [67] Gast, K., Enrichment of Vitamin E and Provitamin A from Palm Oil Derivates with Supercritical Fluids, PhD thesis, Technische Universität Hamburg Harburg, 2005.
- [68] Gebel, J., Zum Einsatz von Horizontalrohrverdampfern in Mehrfacheffektanlagen zur Eindampfung wässriger Lösungen, PhD thesis, Rheinsich-Westfälischen Technischen Hochschule Aachen, 1990.
- [69] Gibbs, J.W., *The Collected Works of J.W.Gibbs*, vol. 1, Longmans, Green, New York, 1931.
- [70] Gillespie, P.C., Wilson, G.M., Vapor-Liquid and Liquid-Liquid Equilibria: Water-Methane, Water- Carbon Dioxide, Water-Hydrogen Sulfide, Water-n-pentane, Water-Methane-n-pentane, Gas Processors Association Gas Processors Association, Tulsa, Research Report RR 48 (1982).
- [71] Girault, H.H.J., Schiffrin, D.J., Smith, B.D.V., The Measurement of Interfacial Tension of Pendant Drops Using a Video Image Profile Digitizer, *J. of Colloid and Interface Sci.* 101 (1984) (1) 257-267.
- [72] Girifalco, L.A., Good, R.J., A Theory for Estimation of Surface and Interfacial Energies III. Estimation of Surface Energies of Solids from Contact Angle Data, *J. Phys. Chem.* 64 (1960) 561-565.
- [73] Girifalco, L.A., Good, R.J., Theory for the Estimation of Surface and Interfacial Energies I. Derivation and Application to Interfacial Tension, *J. Phys. Chem.* 61 (1957) 904-909.
- [74] Good, R. J., Elbing, E., Generalization of Theory for Estimation of Interfacial Energies, *Ind. Eng. Chem.* 62 (1970) (3) 54-79.
- [75] Good, R.J., Contact Angle, Wetting, and Adhesion: A Critical Review, in: Mittal, K.L.(ed.), *Contact Angle, Wettability and Adhesion*, VSP, Utrecht, The Netherlands, 1993, 3-36.
- [76] Good, R.J., Koo, M.N., The Effect of Drop Size on Contact Angle, *J. of Colloid and Interface Sci.* 71 (1979) (2) 283-292.
- [77] Good, R.J., Surface Free Energy of Solids and Liquids: Thermodynamics, Molecular Forces and Structure, *J. of Colloid and Interface Sci.* 59 (1977) (3) 398-419.
- [78] Good, R.J., Theory for the Estimation of Surface and Interfacial Energies, *Adv. Chem. Ser.* 43 (1964) 74-87.

- [79] Hansen, F.K., Rodsrud, G., Surface Tension by Pendant Drop, *J. of Colloid and Interface Sci.* 141 (1991) (1) 1-9.
- [80] Harkins, Brown, Davies, *J. Amer. Chem. Soc.* 39 (1917) 354.
- [81] Heuer, G. J., Interfacial Tension of Water Against Hydrocarbon and Other Gases and Adsorption of Methane on Solids at Reservoir Temperature and Pressures, PhD thesis, University of Texas, 1957.
- [82] Hiller, N., Bestimmung der Grenzflächenspannung in Systemen aus schwerflüchtigen und überkritischen Komponenten unter hohen Drücken, PhD thesis, Universität Erlangen-Nürnberg, 1990.
- [83] Hiller, N., Schiemann, H., Weidner, E., Peter, S., Interfacial Tension in Systems with a Supercritical Component at High Pressures, *Chem. Eng. Technol.* 16 (1993) 206-212.
- [84] Hirohama, S., Takatsuka, T., Miyamoto, S., Muto, T., Measurement and Correlation of Phase Equilibria for the Carbon Dioxide-Ethanol-Water System, *J. Chem. Eng. Jap.* 26 (1993) (4) 408-415.
- [85] Hobbie, M., Bildung von Tropfen in verdichteten Gasen und stationäre Umströmung fluider Partikel bei Drücken bis zu 50 MPa, PhD thesis, Technische Universität Hamburg Harburg, 2005.
- [86] Hodel, M., Untersuchungen zum Einsatz der on-line "supercritical fluid chromatography" für die Messung von Hochdruck-Phasengleichgewichten und zur Bestimmung des Betriebsverhaltens einer SF-Gegenstromextraktionskolonne, PhD thesis, ETH Zürich, 1990.
- [87] Hong, K. T., Imadojemu, H., Webb, R. L., Effects of Oxidation and Surface Roughness on Contact Angle, *Experimental Thermal and Fluid Science* 8 (1994) 279-285.
- [88] Hsu, J.J.C., Nagarajan, N., Robinson Jr., R.L., Equilibrium Phase Compositions, Phase Densities, and Interfacial Tensions for CO₂+Hydrocarbon Systems. 1. CO₂+n-butane, *J. Chem. Eng. Data* 30 (1985) 485-491.
- [89] Huang, H.T.-L., PhD thesis, State University of New York at Buffalo, 1990.
- [90] Israelachvili, I., *Quart. Rev. Biophys.* 6 (1974) 341.
- [91] Israelachvili, J.N., Gee, M.L., Contact Angles on Chemically Heterogeneous Surfaces, *Langmuir* 5 (1989) 288-289.
- [92] Jaeger, P., Grenzflächen und Stofftransport in verfahrenstechnischen Prozessen am Beispiel der Hochdruck-Gegenstromfraktionierung mit überkritischem Kohlendioxid, PhD thesis, Technische Universität Hamburg-Harburg, 1998.
- [93] Jaeger, P.T., v. Schnitzler, J., Eggers, R., Interfacial Tension of Fluid Systems Considering the Nonstationary Case with Respect to Mass Transfer, *Chem. Eng. Technol.* 19 (1996) 197-202.
- [94] Janczuk, B., Bialopiotrowicz, T., Wojcik, W., The Components of Surface Tension of Liquids and Their Usefulness in Determinations of Surface Free Energy of Solids, *J. of Colloid and Interface Sci.* 127 (1999) (1) 59-66.

-
- [95] Janocha, B., Veränderung von Benetzung und Adsorption an Kunststoff-Wasser-Grenzflächen unter dem Einfluß externer elektrischer Felder und der Kunststoffoberflächenpolarität, PhD thesis, Eberhard-Karls-Universität Tübingen, 1998.
- [96] Jennings, D.W., Gude, M.T., Teja, A.S, High-Pressure Vapor-Liquid Equilibria in Carbon Dioxide and 1-Alkanol Mixtures. In: ACS Symposium Series 514. Supercritical Fluid Engineering Science: Fundamentals and Applications. Ed. Erdogan Kiran, and Joan F. Brennecke, American Chemical Society, Washington, DC (1993) 10-45.
- [97] Jho, C., Nealon, D., Shobola, S., King Jr., A.D., Effect of Pressure on the Surface Tension of Water: Adsorption of Hydrocarbon Cases and Carbon Dioxide on Water at Temperatures between 0° and 50°C, *J. of Colloid and Interface Sci.* 65 (1978) 141-154.
- [98] Johnson Jr., R. E., Dettre, R. H., *Surf. Colloid Sci.* 2 (1969) (85).
- [99] Johnson Jr., R.E., Conflicts between Gibbsian Thermodynamics and Recent Treatments of Interfacial Energies in Solid-Liquid-Vapor Systems, *J. Phys. Chem.* 63 (1959) 1655-1658.
- [100] Johnson Jr., R.E., Dettre, R.H., Contact Angle Hysteresis. III. Study of an Idealized Heterogeneous Surface, *J. Phys. Chem.* 68 (1964) 1744-1750.
- [101] Kahlweit, M., Grenzflächenerscheinungen, Steinkopf, Darmstadt, 1981.
- [102] Keesom, W.H., *Phys. Z.*, 22 (1921) 126.
- [103] Keesom, W.H., *Phys. Z.*, 23 (1922) 225.
- [104] Kemmere, M. F., Meyer, T., *Supercritical Carbon Dioxide in Polymer Reaction Engineering*, Wiley-VCH Verlag GmbH, 2005.
- [105] Kern, J., Stabilitätsprobleme der Rinnsalströmung, *Verfahrenstechnik* 5 (7) (1971) 289-294.
- [106] Kern, J., Untersuchungen über die Hydrodynamik der Rinnsale, PhD thesis, Technische Universität Berlin, 1970.
- [107] Kern, J., Zur Hydrodynamik der Rinnsale, *Verfahrenstechnik* 3 (10) (1969) 425-430.
- [108] Kerst, A.W., *Fluiddynamik und flüssigkeitsseitiger Stofftransport bei hohen Drücken*, PhD thesis, Universität Stuttgart, 1998.
- [109] Kihara, T., *Advan. Chem. Phys.*, 5 (1963) 147.
- [110] Kihara, T., *Rev. Mod. Phys.*, 25 (1953) 831.
- [111] Kiran, E., Brennecke, J. F., *Supercritical Fluid Engineering Science*, American Chemical Society, 1993.
- [112] Klante, D., Eggers, R., Holzknacht, C., Kabelac, S., Grenzflächenenergien von Teflon und verschiedenen Flüssigkeiten in einer verdichteten Stickstoffatmosphäre, *Forsch. Ingenieurwes.* 65 (2002) 56-71.

- [113] Kleinrahm, R.; Wagner, W., Entwicklung und Aufbau einer Dichtemeßanlage zur Messung der Siede- und Taudichten reiner fluider Stoffe auf der gesamten Phasengrenzkurve, Fortschritt-Berichte der VDI-Zeitschriften Reihe 3, Nr. 92, VDI-Verlag, Düsseldorf, 1984.
- [114] Kögel, A., Stoffdurchgangsmessungen am hängenden Wassertropfen in verdichtetem Kohlendioxid: Aufbau einer Apparatur und Messungen im binären System und im ternären System mit Phenol bis 25 MPa und 333 K, PhD thesis, Universität Heidelberg, 2000.
- [115] Kordikowski, A., Schenk, A.P., Van Nielsen, R.M., Peters, C.J., Volume Expansions and Vapor-Liquid Equilibria of Binary Mixtures of a Variety of Polar Solvents and Certain Near-Critical Solvents, *J. Supercrit. Fluids* 8 (1995) 205-216.
- [116] Kruse, A., Vogel, H., Heterogene Katalyse in Überkritischen Medien - 1. Kohlendioxid, *Chem. Ing. Tech.* 79 (6) (2007) 707-720.
- [117] Kudra, M., Knapikowski, R., Anwendung der Fuzzy Logik zur Schätzung von Kontaktwinkeln, *Chem. Technik* 47 (1995) (4) 217-221.
- [118] Lecomte du Noüy, P., *J. Gen. Physiol.* 1 (1919) 521.
- [119] Lehnberger, A., Wärmeübergang im Fallfilmverdampfer in glatten und profilierten Rohren bei kleinen Temperaturgefällen, PhD thesis, Technische Universität Braunschweig, 2002.
- [120] Lester, G.R., in: Wetting, S.C.I. Monograph no. 25, Soc. Chem. Ind., London, 1967.
- [121] Li, D., Drop Size Dependence of Contact Angles and Line Tensions of Solid-Liquid Systems, *Colloids Surf. A: Physicochem. Eng. Aspects* 116 (1996) 1-23.
- [122] Li, D., Neumann, A.W., Surface Heterogeneity and Contact Angle Hysteresis, *Colloid Polymer Sci.* 270 (1992) 498-504.
- [123] Li, H., Lee, L.J., Tomasko, D.L., Effect of Carbon Dioxide on the Interfacial Tension of Polymer Melts, *Ind. Eng. Chem. Res.*, 43 (2004) 509-514.
- [124] Lide, D. R. (Ed.), *Handbook of Chemistry and Physics*, 85th ed., CRC Press, New York, 2004-2005.
- [125] Lim, J.S., Lee, Y.Y., Chun, H.S., Phase Equilibria for Carbon Dioxide-Ethanol-Water System at Elevated Pressures, *J. Supercrit. Fluids* 7 (1994) (4) 219-230.
- [126] Lin, F. Y. H., Li, D., The Effect of Surface Heterogeneity on the Drop Size Dependence of Contact Angles, *Chem. Eng. Sci.* 50 (1995) (16) 2633-2639.
- [127] Lockemann, C.A., Flüssigkeitseitiger Stofftransport in Hochdrucksystemen mit einer überkritischen und einer flüssigen Phase, PhD thesis, Universität Karlsruhe, 1994.
- [128] London, F., The General Theory of Molecular Forces, *Trans. Faraday Soc.* 33 (1937) 8-26.

-
- [129] Lösch, H. -W., Entwicklung und Aufbau von neuen Magnetschwebewaagen zur berührungsfreien Messung vertikaler Kräfte, Fortschritt-Berichte der VDI-Zeitschriften Reihe 3, Nr. 138, VDI-Verlag, Düsseldorf, 1987.
- [130] Marckmann, H., Sutjiadi-Sia, Y., Jaeger, P., Eggers, R., Dampfdruck und Grenzflächenspannung bei CO₂-Öl-Gemischen bei unterkritischer Anwendung. Abschlußbericht FKT 75/00, 2004.
- [131] Marckmann, H., Überkritische Extraktion von aufkonzentrierten Kaffeelösungen in Hochdruckkolonnen, PhD thesis, Technische Universität Hamburg-Harburg, 2005.
- [132] Marmur, A., Contact Angle and Thin-Film Equilibrium, *J. of Colloid and Interface Sci.* 148 (2) (1992) 541-550.
- [133] Marmur, A., Equilibrium and Spreading of Liquids on Solid Surfaces, *Adv. Coll. Inter. Sci.* 19 (1983) 75-102.
- [134] Maun, A.H., Experimentelle Untersuchungen zum Wärmeübergang an verdampfenden Fallfilmen binärer Gemische, PhD thesis, Technische Universität Berlin, 2004.
- [135] Mikielewicz, J., Moszynski, J. R., Minimum Thickness of a Liquid Film Flowing Vertically Down a Solid Surface, *Int. J. Heat Mass Transfer* 19 (1976) 771-776.
- [136] Morgner, H., Theoretische Untersuchung der Dynamik der Grenzflächeneigenschaften (Konzentrationsprofil, Stofftransport, Grenzflächenenergie) in Systemen mit Mischungslücke, DFG-Abschlussbericht zum Projekt Mo288/26 im SPP 1105, April 2007.
- [137] Moser, M., Pietzonka, W., Trepp, C., Interfacial Tension Measurements between atocopherol and Carbon Dioxide at High Pressures, *Chem. Eng. Technol.* 19 (1996) 462-466.
- [138] Moser, M., Trepp, C., Investigating the Stability of Falling Films at Round Vertical Film Carriers under High Pressure, *Chem. Eng. Technol.* 20 (1997) 612-616.
- [139] Müller, J., Wärmeübergang bei der Filmkondensation und seine Einordnung in Wärme- und Stoffübertragungsvorgänge bei Filmströmungen, PhD thesis, Universität Karlsruhe, 1992.
- [140] Myers, D., Surfaces, Interfaces, and Colloids: Principles and Applications, second ed., Weinheim, VCH, New York, 1999.
- [141] Nagahama, K., Suzuki, J., Suzuki, T., High Pressure Vapor-Liquid Equilibria for the Supercritical CO₂ + Ethanol + Water System, *Proceedings of the International Symposium on Supercritical Fluids* (1988) 143-151.
- [142] Nagarajan, N., Robinson Jr., R.L., Equilibrium Phase Compositions, Phase Densities, and Interfacial Tensions for CO₂+Hydrocarbon Systems. 2. CO₂+n-decane, *J. Chem. Eng. Data* 31 (1986) 168-171.

- [143] Nakae, H., Yoshida, M., Yokota, M., Effects of Roughness Pitch of Surfaces on Their Wettability, *Journal of Materials Science* 40 (2005) 2287-2293.
- [144] National Institut of Standards and Technology (NIST): Chemistry Webbook. <http://webbook.nist.gov/chemistry/fluid>, 2007.
- [145] Neumann, A.W., Good, R.J., Thermodynamics of Contact Angles. I. Heterogeneous Solid Surface, *J. Colloid Interface Sci.* 38 (1972) 341-358.
- [146] Nusselt, W., Die Oberflächenkondensation des Wasserdampfes, *Zeitschrift des Vereines Deutscher Ingenieure* 60 (1916) (27) 541-546, 569-575.
- [147] Oei, S.B., Dittmar, D., Eggers, R., Grenzflächenspannung und Dichte von Ethanol in Kontakt mit Kohlendioxid, *Chem. Ing. Techn.* 73 (2001) 830-834.
- [148] Oei, S.B., Grenzflächenspannung und Gemischdichte bei Einlösung von Kohlendioxid in Flüssigkeiten, M.S. Thesis, Technische Universität Hamburg-Harburg, 1999.
- [149] Owens, D.K., Wendt, Estimation of the surface Free Energy of Polymers, *J. Appl. Polym. Sci.* 13 (1969) 1741-1747.
- [150] Palzer, S., Hiebl, C., Sommer, K., Lechner, H., Einfluss der Rauigkeit einer Feststoffoberfläche auf den Kontaktwinkel, *Chem. Ing. Techn.* 73 (2001) (8) 1032-1038.
- [151] Parker, S.P.(ed. in chief), *Mc.Graw-Hill Encyclopedia of Chemistry* second ed., Mc Graw-Hill, New York, 1993.
- [152] Pecar, D., Dolecek, V., Volumetric Properties of Ethanol-Water Mixtures under High Temperatures and Pressures, *Fluid Phase Equilib.* 230 (2005) 36-44.
- [153] Peper, S., Präparative Chromatographie mit überkritischen Fluiden, PhD thesis, Technische Universität Hamburg Harburg, 2006.
- [154] Pfaender, H.G., *Schott Guide to Glass*, second ed., Chapman & Hall, London, 1996.
- [155] Pfohl, O., Messung und Berechnung von Phasegleichgewichten mit nahe- und überkritischem Kohlendioxid sowie assoziierenden Komponenten im Hochdruckbereich, PhD thesis, Technische Universität Hamburg Harburg, 1998.
- [156] Pitzer, K.S., *Advances in Chemical Physics*, Prigogine (Eds.), twelfth ed., Wiley-Interscience, New York, 1959.
- [157] Porteous, I.R., *Geometric Differentiation for the Intelligence of Curves and Surfaces*, Cambridge Univ. Press, Cambridge, 1994.
- [158] Quincke, *Wiedemans Ann.* 35 (1888) 593.
- [159] Rabel, W., Einige Aspekte der Benetzungstheorie und ihre Anwendung auf die Untersuchung und Veränderung der Oberflächeneigenschaften von Polymeren, *Farbe und Lack* 77 (10) (1971) 997-1007.
- [160] Rao, D.N., Measurements of Dynamic Contact Angles in Solid-Liquid-Liquid Systems at Elevated Pressures and Temperatures, *Colloids Surf./A: Physicochem. Eng. Aspects* 206 (2002) 203-216.

-
- [161] Renno, D., Hübscher, M., *Glas Werkstoffkunde*, second ed., Deutscher Verlag für Grundstoffindustrie, Stuttgart, 2000.
- [162] Rosen, M.J., *Surfactants and Interfacial Phenomena*, second ed., Wiley, New York, 1989.
- [163] Rotenberg, Y., Boruvka, L., Neumann, A.W., Determination of Surface Tension and Contact Angle from the Shapes of Axisymmetric Fluid Interfaces, *J. of Colloid and Interface Sci.* 93 (1983) (1) 169-183.
- [164] Sander, W., *Z. Phys. Chem., Stoechiom. Verwandtschaftsl.* 78 (1912) 513-549.
- [165] Schiemann, H., *Die Grenzflächenspannung von Lipiden in Gegenwart dichter Gase*, PhD thesis, Universität Erlangen-Nürnberg, 1993.
- [166] Schnabel, G., *Bestimmung des örtlichen Wärmeüberganges bei der Fallfilmverdampfung und Kondensation an gewellten Oberflächen zur Auslegung von Hochleistungsverdampfern*, PhD thesis, Universität Karlsruhe, 1980.
- [167] Schulze, H., *Fallfilmverdampfung und Kondensation an glatten und längsprofilierten Rohren*, PhD thesis, Universität Bochum, 1984.
- [168] Schwuger, M.J., *Lehrbuch der Grenzflächenchemie*, Georg Thieme Verlag Stuttgart New York, 1996.
- [169] Shagiakhmetov, R.A., Tarzimanov, A.A., Deposited Document SPSTL 200 khp-D 81-1982 (1981).
- [170] Shaver, R.D., Robinson Jr., R.L., Gasem, K.A.M., An Automated Apparatus for Equilibrium Phase Compositions, Densities, and Interfacial Tensions: Data for Carbon Dioxide + Decane, *Fluid Phase Equilib.* 179 (2001) 43-66.
- [171] Shinoda, K., Friberg S., *Adv. Colloid Interface Sci.* 4 (1975) 285.
- [172] Shuttleworth, R., Bailey, L., *Discuss. Faraday Soc.* 3 (1948) 16.
- [173] Simoes, P.C., Eggers, R., Jaeger, P.T., Interfacial Tension of Edible Oils in Supercritical Carbon Dioxide, *Eur. J. Lipid Sci. Technol.* (2000) 263-265.
- [174] Sinanoglu, O., *Intermolecular Forces*, Hirschfelder, J.O. (Eds.), Wiley-Interscience, New York, 1967.
- [175] Smyth, C.P., *Dielectric Behavior and Structure*, McGraw-Hill, New York, 1955.
- [176] Song, B., Springer, J., Determination of Interfacial Tension from the Profile of a Pendant Drop Using Computer-Aided Image Processing. 1. Theoretical, *J. of Colloid and Interface Sci.* 184 (1996) 64-76.
- [177] Stahl, E. Quirin, K. W., Gerard, D., *Verdichtete Gase zur Extraktion und Raffination*, Springer Verlag, Berlin, Heidelberg, 1987.
- [178] Starkweather, B. A., Xiaoguang, S. Z., Counce, R. M., An Experimental Study of the Change in the Contact Angle of an Oil on a Solid Surface, *Ind. Eng. Chem. Res.* 39 (2000) 362-366.

- [179] Stockfleth, R., Brunner, G., Film Thickness, Flow Regimes, and Flooding in Countercurrent Annular Flow of a Falling Film at High Pressures, *Ind. Eng. Chem. Res.* 40 (2001) 6014-6020.
- [180] Stockfleth, R., *Fluidodynamik in Hochdruckgegenstromkolonnen für Gasextraktion*, PhD thesis, Technische Universität Hamburg-Harburg, 2002.
- [181] Sulman, H.L., *Trans. Inst. Mining Metall.* 39 (1920) 44-204.
- [182] Sutjiadi-Sia, Y., Marckmann, H., Eggers, R., Holzkecht, C., Kabelac, S., Zum Einfluss von in Flüssigkeiten unter Druck gelösten Gasen auf Grenzflächenspannungen und Benetzungseigenschaften. *Forsch. Ingenieurwes.* 71 (2007) 29-45.
- [183] Suzuki, K., Sue, H., Itou, M., Smith, R.L., Inomata, H., Arai, K., Saito, S., Isothermal Vapor-Liquid Equilibrium Data for Binary Systems at High Pressures: Carbon Dioxide-Methanol, Carbon Dioxide-Ethanol, Carbon Dioxide-1-Propanol, Methane-Ethanol, Methane-1-Propanol, Ethane-Ethanol, and Ethane-1-Propanol Systems, *J. Chem. Eng. Data* 35 (1990) (1) 63-66.
- [184] Tate, T., *Phil. Mag.*, 27 (1864) 176.
- [185] Tegetmeier, A., Dittmar, D., Fredenhagen, A., Eggers, R., Density and Volume of Water and Triglyceride Mixtures in Contact with Carbon Dioxide, *Chem. Eng. Process* 39 (5) (2000) 399-405.
- [186] Timmons, C.O., Zisman, W.A., The Effect of Liquid Structure on Contact Angle Hysteresis, *J. of Colloid and Interface Sci.* 22 (1966) 165-171.
- [187] Towell, G.D., Rothfeld, L.B., Hydrodynamics of Rivulet Flow, *AIChE Journal* 12 (5) (1966) 972-980.
- [188] Trela, M., A Semi-Theoretical Model of Stability of Vertical Falling Liquid Films, *Chem. Eng. Sci.* 49 (1994) (7) 1007-1013.
- [189] van der Avoird, A., Hofelich, F., Second-Order Interactions between Polar Molecules, *J. Chem. Phys.* 47 (1967) 1563.
- [190] Vogel, W., *Glaschemie*, second ed., VEB Deutscher Verlag für Grundstoffindustrie, Leipzig, 1983.
- [191] von Seggern, D.H., *CRC Standard Curves and Surfaces with Mathematica*, second ed., Chapman & Hall/CRC, 2007.
- [192] Wasden, F.K., Dukler, A.E., Insights in to the Hydrodynamics of Free Falling Wavy Films, *AIChE Journal* 35 (2) (1989) 187-195.
- [193] Wenzel, R.N., *Industr. Eng. Chem.* 28 (1936) 988.
- [194] Wesch, A., *Grenzflächen und Tropfenphänomene in überkritischem Kohlendioxid*, PhD thesis, Forschungszentrum Karlsruhe. Technik und Umwelt, 1997.
- [195] Wiebe, R., Gaddy, V.L., The Solubility in Water of Carbon Dioxide at 50, 75, and 100o, at Pressures to 700 Atmospheres, *J. Am. Chem. Soc.* 61 (1939) 315-318.

-
- [196] Wiebe, R., Gaddy, V.L., The Solubility of Carbon Dioxide in Water at Various Temperatures from 12 to 40° and at Pressures to 500 atm, *Am. Chem. Soc.* 62 (1940) 815-817.
- [197] Wiegand, G., Messung der Grenzflächenspannung binärer wäßriger Systeme bei hohen Drücken und Temperaturen, PhD thesis, Universität Karlsruhe, 1993.
- [198] Wilhemy, L., *Ann. Phys.* 119 (1863) 177.
- [199] Wilp, C., Eggers, R., Hochdruckextraktion mit mehrstufiger fraktionierender Separation zur schonenden Gewinnung von Keimölen mit hochverdichtetem Kohlendioxid, *Fat Sci. Technol.* 9 (1991) 348-354.
- [200] Woronow, E.G., Die minimale Reynoldszahl bei Rieselfilmapparaten, *BWK* 44 (5) (1992) 201-205.
- [201] Wünsch, V., *Differentialgeometrie : Kurven und Flächen*, Teubner, Stuttgart, 1997.
- [202] Yang, D., Tontiwachwuthikul, P., Gu, Y., Interfacial Tensions of the Crude Oil + Reservoir Brine + CO₂ Systems at Pressures up to 31 MPa and Temperatures of 27°C and 58°C, *J. Chem. Eng. Data*, 50 (2005) 1242-1249.
- [203] Yoon, J.H., Lee H.S., Lee, H., High-Pressure Vapor-Liquid Equilibria for Carbon Dioxide + methanol, Carbon-Dioxide + Ethanol and Carbon Dioxide + Methanol + Ethanol, *J. Chem. Eng. Data* 38 (1993) (1) 53-55.
- [204] Young, T., An Essay on the Cohesion of Fluids, *Philosophical transactions of the Royal Society of London*, 95 (1805) 65-87.
- [205] Young, T., *Miscellaneous Works*, G. Peacock., J. Murray, London, 1855.
- [206] Zacchi, P., Calvo Bastida, S., Jaeger, P., Cocero, M. J., Eggers, R., Countercurrent De-Acidification of Vegetable Oils Using Supercritical CO₂: Holdup and RTD Experiments, in: *Proceedings of I. Iberoamerican Conference on Supercritical Fluids*, April 10th-13th 2007- Iguazu Falls, Brazil.
- [207] Zisman, W.A., Influence of Constitution on Adhesion, *Industrial and Engineering Chemistry* 55 (1963) (10) 19-39.
- [208] Zisman, W.A., Relation of Equilibrium Contact Angle to Liquid and Solid Constitution, *Advances in Chem. Ser.* 43 (1964) 1-51.

11 Appendix

11.1 Single Drop

Liquid-Vapour Interfacial Tension

Table 11-1: Interfacial tension σ_{lv} of water drop embedded in pressurized CO₂.

T	p	ρ_{conti}	ρ_{drop}	σ_{lv}	T	p	ρ_{conti}	ρ_{drop}	σ_{lv}
[K]	[MPa]	[g/ml]	[g/ml]	[mN/m]	[K]	[MPa]	[g/ml]	[g/ml]	[mN/m]
294	0.1	0.0020	0.9983	70.32	353	0.1	0.0015	0.9721	60.97
	2	0.0406	1.0040	57.27		2	0.0318	0.9773	55.33
	4	0.0966	1.0040	46.69		4	0.0680	0.9826	50.01
	6	0.7678	1.0142	34.38		6	0.1101	0.9876	44.67
	8	0.8186	1.0189	25.92		8	0.1603	0.9922	41.21
	10	0.8490	1.0230	24.53		10	0.2216	0.9963	36.17
313	0.1	0.0017	0.9992	66.17	373	0.1	0.0014	0.9586	57.1
	2	0.0371	0.9976	59.99		2	0.0298	0.9637	52.17
	4	0.0838	1.0030	50.5		4	0.0627	0.9690	48.04
	6	0.1490	1.0081	40.47		6	0.0996	0.9739	44.3
	8	0.2780	1.0128	29.4		8	0.1413	0.9784	40.57
	10	0.6290	1.0170	21.6		10	0.1886	0.9825	36.53
333	0.1	0.0016	0.9835	63.86					
	2	0.0342	0.9887	57.35					
	4	0.0747	0.9941	50.73					
	6	0.1249	0.9992	44.33					
	8	0.1916	1.0038	38.54					
	10	0.2900	1.0080	32.46					

Table 11-2: Interfacial tension σ_{iv} of ethanol drop embedded in pressurized CO₂.

T [K]	p [MPa]	ρ_{conti} [g/ml]	ρ_{drop} [g/ml]	σ_{iv} [mN/m]
294	0.1	0.002	0.7883	22.13
	2	0.041	0.7899	16.85
	4	0.097	0.7916	10.07
	5	0.1407	0.7924	6.74
373	2	0.0298	0.713	13.53
	4	0.0627	0.7159	10.57
	6	0.0996	0.7187	8.19
	8	0.1413	0.7214	6.05
	10	0.1886	0.724	3.57

Table 11-3: Equilibrium interfacial tension σ_{iv} of water drop embedded in CO₂-ethanol mixture ($y_{ethanol} = 9.1\text{-wt}\%$).

T [K]	p [MPa]	ρ_{conti} [g/ml]	ρ_{drop} [g/ml]	σ_{iv} [mN/m]
313	3	0.0589	1.001	33.45
	6	0.1493	1.008	19.50
	10	0.6286	1.017	7.42
	12	0.7178	1.021	7.77
	15	0.7802	1.025	4.03
	18	0.8195	1.029	4.50
	21	0.8488	1.032	4.48
	24	0.8725	1.034	4.82
	27	0.8925	1.035	4.66

Table 11-4: Equilibrium interfacial tension σ_{iv} of water drop embedded in CO₂-ethanol mixture ($y_{ethanol} = 16.7\text{-wt}\%$).

T [K]	p [MPa]	ρ_{conti} [g/ml]	ρ_{drop} [g/ml]	σ_{iv} [mN/m]
313	3	0.0589	1.001	36.10
	6	0.1493	1.008	25.37
	10	0.6286	1.017	2.95
	12	0.7178	1.021	1.27

Sessile Drop Contact AngleTable 11-5: Sessile water drop contact angle on a Teflon surface in CO₂-environment.

T [K]	p [MPa]	θ [°]		T [K]	p [MPa]	θ [°]	
		static	dynamic			static	dynamic
294	0.1	92.4	100.0	333	0.1	99.3	100.4
294	2	98.4	106.4	333	2	96.8	95.8
294	4	101.4	121.8	333	4	99.5	110.6
294	6	127.4	131.9	333	6	108.9	117.4
294	8	135.6	148.4	333	8	124.1	123.7
294	10	140.4	159.1	333	10	126.5	131.9
313	0.1	75.1	92.1	353	0.1	91.8	93.5
313	3	97.0	112.0	353	2	97.2	98.4
313	6	124.7	132.0	353	4	101.1	112.5
313	9	131.5	152.0	353	6	112.6	118.3
313	12	147.1		353	8	117.6	121.7
313	15	155.0		353	10	129.7	131.9
313	18	153.8					
313	21	152.9		373	0.1	87.5	93.7
313	24	151.3		373	2	91.8	88.3
313	27	147.7		373	4	102	98.3
				373	6	105.7	112.8
				373	8	112.4	119.0
				373	10	125.6	119.1

Table 11-6: Sessile water drop contact angle on steel surfaces in CO₂-environment.

T [K]	p [MPa]	$\theta_{\text{static}} [^\circ]$	
		R _a =0.24 μm	R _a =2.56 μm
313	0.1	70.96	-
313	3	86.11	75.23
313	6	102.55	78.04
313	9	106.39	107.38
313	12	114.51	112.97
313	15	113.95	127.60
313	18	115.51	101.70
313	21	119.13	109.18
313	24	122.67	119.22
313	27	119.58	115.24

Table 11-7: Sessile water drop contact angle on a glass surface in CO₂-environment.

T [K]	p [MPa]	$\theta [^\circ]$		T [K]	p [MPa]	$\theta [^\circ]$ static
		static	dynamic			
294	0.1	49.1	49.5	333	0.1	51.2
294	2	50.8	53.2	333	2	55.1
294	4	51.3	66.3	333	4	54.5
294	6	71.1	66.6	333	6	47.9
294	8	72.2	96.6	333	8	53.7
294	10	81.8	91.9	333	10	59.7
313	0.1	30.8	73.1	353	0.1	40.0
313	3	40.3	66.6	353	2	46.2
313	6	46.1	75.8	353	4	52.1
313	9	77.0	95.0	353	6	47.5
313	12	65.8		353	8	52.9
313	15	73.9		353	10	51.7
313	18	77.9				
313	21	73.6		373	0.1	34.4
313	24	68.8		373	2	37.0
313	27	73.8		373	4	36.4
				373	6	47.1
				373	8	50.3
				373	10	46.6

Table 11-8: Ethanol sessile drop contact angle on a Teflon surface in CO₂-environment.

T	p	θ [°]		T	p	θ [°]	
		static	dynamic			static	dynamic
294	0.1	23.8	34.8	353	0.1	-	31.8
294	2	22.7	37.0	353	2	23.8	31.3
294	4	7	15.0	353	4	15.0	30.3
294	6	7	8.7	353	6	7.0	22.4
				353	8	5.0	14.5
313	0.1	0	32.4	353	10	0.0	0
313	2	0	27.9				
313	4	0	21.6	373	2	17.1	29.4
313	6	0	20.0	373	4	11.5	27.3
				373	6	7	18.5
333	0.1	22.9	34.3	373	8	5	0
333	2	25.5	31.0	373	10	0	0
333	4	22.7	31.2				
333	6	13.2	19.6				
333	8	7	0				
333	10	0	0				

Table 11-9: Ethanol sessile drop contact angle on a steel surface ($R_a=0.24 \mu\text{m}$) in CO₂-environment.

T	p	θ_{static}
[K]	[MPa]	[°]
313	0.1	0
313	3	0
313	6	0
313	9	0
313	12	0
313	15	0
313	18	0
313	21	0
313	24	0
313	27	0

Table 11-10: Ethanol sessile drop contact angle on a glass surface in CO₂-environment.

T	p	θ [°]	T	p	θ [°]
[K]	[MPa]	static	[K]	[MPa]	static
294	0.1	0	333	0.1	0
294	2	0	333	2	0
294	4	0	333	4	0
294	6	0	333	6	0
294	8	0	333	8	0
294	10	0	333	10	0
313	0.1	0	353	0.1	0
313	3	0	353	2	0
313	6	0	353	4	0
313	9	0	353	6	0
313	12	0	353	8	0
313	15	0	353	10	0
313	18	0			
313	21	0	373	0.1	0
313	24	0	373	2	0
313	27	0	373	4	0
			373	6	0
			373	8	0
			373	10	0

Solid-Vapour Interfacial Tension

Table 11-11: Molecular properties used to calculate the interaction parameter Φ_{sl}.

	μ	μ	I	I	α	α
	[D]	[Cm]	[eV]	[J]	[10 ⁻²⁴ cm ³]	[Cm ² /V]
H ₂ O	1.8546	6.186E-30	12.6206	2.019E-18	1.45	1.613E-40
Ethanol	1.72	5.737E-30	10.43	1.669E-18	5.11	5.686E-40
CO ₂	0	0	13.773	2.204E-18	2.911	3.239E-40
Teflon	1.2	4.000E-30	10.12	1.619E-18	3.84	4.273E-40
Glass	7.954	2.653E-29	11.49	1.838E-18	2.84	3.161E-40
Steel	3.880	1.294E-29	7.705	1.233E-18	8.885	9.886E-40

Table 11-12: Interfacial tension σ_{sv} and σ_{sl} calculated with help of the interaction parameter Φ_{sl} for the system: water-Teflon-CO₂.

T	p	θ	σ_{lv}	Φ_{sl}	σ_{sv}	σ_{sl}
[K]	[MPa]	[°]	[mN/m]	[-]	[mN/m]	[mN/m]
313	0.1	75.08	73.82	0.754	51.28	32.27
313	3	96.95	61.40	0.763	20.36	27.79
313	6	124.74	48.54	0.769	3.79	31.46
313	9	131.53	35.69	0.772	1.70	25.36
313	12	147.08	26.05	0.773	0.28	22.14
313	15	155.00	26.17	0.774	0.10	23.81
313	18	153.83	26.29	0.774	0.12	23.71
313	21	152.91	26.41	0.775	0.13	23.64
313	24	151.30	26.41	0.775	0.17	23.33
313	27	147.73	26.41	0.776	0.26	22.59

Table 11-13: Interfacial tension σ_{sv} and σ_{sl} calculated with help of the interaction parameter Φ_{sl} for the system: water-glass-CO₂.

T	p	θ	σ_{lv}	Φ_{sl}	σ_{sv}	σ_{sl}
[K]	[MPa]	[°]	[mN/m]	[-]	[mN/m]	[mN/m]
313	0.1	30.76	73.82	0.8951	79.64	16.20
313	3	40.33	61.40	0.8951	59.50	12.70
313	6	46.07	48.54	0.8951	43.46	9.78
313	9	77.04	35.69	0.8951	16.69	8.69
313	12	65.84	26.05	0.8951	16.14	5.48
313	15	73.94	26.17	0.8951	13.31	6.07
313	18	77.91	26.29	0.8951	12.00	6.49
313	21	73.58	26.41	0.8951	13.56	6.09
313	24	68.80	26.41	0.8951	15.28	5.73
313	27	73.80	26.41	0.8951	13.48	6.11

Table 11-14: Interfacial tension σ_{sv} and σ_{sl} calculated with help of the interaction parameter Φ_{sl} for the system: water-steel-CO₂. Roughness of the steel $R_a=0.24 \mu\text{m}$.

T	p	θ	σ_{lv}	Φ_{sl}	σ_{sv}	σ_{sl}
[K]	[MPa]	[°]	[mN/m]	[-]	[mN/m]	[mN/m]
313	0.1	70.96	73.82	0.9916	33.01	8.93
313	3	86.11	61.40	0.9918	17.79	13.63
313	6	102.55	48.54	0.9918	7.56	18.11
313	9	106.39	35.69	0.9917	4.68	14.75
313	12	114.51	26.05	0.9917	2.27	13.07
313	15	113.95	26.17	0.9917	2.35	12.97
313	18	115.51	26.29	0.9917	2.17	13.49
313	21	119.13	26.41	0.9917	1.77	14.62
313	24	122.67	26.41	0.9917	1.42	15.68
313	27	119.58	26.41	0.9917	1.72	14.76

Table 11-15: Interfacial tension σ_{sv} and σ_{sl} calculated with help of the interaction parameter Φ_{sl} for the system: ethanol-Teflon-CO₂.

T	p	θ	σ_{lv}	Φ_{sl}	σ_{sv}	σ_{sl}
[K]	[MPa]	[°]	[mN/m]	[-]	[mN/m]	[mN/m]
313	0.1	0	20.30	0.9654	21.78	1.48
313	3	0	13.25	0.9626	14.30	1.05
313	6	0	5.95	0.9586	6.48	0.52

Table 11-16: Interfacial tension σ_{sv} and σ_{sl} calculated with help of the interaction parameter Φ_{sl} for the system: ethanol-glass-CO₂.

T	p	θ	σ_{lv}	Φ_{sl}	σ_{sv}	σ_{sl}
[K]	[MPa]	[°]	[mN/m]	[-]	[mN/m]	[mN/m]
313	0.1	0	20.30	0.4896	84.67	64.37
313	3	0	13.25	0.4896	55.25	42.01
313	6	0	5.95	0.4896	24.82	18.87

Table 11-17: Interfacial tension σ_{sv} and σ_{sl} calculated with help of the interaction parameter Φ_{sl} for the system: ethanol-steel-CO₂. Roughness of the steel $R_a = 0.24 \mu\text{m}$.

T	p	θ	σ_{lv}	Φ_{sl}	σ_{sv}	σ_{sl}
[K]	[MPa]	[°]	[mN/m]	[-]	[mN/m]	[mN/m]
313	0.1	0	20.30	0.8295	29.50	9.21
313	3	0	13.25	0.7699	22.35	9.10
313	6	0	5.95	0.6918	12.43	6.48

11.2 Rivulet

Rivulet Geometry

Table 11-18: Water film draining along a vertical glass surface embedded in CO₂-environment at 313 K. Film mass flow up to 1.24 g/min.

p	\dot{m}	ρ_f	ρ_{conti}	δ_f	width	θ_0	R	\bar{w}_{exp}
[MPa]	[g/min]	[g/ml]	[g/ml]	[mm]	[mm]	[°]	[mm]	[cm/s]
0.1	0.05	0.9922	0.0017	0.10	1.35	17.2	2.29	0.94
0.1	0.10	0.9922	0.0017	0.10	1.72	13.8	3.61	1.46
0.1	0.21	0.9922	0.0017	0.14	1.35	24.1	1.66	2.65
0.1	0.31	0.9922	0.0017	0.18	1.79	22.3	2.35	2.46
0.1	0.41	0.9922	0.0017	0.20	1.84	24.0	2.26	2.87
0.1	0.62	0.9922	0.0017	0.22	2.00	25.2	2.35	3.46
0.1	0.83	0.9922	0.0017	0.19	2.09	20.2	3.03	5.32
3	0.83	0.9935	0.0589	0.15	1.27	27.4	1.38	10.44
3	0.93	0.9935	0.0589	0.17	1.40	27.8	1.50	9.51
18	0.93	0.9999	0.8195	0.22	1.47	33.9	1.31	6.98
0.1	1.03	0.9922	0.0017	0.19	2.69	15.9	4.90	5.12
3	1.03	0.9935	0.0589	0.18	1.39	28.8	1.45	10.33
6	1.03	0.9948	0.1493	0.09	1.02	20.5	1.45	27.61
12	1.03	0.9974	0.7178	0.25	1.71	32.4	1.59	6.01
18	1.03	0.9999	0.8195	0.50	1.58	64.1	0.88	3.06
9	1.24	0.9961	0.4855	0.25	1.07	50.8	0.69	11.06
12	1.24	0.9974	0.7178	0.38	1.52	53.1	0.95	5.16
15	1.24	0.9987	0.7802	0.36	1.69	46.3	1.17	4.92
18	1.24	0.9999	0.8195	0.43	1.63	56.1	0.98	4.15

Table 11-19: Water film draining along a vertical glass surface embedded in CO₂-environment at 313 K. Film mass flow between 1.45 g/min and 1.86 g/min.

p	\dot{m}	ρ_f	ρ_{conti}	δ_f	width	θ_0	R	\bar{w}_{exp}
[MPa]	[g/min]	[g/ml]	[g/ml]	[mm]	[mm]	[°]	[mm]	[cm/s]
3	1.45	0.9935	0.0589	0.13	1.63	18.8	2.52	16.52
9	1.45	0.9961	0.4855	0.29	1.02	58.6	0.60	11.77
12	1.45	0.9974	0.7178	0.36	1.62	48.0	1.09	5.99
15	1.45	0.9987	0.7802	0.37	1.76	46.0	1.22	5.32
18	1.45	0.9999	0.8195	0.44	1.98	48.1	1.33	3.99
21	1.45	1.0012	0.8488	0.49	2.07	51.0	1.33	3.39
6	1.55	0.9948	0.1493	0.19	1.11	37.2	0.92	18.32
9	1.65	0.9961	0.4855	0.19	1.11	38.5	0.89	18.86
15	1.65	0.9987	0.7802	0.49	1.98	52.7	1.24	4.09
18	1.65	0.9999	0.8195	0.43	2.08	45.3	1.46	4.43
21	1.65	1.0012	0.8488	0.59	1.91	63.5	1.07	3.42
24	1.65	1.0024	0.8725	0.53	2.36	48.2	1.58	3.18
9	1.86	0.9961	0.4855	0.34	1.30	55.7	0.79	9.88
12	1.86	0.9974	0.7178	0.37	1.72	46.8	1.18	7.01
15	1.86	0.9987	0.7802	0.39	1.81	46.0	1.26	6.44
18	1.86	0.9999	0.8195	0.37	2.04	40.2	1.58	5.95
21	1.86	1.0012	0.8488	0.57	2.13	56.1	1.28	3.63
24	1.86	1.0024	0.8725	0.52	2.48	45.9	1.72	3.45
27	1.86	1.0037	0.8925	0.51	2.46	44.9	1.74	3.59

Table 11-20: Water film draining along a vertical glass surface embedded in CO₂-environment at 313 K. Film mass flow between 2.07 g/min and 3.1 g/min.

p	\dot{m}	ρ_f	ρ_{conti}	δ_f	width	θ_0	R	\bar{w}'_{exp}
[MPa]	[g/min]	[g/ml]	[g/ml]	[mm]	[mm]	[°]	[mm]	[cm/s]
0.1	2.07	0.9922	0.0017	0.12	2.68	10.3	7.50	16.15
3	2.07	0.9935	0.0589	0.19	1.90	22.5	2.48	14.41
6	2.07	0.9948	0.1493	0.27	1.61	36.5	1.35	11.94
9	2.07	0.9961	0.4855	0.22	1.46	32.9	1.34	16.27
12	2.07	0.9974	0.7178	0.44	1.66	55.9	1.00	6.74
15	2.07	0.9987	0.7802	0.40	2.15	40.5	1.65	5.92
18	2.07	0.9999	0.8195	0.40	1.91	45.3	1.34	6.57
21	2.07	1.0012	0.8488	0.47	2.22	46.2	1.54	4.74
24	2.07	1.0024	0.8725	0.51	2.43	45.4	1.71	4.03
27	2.07	1.0037	0.8925	0.85	2.51	68.2	1.35	2.23
18	2.58	0.9999	0.8195	0.63	2.13	61.6	1.21	4.47
21	2.58	1.0012	0.8488	0.68	2.22	63.3	1.24	3.97
24	2.58	1.0024	0.8725	0.52	2.87	39.7	2.24	4.23
27	2.58	1.0037	0.8925	0.52	2.74	42.0	2.05	4.36
18	3.10	0.9999	0.8195	0.56	1.99	59.2	1.16	6.50
21	3.10	1.0012	0.8488	0.60	2.20	57.4	1.31	5.53
24	3.10	1.0024	0.8725	0.52	2.57	44.0	1.85	5.61
27	3.10	1.0037	0.8925	0.81	2.94	57.7	1.74	3.07

Table 11-21: Saturated water film draining along a vertical glass surface embedded in CO₂-environment at 313 K. Film mass flow up to 2.07 g/min.

p	\dot{m}	ρ_f	ρ_{conti}	δ_f	width	θ_0	R	\bar{w}_{exp}
[MPa]	[g/min]	[g/ml]	[g/ml]	[mm]	[mm]	[°]	[mm]	[cm/s]
9	1.24	1.015	0.486	0.29	1.12	54.3	0.69	8.99
3	1.45	1.001	0.059	0.14	1.59	19.9	2.34	16.16
9	1.45	1.015	0.486	0.36	1.15	63.8	0.64	8.05
6	1.55	1.008	0.149	0.23	1.68	30.5	1.65	9.85
9	1.65	1.015	0.486	0.29	1.13	54.4	0.70	11.74
12	1.65	1.021	0.718	0.45	1.49	62.4	0.84	5.63
15	1.65	1.025	0.780	0.46	1.66	57.7	0.98	5.02
21	1.65	1.032	0.849	0.58	1.81	65.3	1.00	3.53
24	1.65	1.034	0.872	0.68	2.22	62.6	1.25	2.49
9	1.86	1.015	0.486	0.34	1.31	54.6	0.80	9.88
12	1.86	1.021	0.718	0.46	1.54	61.9	0.87	5.96
15	1.86	1.025	0.780	0.45	1.65	57.1	0.98	5.82
18	1.86	1.029	0.820	0.51	2.16	50.8	1.39	3.92
21	1.86	1.032	0.849	0.69	2.21	64.2	1.23	2.74
24	1.86	1.034	0.872	0.47	2.18	47.0	1.49	4.21
3	2.07	1.001	0.059	0.28	1.75	35.5	1.51	10.31
6	2.07	1.008	0.149	0.22	1.68	29.1	1.73	13.82
9	2.07	1.015	0.486	0.34	1.16	61.3	0.66	11.93
12	2.07	1.021	0.718	0.45	1.70	55.5	1.03	6.36
15	2.07	1.025	0.780	0.43	2.19	42.7	1.61	5.24
18	2.07	1.029	0.820	0.55	2.23	52.3	1.41	3.94
21	2.07	1.032	0.849	0.63	2.18	60.0	1.26	3.43
24	2.07	1.034	0.872	0.49	2.19	48.5	1.46	4.45

Table 11-22: Saturated water film draining along a vertical glass surface embedded in CO₂-environment at 313 K. Film mass flow between 2.58 g/min and 3.62 g/min.

p	\dot{m}	ρ_f	ρ_{conti}	δ_f	width	θ_0	R	\bar{w}_{exp}
[MPa]	[g/min]	[g/ml]	[g/ml]	[mm]	[mm]	[°]	[mm]	[cm/s]
3	2.58	1.001	0.059	0.20	1.59	28.6	1.65	19.88
6	2.58	1.008	0.149	0.19	1.99	21.3	2.74	17.07
9	2.58	1.015	0.486	0.25	1.34	41.0	1.02	18.37
12	2.58	1.021	0.718	0.49	1.60	62.9	0.90	7.56
15	2.58	1.025	0.780	0.47	2.35	43.4	1.71	5.56
18	2.58	1.029	0.820	0.67	2.18	63.3	1.22	4.00
21	2.58	1.032	0.849	0.60	2.16	58.4	1.27	4.52
24	2.58	1.034	0.872	0.70	2.17	65.9	1.19	3.79
6	2.89	1.008	0.149	0.27	1.33	44.0	0.96	19.48
12	2.89	1.021	0.718	0.64	1.70	74.0	0.88	5.90
3	3.10	1.001	0.059	0.22	1.64	30.4	1.62	20.80
6	3.10	1.008	0.149	0.17	1.13	32.9	1.04	40.26
9	3.10	1.015	0.486	0.28	1.57	38.7	1.26	17.16
12	3.10	1.021	0.718	0.45	1.78	53.8	1.11	8.97
15	3.10	1.025	0.780	0.50	2.33	46.2	1.61	6.30
18	3.10	1.029	0.820	0.49	2.18	48.4	1.45	6.81
21	3.10	1.032	0.849	0.51	2.33	47.1	1.59	6.13
24	3.10	1.034	0.872	0.58	2.26	54.7	1.39	5.39
3	3.62	1.001	0.059	0.42	2.02	44.8	1.44	10.37
6	3.62	1.008	0.149	0.32	1.16	57.8	0.68	22.93
9	3.62	1.015	0.486	0.39	1.56	52.9	0.98	14.05
12	3.62	1.021	0.718	0.45	1.85	51.9	1.18	10.20
15	3.62	1.025	0.780	0.45	2.37	41.9	1.78	7.98
18	3.62	1.029	0.820	0.51	2.18	50.2	1.41	7.60
21	3.62	1.032	0.849	0.60	2.24	56.8	1.34	6.13
24	3.62	1.034	0.872	0.63	2.23	58.7	1.30	5.91

Table 11-23: Water film draining along a vertical steel surface embedded in CO₂-environment at 313 K.

p [MPa]	\dot{m} [g/min]	ρ_f [g/ml]	ρ_{conti} [g/ml]	δ_f [mm]	width [mm]	θ_0 [°]	R [mm]	\bar{w}_{exp} [cm/s]
0.1	3	0.9922	0.0017	0.30	1.15	55.8	0.69	20.5
0.1	6	0.9922	0.0017	0.41	1.18	69.4	0.63	28.6
0.1	9	0.9922	0.0017	0.38	1.63	50.3	1.06	34.4
3	3	0.9935	0.0589	0.34	0.96	71.4	0.50	20.8
3	6	0.9935	0.0589	0.38	1.25	62.8	0.70	29.4
3	9	0.9935	0.0589	0.42	1.32	64.4	0.73	37.9
6	3	0.9948	0.1495	0.31	0.91	69.2	0.49	24.1
6	6	0.9948	0.1495	0.37	1.29	59.2	0.75	29.9
6	9	0.9948	0.1495	0.40	1.35	61.3	0.77	39.0
10	6	0.9965	0.6317	0.56	1.29	82.2	0.65	18.2
10	9	0.9965	0.6317	0.62	1.28	87.7	0.64	24.5
12	6	0.9974	0.7194	0.52	1.12	85.5	0.56	22.4
12	9	0.9974	0.7194	0.71	1.19	100.9	0.60	21.7
15	6	0.9987	0.7813	0.55	1.24	83.0	0.62	19.3
15	9	0.9987	0.7813	0.78	1.25	103.7	0.63	18.7
18	9	0.9999	0.8204	0.76	1.31	99.7	0.65	18.4
21	9	1.0012	0.8496	0.86	1.33	107.0	0.67	15.7
24	9	1.0024	0.8732	0.82	1.39	100.4	0.70	16.1
27	9	1.0037	0.8931	0.85	1.34	105.5	0.67	15.9

Table 11-24: Saturated water film draining along a vertical steel surface embedded in CO₂-environment at 313 K.

p	\dot{m}	ρ_f	ρ_{conti}	δ_f	width	θ_0	R	\bar{w}'_{exp}
[MPa]	[g/min]	[g/ml]	[g/ml]	[mm]	[mm]	[°]	[mm]	[cm/s]
3	3	1.0005	0.0589	0.34	0.86	75.7	0.45	23.2
3	6	1.0005	0.0589	0.37	1.06	69.7	0.56	35.2
3	9	1.0005	0.0589	0.40	1.19	67.6	0.65	43.4
6	3	1.0083	0.1495	0.37	0.83	83.6	0.42	21.1
6	6	1.0083	0.1495	0.39	1.05	73.4	0.55	33.0
6	9	1.0083	0.1495	0.40	1.14	69.7	0.61	45.3
10	6	1.0172	0.6317	0.46	1.21	73.8	0.63	24.5
10	9	1.0172	0.6317	0.58	1.19	88.9	0.60	27.6
12	6	1.0209	0.7194	0.49	1.00	88.5	0.50	26.4
12	9	1.0209	0.7194	0.62	1.24	90.2	0.62	24.8
15	6	1.0254	0.7813	0.54	1.12	88.2	0.56	21.2
15	9	1.0254	0.7813	0.68	1.21	97.5	0.60	22.4
18	6	1.0289	0.8204	0.56	1.08	91.6	0.54	21.0
18	9	1.0289	0.8204	0.67	1.26	93.2	0.63	22.3

Rivulet Instability

Table 11-25: Minimal water mass flow required to keep the rivulet draining along a vertical glass surface at 313 K stable.

p [MPa]	mass flow	
	pure [g/min]	sat [g/min]
0.1	0.05	
3	0.62	1.24
6	0.93	1
9	1.00	1.24
12	1.00	1.45
15	1.00	1.45
18	0.93	1.65
21	1.24	1.65
24	1.45	1.65
27	1.65	1.65

Table 11-26: Minimal water mass flow required to keep the rivulet draining along a vertical steel surface at 313 K stable.

p [MPa]	pure		presaturated	
	Mass flow [g/min]		Mass flow [g/min]	
	drop	film	drop	film
0.1	1.01	1.21		
3	1.81	2.02	1.00	1.20
6	2.22	2.42	1.21	1.81
10	3.63	3.83	1.63	2.85
12	4.23	4.64	1.84	3.27
15	4.84	5.24	2.26	3.90
18	5.44	5.85	2.88	4.32
21	5.85	6.25		
24	5.85	6.65		
27	5.85	7.66		

Curriculum Vitae

Life must be understood backward. But it must be lived forward.

Sören Kierkegaard

Persönliche Daten

Yuliana Sutjiadi-Sia

geb. 10.04.1977 in Makassar, Süd Sulawesi, Indonesien

ledig

Schulbildung

06.93-06.96 Gymnasium SMA Kolese Santo Yusup Malang

Ost Java, Indonesien

08.97-06.98 Studienkolleg Universität Hamburg

Studium

10.98-05.03 Studium der Verfahrenstechnik an der
Technischen Universität Hamburg-Harburg

Berufserfahrung und Praktika

06.98-07.98 Grundpraktikum bei der Firma Jungheinrich AG, Hamburg

04.02-09.02 Fachpraktikum bei dem Forschungszentrum der Firma
Beiersdorf AG, Hamburg

06.03-12.07 Wissenschaftliche Mitarbeiterin im Institut Thermische
Verfahrenstechnik bei Prof. Dr.-Ing. R. Eggers an der
Technischen Universität Hamburg-Harburg

01.08 Angestellt bei der BASF AG, Ludwigshafen